Disease Markers

Imaging Disease Markers as a Diagnostic, Prognostic, and Educational Tool 2021

Lead Guest Editor: Zhongjie Shi
Guest Editors: Ospan A. Mynbaev, Ioannis Kosmas, and Dong Pan

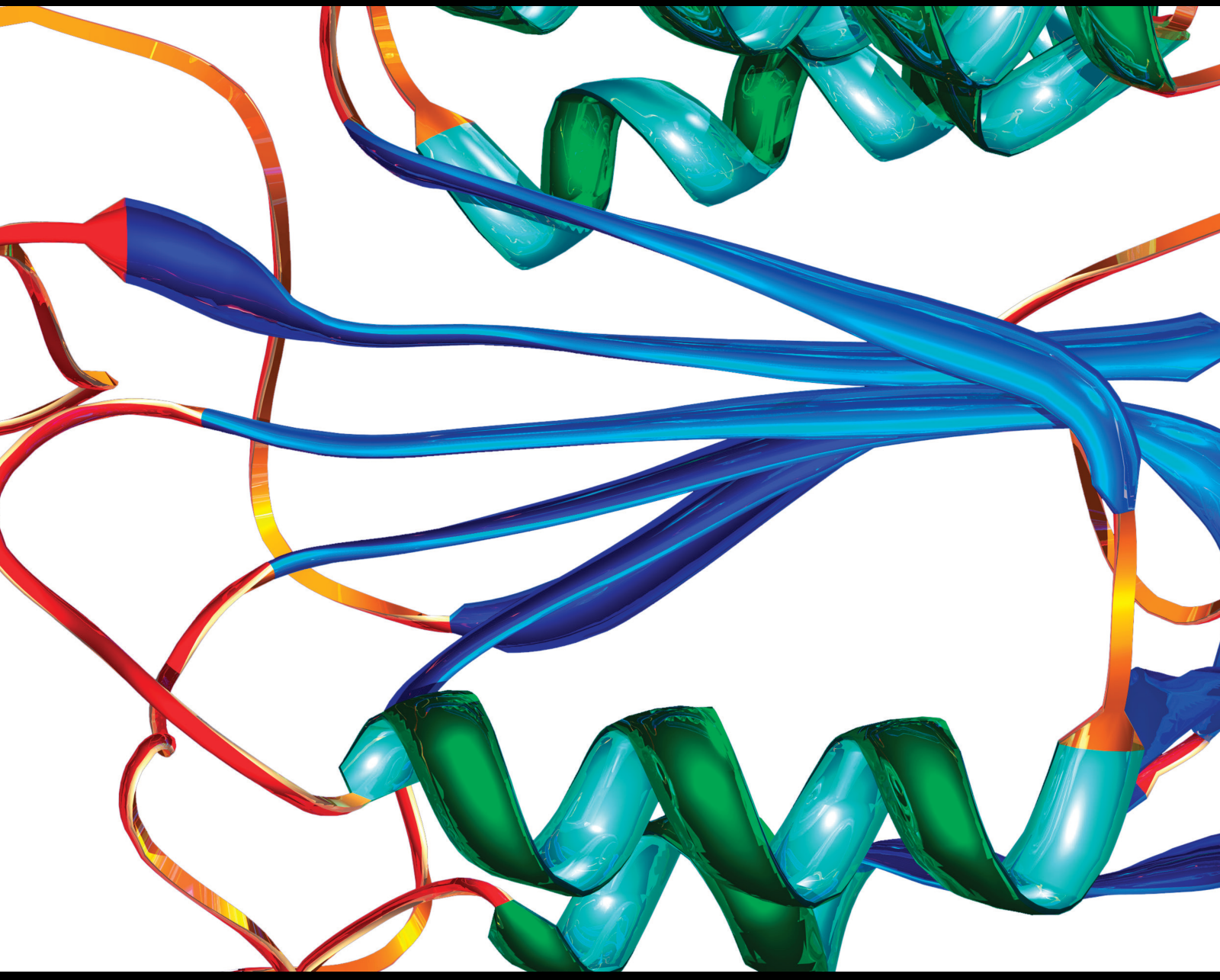

Imaging Disease Markers as a Diagnostic, Prognostic, and Educational Tool 2021

Imaging Disease Markers as a Diagnostic, Prognostic, and Educational Tool 2021

Lead Guest Editor: Zhongjie Shi
Guest Editors: Ospan A. Mynbaev, Ioannis Kosmas, and Dong Pan

Contents

Contents

Hindawi
Disease Markers
Volume 2023, Article ID 9861901, 1 page
https://doi.org/10.1155/2023/9861901

Retraction

Retracted: Pathogenic Characterization of a Porcine Circovirus Type 3 Isolate from Heilongjiang, China

Disease Markers

Received 11 July 2023; Accepted 11 July 2023; Published 12 July 2023

This article has been retracted by Hindawi following an investigation undertaken by the publisher [1]. This investigation has uncovered evidence of one or more of the following indicators of systematic manipulation of the publication process:

(1) Discrepancies in scope
(2) Discrepancies in the description of the research reported
(3) Discrepancies between the availability of data and the research described
(4) Inappropriate citations
(5) Incoherent, meaningless and/or irrelevant content included in the article
(6) Peer-review manipulation

The presence of these indicators undermines our confidence in the integrity of the article's content and we cannot, therefore, vouch for its reliability. Please note that this notice is intended solely to alert readers that the content of this article is unreliable. We have not investigated whether authors were aware of or involved in the systematic manipulation of the publication process.

Wiley and Hindawi regrets that the usual quality checks did not identify these issues before publication and have since put additional measures in place to safeguard research integrity.

We wish to credit our own Research Integrity and Research Publishing teams and anonymous and named external researchers and research integrity experts for contributing to this investigation.

The corresponding author, as the representative of all authors, has been given the opportunity to register their agreement or disagreement to this retraction. We have kept a record of any response received.

References

[1] M. Wang, Y. Yu, J. Wu et al., "Pathogenic Characterization of a Porcine Circovirus Type 3 Isolate from Heilongjiang, China," *Disease Markers*, vol. 2021, Article ID 9434944, 8 pages, 2021.

Hindawi
Disease Markers
Volume 2023, Article ID 9839325, 1 page
https://doi.org/10.1155/2023/9839325

Retraction

Retracted: Introducing V-Line as a New Strategy to Choose Surgical Corridor in Oblique Lumbar Interbody Fusion at the L5-S1 Segment

Disease Markers

Received 11 July 2023; Accepted 11 July 2023; Published 12 July 2023

This article has been retracted by Hindawi following an investigation undertaken by the publisher [1]. This investigation has uncovered evidence of one or more of the following indicators of systematic manipulation of the publication process:

(1) Discrepancies in scope
(2) Discrepancies in the description of the research reported
(3) Discrepancies between the availability of data and the research described
(4) Inappropriate citations
(5) Incoherent, meaningless and/or irrelevant content included in the article
(6) Peer-review manipulation

The presence of these indicators undermines our confidence in the integrity of the article's content and we cannot, therefore, vouch for its reliability. Please note that this notice is intended solely to alert readers that the content of this article is unreliable. We have not investigated whether authors were aware of or involved in the systematic manipulation of the publication process.

Wiley and Hindawi regrets that the usual quality checks did not identify these issues before publication and have since put additional measures in place to safeguard research integrity.

We wish to credit our own Research Integrity and Research Publishing teams and anonymous and named external researchers and research integrity experts for contributing to this investigation.

The corresponding author, as the representative of all authors, has been given the opportunity to register their agreement or disagreement to this retraction. We have kept a record of any response received.

References

[1] W. Zhang, X. Du, Y. Zhu et al., "Introducing V-Line as a New Strategy to Choose Surgical Corridor in Oblique Lumbar Interbody Fusion at the L5-S1 Segment," *Disease Markers*, vol. 2021, Article ID 5584372, 9 pages, 2021.

Hindawi
Disease Markers
Volume 2023, Article ID 9826727, 1 page
https://doi.org/10.1155/2023/9826727

Retraction

Retracted: Therapy Strategy of CD47 in Diffuse Large B-Cell Lymphoma (DLBCL)

Disease Markers

Received 11 July 2023; Accepted 11 July 2023; Published 12 July 2023

This article has been retracted by Hindawi following an investigation undertaken by the publisher [1]. This investigation has uncovered evidence of one or more of the following indicators of systematic manipulation of the publication process:

(1) Discrepancies in scope
(2) Discrepancies in the description of the research reported
(3) Discrepancies between the availability of data and the research described
(4) Inappropriate citations
(5) Incoherent, meaningless and/or irrelevant content included in the article
(6) Peer-review manipulation

The presence of these indicators undermines our confidence in the integrity of the article's content and we cannot, therefore, vouch for its reliability. Please note that this notice is intended solely to alert readers that the content of this article is unreliable. We have not investigated whether authors were aware of or involved in the systematic manipulation of the publication process.

Wiley and Hindawi regrets that the usual quality checks did not identify these issues before publication and have since put additional measures in place to safeguard research integrity.

We wish to credit our own Research Integrity and Research Publishing teams and anonymous and named external researchers and research integrity experts for contributing to this investigation.

The corresponding author, as the representative of all authors, has been given the opportunity to register their agreement or disagreement to this retraction. We have kept a record of any response received.

References

[1] W. Zhang, Y. Fan, M. Li, L. Yang, Z. Zhang, and L. Liu, "Therapy Strategy of CD47 in Diffuse Large B-Cell Lymphoma (DLBCL)," *Disease Markers*, vol. 2021, Article ID 4894022, 8 pages, 2021.

Hindawi
Disease Markers
Volume 2023, Article ID 9791279, 1 page
https://doi.org/10.1155/2023/9791279

Retraction

Retracted: The Mechanism of Xiaoyao San in the Treatment of Ovarian Cancer by Network Pharmacology and the Effect of Stigmasterol on the PI3K/Akt Pathway

Disease Markers

Received 11 July 2023; Accepted 11 July 2023; Published 12 July 2023

This article has been retracted by Hindawi following an investigation undertaken by the publisher [1]. This investigation has uncovered evidence of one or more of the following indicators of systematic manipulation of the publication process:

(1) Discrepancies in scope
(2) Discrepancies in the description of the research reported
(3) Discrepancies between the availability of data and the research described
(4) Inappropriate citations
(5) Incoherent, meaningless and/or irrelevant content included in the article
(6) Peer-review manipulation

The presence of these indicators undermines our confidence in the integrity of the article's content and we cannot, therefore, vouch for its reliability. Please note that this notice is intended solely to alert readers that the content of this article is unreliable. We have not investigated whether authors were aware of or involved in the systematic manipulation of the publication process.

Wiley and Hindawi regrets that the usual quality checks did not identify these issues before publication and have since put additional measures in place to safeguard research integrity.

We wish to credit our own Research Integrity and Research Publishing teams and anonymous and named external researchers and research integrity experts for contributing to this investigation.

The corresponding author, as the representative of all authors, has been given the opportunity to register their agreement or disagreement to this retraction. We have kept a record of any response received.

References

[1] M. Li, W. Zhang, L. Yang et al., "The Mechanism of Xiaoyao San in the Treatment of Ovarian Cancer by Network Pharmacology and the Effect of Stigmasterol on the PI3K/Akt Pathway," *Disease Markers*, vol. 2021, Article ID 4304507, 10 pages, 2021.

Hindawi
Disease Markers
Volume 2023, Article ID 9759372, 1 page
https://doi.org/10.1155/2023/9759372

Retraction

Retracted: Environmental and Genetic Factors in the Pathogenesis of COPD in the Road-Working Population

Disease Markers

Received 11 July 2023; Accepted 11 July 2023; Published 12 July 2023

This article has been retracted by Hindawi following an investigation undertaken by the publisher [1]. This investigation has uncovered evidence of one or more of the following indicators of systematic manipulation of the publication process:

(1) Discrepancies in scope
(2) Discrepancies in the description of the research reported
(3) Discrepancies between the availability of data and the research described
(4) Inappropriate citations
(5) Incoherent, meaningless and/or irrelevant content included in the article
(6) Peer-review manipulation

The presence of these indicators undermines our confidence in the integrity of the article's content and we cannot, therefore, vouch for its reliability. Please note that this notice is intended solely to alert readers that the content of this article is unreliable. We have not investigated whether authors were aware of or involved in the systematic manipulation of the publication process.

Wiley and Hindawi regrets that the usual quality checks did not identify these issues before publication and have since put additional measures in place to safeguard research integrity.

We wish to credit our own Research Integrity and Research Publishing teams and anonymous and named external researchers and research integrity experts for contributing to this investigation.

The corresponding author, as the representative of all authors, has been given the opportunity to register their agreement or disagreement to this retraction. We have kept a record of any response received.

References

[1] Y. Zhou, M. Wang, W. Yang et al., "Environmental and Genetic Factors in the Pathogenesis of COPD in the Road-Working Population," *Disease Markers*, vol. 2021, Article ID 9953234, 10 pages, 2021.

Hindawi
Disease Markers
Volume 2022, Article ID 1819841, 14 pages
https://doi.org/10.1155/2022/1819841

Review Article

The Value of Artificial Intelligence-Assisted Imaging in Identifying Diagnostic Markers of Sarcopenia in Patients with Cancer

Ying-Tzu Huang,[1] Yi-Shan Tsai,[2] Peng-Chan Lin,[1] Yu-Min Yeh,[1] Ya-Ting Hsu,[3] Pei-Ying Wu,[4] and Meng-Ru Shen[4]

[1]*Division of Medical Oncology, Department of Oncology, National Cheng Kung University Hospital, College of Medicine, National Cheng Kung University, Tainan, Taiwan*
[2]*Department of Medical Imaging, National Cheng Kung University Hospital, College of Medicine, National Cheng Kung University, Tainan, Taiwan*
[3]*Division of Hematology, Department of Internal Medicine, National Cheng Kung University Hospital, College of Medicine, National Cheng Kung University, Tainan, Taiwan*
[4]*Department of Obstetrics and Gynecology, National Cheng Kung University Hospital, College of Medicine, National Cheng Kung University, Tainan, Taiwan*

Correspondence should be addressed to Yi-Shan Tsai; n506356@gmail.com

Received 30 April 2021; Revised 15 February 2022; Accepted 14 March 2022; Published 29 March 2022

Academic Editor: Zhongjie Shi

Sarcopenia is defined as the loss of skeletal muscle mass and muscle function. It is common in patients with malignancies and often associated with adverse clinical outcomes. The presence of sarcopenia in patients with cancer is determined by body composition, and recently, radiologic technology for the accurate estimation of body composition is under development. Artificial intelligence- (AI-) assisted image measurement facilitates the detection of sarcopenia in clinical practice. Sarcopenia is a prognostic factor for patients with cancer, and confirming its presence helps to recognize those patients at the greatest risk, which provides a guide for designing individualized cancer treatments. In this review, we examine the recent literature (2017-2021) on AI-assisted image assessment of body composition and sarcopenia, seeking to synthesize current information on the mechanism and the importance of sarcopenia, its diagnostic image markers, and the interventions for sarcopenia in the medical care of patients with cancer. We concluded that AI-assisted image analysis is a reliable automatic technique for segmentation of abdominal adipose tissue. It has the potential to improve diagnosis of sarcopenia and facilitates identification of oncology patients at the greatest risk, supporting individualized prevention planning and treatment evaluation. The capability of AI approaches in analyzing series of big data and extracting features beyond manual skills would no doubt progressively provide impactful information and greatly refine the standard for assessing sarcopenia risk in patients with cancer.

1. Introduction

Sarcopenia was first introduced by Dr. Irwin Rosenberg in 1989, who described it as "age-related loss of skeletal muscle" [1]. It was initially regarded as the progressive decline in skeletal muscle mass, muscle strength, and physical performance associated with aging [2], but the definition and management of sarcopenia have expanded in recent years. In today's broader view, besides associations with aging, the shared risk factors for development of sarcopenia include chronic diseases, nutrition deficiencies, physical inactivity, hormonal changes, insulin resistance, loss of the neurons that stimulate muscle, and fat infiltration into muscle [3]. Among possible comorbidities, malignancy is a major category of disease-related sarcopenia. The causes of muscle loss in patients with cancer are multifactorial, especially in older adults [4].

Gender differences have been found in the prevalence of sarcopenia for people younger than 70 years and those older than 80 years; sarcopenia is diagnosed more often in women in those aged <70 years, while among those aged >80 years, more men will have sarcopenia than women [5]. This gender difference is clearly influenced by age, and sarcopenia must be considered when evaluating people of all ages who have cancer.

The etiology of sarcopenia in patients with cancer may vary between different ages and genders and can be associated with genetic predisposition, underlying comorbidities, reduced physical performance, and age-related declines in various hormones. Cancer-induced inflammatory cytokines and anorexia that cause decreased protein intake and synthesis and increased protein degradation may also be markers of sarcopenia in cancer patients. Treatment-related causes may include the side effects of chemotherapy, surgery, or radiotherapy [4, 6].

Sarcopenia is a prognostic factor for patients with cancer, and confirming its presence helps to recognize those patients at the greatest risk and to guide individualized cancer treatment [7]. The diagnosis of sarcopenia is determined through the assessment of body composition (analysis of adipose and muscle tissue components), and recently, artificial intelligence- (AI-) assisted image measurement is being used to facilitate the detection of sarcopenia in clinical practice [8].

The purpose of this review was to synthesize current information in recent studies addressing AI-assisted imaging assessment of body composition and sarcopenia, particularly to gain a clearer understanding of the mechanism and the importance of sarcopenia in cancer and its diagnostic image markers and interventions for sarcopenia in the medical care of patients with cancer.

2. Literature Review

We searched the recent literature in PubMed from 2017 to 2021 using ("deep learning"[MeSH Terms] OR ("deep"[All Fields] AND "learning"[All Fields]) OR "deep learning"[All Fields]) AND ("sarcopenia"[MeSH Terms] OR "sarcopenia"[All Fields]). A total of 28 articles addressing AI-assisted imaging assessment of body composition and sarcopenia were found, of which 20 reporting DICE coefficients were finally included for review. They are discussed below along with other supportive studies for background, focusing on cancer-related sarcopenia and the current status of AI-assisted imaging in the evaluation of sarcopenia in cancer patients.

2.1. The Definition/Mechanism of Sarcopenia in Cancer Patients. Complex metabolic pathways are involved in the development process of sarcopenia. Several discriminating metabolites have been identified and investigated as potential biomarkers for the presence of sarcopenia. For example, one study demonstrated that low levels of plasma lysophosphatidylcholine 18 : 2 predict a greater decline of gait speed in older adults [9]. Another study reported that increased asparagine, aspartic acid, citrulline, ethanolamine, glutamic acid, sarcosine, and taurine are found in older adult patients with sarcopenia [10]. As for patients with cancer, a serum and urine metabolomics study found that cancer-related metabolic reprograming may represent a distinct diagnostic model [11].

2.2. Diagnostic Image Markers for Sarcopenia. In clinical practice, assessment techniques for sarcopenia include handgrip strength to measure muscle strength and gait speed and chair stand tests to evaluate physical performance [12]. Bioimpedance analysis and dual-energy X-ray absorptiometry are the most common diagnostic tools for confirmation of muscle quantity and quality [13]. In the field of oncology, the use of abdominal computed tomography (CT) to measure body composition helps to identify sarcopenia in patients with cancer by providing precise and simplified data for describing sarcopenia and its correlation with clinical factors [14]. Thus, the performance of routine abdominal CT at cancer diagnosis, posttreatment evaluation, and regular follow-up provides the means for gauging body composition throughout the course of cancer.

The cross-sectional area (CSA) of muscle tissue at the level of the 3rd lumbar spine (L3) provides reproducible evaluation of muscle size in cancer patients without the need for additional examinations. The measurements collected from a single slice CT image reveal solid evidence that correlates strongly with whole-body adipose tissue and skeletal muscle [15–17]. The common method is to manually draw the total CSA of all muscle groups at L3 or to quantify the CSA using thresholds of Hounsfield units (HU) from -29 to 150 for skeletal muscle using the available software [18]. The third lumbar vertebra, L3, is chosen because it is the current gold standard for quantification of muscle mass by obtaining parameters from the analysis of a single-slice CT scan [19]. The cross-sectional skeletal muscle area (SMA) calculated at the level of L3 can correctly estimate total body muscle mass [17]. A review has shown that attempts to use alternate vertebral levels to L3 (cervical, thoracic, and lumbar CT slices) for evaluating SMA in cancer patients have shown no validation of whole-body skeletal muscle mass in various types of cancer (lung, head, and neck) and a lack of consensus [20]. The skeletal muscle index (SMI, cm^2/m^2) is calculated by dividing the CSA by the square of body height with various cut-off values according to gender and different body mass index (BMI $\geqq$ 25.0 or <25.0) [21]. The formula used was $\text{SMI} = \text{L3 skeletal muscle CSA } (cm^2)/\text{height}^2\ (m^2)$. The muscle groups for SMI consist of psoas major, paraspinal muscle, and abdominal wall muscles (Figure 1). The solitary muscle indices such as psoas muscle index (PMI) and paravertebral muscle index (PSMI) also achieve good performance for sarcopenia evaluation [16, 22, 23]. The CT-derived measurement of muscle mass is usually evaluated using the method with thresholds of HU from -29 to 150 that will limit the evaluation of myosteatosis (fat infiltrates into muscle) technologically. The patients with higher BMI had greater SMI but lower skeletal muscle density (SMD) [24, 25]. In the future, CT-derived measurement of muscle mass (area) and quality (myosteatosis) could be achieved with fully automated segmentation for contouring of muscle groups using deep learning systems [26].

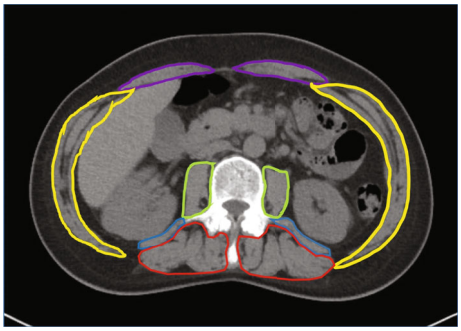

Figure 1: The muscle groups for the skeletal muscle index consist of psoas major (green), quadratus lumborum (blue), erector spinae (red), and abdominal wall muscles (transversus abdominis muscle, internal and external oblique muscle (yellow), and rectus abdominis (purple)).

2.3. The Importance of Sarcopenia in Patients with Cancer. The presence of sarcopenia in older adults may manifest as impaired daily function, disability, increased falls, risk of fractures, loss of independence, poorer quality of life, increased mortality, and high healthcare expenditures [27–31]. In patients with malignancies, sarcopenia is strongly associated with poor oncologic outcomes. A meta-analysis of 4262 participants with ovarian cancer revealed a significant association between the SMI and overall survival (OS) ($P = 0.007$; hazard ratio (HR): 1.11; 95% confidence interval (CI): 1.03-1.20) [32]. Another meta-analysis of 5497 participants with breast cancer reported similar result (pooled HR: 1.71; 95% CI: 1.25-2.33) [33].

Sarcopenia is also an independent predictor of treatment-related toxicities, including surgical complications, prolonged hospitalization, and more adverse effects of chemotherapy. A cohort study of 234 patients undergoing liver resection for malignant tumors demonstrated that sarcopenic patients had longer hospital stays (10 days vs. 6-8 days; $P < 0.001$) and more readmission (8.8% vs. 0-7.7%; $P = 0.02$) than those without sarcopenia [34]. A study of 533 patients with nonmetastatic colon cancer receiving a FOLFOX regimen reported that lower muscle mass is associated with early discontinuation of chemotherapy (odds ratio (OR): 2.34; 95% CI: 1.04-5.24; $P = 0.03$), treatment delay (OR: 2.24; 95% CI: 1.37-3.66; $P = 0.002$), and dose reduction (OR: 2.28; 95% CI: 1.19-4.36; $P = 0.01$) [35].

Body weight or BMI as an indication of body composition was previously used to predict the clinical outcomes of patients with cancer [36, 37]. Emerging evidence suggests that SMI correlates better with negative outcomes and complications than does BMI. A study of 484 patients with pancreatic cancer showed that the changes in BMI during chemotherapy did not have an impact on OS in patients with maintained SMI values ($P = 0.750$), while decreases in SMI were associated with poor OS in patients with maintained BMI (HR: 1.502; $P = 0.002$) [38]. This can be explained by the fact that patients with the same BMI may have different SMI values due to different amounts of muscle mass and differences in the level of fat infiltration. Similarly, patients with the same body surface area (BSA) but different SMI value receiving the same dose of chemotherapy may have different severity of adverse effects [39, 40].

2.4. Interventions for Sarcopenia within the Medical Care of Patients with Cancer. The prevalence of sarcopenia in patients with cancer ranges widely from 16% to 71%, depending on the definition in various study settings [7]. The understanding of the presence and the progression of sarcopenia helps to identify high-risk patients and guide the development of treatment plans. Since sarcopenia is significantly associated with treatment-related toxicity [34, 35], the dose titration of chemotherapy, the intensity of surgical intervention, and the schedule of postoperative care should be carefully assessed in sarcopenic patients. For the impact of sarcopenia on oncologic outcomes, it also implies the physician about the disease explanation, prognosis expectation, and treatment decision-making.

The interventions for sarcopenia in patients with cancer include nutritional support, resistance exercise, and specific treatments for sarcopenia and the underlying disease [6, 41–45]. Many studies support the use of nutritional supplements [45], pharmacologic agents to increase muscle mass [44], and exercise programs [42]. Some studies show conflicting results for interventions for increasing muscle mass [6, 41], and the impact of those interventions on clinical outcomes is still being investigated. Prospective studies on interventions for sarcopenia in patients with cancer are limited.

2.5. Medical AI Perspectives in the Diagnosis of Sarcopenia. The present review identified a total of 20 articles reporting DICE similarity coefficient scores [16, 19, 46–63]. Table 1 lists the included articles with the population characteristics and segmentation approaches. The reported CT threshold and DICE coefficients of these included studies ranged between 0.93 and 0.98 (Table 2), indicating great promise in the clinical application of AI-assisted imaging. However, as shown in Tables 1 and 2, there is currently no standardized methodology for assessment of sarcopenia. The slicing regions, methods of segmentation, tissues of interest, and ground truth applied varied between the studies. A total of 18 articles used deep learning methods to perform automated segmentation (16 applied fully convolutional networks (FCN) or U-Net, and 2 used ResNet-18). The region of segmentation varied across different systems, but the L3-level axial slice was analyzed most frequently due to its strong correlation with whole-body composition [19]. As reference for segmentation (ground truth), 10 studies reported use of a combination of automated or semiautomated commercial segmentation software or cloud-based annotation tool with manual correction; 1 study specified that expert-labeled annotation was used as ground truth; details of the ground truth reference was not specified in the remaining articles (Table 1). Thirteen studies reported CT threshold HU values. However, the CT threshold is likely affected by whether or not contrast medium was used for imaging. Of the 20 articles reporting DICE scores, 10 articles reported DICE coefficients for skeletal muscle only; in the other 10 articles, tissues including visceral adipose tissue, subcutaneous adipose tissue, and intermuscular adipose

Table 1: Summary of segmentation methods.

	Author (year)	Population	Mean age (year)	Localization	Neural network	Segmentation algorithm	Segmentation ground truth
1	Ackermans (2021) [19]	Cancer surgery cases, colorectal, ovarian, pancreatic cancers (training); polytrauma patients (testing)	Testing: 74	L3 muscle (L3M), intramuscular adipose tissue (IMAT), visceral adipose tissue (VAT), and subcutaneous adipose tissue (SAT)	DLNN	2D U-Net	Manual segmentation using software (TomoVision software "sliceOmatic")
2	Borrelli (2021) [51]	Lymphoma (training) Prostate cancer (testing)	Training: 61 Testing: 67	L3	CNN	RECOMIA platform U-Net	Manual segmentation using cloud-based annotation tool (RECOMIA, http://www.recomia.org)
3	Castiglione (2021) [52]	Pediatric patients	0-18	Skeletal muscle area at the L3 level; 12-section or 18-section MIP images	CNN	U-Net	Manual segmentation
4	Amarasinghe (2021) [49]	Non-small-cell lung cancer	67	Skeletal muscle at the L3 vertebra	CNN+DL	2.5D U-Nets	Manual segmentation based on the Alberta protocol
5	Kim (2021) [58]	Gastric cancers receiving gastrectomy	60.4	L3	CNN	ResNet-18	Manual segmentation with software (Aquarius 3D workstation, TeraRecon)
6	Magudia (2021) [61]	Pancreatic adenocarcinoma	52	L3	CNN	DenseNet architecture model to predict spatial offset U-Net architecture model for segment	Manual segmentation with software internal data set: sliceOmatic (TomoVision, Magog, Canada); external data set: OsiriX (Pixmeo, Bernex, Switzerland)
7	Koitka (2021) [59]	Individuals with abdominal CT scans (unknown patients)	Training: 62.6 Test: 65.6	Whole abdomen and not just on L3 slices	CNN	Multiresolution U-Net 3D	For annotation, the ITK Snap software (version 3.8.0) was used. Region segmentation was performed manually with a polygon tool
8	Hsu (2021) [57]	Pancreatic cancer	67	L3	CNN	ResNet-18 model for slice 2D U-Net to segment	Manual annotated, expert labeled
9	Zopfs (2020) [16]	The Cancer Imaging Archive's collection "CT Lymph Nodes" and the institutional picture archiving and communication system	62	Containing the abdomen and images above (cranial) and below (caudal) this region	DCNN	U-Net	Manual segmentation

Table 1: Continued.

	Author (year)	Population	Mean age (year)	Localization	Neural network	Segmentation algorithm	Segmentation ground truth
10	Edwards (2020) [54]	Adult patients	18-75	L3	CNN	Supervised U-Net	Manual segmentation
11	Hemke (2020) [56]	200 subjects	49.9	Pelvic content	DCNN	U-Net	Manual segmentation using manual and semiautomated thresholding using the Osirix DICOM viewer (version 6.5.2, http://www.osirix-viewer.com/index.html)
12	Burns (2020) [47]	102 sequential patients	68	L1-L5	CNN	U-Net	Annotation utilizing ITK-SNAP software. Region segmentation was performed manually
13	Paris (2020) [48]	Critically ill, liver cirrhosis, pancreatic cancer, and clear cell renal cell carcinoma patients, renal and liver donors	Training/validation: 52.6 Test: 53.9	L3	DCNN	Adapt U-Net	Manually segmented by using SliceOmatic (TomoVision, Montreal, Canada, version 4.2, 4.3, and 5.0)
14	Blanc-Durand (2020) [46]	Unknown subjects	N/A	L3	DCNN	2D U-Net	Manually annotated using the public freeware 3DSlicer
15	Park (2020) [62]	Gastric cancer, pancreatic cancer, and sepsis and healthy individuals	Training: 56.1 Internal validation: 56.6 External validation: 61.1	L3	CNN	FCN-based	Semiautomated segmentation software (AsanJ-Morphometry) followed by manual correction
16	Barnard (2019) [50]	Older adults, who were current or former smokers	71.6	T12	CNN	U-Net	Manual segmentation using Mimics software (Materialise, Leuven, Belgium)
17	Graffy (2019) [55]	Asymptomatic adults	57.1	L3	CNN	U-Net	Manual segmentation
18	Dabiri (2019) [53]	Data from Cross Cancer Institute (CCI), University of Alberta, Canada	N/A	L3 and T4	CNN	FCN with VGG16	Manual segmentation using Slice-O-Matic V4.3 software (TomoVision, Montreal, Canada)
19	Lee (2017) [60]	Patients with lung cancer	63	L3	CNN	FCN of ImageNet pretrained model	Semiautomated threshold-based segmentation, followed by manual correction
20	Shephard (2015) [63]	N/A	N/A	N/A	N/A	N/A	

L3M: L3 muscle; IMAT: intramuscular adipose tissue; VAT: visceral adipose tissue; SAT: subcutaneous adipose tissue; DLNN: deep learning neural network; CNN: convolutional neural network; MIP: maximum intensity projections; DL: deep learning; DCNN: deep convolutional neural network; N/A: not available; FCN: fully convolutional network.

Table 2: Summary of review of 20 articles reporting the CT threshold, DICE similarity coefficient scores, and study limitations.

	Author (year)	Population	Patients (*N*)	CT threshold (HU value)	DICE score	Limitations
1	Ackermans (2021) [19]	Cancer surgery cases, colorectal, ovarian, pancreatic cancers (training); polytrauma patients (testing)	Training: 3,413 Testing: 233	Muscle: -29 to +150 HU	L3M: 0.926 (0.866–0.959)† VAT: 0.951 (0.888-0.974)† SAT: 0.953 (0.916-0.975)†	(1) This algorithm systematically overestimates muscle area (2) Overlapping adjacent internal organs with muscle and CT Hounsfield units being similar between some organs and muscle also lead to a degree of misidentification as muscle
2	Borrelli (2021) [51]	Lymphoma (training) Prostate cancer (testing)	Training: 50 Testing: 74	SAT: -190 to -30 HU Muscle: -30 to +150 HU	SAT: mean = 0.96 Muscle: mean = 0.94	(1) Used manual segmentations of SAT and muscle in a single CT slice at the L3 level to validate the AI-based method (2) In 9% of the cases, a manual correction was needed due to difficulty to detect T11 by the AI-based tool (3) The VAT compartment was not included in the analysis
3	Castiglione (2021) [52]	Pediatric patients	Training: 296 Testing:74	N/A	DSC: 0.93 ± 0.03‡	(1) The limited availability of ground truth data for a pediatric population (2) Did not attempt to account for variant anatomy, including patients who only had 11 rib-bearing thoracic-type vertebral bodies and patients who had transitional vertebrae at the lumbosacral junction
4	Amarasinghe (2021) [49]	Non-small-cell lung cancer	Training and validation: 66 Testing (internal): 42	Muscle: -29 to +150 HU	5-fold cross-validation: mean = 0.92 Internal test: mean = 0.96	(1) In some cases, with very low SM area, the model tends to misclassify other organs as belonging to skeletal muscle (2) Observed limited benefit of data augmentation apart from flipping and addition of Gaussian noise, which may suggest limited variability in the validation set (3) Systematic difference between the manual and automated segmentation occurred when the patient was scanned with arms down (4) Specific image normalization methods and model parameter tuning are needed to extend our method to other modalities, including diagnostic quality CTs and magnetic resonance imaging (MRI)

Table 2: Continued.

	Author (year)	Population	Patients (*N*)	CT threshold (HU value)	DICE score	Limitations
5	Kim (2021) [58]	Gastric cancers receiving gastrectomy	840	Skeletal muscle: -29 to +150 HU Adipose tissue: -190 to -30 HU	ICC for SMA: 0.604	(1) Not all of the automatically derived segmentation data could be used
6	Magudia (2021) [61]	Pancreatic adenocarcinoma	Training: 421 Validation: 94 Testing (internal): 89	Muscle: -29 to +150 HU Fat: -190 to -30 HU	Testing (internal): Muscle: $0.97 \pm 0.03^{\ddagger}$ SF: $0.98 \pm 0.02^{\ddagger}$ VF: $0.95 \pm 0.10^{\ddagger}$	(1) Although the aim was to focus on patients without a major cardiovascular or oncologic diagnosis at the time of imaging, the included patients underwent imaging for a reason and may have been less healthy than the average American adult (2) Volumetric BC segmentation, which required large-scale collection of many manually segmented CT slices per patient examination for model training and validation
7	Koitka (2021) [59]	Individuals with abdominal CT scans (unknown patients)	Training: 32 Validation: 8 Testing: 10	Muscle: -29 to +150 HU Fat: -190 to -30 HU	Mean = 0.9553	The collected dataset was from slice thickness of 5 mm
8	Hsu (2021) [57]	Pancreatic cancer	Experiment 1: (i) Training: 28 (ii) Testing: 12 Experiment 2a: (i) Training: 28 (ii) Testing: 12 Experiment 2b: (i) Training: 56 (ii) Testing: 12 Clinical application: 136	-150 to 250 HU	Experiment 1: Training: Muscle: 0.92 [0.91, 0.93]$^{\&}$ SF: 0.93 [0.90, 0.95]$^{\&}$ VF: 0.89 [0.86, 0.92]$^{\&}$ Testing: Muscle: 0.83 [0.80, 0.86]$^{\&}$ SF: 0.90 [0.88, 0.93]$^{\&}$ VF: 0.76 [0.70, 0.81]$^{\&}$ Experiment 2: Muscle: 0.85 [0.83, 0.88]$^{\&}$ SF: 0.92 [0.91, 0.93]$^{\&}$ VF: 0.80 [0.77, 0.83]$^{\&}$	(1) There was a generalization gap across datasets when tested on local pancreatic cancer data (2) Analysis was restricted to a single slice using a 2D U-Net architecture (3) All image labels were performed by two radiologists, and disagreement was solved by consensus, without documenting the disagreement systematically
9	Zopfs (2020) [16]	The Cancer Imaging Archive's collection "CT Lymph Nodes" and the institutional picture archiving and communication system	Training cohort: (i) Training: 72 (ii) Validation: 14 Validation cohort: (A) 24 patients used to assess the consistency of the developed method (B) 39 patients underwent concurrent SDCT and BIA	Muscle: 15 to 200 HU Fat: -200 to -50 HU	Validation: 0.95 Muscle and SF: 0.99 VF: 0.98	(1) The included patients may be subject to a selection bias (2) This study used iodine maps derived from SDCT, a dual-layer based method of dual-energy CT (3) While parenchymatous organs are reliably excluded due to their clearly higher perfusion, portions of the bowel wall, feces, gall bladder, and bile may

Table 2: Continued.

	Author (year)	Population	Patients (*N*)	CT threshold (HU value)	DICE score	Limitations
						be misclassified as muscle (4) This study used an independent test set of patients with repetitive examinations to validate the whole chain of DCNN and thresholding in addition to independent test sets for every step in DCNN-based processing
10	Edwards (2020) [54]	Adult patients	Training: 61 (682 images) Validation: 3 (85 image) Testing: 5 (137 images)	N/A	Training: $0.92 \pm 0.032^{\ddagger}$ Validation: $0.92 \pm 0.035^{\ddagger}$ Testing: $0.92 \pm 0.024^{\ddagger}$	(1) The limitation to this approach is undermining significant muscle mass changes that may be characteristic of sarcopenia (2) Better understanding of what determines a "significant" skeletal abdominal muscle mass changes must be understood further to introduce postprocessing image correction in the clinical setting
11	Hemke (2020) [56]	200 subjects	Training: 180 Testing: 20	Muscle -29 to +150 HU SAT: -190 to -30 HU	Miscellaneous intrapelvic content: 0.98 SAT: 0.97 Muscle: 0.95 IMAT: 0.91 Bone: 0.92	(1) The model being trained using a single standardized slice at the pelvis (2) Cohort trending towards overweight BMIs, with possible variations in accuracy for subjects with very low BMI
12	Burns (2020) [47]	102 sequential patients	Training: 51 Testing: 51	N/A	Train: abdominal muscle Third lumbar vertebrae: $0.953 \pm 0.015^{\ddagger}$ Fourth lumbar vertebrae: $0.953 \pm 0.011^{\ddagger}$ Test: abdominal muscle Third lumbar vertebrae: $0.938 \pm 0.028^{\ddagger}$ Fourth lumbar vertebrae: $0.940 \pm 0.026^{\ddagger}$ Train: psoas muscle Third lumbar vertebrae: $0.942 \pm 0.040^{\ddagger}$ Fourth lumbar vertebrae: $0.951 \pm 0.037^{\ddagger}$	Inclusion criterion of 59 years and older

Table 2: Continued.

	Author (year)	Population	Patients (*N*)	CT threshold (HU value)	DICE score	Limitations
					Test: psoas muscle Third lumbar vertebrae: $0.939 \pm 0.028^{\ddagger}$ Fourth lumbar vertebrae: $0.946 \pm 0.032^{\ddagger}$	
13	Paris (2020) [48]	Critically ill, liver cirrhosis, pancreatic cancer, and clear cell renal cell carcinoma patients, renal and liver donors	Training and validation: 804 Testing: 89	Muscles: -29 to +150 HU IMAT: -190 to -30 HU VAT: -150 to -50 HU SAT: -190 to -30 HU	Muscle: $0.983 \pm 0.013^{\ddagger}$ IMAT: $0.9 \pm 0.034^{\ddagger}$ VAT: $0.979 \pm 0.019^{\ddagger}$ SAT: $0.986 \pm 0.016^{\ddagger}$	
14	Blanc-Durand (2020) [46]	Unknown subjects	Training: 1,025 Testing: 500	Muscle: -29 to 150 HU	Testing: $0.97 \pm 0.02^{\ddagger}$	(1) Independent cohort would be mandatory to validate the algorithm (2) Because of the anonymization process, height and weight were not available for stratification
15	Park (2020) [62]	Gastric cancer, pancreatic cancer, and sepsis and healthy individuals	Training: 467 (883 images) Validation (internal): 308 (426 images) Validation (external): 171 (171 images)	Muscle: -29 to +150 HU Fat tissue: -190 to -30 HU	Internal validation:$0.96 \pm 0.03^{\dagger}$ Muscle: 0.96 SF: 0.97 VF: 0.97 External validation: $0.97 \pm 0.01^{\dagger}$ Muscle: 0.97 SF: 0.97 VF: 0.97	(1) Patient recruitment process was not consecutive; this may have resulted in selection bias (2) External validation was performed using data from a limited number of subjects from only two institutions; large-scale external validation might be necessary
16	Barnard (2019) [50]	Older adults, who were current or former smokers	Training: 1,875 Testing: 209	Muscle: -29 to +150 HU	Testing: $0.94 \pm 0.04^{\#}$	(1) The CT slice cannot be automatically selected (2) Only low-dose CT scans were used
17	Graffy (2019) [55]	Asymptomatic adults	8037	N/A	DSC: $0.938 \pm 0.028^{\ddagger}$	(1) All cases were derived from a single medical center on symptomatic adults employing scanners from a single CT vendor, with a fairly uniform unenhanced protocol (2) Did not correlate muscle segmentation values with downstream adverse clinical outcomes

Table 2: Continued.

	Author (year)	Population	Patients (*N*)	CT threshold (HU value)	DICE score	Limitations
18	Dabiri (2019) [53]	Data from Cross Cancer Institute (CCI), University of Alberta, Canada	Dataset-1: 1075 images Dataset-2: 5101 images Dataset-3: 3003 images	Muscle: -29 to +150 HU	From 0.9713 to 0.9912 (mean ranges)	(1) The performance of the model depends profoundly on the provided ground truth labels and their accuracy. Mistakes in the labeling process will transmit through to the network's definition of skeletal muscle tissue and can result in the model making the same mistakes. Availability of standardized labels using a common protocol would help mitigate the errors due to protocol differences
19	Lee (2017) [60]	Patients with lung cancer	Entire cohort: 400 (250 training images and ground truth)	Skeletal muscle CSA: -29 to +150 HU	DSC: 0.93 ± 0.02‡	(1) The network statistically tends to underestimate muscle CSA, probably due to a combination of overlapping HUs between muscle and adjacent organs and variable organ textural appearance. On the other end of the spectrum, segmentation is also confused by the radiographic appearance of edema particularly in obese patients, which has a similar HU range to muscle, leading to higher CSA than expected. Extensive edema tends to occur in critically ill patients, leading to potentially falsely elevated CSA in patients actually at higher risk for all interventions (2) The network should be trained to segment CT examinations performed without intravenous contrast and ultralow radiation dose
20	Shephard (2015) [63]	N/A	N/A	N/A	Normal liver: DSC = 0.93 Enhancing tumor DSC = 0.74 Necrotic tumor: DSC = 0.72	N/A

L3M: L3 muscle; IMAT: intramuscular adipose tissue; VAT: visceral adipose tissue; SAT: subcutaneous adipose tissue; SMA: skeletal muscle area; SF: subcutaneous fat; VF: visceral fat; CSA: cross-sectional area; DSC: DICE similarity coefficient; ICC: intraclass correlation coefficient; SDCT: spectral detector computed tomography; BIA: bioelectrical impedance analysis; N/A: not available. DICE scores were summarized as follows: †, median (IQR); ‡, mean ± SD; &, mean (95% CI); and #, median ± SD.

tissue were also analyzed. Most of the articles reported training and testing cohort results only; 7 studies performed independent validations (internal or external) (Table 2).

In the evaluation of sarcopenia, abdominal musculature segmentation is accomplished using deep learning with a DICE similarity coefficient of 0.93-0.98 [46, 48]. Successful individual segmentation of different muscle groups for SMI are achieved using a DICE similarity coefficient of 0.82-0.95, consisting of psoas major, quadratus lumborum, erector spinae (paraspinal muscle), and abdominal wall muscles (transversus abdominis muscle, internal and external oblique muscle, and rectus abdominis) [47]. The highly accurate segmentation of individual muscle groups provides an opportunity to assess muscle mass and myosteatosis separately. The area of muscular CSA could be reserved for mass evaluation. Using the cut point of CT HU inside the segmented CSA is aimed at assessing myosteatosis [64]. The CT-derived measurement of myosteatosis is associated with cut points of muscle attenuation less than 41 or less than 33 HU, which is consistent with the most common threshold for low-density muscle (0-30 HU) [64]. Knowledge about changes in body composition during cancer treatments and the disease course is currently lacking. The lack of standardized assessment method to determine muscle mass in cancer patients is evident from the varied cut-off values used in different studies, even for the same cancer type (as reviewed by Rier et al. [65] in 2016). The variations in cut-off value between the same cancer types likely have resulted from the different population characteristics between studies including age, BMI, disease severity, and different methods of evaluation [65]. Recent studies have focused on developing reference diagnostic cut-off values among the normal population. For people under 60 years old, the cut-off SMI value ranged between 40 and 45 in male and 30 and 35 in female (Supplement Table 1) [66–72]. However, the population characteristics were different between these studies, and determination of normal reference cut-off values for different population characteristics using larger series of data via an AI-assisted approach may fasten the development of standardized assessment. AI-assisted body composition measurement would increase the accuracy and efficiency of the sarcopenia evaluation and provides a trend of standardization by which the serial changes in cancer-related sarcopenia are explored [26].

3. Conclusion

In conclusion, the presence of sarcopenia is represented by prognostic and predictive values in patients with cancer. AI-assisted image analysis is a reliable automatic technique for segmentation of abdominal adipose tissue with the potential to improve diagnosis of sarcopenia and facilitates identification of oncology patients at the greatest risk, supporting individualized prevention planning and treatment evaluation. The capability of AI approaches in analyzing series of big data and extracting high-level abstractions beyond manual skills would no doubt progressively provide impactful information and greatly refine the standard for assessing sarcopenia risk in patients with cancer.

Data Availability

No data were used to support this study.

Conflicts of Interest

The authors declare that they have no conflicts of interest.

Supplementary Materials

Supplement Table S1 Normal reference and cut-off for sarcopenia [58, 66, 68–72]. *(Supplementary Materials)*

References

[1] I. H. Rosenberg, "Sarcopenia: origins and clinical relevance," *The Journal of Nutrition*, vol. 127, no. 5, pp. 990S-991S, 1997.

[2] A. J. Cruz-Jentoft, G. Bahat, J. Bauer et al., "Sarcopenia: revised European consensus on definition and diagnosis," *Age and Ageing*, vol. 48, no. 1, pp. 16–31, 2019.

[3] R. A. Fielding, B. Vellas, W. J. Evans et al., "Sarcopenia: an undiagnosed condition in older adults. Current consensus definition: prevalence, etiology, and consequences. International working group on sarcopenia," *Journal of the American Medical Directors Association*, vol. 12, no. 4, pp. 249–256, 2011.

[4] G. R. Williams, H. N. Rier, A. McDonald, and S. S. Shachar, "Sarcopenia & aging in cancer," *Journal of Geriatric Oncology*, vol. 10, no. 3, pp. 374–377, 2019.

[5] S. Kirchengast and J. Huber, "Gender and age differences in lean soft tissue mass and sarcopenia among healthy elderly," *Anthropologischer Anzeiger*, vol. 67, no. 2, pp. 139–151, 2009.

[6] M. Anjanappa, M. Corden, A. Green et al., "Sarcopenia in cancer: risking more than muscle loss," *Technical Innovations & Patient Support in Radiation Oncology*, vol. 16, pp. 50–57, 2020.

[7] J. Chindapasirt, "Sarcopenia in cancer patients," *Asian Pacific Journal of Cancer Prevention*, vol. 16, no. 18, pp. 8075–8077, 2015.

[8] M. Rozynek, I. Kucybała, A. Urbanik, and W. Wojciechowski, "Use of artificial intelligence in the imaging of sarcopenia: a narrative review of current status and perspectives," *Nutrition*, vol. 89, article 111227, 2021.

[9] M. Gonzalez-Freire, R. Moaddel, K. Sun et al., "Targeted metabolomics shows low plasma lysophosphatidylcholine 18:2 predicts greater decline of gait speed in older adults: the Baltimore Longitudinal Study of Aging," *The Journals of Gerontology. Series A, Biological Sciences and Medical Sciences*, vol. 74, no. 1, pp. 62–67, 2019.

[10] R. Calvani, A. Picca, F. Marini et al., "A distinct pattern of circulating amino acids characterizes older persons with physical frailty and sarcopenia: results from the BIOSPHERE Study," *Nutrients*, vol. 10, no. 11, p. 1691, 2018.

[11] Q. J. Yang, J. R. Zhao, J. Hao et al., "Serum and urine metabolomics study reveals a distinct diagnostic model for cancer cachexia," *Journal of Cachexia, Sarcopenia and Muscle*, vol. 9, no. 1, pp. 71–85, 2018.

[12] L. K. Chen, J. Woo, P. Assantachai et al., "Asian Working Group for Sarcopenia: 2019 consensus update on sarcopenia diagnosis and treatment," *Journal of the American Medical Directors Association*, vol. 21, no. 3, pp. 300–307.e2, 2020.

[13] G. Rubbieri, E. Mossello, and M. Di Bari, "Techniques for the diagnosis of sarcopenia," *Clinical Cases in Mineral and Bone Metabolism*, vol. 11, no. 3, pp. 181–184, 2014.

[14] R. Thibault, L. Genton, and C. Pichard, "Body composition: why, when and for who?," *Clinical Nutrition*, vol. 31, no. 4, pp. 435–447, 2012.

[15] M. A. Waduud, P. Adusumilli, M. Drozd et al., "Volumetric versus single slice measurements of core abdominal muscle for sarcopenia," *The British Journal of Radiology*, vol. 92, no. 1097, p. 20180434, 2019.

[16] D. Zopfs, K. Bousabarah, S. Lennartz et al., "Evaluating body composition by combining quantitative spectral detector computed tomography and deep learning-based image segmentation," *European Journal of Radiology*, vol. 130, article 109153, 2020.

[17] W. Shen, M. Punyanitya, Z. Wang et al., "Total body skeletal muscle and adipose tissue volumes: estimation from a single abdominal cross-sectional image," *Journal of Applied Physiology*, vol. 97, no. 6, pp. 2333–2338, 2004.

[18] A. M. Ryan, D. G. Power, L. Daly, S. J. Cushen, Ē. Ní Bhuachalla, and C. M. Prado, "Cancer-associated malnutrition, cachexia and sarcopenia: the skeleton in the hospital closet 40 years later," *The Proceedings of the Nutrition Society*, vol. 75, no. 2, pp. 199–211, 2016.

[19] L. L. G. C. Ackermans, L. Volmer, L. Wee et al., "Deep learning automated segmentation for muscle and adipose tissue from abdominal computed tomography in polytrauma patients," *Sensors*, vol. 21, no. 6, p. 2083, 2021.

[20] B. Vangelov, J. Bauer, D. Kotevski, and R. I. Smee, "The use of alternate vertebral levels to L3 in computed tomography scans for skeletal muscle mass evaluation and sarcopenia assessment in patients with cancer: a systematic review," *The British Journal of Nutrition*, vol. 127, no. 5, pp. 722–735, 2022.

[21] T. Nishigori, K. Obama, and Y. Sakai, "Assessment of body composition and impact of sarcopenia and sarcopenic obesity in patients with gastric cancer," *Translational Gastroenterology and Hepatology*, vol. 5, p. 22, 2020.

[22] G. Simpson, N. Manu, C. Magee, J. Wilson, S. Moug, and D. Vimalachandran, "Measuring sarcopenia on pre-operative CT in older adults undergoing emergency laparotomy: a comparison of three different calculations," *International Journal of Colorectal Disease*, vol. 35, no. 6, pp. 1095–1102, 2020.

[23] M. Tomov, M. A. Alvi, M. Elminawy et al., "An objective and reliable method for identifying sarcopenia in lumbar spine surgery patients: using morphometric measurements on computed tomography imaging," *Asian Spine Journal*, vol. 14, no. 6, pp. 814–820, 2020.

[24] M. S. Weinberg, S. S. Shachar, H. B. Muss et al., "Beyond sarcopenia: characterization and integration of skeletal muscle quantity and radiodensity in a curable breast cancer population," *The Breast Journal*, vol. 24, no. 3, pp. 278–284, 2018.

[25] J. Xiao, B. J. Caan, E. M. Cespedes Feliciano et al., "The association of medical and demographic characteristics with sarcopenia and low muscle radiodensity in patients with nonmetastatic colorectal cancer," *The American Journal of Clinical Nutrition*, vol. 109, no. 3, pp. 615–625, 2019.

[26] Q. Dong, "Fully-automated segmentation of muscle measurement on CT in detecting central sarcopenia: a trend of standardization," *Academic Radiology*, vol. 27, no. 3, pp. 321-322, 2020.

[27] J. M. Cousins, M. A. Petit, M. L. Paudel et al., "Muscle power and physical activity are associated with bone strength in older men: the osteoporotic fractures in men study," *Bone*, vol. 47, no. 2, pp. 205–211, 2010.

[28] C. R. Gale, C. N. Martyn, C. Cooper, and A. A. Sayer, "Grip strength, body composition, and mortality," *International Journal of Epidemiology*, vol. 36, no. 1, pp. 228–235, 2007.

[29] I. Janssen, D. S. Shepard, P. T. Katzmarzyk, and R. Roubenoff, "The healthcare costs of sarcopenia in the United States," *Journal of the American Geriatrics Society*, vol. 52, no. 1, pp. 80–85, 2004.

[30] A. A. Sayer, H. E. Syddall, H. J. Martin, E. M. Dennison, H. C. Roberts, and C. Cooper, "Is grip strength associated with health-related quality of life? Findings from the Hertfordshire Cohort Study," *Age and Ageing*, vol. 35, no. 4, pp. 409–415, 2006.

[31] J. Woo, J. Leung, A. Sham, and T. Kwok, "Defining sarcopenia in terms of risk of physical limitations: a 5-year follow-up study of 3,153 Chinese men and women," *Journal of the American Geriatrics Society*, vol. 57, no. 12, pp. 2224–2231, 2009.

[32] J. Ubachs, J. Ziemons, I. J. G. Minis-Rutten et al., "Sarcopenia and ovarian cancer survival: a systematic review and meta-analysis," *Journal of Cachexia, Sarcopenia and Muscle*, vol. 10, no. 6, pp. 1165–1174, 2019.

[33] X. M. Zhang, Q. L. Dou, Y. Zeng, Y. Yang, A. S. K. Cheng, and W. W. Zhang, "Sarcopenia as a predictor of mortality in women with breast cancer: a meta-analysis and systematic review," *BMC Cancer*, vol. 20, no. 1, p. 172, 2020.

[34] G. Berardi, G. Antonelli, M. Colasanti et al., "Association of sarcopenia and body composition with short-term outcomes after liver resection for malignant tumors," *JAMA Surgery*, vol. 155, no. 11, article e203336, 2020.

[35] E. M. Cespedes Feliciano, V. S. Lee, C. M. Prado et al., "Muscle mass at the time of diagnosis of nonmetastatic colon cancer and early discontinuation of chemotherapy, delays, and dose reductions on adjuvant FOLFOX: the C-SCANS study," *Cancer*, vol. 123, no. 24, pp. 4868–4877, 2017.

[36] E. M. Cespedes Feliciano, C. H. Kroenke, P. T. Bradshaw et al., "Postdiagnosis weight change and survival following a diagnosis of early-stage breast cancer," *Cancer Epidemiology, Biomarkers & Prevention*, vol. 26, no. 1, pp. 44–50, 2017.

[37] H. Greenlee, J. M. Unger, M. LeBlanc, S. Ramsey, and D. L. Hershman, "Association between body mass index and cancer survival in a pooled analysis of 22 clinical trials," *Cancer Epidemiology, Biomarkers & Prevention*, vol. 26, no. 1, pp. 21–29, 2017.

[38] Y. Choi, D. Y. Oh, T. Y. Kim et al., "Skeletal muscle depletion predicts the prognosis of patients with advanced pancreatic cancer undergoing palliative chemotherapy, independent of body mass index," *PLoS One*, vol. 10, no. 10, article e0139749, 2015.

[39] S. Strulov Shachar and G. R. Williams, "The obesity paradox in cancer-moving beyond BMI," *Cancer Epidemiology, Biomarkers & Prevention*, vol. 26, no. 1, pp. 13–16, 2017.

[40] J. Aubrey, N. Esfandiari, V. E. Baracos et al., "Measurement of skeletal muscle radiation attenuation and basis of its biological variation," *Acta Physiologica (Oxford, England)*, vol. 210, no. 3, pp. 489–497, 2014.

[41] Y. Yoshimura, H. Wakabayashi, M. Yamada, H. Kim, A. Harada, and H. Arai, "Interventions for treating sarcopenia: a systematic review and meta-analysis of randomized

controlled studies," *Journal of the American Medical Directors Association*, vol. 18, no. 6, pp. 553.e1–553.e16, 2017.

[42] C. M. Dieli-Conwright, K. S. Courneya, W. Demark-Wahnefried et al., "Effects of aerobic and resistance exercise on metabolic syndrome, sarcopenic obesity, and circulating biomarkers in overweight or obese survivors of breast cancer: a randomized controlled trial," *Journal of Clinical Oncology*, vol. 36, no. 9, pp. 875–883, 2018.

[43] A. Vigano, P. Kasvis, J. Di Tomasso, C. Gillis, R. Kilgour, and F. Carli, "Pearls of optimizing nutrition and physical performance of older adults undergoing cancer therapy," *Journal of Geriatric Oncology*, vol. 8, no. 6, pp. 428–436, 2017.

[44] T. J. Wright, E. L. Dillon, W. J. Durham et al., "A randomized trial of adjunct testosterone for cancer-related muscle loss in men and women," *Journal of Cachexia, Sarcopenia and Muscle*, vol. 9, no. 3, pp. 482–496, 2018.

[45] S. T. Burden, D. J. Gibson, S. Lal et al., "Pre-operative oral nutritional supplementation with dietary advice versus dietary advice alone in weight-losing patients with colorectal cancer: single-blind randomized controlled trial," *Journal of Cachexia, Sarcopenia and Muscle*, vol. 8, no. 3, pp. 437–446, 2017.

[46] P. Blanc-Durand, J. B. Schiratti, K. Schutte et al., "Abdominal musculature segmentation and surface prediction from CT using deep learning for sarcopenia assessment," *Diagnostic and Interventional Imaging*, vol. 101, no. 12, pp. 789–794, 2020.

[47] J. E. Burns, J. Yao, D. Chalhoub, J. J. Chen, and R. M. Summers, "A machine learning algorithm to estimate sarcopenia on abdominal CT," *Academic Radiology*, vol. 27, no. 3, pp. 311–320, 2020.

[48] M. T. Paris, P. Tandon, D. K. Heyland et al., "Automated body composition analysis of clinically acquired computed tomography scans using neural networks," *Clinical Nutrition*, vol. 39, no. 10, pp. 3049–3055, 2020.

[49] K. C. Amarasinghe, J. Lopes, J. Beraldo et al., "A deep learning model to automate skeletal muscle area measurement on computed tomography images," *Frontiers in Oncology*, vol. 11, article 580806, 2021.

[50] R. Barnard, J. Tan, B. Roller et al., "Machine learning for automatic paraspinous muscle area and attenuation measures on low-dose chest CT scans," *Academic Radiology*, vol. 26, no. 12, pp. 1686–1694, 2019.

[51] P. Borrelli, R. Kaboteh, O. Enqvist et al., "Artificial intelligence-aided CT segmentation for body composition analysis: a validation study," *European Radiology Experimental*, vol. 5, no. 1, p. 11, 2021.

[52] J. Castiglione, E. Somasundaram, L. A. Gilligan, A. T. Trout, and S. Brady, "Automated segmentation of abdominal skeletal muscle on pediatric CT scans using deep learning," *Radiology: Artificial Intelligence*, vol. 3, no. 2, article e200130, 2021.

[53] S. Dabiri, K. Popuri, E. M. Cespedes Feliciano, B. J. Caan, V. E. Baracos, and M. F. Beg, "Muscle segmentation in axial computed tomography (CT) images at the lumbar (L3) and thoracic (T4) levels for body composition analysis," *Computerized Medical Imaging and Graphics*, vol. 75, pp. 47–55, 2019.

[54] K. Edwards, A. Chhabra, J. Dormer et al., "Abdominal muscle segmentation from CT using a convolutional neural network," *Proceedings of SPIE The International Society for Optical Engineering*, vol. 11317, 2020.

[55] P. M. Graffy, J. Liu, P. J. Pickhardt, J. E. Burns, J. Yao, and R. M. Summers, "Deep learning-based muscle segmentation and quantification at abdominal CT: application to a longitudinal adult screening cohort for sarcopenia assessment," *The British Journal of Radiology*, vol. 92, no. 1100, article 20190327, 2019.

[56] R. Hemke, C. G. Buckless, A. Tsao, B. Wang, and M. Torriani, "Deep learning for automated segmentation of pelvic muscles, fat, and bone from CT studies for body composition assessment," *Skeletal Radiology*, vol. 49, no. 3, pp. 387–395, 2020.

[57] T. H. Hsu, K. Schawkat, S. J. Berkowitz et al., "Artificial intelligence to assess body composition on routine abdominal CT scans and predict mortality in pancreatic cancer- a recipe for your local application," *European Journal of Radiology*, vol. 142, article 109834, 2021.

[58] J. Kim, S. H. Han, and H. I. Kim, "Detection of sarcopenic obesity and prediction of long-term survival in patients with gastric cancer using preoperative computed tomography and machine learning," *Journal of Surgical Oncology*, vol. 124, no. 8, pp. 1347–1355, 2021.

[59] S. Koitka, L. Kroll, E. Malamutmann, A. Oezcelik, and F. Nensa, "Fully automated body composition analysis in routine CT imaging using 3D semantic segmentation convolutional neural networks," *European Radiology*, vol. 31, no. 4, pp. 1795–1804, 2021.

[60] H. Lee, F. M. Troschel, S. Tajmir et al., "Pixel-level deep segmentation: artificial intelligence quantifies muscle on computed tomography for body morphometric analysis," *Journal of Digital Imaging*, vol. 30, no. 4, pp. 487–498, 2017.

[61] K. Magudia, C. P. Bridge, C. P. Bay et al., "Population-scale CT-based body composition analysis of a large outpatient population using deep learning to derive age-, sex-, and race-specific reference curves," *Radiology*, vol. 298, no. 2, pp. 319–329, 2021.

[62] H. J. Park, Y. Shin, J. Park et al., "Development and validation of a deep learning system for segmentation of abdominal muscle and fat on computed tomography," *Korean Journal of Radiology*, vol. 21, no. 1, pp. 88–100, 2020.

[63] R. J. Shephard, *An Illustrated History of Health and Fitness, from Pre-History to our Post-Modern World*, Springer International Publishing, 2015.

[64] B. Amini, S. P. Boyle, R. D. Boutin, and L. Lenchik, "Approaches to assessment of muscle mass and myosteatosis on computed tomography: a systematic review," *The Journals of Gerontology. Series A, Biological Sciences and Medical Sciences*, vol. 74, no. 10, pp. 1671–1678, 2019.

[65] H. N. Rier, A. Jager, S. Sleijfer, A. B. Maier, and M. D. Levin, "The prevalence and prognostic value of low muscle mass in cancer patients: a review of the literature," *The Oncologist*, vol. 21, no. 11, pp. 1396–1409, 2016.

[66] Z. Feng, P. Rong, M. Luo, X. Sun, and W. Wang, "Influence of methods used to establish sarcopenia cutoff values for skeletal muscle measures using unenhanced and contrast-enhanced computed tomography images," *JPEN Journal of Parenteral and Enteral Nutrition*, vol. 43, no. 8, pp. 1028–1036, 2019.

[67] H. K. Kim, K. W. Kim, E. H. Kim et al., "Age-related changes in muscle quality and development of diagnostic cutoff points for myosteatosis in lumbar skeletal muscles measured by CT scan," *Clinical Nutrition*, vol. 40, no. 6, pp. 4022–4028, 2021.

[68] F. Ufuk and D. Herek, "Reference skeletal muscle mass values at L3 vertebrae level based on computed tomography in healthy Turkish adults," *International Journal of Gerontology*, vol. 13, no. 3, pp. 221–225, 2019.

[69] J. K. Yoon, S. Lee, K. W. Kim et al., "Reference values for skeletal muscle mass at the third lumbar vertebral level measured by computed tomography in a healthy Korean population," *Endocrinology and Metabolism*, vol. 36, no. 3, pp. 672–677, 2021.

[70] B. A. Derstine, S. A. Holcombe, R. L. Goulson et al., "Quantifying sarcopenia reference values using lumbar and thoracic muscle areas in a healthy population," *The Journal of Nutrition, Health & Aging*, vol. 22, no. 1, pp. 180–185, 2017.

[71] B. A. Derstine, S. A. Holcombe, B. E. Ross, N. C. Wang, G. L. Su, and S. C. Wang, "Skeletal muscle cutoff values for sarcopenia diagnosis using T10 to L5 measurements in a healthy US population," *Scientific Reports*, vol. 8, no. 1, p. 11369, 2018.

[72] A. van der Werf, J. A. E. Langius, M. A. E. de van der Schueren et al., "Percentiles for skeletal muscle index, area and radiation attenuation based on computed tomography imaging in a healthy Caucasian population," *European Journal of Clinical Nutrition*, vol. 72, no. 2, pp. 288–296, 2018.

Hindawi
Disease Markers
Volume 2023, Article ID 9826727, 1 page
https://doi.org/10.1155/2023/9826727

Retraction

Retracted: Therapy Strategy of CD47 in Diffuse Large B-Cell Lymphoma (DLBCL)

Disease Markers

Received 11 July 2023; Accepted 11 July 2023; Published 12 July 2023

This article has been retracted by Hindawi following an investigation undertaken by the publisher [1]. This investigation has uncovered evidence of one or more of the following indicators of systematic manipulation of the publication process:

(1) Discrepancies in scope
(2) Discrepancies in the description of the research reported
(3) Discrepancies between the availability of data and the research described
(4) Inappropriate citations
(5) Incoherent, meaningless and/or irrelevant content included in the article
(6) Peer-review manipulation

The presence of these indicators undermines our confidence in the integrity of the article's content and we cannot, therefore, vouch for its reliability. Please note that this notice is intended solely to alert readers that the content of this article is unreliable. We have not investigated whether authors were aware of or involved in the systematic manipulation of the publication process.

Wiley and Hindawi regrets that the usual quality checks did not identify these issues before publication and have since put additional measures in place to safeguard research integrity.

We wish to credit our own Research Integrity and Research Publishing teams and anonymous and named external researchers and research integrity experts for contributing to this investigation.

The corresponding author, as the representative of all authors, has been given the opportunity to register their agreement or disagreement to this retraction. We have kept a record of any response received.

References

[1] W. Zhang, Y. Fan, M. Li, L. Yang, Z. Zhang, and L. Liu, "Therapy Strategy of CD47 in Diffuse Large B-Cell Lymphoma (DLBCL)," *Disease Markers*, vol. 2021, Article ID 4894022, 8 pages, 2021.

Hindawi
Disease Markers
Volume 2021, Article ID 4894022, 8 pages
https://doi.org/10.1155/2021/4894022

Review Article

Therapy Strategy of CD47 in Diffuse Large B-Cell Lymphoma (DLBCL)

Wenqi Zhang,[1] **Yanfeng Fan**,[2] **Meng Li**,[3] **Linqi Yang**,[3] **Zhenya Zhang**,[4] **and Lihong Liu**[1,5]

[1]*Department of Hematology, The Fourth Hospital of Hebei Medical University, Shijiazhuang, 050000 Hebei Province, China*
[2]*Department of Chemistry, Temple University, Philadelphia, Pennsylvania 19087, USA*
[3]*School of Basic Medical Sciences, Hebei University of Chinese Medicine, Shijiazhuang, 050200 Hebei Province, China*
[4]*Department of General Surgery, The Fourth Hospital of Hebei Medical University, Shijiazhuang, 050000 Hebei Province, China*
[5]*Hebei Provincial Key Laboratory of Tumor Microenvironment and Drug Resistance, Shijiazhuang 050011, China*

Correspondence should be addressed to Lihong Liu; 13831177920@163.com

Received 11 April 2021; Accepted 30 August 2021; Published 17 September 2021

Academic Editor: Zhongjie Shi

At present, the use of the common chemotherapy regimen CHOP/R-CHOP for diffuse large B-cell lymphoma (DLBCL) has some shortcomings, especially for relapsed and refractory DLBCL. CD47 is now considered as a prominent target in cancer therapies, and CD47 blockade mainly inhibits the CD47-SIRPα axis to prevent tumor immune escape. Here, we evaluated the effects of the latest CD47 antibodies reported and the correlations of closely related genes with CD47 in this disease. In the future, therapeutic strategies for DLBCL will focus on multitarget antibody combined treatment and multigene joint attacks.

1. Introduction

CD47 is a receptor that is widely expressed on the surfaces of numerous cell types and consists of *N*-terminal extracellular IgV-like domains, 5 transmembrane domains, and a short C-terminal cytoplasmic tail that functions as a transmembrane region for its immunoregulatory functions. CD47 mediates cellular phagocytosis by macrophages, the transmigration of neutrophils, and the activation of dendritic cells, T-cells, and B-cells by interacting with their ligands, including thrombospondin-1 (TSP-1), signal regulatory protein α (SIRPα), integrin, and SH2-domain bearing protein tyrosine phosphatase substrate-1 (SHPS-1). The mechanism of CD47 in tumors can be described as follows. First, CD47 is overexpressed in diverse cancers, preventing tumor cell phagocytosis and promoting tumor progression by activating the SIRPα-CD47 axis to thereby avoid immune surveillance. The process of macrophages phagocytosing tumor cells by blocking CD47 is demonstrated in Figure 1. Second, CD47 expression on the surface of neutrophils, dendritic cells, and T-cells inactivates immune responses to tumors by initiating reverse signaling pathways. Third, the interaction of CD47 with TSP-1 has direct anticancer and antiangiogenic effects [1]. The downregulation of CD47 expression may induce the removal of aged and superfluous cells through phagocytosis, which plays a crucial role in various homeostatic systems [2]. However, the role of CD47 in several malignant tumors, including hematological malignancies, such as leukemia, lymphoma, and multiple myeloma, has been assessed in many studies. This molecule is expressed at varying levels on a variety of hematopoietic and nonhematopoietic cells. Most cancer cells overexpress CD47, and its expression level independently correlates with poor clinical outcomes in patients with hematological and solid tumor malignancies [3, 4].

Diffuse large B-cell lymphoma (DLBCL) is the most common aggressive lymphoid malignancy, and rituximab, cyclophosphamide, doxorubicin, and prednisone (R-CHOP) therapy is one of the most effective treatment strategies for most DLBCL subtypes [5]. Currently, CHOP and R-CHOP

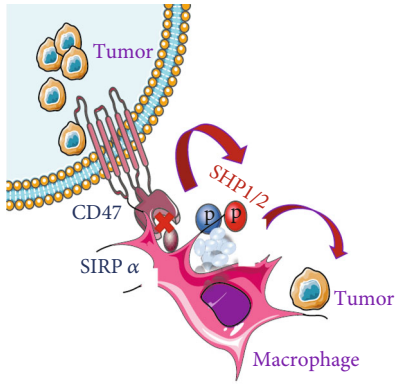

Figure 1: Blocking CD47 induces the phagocytosis of tumor cells by macrophages.

are the most widely used chemotherapies for DLBCL. Patients with DLBCL who become resistant to standard chemotherapies and antibody-based regimens or relapse might have poor prognoses. Approximately 40% of patients treated with R-CHOP die after developing intrinsic resistance or relapsing. Unlike the limited effects of single-drug therapies for DLBCL, combination therapies were suggested to yield good treatment responses in several studies. As a promising immunomodulatory therapeutic strategy, blockade of CD47 has been evaluated in early clinical trials. High CD47 mRNA expression was correlated with the poor survival of DLBCL patients, highlighting DLBCL as a candidate for future CD47-targeted therapies. This review focuses on the latest studies on DLBCL treatments related to CD47.

2. Applications of CD47 in Clinical Therapies

SIRPα and TSP-1 are the two most important endogenous ligands of CD47. SIRPα is expressed on the plasma membranes of all myeloid and neuronal cells as a transmembrane glycoprotein [6]. The CD47-SIRPα axis plays a crucial role in tumor development. CD47 acts as a "do not eat me" receptor by interacting with SIRPα on the healthy macrophage surface membrane and prevents phagocytosis by triggering a dephosphorylation cascade [7–9]. Vascular growth factor (VEGF) and its receptor (VEGFR2) can be activated by TSP-1 and CD47 in combination to stimulate angiogenesis, and the interaction between CD47 and integrin $\alpha V\beta 3$ enhances neovascularization to allow tumor growth [10]. Studies have shown that the overall survival (OS) and progression-free survival (PFS) of DLBCL patients, especially those with the activated B-cell-like (ABC) subtype, are significantly reduced when both CD47 on tumor cells and SIRPα in stromal cells are upregulated or when only SIRPα expression is increased. In an *in vitro* study of bone marrow-derived macrophages, the interaction between CD47 and SIRPα polarized macrophages toward an M2 immunosuppressive phenotype, which provided an abundant tumor-associated macrophage (TAM) microenvironment [11]. This result indicated that tumor cells and stromal cells might interact with each other, worsening the prognoses of patients. As the combined expression of CD47 and SIRPα is potentially an independent prognostic factor for DLBCL, the levels of CD47 and SIRPα before CD47 blockade therapy need to be evaluated [12].

Previous studies reported that calreticulin and phosphatidylserine could induce phagocytosis by binding to the low-density lipoprotein receptor-associated protein (LRP) on phagocytes, as blocking the CD47-SIRPα antiphagocytic signal induced an effective prophagocytic signal to trigger tumor phagocytosis [13, 14]. In humans, calreticulin is commonly expressed at higher levels in the cells of several hematological malignancies, including non-Hodgkin's lymphoma (NHL), than in normal bone marrow and peripheral blood cells. In addition to interfering with the SIRPα-CD47 interaction, CD47 antibodies can cause tumor-specific T-cell reactions, such as CD8+ cell activations [15]. Functional CD47 antibody blockades could be targeted to tumor stem cells to promote radiotherapy sensitivity in tumors and protect normal tissues [16–19].

Treatment with 9-cis-retinoic acid and interferon α (RA/IFN-α) triggers early membrane exposure to calreticulin, the expression of heat shock proteins (HSPs) 70 and 90, the downregulation of CD47 expression, and the enhancement of HMGB1 secretion [20]. This drug was shown to upregulate the expression of the NOXA protein in DOHH2 DLBCL cell lines to induce a strong apoptotic response [21, 22]. This study provides a new approach for dendritic cell (DC) immunotherapies based on therapeutically relevant immunogenic cell death (ICD) for relapsed and/or refractory (R/R) lymphoma, which promotes intense antitumor responses by inducing Th1 immunity [23–25].

3. Preclinical Trials on CD47 Antibodies

As shown in preclinical studies, anti-CD47 antibodies can be used in combination. In current clinical trials, four different antibody molecules designed to target CD47-SIRPα, Hu5F9-G4, CC-90002, TTI-621, and ALX-148 are being assessed for their ability to treat malignant tumors. Among them, Hu5F9-G4 and TTI-621 were demonstrated to effectively treat DLBCL in several studies [26].

3.1. Hu5F9-G4. Hu5F9-G4 (hereafter, 5F9), an anti-CD47 humanized IgG4 antibody that binds to monomeric human CD47, is currently being assessed in four different phase I trials and has received fast-track designation by the US Food and Drug Administration for further development for the treatment of DLBCL and follicular lymphoma (FL). Treatment with 5F9 induces macrophages to recognize and attack cancer cells by preventing the activation of the CD47-SIRPα axis and promoting the phagocytosis of tumor cells via innate immune cells [1, 27].

Moreover, 5F9 was shown to augment the activity of rituximab (Rituxan; Genentech) and to synergistically affect lymphoma in preclinical models. A recent phase 1b trial involving heavily pretreated patients with R/RDLBCL and FL indicated that the combination of 5F9 and rituximab (NCT02953509) induced a high rate of tolerable and durable complete responses. This combination therapy resulted in a 40% overall response (OR) and a 33% complete response

(CR) in R/R DLBCL patients. However, the objective response rate achieved with this treatment was higher for patients with ABC-DLBCL than GCB-DLBCL (67% for ABC-DLBCL vs. 17% for GCB-DLBCL) [28].

Moreover, 5F9 was recently assessed in a first-in-human phase I trial on patients with advanced solid tumors and lymphomas to evaluate its safety, pharmacokinetics (PK), and pharmacodynamics. The trial showed that 5F9 was well tolerated at a priming dose of 1 mg/kg on day 1 and maintenance dose of up to 45 mg/kg weekly. A linear PK curve was observed for 5F9 doses exceeding 10 mg/kg. In regard to saturating concentrations, the agent was administered biweekly and had a terminal half-life of approximately 13 days. The most common drug-related adverse event (AE) resulting from 5F9 treatment was expected, on-target, mild, transient, and predictable anemia which was mitigated by administering priming and maintenance doses in cycle 1. As younger red blood cells (RBCs) lack prophagocytic signals, older RBCs were perturbed by CD47 blockade in most cases. To circumvent the hemolytic anemia and thrombocytopenia caused by the expression of CD47 on red blood cells and platelets, different strategies, such as newly developed BsAbs and priming with low-dose levels to eliminate aging RBCs, are being investigated. Additional clinical trials are required to assess the clinical efficacies of these strategies.

At doses of 20 mg/kg and higher, chills, headache, fatigue, and fever were frequently observed, with most occurring within the first cycle of grade 1 or 2. Pretreatment with acetaminophen and diphenhydramine before the first two doses of 5F9 was recommended to decrease the incidence and severity of these side effects. Abdominal, back, and chest pain in a few patients during infusion were not related to other clinical findings. Temporarily stopping or slowing the rate of infusion often mitigated these effects. Nevertheless, dose-related thrombocytopenia and neutropenia were not observed. Thus, 5F9 might be readily combined with other antitumor antibodies according to this favorable safety assessment.

Due to the mild and manageable 5F9-related AEs and easy administration of 5F9 infusions in an outpatient setting, this treatment might be beneficial in older patients with aggressive and relapsed lymphomas who cannot tolerate other treatments [27, 29, 30].

3.2. TTI-621. As a novel checkpoint inhibitor, TTI-621 (SIRPα-IgG1 Fc) is a soluble, fully human recombinant fusion protein designed to block the CD47 "do not eat me" signal by IFN primed macrophages that triggers tumor cell phagocytosis. TTI-622 is another SIRPα Fc decoy receptor under investigation for anticancer treatment. Although they have very similar effects, most studies have focused on TTI-621 [1].

TTI-621 could improve the treatment toleration of R/R DLBCL patients. Moreover, TTI-621 effectively induced the destruction of cancer cells by various sets of TAMs and the phagocytosis of lymphoma cells by all macrophage subtypes in vivo. TTI-621 has a synergistic effect on the phagocytosis of tumor cells mediated by FC γ r CD64 and CD32. Early results from an *in vitro* study showed that M (-), M (IL-4), and M (HAGG+IL-1 β) macrophages had a slightly worse phagocytic response to TTI-621 than the M (IFN-γ+-LPS) and M (IL-10+TGF β) subtypes. Cytokines (IFN-γ, IFN-α, or IL-10) or TLR agonists (LPS, poly (I: C) or R848) could easily repolarize these cells into highly phagocytic macrophages [31].

TLR-3, TLR-4, and TLR-7 synergize with CD47 blockade on tumor cells by enhancing secretion and exposing calreticulin on the macrophage surface in a Btk-dependent manner [32]. TTI-621 and TLR agonists in combination are a potential strategy for the treatment of hematological malignancies in the future (NCT02663518).

The safety and activity of TTI-621 in R/R hematologic malignancies were evaluated in a first-in-human phase I study (NCT02663518). Among evaluable patients with DLBCL, 23% had objective responses, including 29% patients who received TTI-621 monotherapy and 21% patients who received TTI-621 combination therapy with rituximab (0.1 mg/kg). The median overall response time of DLBCL patients was 78 days, and the median treatment duration was 143 days. The observed activity suggests that TTI-621 can be used as a monotherapy. Combination with a second agent to elicit the necessary prophagocytic signal is not required, since TTI-621 provides adequate intrinsic activation signals and active Fc regions. The clinical efficacy of TTI-621 is better than those of anti-CD47 agents with less active Fc regions, such as Ig4-based molecules (5F9). The next stage of this ongoing study is to determine the recommended dose of TTI-621 in phase II trial.

The most common side effects of TTI-621 during treatment were infusion-related reactions (43%), thrombocytopenia (26%), chills (18%), fatigue (15%), anemia (13%), nausea (12%), pyrexia (10%), and diarrhea (10%). Infusion-related treatment reactions usually occurred after the first dose and were rarely grade 3 or higher. The incidence of treatment-related anemia for any grade was 13%, and 9% of patients had anemia of grade 3, which was lower than that of a phase I study on 5F9. Treatment-related anemia occurred in 41% of patients with R/R NHL treated with TTI-621 combined with rituximab, and most of them were grade 3 [28].

In contrast with 5F9, the use of an anemia-mitigating priming dose regimen is not required for anemia caused by TTI-621. Both TTI-621 and TTI-622 exhibit minimal binding to human red blood cells. Compared to those treated with 5F9, patients treated with TTI-621 and TTI-662 have a lower risk of anemia during treatment. However, 20% of subjects receiving TTI-621 exhibited treatment-related thrombocytopenia of grade 3 or higher, which was higher than that of 5F9 (5%), and this percentage did not increase as the dose increased. Nevertheless, this effect was reversible, and the patients recovered within 1 week without severe bleeding or dosing interruptions. Overall, TTI-621 is promising as both a monotherapy and in combination [33].

3.3. NI-1701. NI-1701 is a new high-affinity fully human bispecific antibody (biAb) designed to selectively coengage CD47 and CD19 on B-cells to maximally inhibit tumor growth by phagocytosing the targeted cells. NI-1701 is a

Table 1: The comparison of anti-CD47 antibodies for treatment of DLBCL.

Name	Hu5F9-G4	TTI-621	NI-1701
Characteristic	Monoclonal antibody	Fusion protein	Bispecific antibody
Target	CD47	CD47 SIRPα	CD47 CD19
Phase	Phase I/II clinical	Phase I clinical	Phase I clinical
IgG subclass	IgG4	IgG1	Engineered IgG1
AEs	Anemia, thrombocytopenia ≥ 20 mg/kg: chills, headache fatigue, fever	Infusion-related reactions, thrombocytopenia, chills, fatigue, anemia, nausea, pyrexia, diarrhea	

$\kappa\lambda$-body consisting of a high-affinity CD19 targeting arm and an appropriate CD47 blocking arm on a human IgG1 Fc backbone [34, 35]. The Fc domain of anti-CD47 monoclonal antibodies, such as IgG4 (5F9), has been selected to weaken effector functions. Mediated by Fc, this function can prevent CD47 targeted monoclonal antibodies from selectively eliminating healthy host cells. However, this function limits tumor lethality as a monotherapy at the same time. NI-1701 has an Fc-mediated full spectrum effector function. The combination of a high-affinity CD19 binding arm and a low-affinity CD47 arm could highly expand the safety range of CD47-targeted therapies [36]. Therefore, this treatment shows favorable elimination kinetics and overcomes the limitations of other CD47-targeted agents, such as rapid drug elimination and hemotoxicity which can significantly shift the signal for binding to only B-cells and weakly binding to platelets, T-cells, and erythrocytes. ACD47 mAb (hB6H12) could combine with all cells as a control group for CD47 expression. The final tumor growth inhibition (TGI) of NI-1701 was 79%, which was substantially better for controlling tumor growth than rituximab, with a TGI of 48%. NI-1701 also slowed tumor growth for a longer period. Interestingly, NI-1701 and rituximab in combination had a higher TGI (92%) at the end of the treatment period. The survival time was increased by 2.45-fold for patients treated with the two drugs in combination (60 days in the combined treatment group compared to 24.5 days in the control group) [37]. The comparison between Hu5F9-G4, TTI-621, and NI-1701 is listed in Table 1.

4. Crosstalk between CD47 and Other Genes

Studies and bioinformatics analyses have demonstrated that CD47 is associated with other DLBCL-related genes, such as PD-L1, LAG-3, TIM-3, and CD4.

4.1. PD-L1. Cancer cells utilize the programmed cell death 1/programmed cell death ligand 1 (PD-1/PD-L1) pathway to suppress immune cells (including T-cells, B-cells, natural killer cells, lymphocytes, and dendritic cells), leading to poor prognoses in various cancers. As a predictive biomarker, PD-L1 is better used in anticancer monotherapy than combination therapies [38]. PD-1/PD-L1 inhibitors can restore T-cells and improve antitumor immune responses. A clinical study of 121 DLBCL patients showed that immune chemotherapy lowered the levels of soluble PD-1 (sPD-1), and high pretreatment PD-1 levels were associated with poor clinical outcomes. PD-1 is a predictor of the histological transformation (HT) of FL to DLBCL [39–43]. In primary central nervous system diffuse large B-cell lymphoma (PCNS-DLBCL), the PD-1/PD-L1 signaling pathway plays an important role in the immune microenvironment, which correlates with increased sensitivity to chemotherapy and OS. Both PD-1 and PD-L1 are expressed on TILs and tumor cells.

The overexpression of PD-L1 in tumor B-cells was shown to be significantly associated with PD-1 in TILs, and patients with high PD-1 levels in TILs have low survival rates. Epstein–Barr virus (EBV) may be affected by lymphoma cells in posttransplant lymphoma proliferative disorder (PTLD) due to immune surveillance escape.

PD-L1 was reported to be overexpressed in 60% of PTLD patients in immunodeficiency states, and the EBV induced PD-L1 expression in TAMs. A study on 273 patients showed that the upregulation of PD-L1 and mPD-L1 expression in DLBCL cells was significantly associated with non-GCB type and EBV positively, and these patients had a lower OS than DLBCL patients with downregulated PD-L1 expression [41, 44, 45].

4.2. LAG-3. Lymphocyte activation gene-3 (LAG-3, CD223) belongs to the immunoglobulin superfamily and plays a negative regulatory role in T-cell homeostasis. The upregulation of LAG-3 expression was first discovered in activated CD4+, CD8+, and NK cell subsets, but this molecule was also shown to be highly expressed on Treg27 cells as an immunosuppressive molecule.

LAG-3 can be activated upon binding to major histocompatibility (MHC) class II molecules, inhibiting the activity of T lymphocytes and eventually leading to T-cell anergy. A set of genes in cancer immune evasion pathways (immune escape gene set, IEGS) includes TIMP1, LGALS3, CCL2, IL6ST, LGALS1, CD163, IDO1, VEGFA, CSF1, IL-10, LAG-3, MRC1, CTLA4, CD274 (PDCD1LG1), TIGIT, SOCS3, PDCD1LG2, PVR, HGF, GDF15, IDO2, HAVCR2, MSR1, JAK2, LAIR1, CCL22, MCL1, PDCD1, and PIM1 (p values from 5.10^{-12} to 3.10^{-2}). The IEGS gene sets were highly enhanced in DLBCL cells compared to normal B-cells. The LAG-3 gene was upregulated by 3.4-fold in DLBCL cells relative to the control groups ($p < 10^{-13}$), and LAG-3 might promote tumor escape in DLBCL [42].

4.3. TIM-3. T-cell immunoglobulin and mucin domain-containing protein-3 (TIM-3, HAVCR2) is a type I transmembrane protein that is most notably expressed on CD4 + Th1 and CD8+ cytotoxic T-cells to limit the duration and magnitude of T-cell responses. TIM-3 is encoded by HAVCR2, which is located on human chromosome 5. TIM-3 is comprised of 301 amino acids, and its structure includes four regions: an extracellular IgV domain, a mucin domain, a transmembrane region, and a cytoplasmic tail.

Immunohistochemistry analysis of tumor cells and TIL samples from 123 untreated DLBCL patients indicated that TIM-3 was highly expressed in DLBCL tumor cells, and more than one-third of patients (39%) also exhibited TIM-3 expression in TILs. In univariate analysis by controlling for the international prognostic index (IPI) score, a correlation was observed between TIM-3 overexpression and poor OS, resulting in decreased immune surveillance and tumor clearance, was reported [43]. TIM-3 is also highly expressed in peripheral blood CD3+ T-cells from patients with DLBCL and is related to tumor stage and responses to conventional chemotherapy [46, 47].

LAG-3 and TIM are associated. In an EBV-DLBCL study, the Colm Keane research group performed EBV-encoded small RNA in situ hybridization, and the results were digitally quantified (EBER-digital) in 390 cases, comparing the host gene expression results, stratified by the EBER-digital status. Strong associations were observed among immune-related genes in EBV-positive tumors. The immune checkpoints PD-L1 ($p < 0.0001$), PD-L2 ($p = 0.08$), LAG-3 ($p = 0.01$), and TIM-3 ($p = 0.05$) were expressed at higher levels in EBV-positive patients than in EBV-negative patients, and the EBV-negative biopsies revealed similar results. In EBV-DLBCL, LAG-3 and TIM-3 might interact to balance the high level of immunosuppression in the tumor microenvironment (TME) with the increased level of immune checkpoints and tumor-associated macrophages, thus affecting the survival rate [48].

4.4. CD4. CD4 expression serves as a T-cell marker, and its expression in DLBCL is rare and aberrant. Under normal circumstances, T-cell antigens are not abnormally expressed in B-cell lymphoma, and only 10 cases of CD4+ DLBCL have been reported thus far. ALK- CD4+ was observed in all ten cases, including nine cases of DLBCL and one case of primary mediastinal large B-cell lymphoma (PMLBCL) [49].

The density of CD4+ lymphoma cells was increased among ALK+ DLBCL patients. However, CD4 is rarely expressed in DLBCL, not otherwise specified (NOS), with only 4 cases being reported worldwide. This intriguing phenomenon raises questions regarding lineage fidelity and the biology underlying such unusual expression. A few hypotheses have been proposed to explain this phenomenon: for example, the dysregulation of malignant B-cell gene expression may lead to the activation of other silenced or inhibited T-cell differentiation genes, and tumors may cause abnormal expression at the stem cell level. Although the mechanism and importance of this phenomenon are currently uncertain, it leads to interesting biological and diagnostic considerations.

4.4.1. Data Source. The study was carried out using these two strategies and several steps. The data shown in graphs (a) through (d) in Figure 2 were obtained from the GEPIA database (http://gepia.cancer-pku.cn/detail.php). This dataset was selected from DLBCL tumor cells. The Pearson correlation coefficients were calculated on a nonlog scale, and the log-scale axis was used for visualization. The target genes of Figure 2(e) were identified from the whole-genome expression data of human lymphoblast cells found on the GeneNetwork website (http://www.genenetwork.org/webqtl/main.py). This dataset was produced by using lymphoblast B-cell mRNA from UTHSC CEPH B-cells Illumina (Sep09) RankInv. Because GEPIA and the gene network data sources differ, DLBCL tumor cells were not collected from the GeneNetwork database, and the results from these two platforms might thus be slightly biased [50].

4.5. GEPIA Correlation Analysis. In DLBCL, CD47 was positively correlated with TIM-3, LAG-3, and CD4, among which the correlation between CD47 and LAG-3 was the strongest ($r = 0.68$), and CD47 and PD-L1 had the weakest correlation ($r = 0.32$). The R value of CD47 and TIM-3 was 0.51, and that of CD47 and CD4 was 0.58. All of the correlation coefficients of CD47 with other genes, except for PD-L1, were greater than 0.5, indicating that they were closely related.

4.6. QTL Mapping of Four Gene Probes. Since CD4 was not associated with the other four genes after several R values were adjusted, only the remaining four genes in the QTL analysis will be discussed. The expression data from only one of CD47, LAG-3, TIM-3 (HAVCR2), and PD-L1 (CD274) probes were extracted from the human lymphoblastoid cell database. In Figure 2(e), CD47 was shown to be directly related to LAG-3 and TIM-3, while PD-L1 was directly connected to LAG-3, thus indicating an indirect relationship with CD47. The R value of CD47 and TIM-3 was 0.48, suggesting the strongest and most positive correlation, while the absolute value of CD47 and LAG-3 was 0.35 and negatively correlated. In the QTL data analysis, CD47 and TIM-3 had the closest relationship among the four genes. However, CD47 and PD-L1 were not related, with a low R value of 0.03. The R value of PD-L1 and LAG-3 was 0.36, demonstrating a positive correlation.

Although no direct correlation between CD47 and PD-L1 in DLBCL has been reported to date, they both undeniably play important roles in DLBCL, and their "do not eat me" and "do not find me" signaling relationship is essentially interesting. While these two genes did not have a high correlation value, a strong correlation was observed between LAG-3 and CD47, indicating that CD47 and PD-L1 might be linked through LAG-3 via other potential pathways.

TIM-3 and LAG-3 are the most frequently reported genes in DLBCL among these four genes, and they are also closely related to CD47 as immune checkpoints. Moreover, CD47 exhibited direct relationships with TIM-3 and LAG-3, which indicates the potential and value of a follow-up study on the interactions among CD47, LAG-3, and TIM-3 in DLBCL.

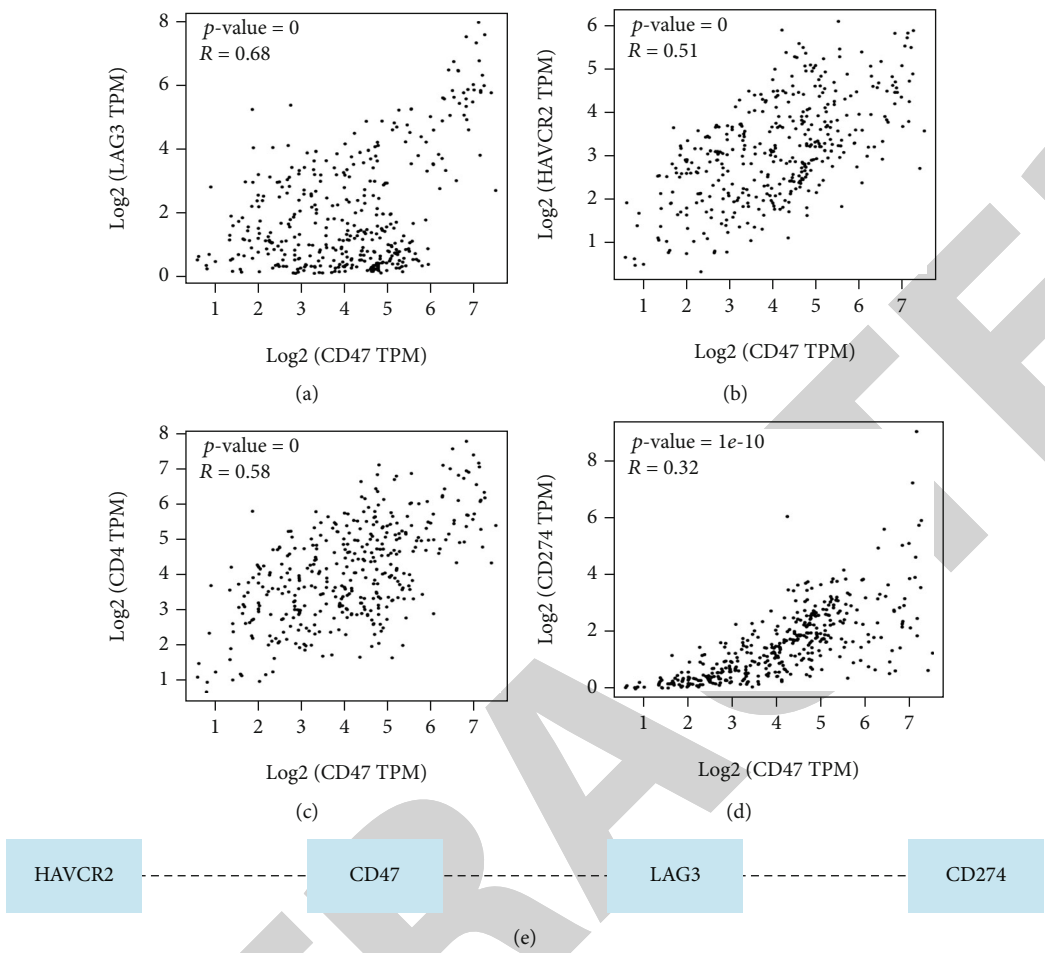

Figure 2: The quantitative trait locus (QTL) mapping and GEPIA correlation analysis of CD47 with Programmed Death-Ligand 1(PD-L1, CD274), lymphocyte activation gene-3 (LAG-3), T-cell immunoglobulin and mucin domain-containing protein-3 (TIM-3, HAVCR2), and CD4. (a) Positive correlation between LAG-3 and CD47 probes. (b) Positive correlation between TIM-3 (HAVCR2) and CD47 probes. (c) Positive correlation between CD4 and CD47 probes. (d) Positive correlation between PD-L1 (CD274) and CD47 probes. (e) The 4 nodes in the network graphs display the 3 traits among the CD47 (1771333), PD-L1 (1794040, CD274), LAG-3 (1813338), and TIM-3 (1693826, HAVCR2) genes. Only Pearson correlation coefficients greater than 0.35 or less than −0.35 are shown.

The expression of CD4 in DLBCL is an unexpected phenomenon. Interestingly, CD47 and CD4 were strongly correlated in the GEPIA analysis. Although the mechanism by which CD4 functions as a T-cell antigen in DLBCL remains unclear and there are no reports of this molecule interacting with CD47 in this disease, these findings can be used as a reference for further studies on the role of CD4 in DLBCL.

5. Conclusion and Future Perspectives

In conclusion, CD47 is a potential target for the treatment of DLBCL, especially for relapsed and refractory DLBCL. Treatment strategies include multitarget combination therapies, such as CD47 monoclonal antibodies combined with CD20 and CD19. The emerging antibodies TTI-621 and NI-1701 were not limited by the adverse reactions of Hu5F9-G4, such as anemia, and showed better therapeutic effects. Moreover, CD47 was highly associated with TIM-3 and LAG-3 in DLBCL at the gene level. Additionally, PD-L1 is a checkpoint commonly used for targeted hematological cancer therapies, and PD-L1 and CD47 in combination have attracted increased attention. A pathway involving CD47 and these genes may exist in this disease, which needs to be verified in ongoing clinical studies to provide new insights for future DLBCL treatment strategies.

Conflicts of Interest

All authors declare that there are no conflicts of interest regarding the publication of this paper.

Acknowledgments

This study was financially supported by the Construction of International Platform for Clinical Evaluation of Hematological Tumor and Major Solid Tumor Drugs (No. 2020ZX09201006) to L.L.H.

References

[1] S. M. G. Hayat, V. Bianconi, M. Pirro, M. R. Jaafari, M. Hatamipour, and A. Sahebkar, "CD47: role in the immune

system and application to cancer therapy," *Cellular Oncology*, vol. 43, no. 1, pp. 19–30, 2020.

[2] P. A. Oldenborg, A. Zheleznyak, Y. F. Fang, C. F. Lagenaur, H. D. Gresham, and F. P. Lindberg, "Role of CD47 as a marker of self on red blood cells," *Science*, vol. 288, no. 5473, pp. 2051–2054, 2000.

[3] M. P. Chao, A. A. Alizadeh, C. Tang et al., "Anti-CD47 antibody synergizes with rituximab to promote phagocytosis and eradicate non-Hodgkin lymphoma," *Cell*, vol. 142, pp. 699–713, 2010.

[4] S. B. Willingham, J. P. Volkmer, A. J. Gentles et al., "The CD47-signal regulatory protein alpha (SIRPa) interaction is a therapeutic target for human solid tumors," *Proceedings of the National Academy of Sciences*, vol. 109, no. 17, pp. 6662–6667, 2012.

[5] H. Yu, S. Peng, S. Han, X. Chen, Q. Lyu, and T. Lei, "Distinct molecular subtypes of diffuse large B cell lymphoma patients treated with rituximab-CHOP are associated with different clinical outcomes and molecular mechanisms," *BioMed Research International*, vol. 2021, Article ID 5514726, 13 pages, 2021.

[6] S. Adams, L. J. van der Laan, E. Vernon-Wilson et al., "Signal-regulatory protein is selectively expressed by myeloid and neuronal cells," *Journal of Immunology*, vol. 161, pp. 1853–1859, 1998.

[7] E. J. Brown and W. A. Frazier, "Integrin-associated protein (CD47) and its ligands," *Trends in Cell Biology*, vol. 11, no. 3, pp. 130–135, 2001.

[8] K. Weiskopf, "Cancer immunotherapy targeting the CD47/SIRPα axis," *European Journal of Cancer*, vol. 76, pp. 100–109, 2017.

[9] H. L. Matlung, K. Szilagyi, N. A. Barclay, and T. K. van den Berg, "The CD47-SIRPα signaling axis as an innate immune checkpoint in cancer," *Immunological Reviews*, vol. 276, no. 1, pp. 145–164, 2017.

[10] M. Dou, Y. Chen, J. Hu, D. Ma, and Y. Xing, "Recent advancements in CD47 signal transduction pathways involved in vascular diseases," *BioMed Research International*, vol. 2020, Article ID 4749135, 11 pages, 2020.

[11] Y. Lin, J. L. Zhao, Q. J. Zheng et al., "Notch signaling modulates macrophage polarization and phagocytosis through direct suppression of signal regulatory protein α expression," *Frontiers in Immunology*, vol. 9, article 1744, 2018.

[12] R. Kazama, H. Miyoshi, M. Takeuchi et al., "Combination of CD47 and signal-regulatory protein-α constituting the "don't eat me signal" is a prognostic factor in diffuse large B-cell lymphoma," *Cancer Science*, vol. 111, no. 7, pp. 2608–2619, 2020.

[13] S. J. Gardai, K. A. McPhillips, S. C. Frasch et al., "Cell-Surface Calreticulin Initiates Clearance of Viable or Apoptotic Cells through *trans* -Activation of LRP on the Phagocyte," *Cell*, vol. 123, no. 2, pp. 321–334, 2005.

[14] M. P. Chao, S. Jaiswal, R. Weissman-Tsukamoto et al., "Calreticulin is the dominant pro-phagocytic signal on multiple human cancers and is counterbalanced by CD47," *Science Translational Medicine*, vol. 2, no. 63, pp. 63ra94–63r94r, 2010.

[15] A. Russ, A. B. Hua, W. R. Montfort et al., "Blocking "don't eat me" signal of CD47-SIRPα in hematological malignancies, an in-depth review," *Blood Reviews*, vol. 32, no. 6, pp. 480–489, 2018.

[16] S. Kaur, A. G. Elkahloun, S. P. Singh et al., "A function-blocking CD47 antibody suppresses stem cell and EGF signaling in triple-negative breast cancer," *Oncotarget*, vol. 7, no. 9, pp. 10133–10152, 2016.

[17] S. Kaur and D. D. Roberts, "Divergent modulation of normal and neoplastic stem cells by thrombospondin-1 and CD47 signaling," *The International Journal of Biochemistry & Cell Biology*, vol. 81, Part A, pp. 184–194, 2016.

[18] D. R. Soto-Pantoja, L. A. Ridnour, D. A. Wink, and D. D. Roberts, "Blockade of CD47 increases survival of mice exposed to lethal total body irradiation," *Scientific Reports*, vol. 3, no. 1, p. 1038, 2013.

[19] T. W. Miller, D. R. Soto-Pantoja, A. L. Schwartz et al., "CD47 Receptor Globally Regulates Metabolic Pathways That Control Resistance to Ionizing Radiation," *The Journal of Biological Chemistry*, vol. 290, no. 41, pp. 24858–24874, 2015.

[20] B. Montico, C. Lapenta, M. Ravo et al., "Exploiting a new strategy to induce immunogenic cell death to improve dendritic cell-based vaccines for lymphoma immunotherapy," *OncoImmunology*, vol. 6, no. 11, article e1356964, 2017.

[21] J. Dal Col, K. Mastorci, D. A. Faè et al., "Retinoic acid/alpha-interferon combination inhibits growth and promotes apoptosis in mantle cell lymphoma through Akt-dependent modulation of critical targets," *Cancer Research*, vol. 72, no. 7, pp. 1825–1835, 2012.

[22] K. Mastorci, B. Montico, D. A. Faè et al., "Phospholipid scramblase 1 as a critical node at the crossroad between autophagy and apoptosis in mantle cell lymphoma," *Oncotarget*, vol. 7, no. 27, pp. 41913–41928, 2016.

[23] O. Kepp, L. Senovilla, I. Vitale et al., "Consensus guidelines for the detection of immunogenic cell death," *Oncoimmunology*, vol. 3, no. 9, article e955691, 2014.

[24] G. Kroemer, L. Galluzzi, O. Kepp, and L. Zitvogel, "Immunogenic cell death in cancer therapy," *Annual Review of Immunology*, vol. 31, no. 1, pp. 51–72, 2013.

[25] A. D. Garg, L. Vandenberk, C. Koks et al., "Dendritic cell vaccines based on immunogenic cell death elicit danger signals and T cell-driven rejection of high-grade glioma," *Science Translational Medicine*, vol. 8, no. 328, pp. 328ra27–328328r, 2016.

[26] R. Bouwstra, Y. He, J. de Boer et al., "CD47 expression defines efficacy of rituximab with CHOP in non–germinal center B-cell (non-GCB) diffuse large B-cell lymphoma patients (DLBCL), but not in GCB DLBCL," *Cancer Immunology Research*, vol. 7, no. 10, pp. 1663–1671, 2019.

[27] B. I. S. N. Patnaik, "First-in-human, first-in-class phase I trial of the anti-CD47 antibody Hu5F9-G4 in patients with advanced cancers," *Journal of Clinical Oncology*, vol. 37, p. 946, 2019.

[28] R. Advani, I. Flinn, L. Popplewell et al., "CD47 blockade by Hu5F9-G4 and rituximab in non-Hodgkin's lymphoma," *The New England Journal of Medicine*, vol. 379, no. 18, pp. 1711–1721, 2018.

[29] C. Caruso, "Anti-CD47 agent boosts macrophage activity in NHL," *Cancer Discovery*, vol. 9, no. 1, pp. 7-8, 2019.

[30] E. Eladl, R. Tremblay-LeMay, N. Rastgoo et al., "Role of CD47 in hematological malignancies," *Journal of Hematology & Oncology*, vol. 13, no. 1, p. 96, 2020.

[31] G. H. Y. Lin, V. Chai, V. Lee et al., "TTI-621 (SIRPαFc), a CD47-blocking cancer immunotherapeutic, triggers phagocytosis of lymphoma cells by multiple polarized macrophage subsets," *PLoS One*, vol. 12, no. 10, article e187262, 2017.

[32] M. Feng, J. Y. Chen, R. Weissman-Tsukamoto et al., "Macrophages eat cancer cells using their own calreticulin as a guide:

Hindawi
Disease Markers
Volume 2023, Article ID 9791279, 1 page
https://doi.org/10.1155/2023/9791279

Retraction

Retracted: The Mechanism of Xiaoyao San in the Treatment of Ovarian Cancer by Network Pharmacology and the Effect of Stigmasterol on the PI3K/Akt Pathway

Disease Markers

Received 11 July 2023; Accepted 11 July 2023; Published 12 July 2023

This article has been retracted by Hindawi following an investigation undertaken by the publisher [1]. This investigation has uncovered evidence of one or more of the following indicators of systematic manipulation of the publication process:

(1) Discrepancies in scope
(2) Discrepancies in the description of the research reported
(3) Discrepancies between the availability of data and the research described
(4) Inappropriate citations
(5) Incoherent, meaningless and/or irrelevant content included in the article
(6) Peer-review manipulation

The presence of these indicators undermines our confidence in the integrity of the article's content and we cannot, therefore, vouch for its reliability. Please note that this notice is intended solely to alert readers that the content of this article is unreliable. We have not investigated whether authors were aware of or involved in the systematic manipulation of the publication process.

Wiley and Hindawi regrets that the usual quality checks did not identify these issues before publication and have since put additional measures in place to safeguard research integrity.

We wish to credit our own Research Integrity and Research Publishing teams and anonymous and named external researchers and research integrity experts for contributing to this investigation.

The corresponding author, as the representative of all authors, has been given the opportunity to register their agreement or disagreement to this retraction. We have kept a record of any response received.

References

[1] M. Li, W. Zhang, L. Yang et al., "The Mechanism of Xiaoyao San in the Treatment of Ovarian Cancer by Network Pharmacology and the Effect of Stigmasterol on the PI3K/Akt Pathway," *Disease Markers*, vol. 2021, Article ID 4304507, 10 pages, 2021.

Hindawi
Disease Markers
Volume 2021, Article ID 4304507, 10 pages
https://doi.org/10.1155/2021/4304507

Research Article

The Mechanism of Xiaoyao San in the Treatment of Ovarian Cancer by Network Pharmacology and the Effect of Stigmasterol on the PI3K/Akt Pathway

Meng Li,[1] Wenqi Zhang,[2] Linqi Yang,[1] Huibing Wang,[1] Yihan Wang,[1] Kai Huang,[1] and Wei Zhang[1]

[1]*Department of Pharmacology, College of Basic Medicine, Hebei University of Chinese Medicine, Shijiazhuang, 050200 Hebei Province, China*
[2]*Department of Hematology, The Fourth Hospital of Hebei Medical University, Shijiazhuang, 050000 Hebei Province, China*

Correspondence should be addressed to Wei Zhang; zhangwei@hebcm.edu.cn

Received 26 April 2021; Accepted 19 June 2021; Published 30 June 2021

Academic Editor: Zhongjie Shi

Purpose. This study was aimed at exploring the regulatory mechanism of Xiaoyao San (XYS) and its main compound, Stigmasterol, in the biological network and signaling pathway of ovarian cancer (OC) through network pharmacology-based analyses and experimental validation. *Methods*. The active compounds and targets of XYS were studied by the Traditional Chinese Medicine Systems Pharmacology Database and Analysis Platform (TCMSP). The GeneCards and OMIM databases were used to screen common targets of XYS in the treatment of OC. Combined with the STRING database and Cytoscape 3.6.0, the core compounds and targets of XYS were obtained. GO and KEGG pathway enrichment analyses of core target genes were carried out by using the Metascape and DAVID databases. Molecular docking has been achieved by using the AutoDock Vina program to discuss the interaction of the core targets and compounds of XYS in the treatment of OC. The effect of Stigmasterol on proliferation and migration were assessed by CCK8 and wound healing assay. Western blot and qRT-PCR were used to analyze the protein and mRNA expressions of PI3K, Akt, and PTEN after treatment of Stigmasterol. *Results*. A total of 113 common targets of XYS for the treatment of OC were obtained from 975 targets related to OC and 239 targets of XYS's effect. The main compounds of XYS include Quercetin, Naringenin, Isorhamnetin, and Stigmasterol, which mainly regulate the targets such as TP53, Akt1, and MYC and PI3K/Akt, p53, and cell cycle signal pathways. At the same time, molecular docking showed that Stigmasterol and Akt1 had good docking conformation. Stigmasterol inhibited OC cell proliferation and migration in vitro and reduced the protein and mRNA expressions of the PI3K/Akt signaling pathway. *Conclusion*. Stigmasterol as the one of the main compounds of XYS suppresses OC cell activities through the PI3K-Akt signaling pathway.

1. Introduction

Ovarian cancer (OC) is the most frequently diagnosed and highest mortality in gynecological cancers. The 5-year overall survival rate was about 40% when most patients were late at the time of discovery because the lack of symptoms was not obvious [1, 2]. Currently, the main treatment of OC is surgery, platinum-based chemotherapy, and radiotherapy. In a clinical study, 30-45% BRCA1/2 mutation patients showed response to the PARP inhibitor Olaparib. But relapse and metastasis were considered to be due to resistance and toxicities. Therefore, how to increase the response rate and relieve side effects still remains to be completed. A number of clinical trials have shown that the traditional Chinese medicine combination with chemotherapy or radiotherapy may benefit OC patients [3–5].

XYS from Prescriptions of Peaceful Benevolent Dispensary can soothe the liver, nourish the blood, invigorate the spleen, and harmonize the heart. It is mostly used for hepatic stagnation, spleen deficiency, and blood deficiency syndrome. However, the mechanism of XYS in the treatment of OC is unknown and needs further discussion.

With the rapid development of bioinformatics, systems biology, and polypharmacology, network-based drug discovery is considered to be an economical and effective drug development method [6]. In recent years, increasing evidence has shown that many drugs can stimulate their therapeutic activities by regulating multiple targets [7]. Due to the abundant ingredients in Chinese herbs and the complex changes of disease-related molecules, the mechanism of most traditional Chinese medicines (TCM) and their derivatives in complex diseases remains to be elucidated.

In this study, several drug target prediction databases were used to analyze XYS, and the protein-protein interaction network (PPI) of the main targets of XYS in the treatment of OC was constructed to explore its main biological functions and signaling pathways. Finally, the effect of Stigmasterol on the PI3K/Akt signaling pathway was verified by a cell experiment in vitro, which provides a new basis for the development and application of XYS and its compound Stigmasterol.

2. Materials and Methods

2.1. Main Drugs and Reagents. Fetal bovine serum (FBS) was obtained from HyClone (USA), and RPMI (Roswell Park Memorial Institute) 1640 medium, penicillin, streptomycin, and all other reagents were obtained from GIBCO (USA). Stigmasterol (purity: 98%, APExBIO Technology LLC) was dissolved in DMSO and stored at -20°C. The final concentration of DMSO in cultures was ≤0.1% (*v*/*v*).

2.2. Common Targets of XYS in the Treatment of OC. The Traditional Chinese Medicine Systems Pharmacology Database and Analysis Platform (TCMSP, http://www.tcmspw.com/tcmsp.php) was used to collect the active compounds of XYS, including Bupleurum, Radix Paeoniae Alba, Angelica sinensis, Atractylodes macrocephala, Poria cocos, Glycyrrhiza uralensis, ginger, and peppermint. The active compounds and their targets in the composition of XYS were selected by ADME evaluation systems, the main parameters of which were oral bioavailability (OB ≥ 30%) and drug-likeness (DL ≥ 0.18). Through the STRING database (https://string-db.org/) [8], the collected target names of XYS were standardized gene IDs, and species sources were humans ("Homo sapiens"). GeneCards (https://www.genecards.org/) and OMIM (https://omim.org/) were utilized to collect genes and targets related with OC [9]. The 113 common targets of OC and active components were obtained by Draw Venn Diagram (http://bioinformatics.psb.ugent.be/webtools/Venn/) (Figure 1).

2.3. Protein-Protein Interaction (PPI) Network. The PPI network was obtained from the above 113 common targets by STRING and "Homo species" was selected. The minimum interaction threshold was selected as "medium confidence >0.4." The Cytoscape 3.6.0 software was used to analyze the core targets of the network, and "PNG" format was the output (Figure 1). The top 3 targets (TP53, Akt1, MYC) were identified as the hub genes of XYS in the treatment of OC, which were used in following studies. The expressions of the top 3 targets were acquired in https://www.helixlife.cn/.

2.4. Gene Ontology (GO) and Kyoto Encyclopedia of Genes and Genomes (KEGG) Pathway Enrichment Analyses. The GO and KEGG enrichment analyses were obtained from the above 113 common targets by the Metascape database (http://metascape.org/) and DAVID database (https://david.ncifcrf.gov/); $P < 0.05$ was significant.

2.5. Construction of Herb-Active Compound-Target Network. Cytoscape 3.6.0 was used to construct the "herb-active compound-target" network of XYS in the treatment of OC. We identify the top 10 active compounds as the core compounds of XYS in the treatment of OC.

2.6. Molecular Docking. The interaction between the core compounds and targets of XYS in the treatment of OC was checked by using molecular docking technology. The target protein structures were downloaded from the PDB website (http://www.rcsb.org/), and the 3D structures of the core compounds were downloaded from the TCMSP database. The molecular docking and conformation scoring were carried out in the AutoDock Vina.

The heat map was obtained by the GraphPad Prism 8. The PyMOL and Maestro 11.9 were used to draw the structure of the best docking results.

2.7. Relationship between the mRNA Levels of Akt1 and the Survival Outcomes of Patients with OC. We utilized R3.6.3 software to carry out the receiver operating characteristic curve (ROC curve) and Kaplan-Meier curve (KM curve) enrichment analyses. We prepared the RNAseq data and clinical data from the ovarian serous cystadenocarcinoma (OV) project in TCGA (https://portal.gdc.cancer.gov/) and transformed them into transcripts per million read (TPM) format and then analyzed them according to the molecular expression.

2.8. Culture of OC Cell Lines. A2780 and SKOV3 cell lines were cultured in RPMI1640 medium with 10% (*v*/*v*) FBS and 100 U/ml penicillin/100 mg/ml streptomycin at 37°C in the 5% CO_2 atmosphere.

2.9. Cell Proliferation Assay. Ovarian cancer A2780 and SKOV3 cells were seeded into 96-well plates with gradient concentration (0 μM, 10 μM, 25 μM, 50 μM, 100 μM, and 500 μM) Stigmasterol for 24, 48, and 72 hours at 37°C. The OC cells were replaced with a 10% Cell Counting Kit-8 (CCK8; Beijing Zoman Biotechnology Co., Ltd., Beijing, China) diluted with normal culture medium and incubated for 1 h. The absorbance of each well was measured with a Motic digital medical image analysis system (Leica DM2500, Heidelberg, Germany) at 450 nm. All tests were repeated three times [10].

2.10. Preparation of Stigmasterol. Stigmasterol was dissolved in DMSO, mixed and filtered through a 0.22 μm filter. The stock solution at 10 mM concentration was prepared and stored in a refrigerator at -20°C, and it was defrosted and

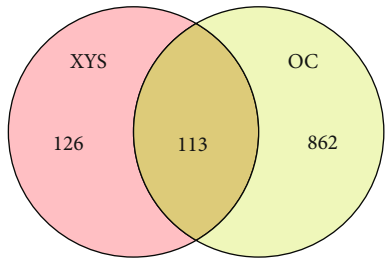

(a)

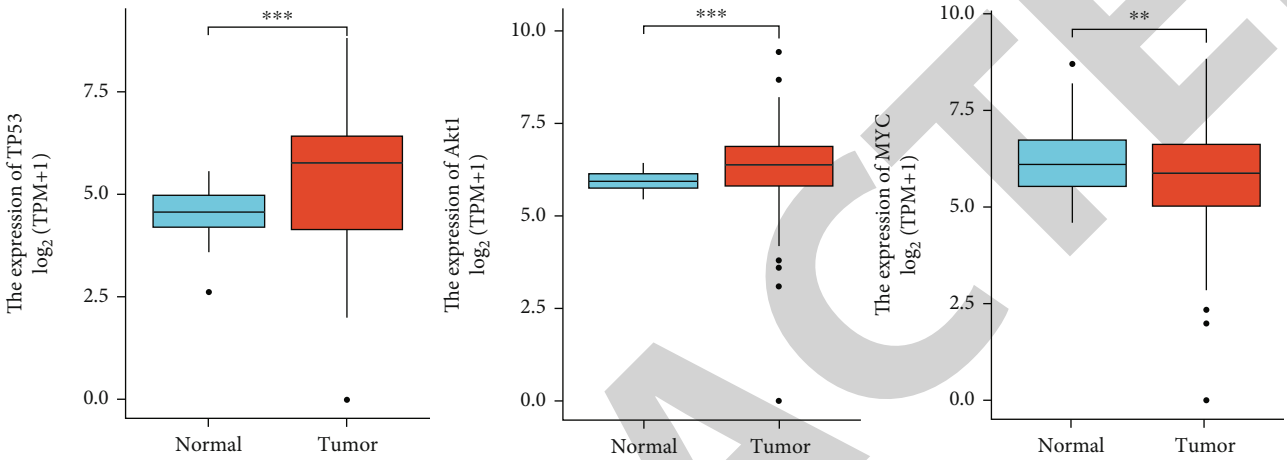

(b)

Figure 1: Continued.

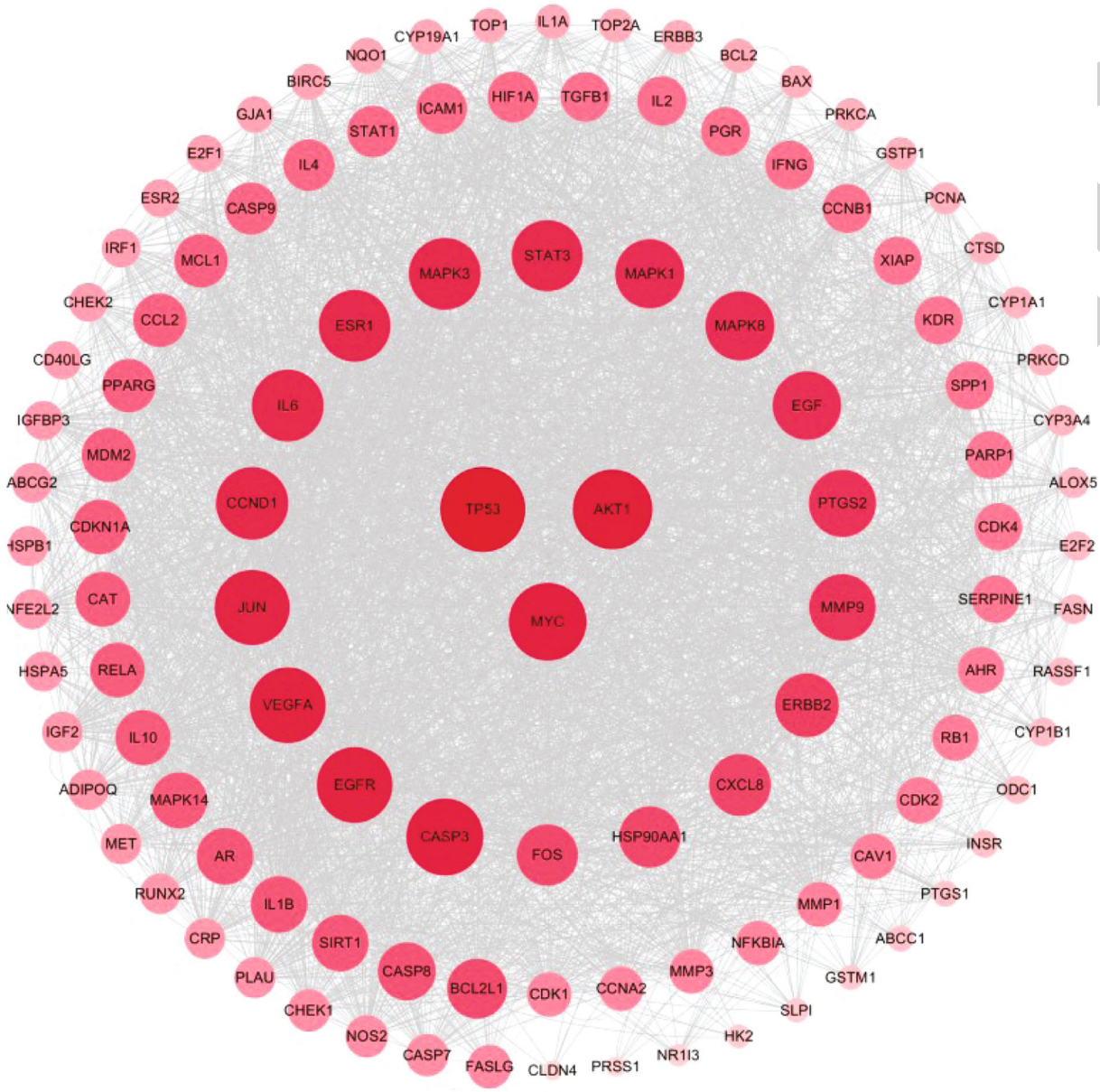

(c)

Figure 1: (a) The targets of XYS in treatment of OC. Venn diagram showing 975 targets associated with OC and 239 targets of XYS. Overlap represents 113 common target genes. (b) The high expression of Akt1 and TP53 and low expression of MYC in OC. $^{**}P < 0.01$, $^{***}P < 0.001$. (c) Interaction target network of XYS treatment of OC. The top 3 targets in terms of degree value are TP53, Akt1, and MYC.

diluted to the desired concentration with 1640 complete medium before use.

2.11. Wound Healing Assay. The comparison of the cell culture area for the wound-healing assay was generated by a 10 μl pipette tip, after A2780 and SKOV3 cells were cultured in the RPMI1640 medium with 10% FBS without or with 25 and 50 μM Stigmasterol, respectively. The Motic digital medical image analysis system was used by Leica DM2500, Heidelberg, Germany [11].

2.12. Real-Time Fluorescence Quantitative Polymerase Chain Reaction (qRT-PCR). Total RNA from the above-mentioned cells was isolated with a TRIzol Reagent (Life Technologies, USA) according to the manufacturer's instructions. RNA concentration and purity were assessed by spectrophotometry at 260 nm. A total of 1 μg RNA was converted into cDNA by a Prime Script RT reagent Kit (Takara Co. Ltd., USA). qRT-PCR was performed by using a Real-Time PCR System (Bio-Rad Co. Ltd., USA) in reaction mixtures (25 μl) containing cDNA, primer pairs (Table 1), and TB Green Premix Ex Taq II (Takara Co. Ltd., USA).

2.13. Western Blot (WB). A2780 and SKOV3 cells were treated with Stigmasterol for 48 h. After washing with PBS three times, the cells were lysed for 30 min on ice and

Table 1: The primers of genes.

Primers	Forward (5′-3′)	Reverse (5′-3′)
PI3K	AGTAGGCAACCGTGAAGAAAAG	GAGGTGAATTGAGGTCCCTAAGA
AKT	AGCGACGTGGCTATTGTGAAG	GCCATCATTCTTGAGGAGGAAGT
PTEN	TGGATTCGACTTAGACTTGACCT	GGTGGGTTATGGTCTTCAAAAGG
β-Actin	TGACGTGGACATCCGCAAAG	CTGGAAGGTGGACAGCGAGG

centrifuged at 10000 × g for 5 min at 4°C. The contents of segregated proteins in cell lysates were quantified using an ND-1000 Spectrophotometer (NanoDrop, Wilmington, Delaware, USA). Equal amounts of protein samples were electrophoresed through 10% SDS-PAGE (polyacrylamide gel electrophoresis) and transferred to PVDF membranes (Millipore, Bedford, Massachusetts, USA). After 5% BSA block for 2 h, they were immunoblotted with primary antibodies for overnight at 4°C. The primary antibodies include p-Akt (GB13012-3, 1 : 500), Akt (GTX28805, 1 : 800), p-PI3K (GTX132597, 1 : 800), PI3K (ab40755, 1 : 1000), PTEN (ET1606-43, 1 : 800), and β-actin (AC026, 1 : 10000). Next, the membranes were incubated with secondary antibodies of goat anti-rabbit IG (KPL074-1506, at 1 : 5000 dilution) for 1 h at 37°C. The intensity of protein bands was estimated via executing the Fusion FX5 Spectra (Fusion, France).

3. Results

3.1. PPI Network of XYS in Treatment of OC. In Figure 1, the XYS in the treatment of the OC interaction network with 113 nodes and 1805 edges is shown. The Cytoscape was adopted to obtain the top 3 hub targets of interactions including TP53, Akt1, and MYC. As a result, the expression of Akt1 and TP53 was higher and that of MYC was lower in OC tissues than in normal tissues (Figure 1).

3.2. GO and KEGG Pathway Enrichment Analyses. The GO and KEGG pathway of targets of XYS in the treatment of OC were involved in 338 signaling pathways, including the PI3K-Akt signaling pathway, bladder cancer, pancreatic cancer, hepatitis B, microRNAs in cancer, and HIF-1 signaling pathway. The top 20 pathways are shown in Figure 2.

3.3. Herb-Active Compound-Target Network. This network graph directly evaluates the mechanism of XYS in the treatment of OC through multicompound and multitarget synergistic action. The herb-active compound-target network has shown the top 10 active compounds of XYS in the treatment of OC including Quercetin, Kaempferol, and Stigmasterol (Table 2).

3.4. Molecular Docking. The top 10 main compounds of XYS were docked with the protein structures of Akt1, TP53, and MYC. The results showed that Stigmasterol was the best binding ability to Akt1 and the Vina score (ΔG) was -10.60 kca1/mol (Figure 2). The molecular docking revealed the Stigmasterol bond with Akt1 through hydrophobic interaction at sites such as LEU264, VAL270, LEU210, and LEU264 (Figure 2).

3.5. Relationship between the mRNA Levels of Akt1 and the Survival Outcomes of Patients with OC. We further explored the critical efficiency of Akt1 in the survival of patients with OC. The ROC curve analysis for Akt1 in OC determined that AUC of the ROC curve is 0.702. The Kaplan–Meier curve and log-rank test analysis revealed that the increased Akt1 mRNA levels were significantly associated with the overall survival (OS) of OC patients (Figure 2). Higher expression of Akt1 showed the longer overall survival.

3.6. Effect of Stigmasterol on the Proliferation of A2780 and SKOV3 Cells. The CCK8 assay result suggested that Stigmasterol could significantly inhibit A2780 and SKOV3 cell proliferation in a dose-dependent manner ($P < 0.05$). The IC_{50} values are shown in Table 3. The following experiments were carried out with Stigmasterol at concentrations of 25 μM and 50 μM for 48 h.

3.7. Effect of Stigmasterol on the Migration of A2780 and SKOV3 Cells. As the result of compound Stigmasterol displayed a significant cytotoxic activity against ovarian cancer A2780 and SKOV3 cell lines, the wound healing assay showed that Stigmasterol inhibited migration of A2780 and SKOV3 cells (Figure 3).

3.8. Stigmasterol Inhibited the mRNA Expression of PI3K-Akt Signaling Pathway in A2780 and SKOV3 Cell Lines by qRT-PCR. The results of qRT-PCR showed that comparing with the control and DMSO groups, the mRNA expression of PI3K and Akt1 was significantly reduced by Stigmasterol. The mRNA expression of PTEN was increased in Stigmasterol groups ($P < 0.05$) (Figure 3).

3.9. Stigmasterol Inhibited the Protein Expression of PI3K-Akt Signaling Pathway in A2780 and SKOV3 Cell Lines by Western Blot Assay. The protein expressions of p-PI3K/PI3K and p-Akt/Akt were significantly decreased, and the PTEN expression was increased in Stigmasterol groups compared with the control and DMSO groups ($P < 0.05$) (Figure 3). This result showed that Stigmasterol can effectively inhibit the PI3K-Akt signaling pathway in human A2780 and SKOV3 cells.

4. Discussion

In traditional Chinese medicine, XYS has been proposed for anticancer activities and was used in the treatment of breast hyperplasia, breast cancer, and OC by reinforcing qi and nourishing the blood. XYS is a classic Chinese prescription which was first described in the Prescriptions of Peaceful Benevolent Dispensary in the Song Dynasty (A.D. 1151).

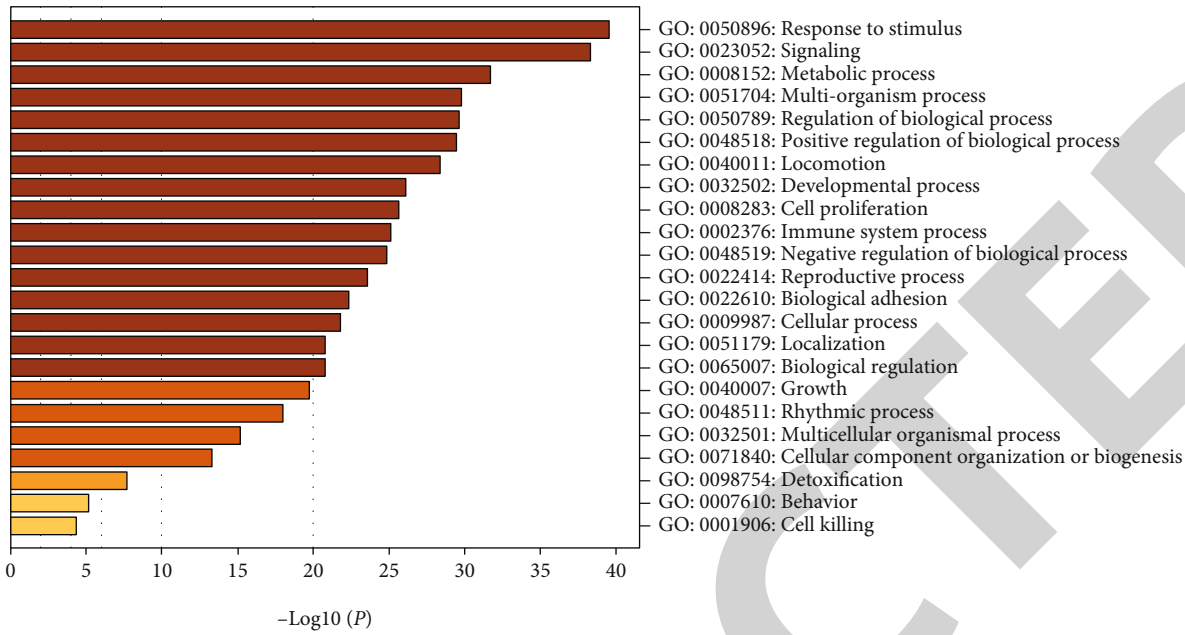

(a)

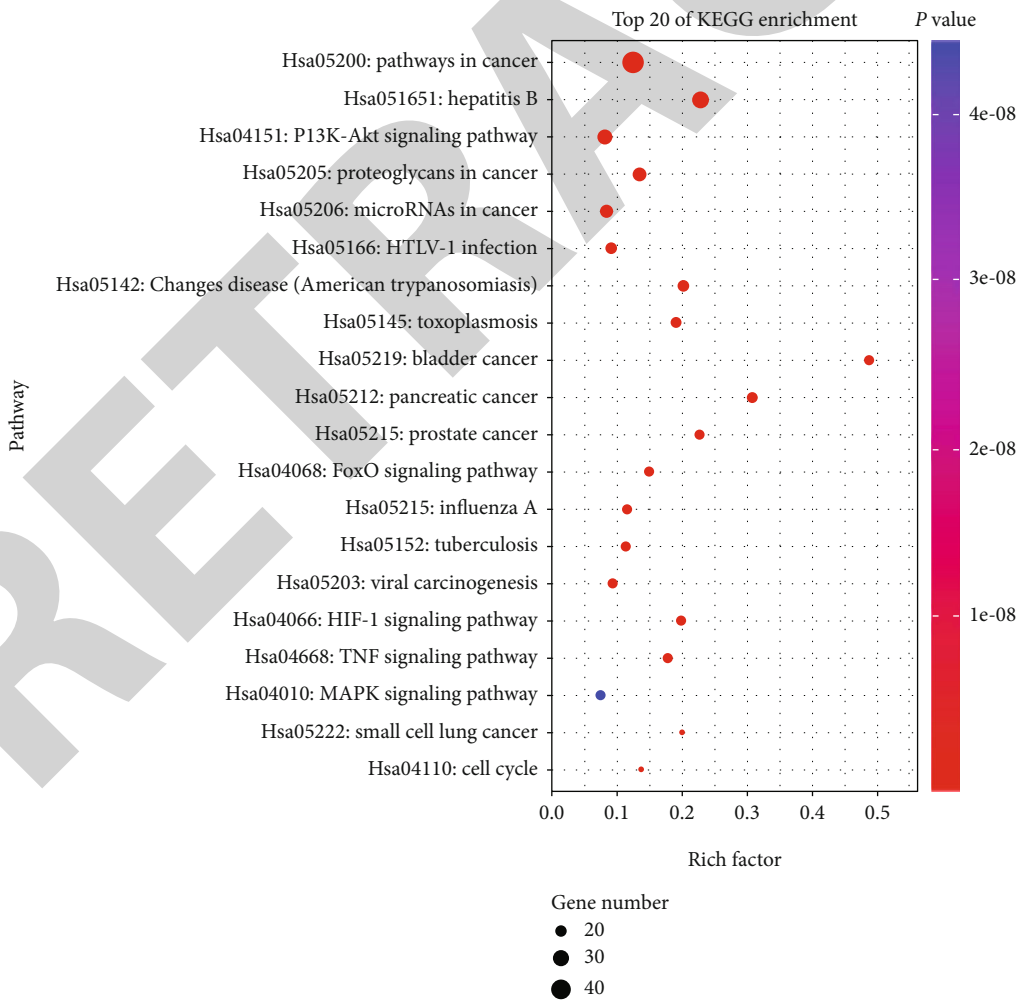

(b)

Figure 2: Continued.

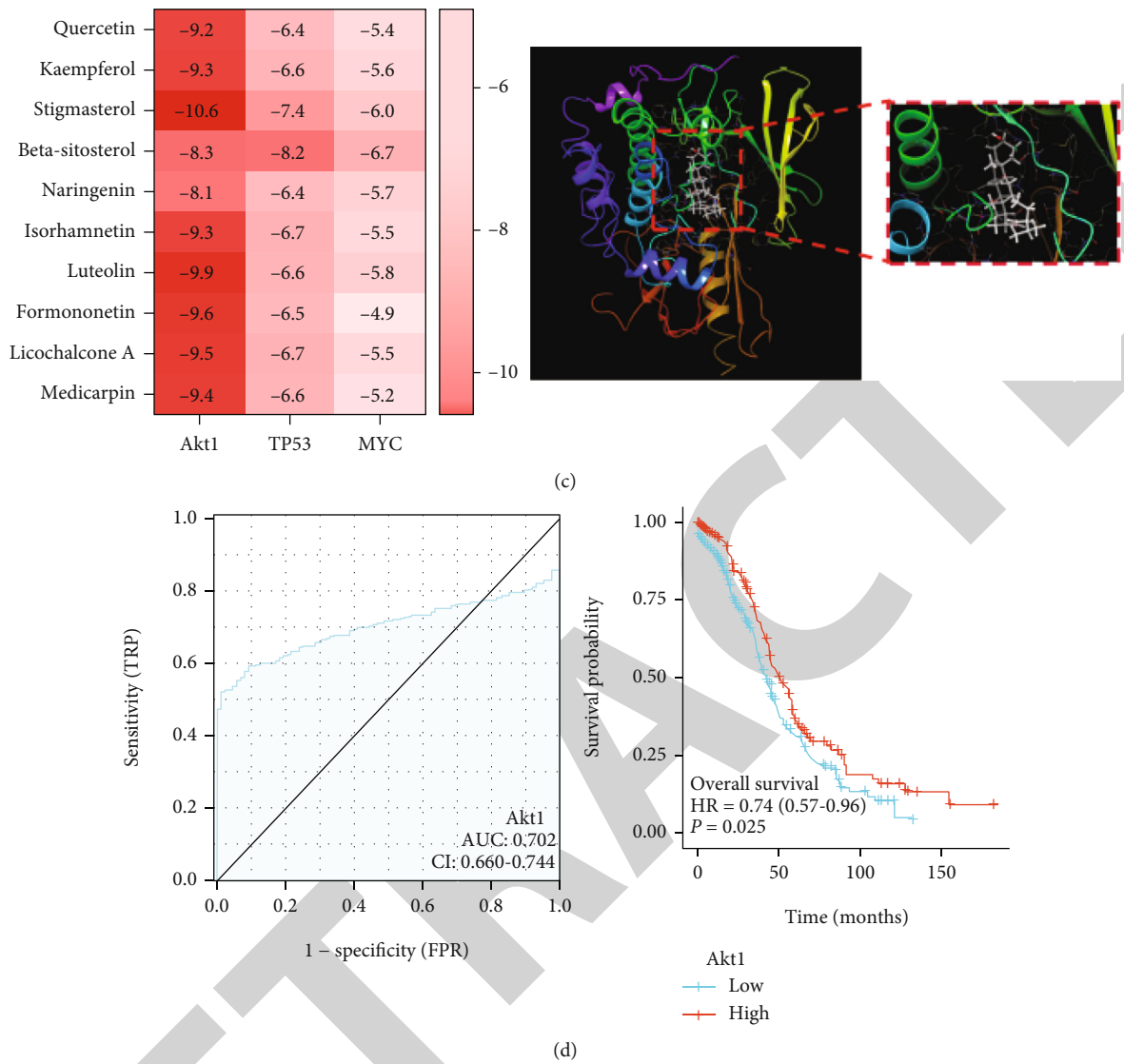

Figure 2: (a) GO enrichment in targets of XYS treatment of OC. (b) Top 20 of KEGG pathway enrichment in targets of XYS treatment of OC. (c) Results of molecular docking. Diagram of interaction between Akt1 protein and Stigmasterol (3D). (d) Relationship between the mRNA levels of Akt1 and the survival outcomes of patients with OC. A is the ROC curve of Akt1 in OC. B is the KM curve of Akt1 in OC.

Table 2: The top 10 active compounds of XYS in the treatment of OC.

No.	Active compounds
1	Quercetin
2	Kaempferol
3	Stigmasterol
4	Beta-sitosterol
5	Naringenin
6	Isorhamnetin
7	Luteolin
8	Formononetin
9	Licochalcone A
10	Medicarpin

Table 3: IC_{50} of Stigmasterol on A2780 and SKOV3 cells.

Time (hour)	IC_{50} (μM) (mean ± SD)	
	A2780	SKOV3
24	69.24 ± 7.31	83.39 ± 3.75
48	49.74 ± 3.18	77.68 ± 5.43
72	38.12 ± 4.69	67.02 ± 3.13

In this study, as the result of the network pharmacology, XYS possessed the multicomponent, multitarget synergistic effect in the treatment of OC. The main active compounds of XYS in this network include Quercetin, β-sitosterol, Kaempferol, and Stigmasterol. Previous studies indicated that Quercetin has the anticancer activities involved in down-regulating the levels of RAS, BCL-2, mutant P53, and upregulating BAX [12]. Studies have shown that β-sitosterol has

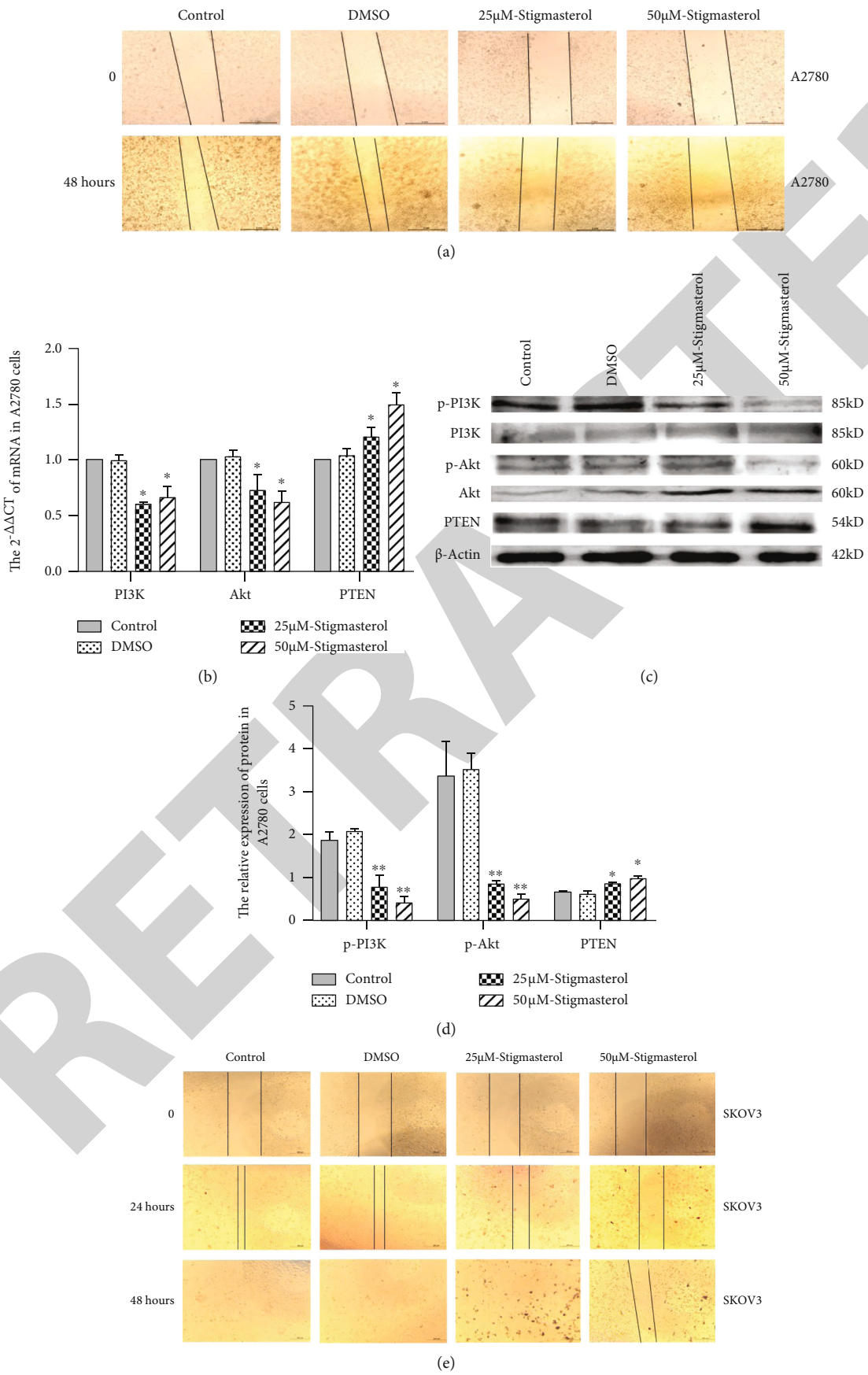

Figure 3: Continued.

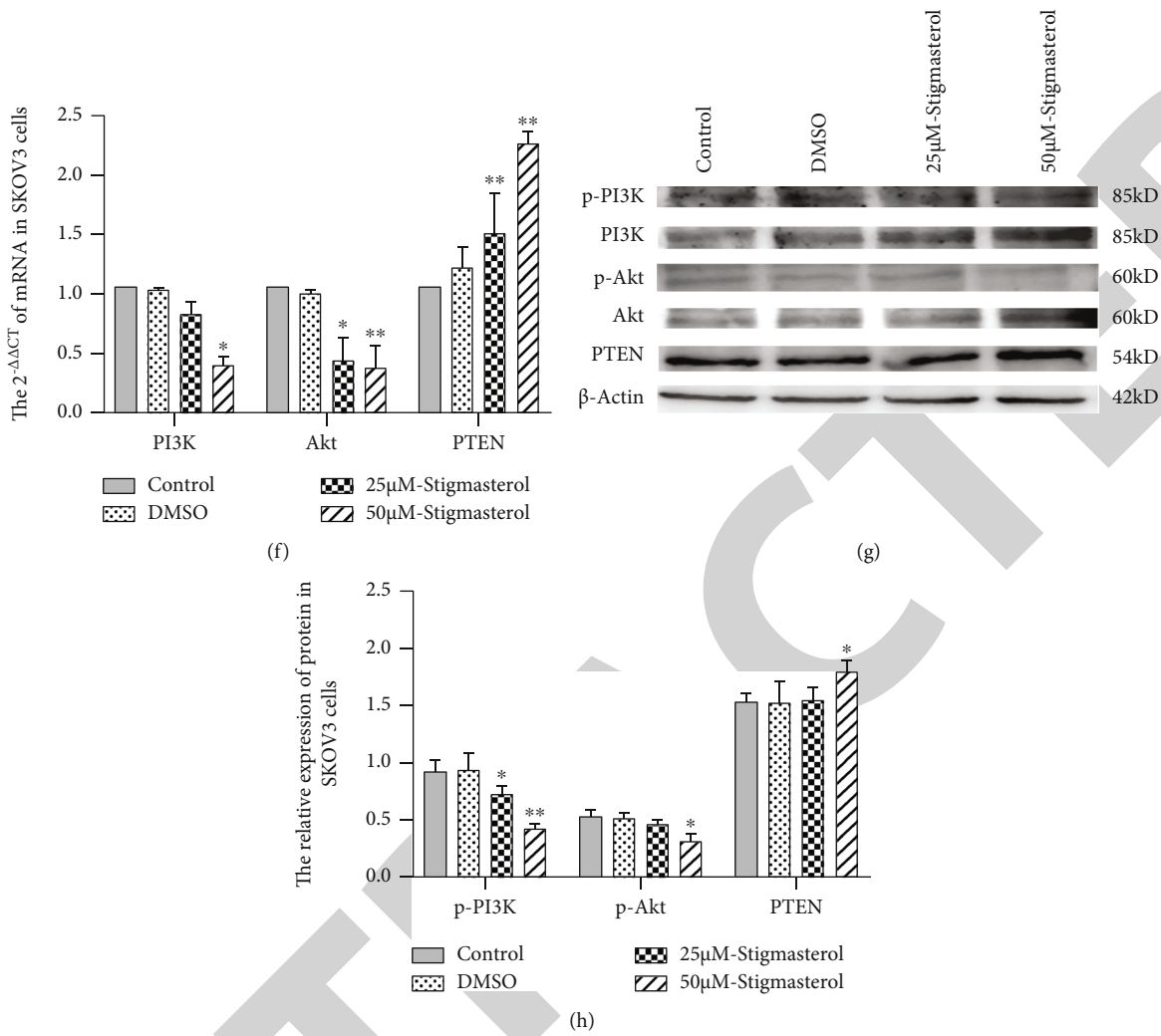

Figure 3: (a) Stigmasterol inhibited the migration in A2780 cells. (b) The effect of Stigmasterol on expressions of the PI3K-Akt signaling pathway by qRT-PCR in A2780 cells. (c, d) Western blot assay showed that Stigmasterol downregulated the expression of p-PI3K and p-Akt protein levels and upregulated the expression of PI3K, Akt, and PTEN protein levels in A2780 cells. (e) Stigmasterol inhibited the migration in SKOV3 cells. (f) The effect of Stigmasterol on expressions of the PI3K-Akt signaling pathway by qRT-PCR in SKOV3 cells. The effect of Stigmasterol on expression of the PI3K-Akt signaling pathway in SKOV3 cells. Stigmasterol increased the mRNA expression level of PTEN and decreased the mRNA expression level of PI3K and Akt. (g, h) Western blot assay showed that Stigmasterol downregulated the expression of p-PI3K and p-Akt protein levels and upregulated the expression of PI3K, Akt, and PTEN protein levels in SKOV3 cells. $^{*}P < 0.05$, $^{**}P < 0.01$ vs. control group. The dosage of Stigmasterol was 25 μM and 50 μM in A2780 and SKOV3 cells, respectively.

the wide anticancer properties such as inducing apoptosis and inhibiting proliferation, invasion, metastasis, and angiogenesis in colon cancer, ovarian cancer, lung cancer, breast cancer, and prostate cancer. β-Sitosterol exerted against ovarian cancers by estrogen reabsorption. Also, β-sitosterol decreased the expression of β-catenin, PCNA (proliferating cell nuclear antigen), and Bcl-2 in colon cancer [13]. Kaempferol can reduce the expressions of p-Akt (phosphorylated Akt) protein in OC cells. It inhibits cell migration and angiogenesis in human OC cells, induces apoptosis and ROS production, and thus inhibits the growth and development of human OC cells [14]; Stigmasterol effectively targets tumor endothelial cells by suppressing the expressions of TNF-2, VEGFR-2 and p-Akt, PCL, and FAK [15].

The PPI network of XYS in the treatment of OC indicated that the core targets include Akt1, TP53, and MYC. Therefore, we used the database to analyze the expression of the above 3 hub genes in OC tissues and normal tissues. The results showed that Akt1 and TP53 were highly expressed in OC tissues and MYC expression was lower in OC tissues than in normal tissues. GO and KEGG pathway enrichment analyses of XYS in the treatment of OC also found that the PI3K/Akt signaling pathway plays a role in OC signaling pathways. From the molecular docking result, Stigmasterol showed a strong interaction with Akt1. Meanwhile, the expression of Akt1 in OC is closely related to OS of clinical patients. Therefore, we predict that Akt1 may be a potential core target of Stigmasterol for the treatment of OC.

In clinical researches, the dysregulations of the PI3K/Akt signaling pathway were found in 70% OC, involving PTEN deletion and PIK3CA mutations [16]. Genetic alterations and aberrant activation of AKT are due to the ovarian cell

Hindawi
Disease Markers
Volume 2021, Article ID 4745853, 8 pages
https://doi.org/10.1155/2021/4745853

Research Article

Comparison of Percutaneous Kyphoplasty with or without Pedicle Screw Fixation in Osteoporotic Thoracolumbar Vertebral Fractures: A Retrospective Study

Dichao Huang, Jichong Ying, Dingli Xu, Jianming Chen, Jianlei Liu, Tianming Yu, Yunqiang Zhuang, and Long Zhou

Ningbo No.6 Hospital, Zhejiang, Ningbo 315000, China

Correspondence should be addressed to Yunqiang Zhuang; 1327887510@qq.com and Long Zhou; bruce_zhou1976@163.com

Received 28 April 2021; Revised 21 May 2021; Accepted 18 June 2021; Published 30 June 2021

Academic Editor: Zhongjie Shi

Background. Osteoporotic thoracolumbar compression fractures have become a great social burden due to the aging tendency of population. This study is aimed at comparing the clinical and radiological outcomes of percutaneous kyphoplasty with or without pedicle screw fixation in patients with osteoporotic thoracolumbar fractures. *Hypothesis*. There is a difference in clinical outcomes between percutaneous kyphoplasty with pedicle screw fixation and percutaneous kyphoplasty. *Methods*. This retrospective study included 87 patients who received percutaneous kyphoplasty with or without pedicle screw fixation between October 2015 and October 2017 at Ningbo No.6 Hospital and were followed for 2 years. A total of 40 patients received percutaneous kyphoplasty with pedicle screw fixation (PKPF group), and the other 47 patients had percutaneous kyphoplasty only (PKP group). The outcomes were measured using the visual analogue scale (VAS), Oswestry Disability Index (ODI), Cobb angle (CA), and anterior vertebra height rate (AVHr), which were calculated at preoperative admission and each follow-up visit. Complications including postoperative back pain, refracture, and fixation failure were collected from medical records. *Results*. There was no significant difference in baseline characteristics or preoperative data between the two groups ($p < 0.05$) but significantly better improvements in VAS, ODI, CA, and AVHr at 12- and 24-month follow-up visits in the PKPF group compared with those of the PKP group. 23 (48.9%) patients in the PKP group had complications, whereas only 5 (12.5%) patients in the PKPF group presented complications including 2 postoperative back pain and 1 fixation failure ($p = 0.04$). *Conclusions*. PKPF obtained longer correction and better improvement in VAS, ODI, and CA in patients with osteoporotic thoracolumbar vertebral fractures than PKP.

1. Background

Osteoporosis vertebral compression fracture (OVCF) is prevailing with the aging of population. With around 1.4 million new cases every year, it has become a great social, health, and economic burden since patients will be unable to perform daily activities due to severe back pain [1]. Over the past decades, percutaneous kyphoplasty (PKP) has been widely used for the treatment of osteoporosis and vertebral compression fractures, because it is a minimal invasive surgery to achieve many benefits on short-term prognosis including pain relief, shortened hospital stay, and restoration of vertebral body height [2]. Hu et al. reported that after percutaneous balloon kyphoplasty, 91 patients with osteoporotic vertebral compression fracture achieved satisfactory improvement in visual analogue scale (VAS), Cobb angle (CA), and anterior vertebra height rate (AVHr) compared with those preoperative indices ($p < 0.05$) [3].

However, some researchers found the disadvantages of PKP including kyphosis, refracture, back pain, infection, and adjacent vertebral fracture [4]. Li et al. reported that 30 out of 230 patients who received PKP with bilateral approach had recollapse during follow-up visits, and the possible reasons were low bone mineral density and low volume of injected cement [5]. To minimize the postoperative complications of OVCF, pedicle screw fixation combined with

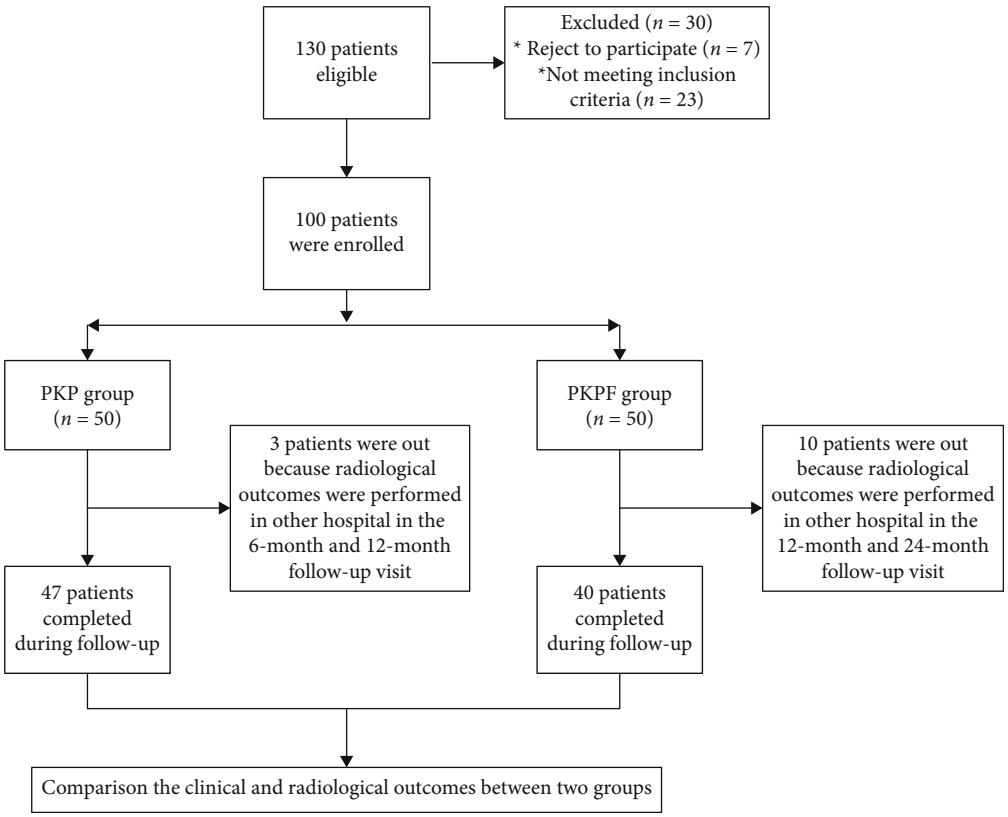

Figure 1: Flow of participants through in this study.

percutaneous kyphoplasty (PKPF) is prevailing, because PKPF can decrease vertebral refracture, adjacent vertebral fracture, and kyphosis [6]. Korovessis et al. retrospectively collected clinical and radiological data of 36 patients treated with percutaneous short fixation plus kyphoplasty and documented that this surgical method significantly reduced spinal deformity and pain with few complications [7], whereas there was no comparison of percutaneous kyphoplasty with or without pedicle screw fixation in the treatment of single segment osteoporosis vertebral compression fracture on follow-up. Our present study is aimed at comparing the clinical outcomes and complications of osteoporosis vertebral compression fracture patients who received kyphoplasty with or without pedicle screw fixation.

2. Patients and Methods

This is a retrospective study, and all data were retrieved from Ningbo No.6 Hospital. All enrolled cases met the following inclusion criteria: (1) patients aged > 55 years old without trauma history, previous lumbar fracture, or thoracolumbar surgery; (2) diagnosed as T11-L2 single segment thoracolumbar osteoporotic vertebral compression fracture by MRI and CT scan (defined as vertebral height loss > 25%) [8]; and (3) bone mineral density less than -2.5 standard deviation (SD) of normal. The exclusion criteria were as follows: (1) without intact pedicle or posterior wall of the fractured vertebral; (2) more than two-segment vertebrae fractured, pathological fracture, or other diseases which might affect clinical outcomes including serious cardiovascular disease, mental disorder, or uremia; and (3) without complete follow-up data. A total of 87 qualified patients who received percutaneous kyphoplasty with or without pedicle screw fixation in Ningbo No.6 Hospital from October 2015 and October 2017 and had 2 years followed up visit were enrolled for analysis, including 47 patients treated with percutaneous kyphoplasty (the PKP group) and 40 patients treated with percutaneous kyphoplasty with pedicle screw fixation (the PKPF group), shown in Figure 1. The clinical outcomes, radiological, and demographic data were collected from medical records, and there was no difference between the two groups in rehabilitation protocols. Institutional ethical approval was obtained before data collection. All patients signed informed consent for unnamed involvement for research purposes at admission.

2.1. Surgery Procedure. In the PKP group, all procedures were performed under local anesthesia in the prone position; then, the fractured vertebra was located by C-arm fluoroscopy. A cannula was placed percutaneously into the vertebral body through a bilateral pedicles, which allowed the placement of two inflatable balloons. The position of the cannula was identified by intraoperative X-rays. After that, the balloons were inflated to compact the surrounding trabecular bone and create an enclosed cavity filled with PK and PMMA bone cement.

In the PKPF group, all patients received endotracheal anesthesia. Procedures were monitored under biplane fluoroscopy and continuous neuromonitoring during operation.

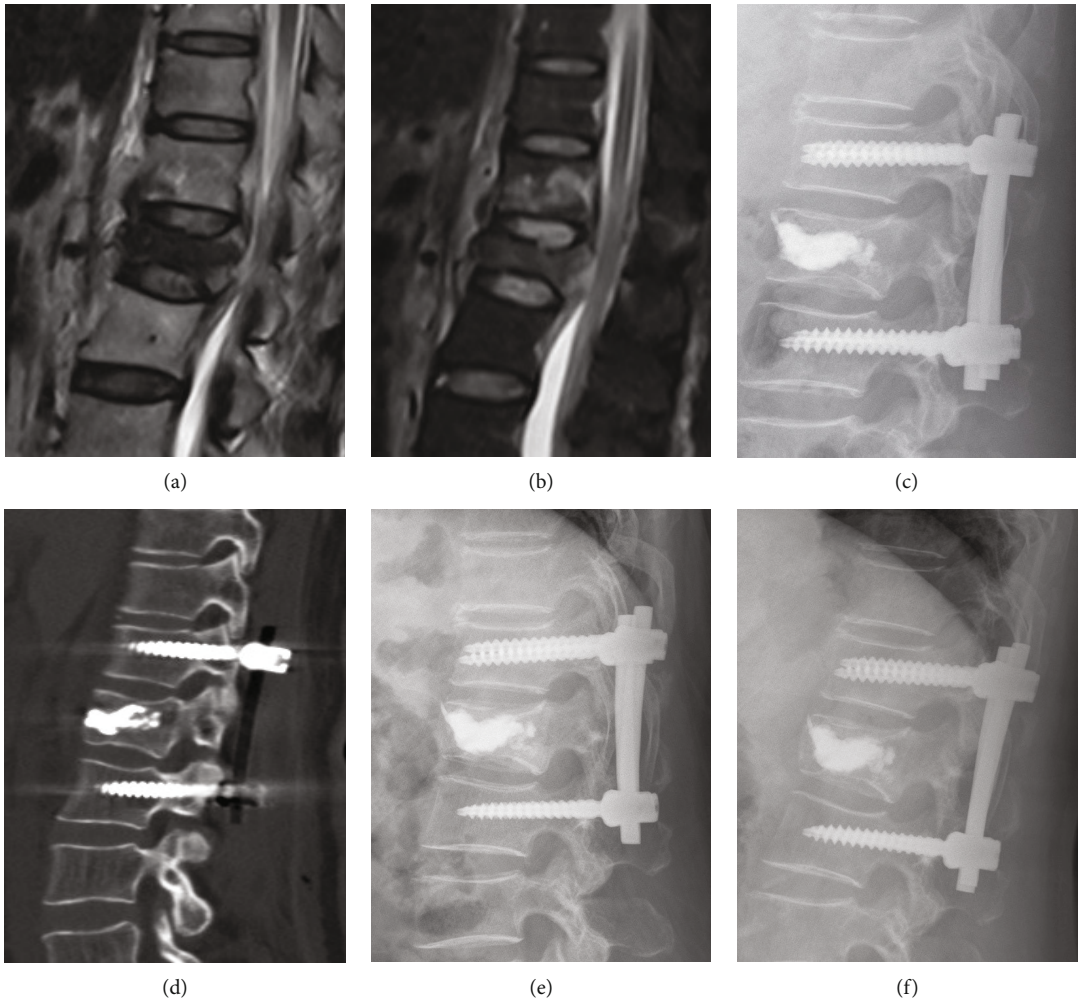

Figure 2: A female patient aged 62 years old, L1 OVCF caused by fall. (a, b) Postoperative magnetic resonance imaging showed L1 vertebral compression fracture. (c, d) Immediately postoperative CT scans and lateral X-ray showed that the fractured vertebra was filled with bone cement, and pedicle screws were placed into the adjacent vertebral. (e, f) Lateral X-rays at 6-month and 2-year follow-up visit indicated that satisfying correction and no recollapsed or refracture.

The fractured vertebra was augmented with PK and PMMA bone cement as aforementioned. The adjacents above and below the intact vertebrae were located with four targeting cannulated needles at each pedicle, and all additional instruments were arranged by K-wires, which passed through each cannulated needle. Then, the multiaxial cannulated pedicle screws (Sanyou, Shanghaisanyou, China) were inserted by the extender sleeves into the pedicles of adjacent vertebras above and below the injured vertebra. Finally, two appropriate length and preflexed rods were placed through the minimal stab wound, and the position was controlled by C-arm fluoroscopy (Figure 2). Both groups retained a brace for 3 months and oral nonsteroid anti-inflammatory drugs accordingly, and all patients were oral alendronate sodium to antiosteoporosis after they were diagnosed osteoporosis.

2.2. Outcome Assessments. Clinical outcomes include VAS and Oswestry Disability Index (ODI). The VAS (from 0, no pain, to 10, worst pain) was used to measure the back pain at preoperative admission and each follow-up visit [9]. And the ODI scores consisting of 10 questions were used to evaluate functional capacity, indicating a worse prognosis with higher percentage [10]. The ODI score is a prevailing method of high reproducible and reliable measurement in patients with lower back pain.

The immediate postsurgical anteroposterior and lateral X-rays were used to assess the reduction of the injured vertebra, bone cement distribution, and position of implements. The CA and AVHr were measured under lateral lumbar X-rays at preoperative admission and each follow-up visit, which were used to evaluate the thoracolumbar alignment [11], and all data were measured by two radiological doctors. The definition of recollapse of the operated vertebra is a ≥4 mm decrease of vertebral body height compared with that in immediately postoperative lateral X-rays [12]. Complications including wound infection, postoperative kyphosis, refracture, and implement failure were collected from medical records by two independent orthopedic surgeons.

2.3. Statistics. Continuous data were shown as mean ± SD. The baseline characteristics were analyzed by χ^2 test or

Table 1: The baseline characteristics of patients in the two groups.

Variable	PKP group ($n = 47$)	PKPF group ($n = 40$)	p value
Age (years)	65.1 ± 13.8	63.3 ± 14.9	0.53
Body mass index	22.7 ± 2.1	22.1 ± 1.9	
Gender			
Male	17	13	0.45
Female	30	27	
Fracture cause, n			
Fall	35	31	0.47
Vehicle injure	12	9	
Fracture vertebra			
T11	10	7	0.89
T12	12	11	
L1	17	13	
L2	8	9	
Hospital stay (days)	3.5 ± 1.4	6.9 ± 2.1	0.03*

*$p < 0.05$.

independent t-test. The outcomes of preoperative and postoperative follow-up visits in each group were analyzed using the paired t-test, and the independent t-test was used to compare the difference between the two groups at preoperative and each follow-up visit. Statistical analyses were performed by SPSS for Windows version 22 (SPSS Inc., Chicago, USA). And the survival analysis was used for the comparison of complications between the two groups. A two-tailed p value less than 0.05 was considered statistically significant.

3. Results

A total of 87 OVCF patients treated with either operation were enrolled in this retrospective study, including 47 patients treated with PKP and 40 patients treated with PKPF. There was no significant difference in the baseline characteristics between the two groups ($p < 0.05$), such as age, gender, body mass index, and fractured level (Table 1), whereas the hospital stay was significantly shorter in the PKP group than in the PKPF group (3.5 ± 1.4 vs. 6.9 ± 2.1, $p < 0.05$).

As for the clinical outcomes (Table 2), there were significantly longer operation times and more operation blood loss in the PKPF group compared with those in the PKP group (8.6 ± 2.1 ml and 46.8 ± 9.7 min vs. 74.7 ± 9.3 ml and 81.7 ± 12.7 min, respectively, $p < 0.05$ for both). There was a significantly better decrease in VAS at 1- and 6-month follow-up visit in the PKPF group compared with that in the PKP group ($p < 0.05$), whereas there was no significant difference between the two groups at 12- and 24-month follow-up visit ($p > 0.05$). Significant improvement in ODI was found in the two groups at 1-, 6-, and 12-month follow-up visits ($p < 0.05$), and there was significantly improvement of ODI in the PKPF groups at 12- and 24-month follow-up visits (9.1 ± 3.4 and 7.4 ± 2.1 vs. 13.7 ± 5.2 and 12.4 ± 3.5, respectively, $p < 0.05$ for both).

In all patients, the X-rays and CT scan at preoperative admission and each follow-up visit were used to analyze the radiological paraments including CA and AVHr (Table 3). All patients achieved satisfactory recovery in AVHr at 1-month follow-up visit compared with that at preoperative admission in both groups ($p < 0.05$), whereas the AVHr was significantly lower at 12-month follow-up visit in the PKP group (81.7 ± 3.2 vs. 91.3 ± 1.5, $p < 0.05$). There were significantly higher AVHr in the PKPF group than the PKP group at each follow-up visit ($p < 0.05$), and the PKPF group showed longer improvement maintaining than the PKP group. As for CA, both groups yielded satisfactory recovery after operation (6.4 ± 3.1° and 3.1 ± 2.5° vs. 20.5 ± 2.5° and 21.1 ± 3.1°, $p < 0.05$), and there were significantly better recoveries at each follow-up visit in the PKPF group than in the PKP group. There was no significant difference in CA between each follow-up visit in the PKPF group. However, the CA was significantly increased at 6-month follow-up visit compared with that at 1-month follow-up in the PKP group (9.7 ± 4.5 vs. 6.4 ± 3.1, $p < 0.05$).

In the PKP group, a total of 23 (48.9%) patients had complications, including cement leakage ($n = 10$), fractured vertebra recollapse ($n = 12$), and reoperation due to refracture ($n = 2$), and there were significantly fewer complications in the PKPF group including cement leakage ($n = 2$), wound infection ($n = 1$), and recollapse at final follow-up visit ($n = 2$, $p < 0.05$). The survival analysis (Figure 3) showed that the surgery method was an independent factor affecting osteoporotic thoracolumbar compression fractures ($p < 0.001$). Compared with PKP, patients receiving PKPF had a lower risk of complications, HR = 7.74 (95% CI: 2.812~ 21.298).

4. Discussion

Nowadays, the incidence of osteoporotic vertebra fracture is trending upwards in an aged society, creating considerable social and economic burdens and decreasing patient living quality. Many patients may have kyphosis and other comorbidities including pneumonia and thrombosis without proper treatments [13]. The most commonly used operation is PKP, which has achieved satisfactory outcomes evaluated by VAS, ODI, and local CA at each follow-up visit compared with those at preoperative admission ($p < 0.05$) [14]. However, with the accumulation of clinical cases and prolonged follow-up period, some disadvantages were documented including cement leakage, recollapse, infection, and even refracture [15, 16]. Wei et al. reported that 1 (5%) patient had an adjacent vertebral fracture after PKP [17], and Wang et al. found that 79 (38.9%) patients who were treated with PKP had recollapse during followed up visits [18].

To minimize complications and maintain stronger support to vertebras, Pingel et al. developed PKPF for the treatment of OVCF [19], and some publications showed that PKPF achieved satisfactory clinical outcomes. Wu et al. reported that a total of 36 patients with osteoporotic single segment vertebral fracture received percutaneous kyphoplasty combined with posterior pedicle screw-rod fixation. All patients achieved significant recovery in VAS compared with those at preoperative admission, and there was no recollapse up to the final followed up visit [20]. Similarly, Elmasry

Table 2: Comparison of clinical outcomes between the two groups.

Variable	PKP group ($n = 47$)		PKPF group ($n = 40$)		p_1
VAS		p_2		p_2	
Preoperative	6.9 ± 2.7		6.5 ± 2.2		0.58
1 month	2.8 ± 1.6	<0.001	2.1 ± 0.8	<0.001	0.03*
6 months	1.7 ± 1.1	0.04	1.0 ± 0.4	0.03	0.04*
12 months	1.3 ± 0.5	0.45	0.7 ± 0.5	0.63	0.35
24 months	0.9 ± 0.7	0.52	0.6 ± 0.4	0.45	0.19
ODI					
Preoperative	68.3 ± 9.7		65.8 ± 8.4		0.75
1 month	27.3 ± 5.9	<0.001	23.4 ± 6.7	<0.001	0.51
6 months	19.3 ± 4.2	0.04	15.7 ± 48	0.02	0.16
12 months	13.7 ± 5.2	0.03	9.1 ± 3.4	0.04	0.03*
24 months	12.4 ± 3.5	0.24	7.4 ± 2.1	0.14	0.04*
Complications					
Cement leakage	9		2		<0.001
Wound infection	0		1		
Recollapse	12		2		
Refracture	2		0		
Operation time (mins)	46.8 ± 9.7		81.7 ± 12.7		0.02*
Blood loss (ml)	8.6 ± 2.1		74.7 ± 9.3		0.01*

*$p < 0.05$; p_1: the comparison between two groups; p_2: the comparison with last follow-up; VAS: visual analogue scale; ODI: Oswestry Disability Index.

Table 3: Comparison of AVHr and CA between the two groups.

Variable	PKP group ($n = 47$)		PKPF group ($n = 40$)		p_1
AVHr (%)		p_2		p_2	
Preoperative	48.9 ± 9.1		47.3 ± 11.3		0.73
1 month	92.1 ± 2.6	<0.001*	95.7 ± 3.1	<0.001*	0.02*
6 months	91.3 ± 1.5	0.24	93.2 ± 2.8	0.15	0.03*
12 months	81.7 ± 3.2	0.04*	92.7 ± 2.3	0.67	0.01*
24 months	80.1 ± 3.2	0.36	92.8 ± 2.5	0.82	0.02*
CA (degree)					
Preoperative	20.5 ± 2.5		21.1 ± 3.1		0.57
1 month	6.4 ± 3.1	<0.001*	3.1 ± 2.5	<0.001*	0.02*
6 months	9.7 ± 4.5	0.03*	3.4 ± 2.1	0.23	0.01*
12 months	9.6 ± 2.5	0.72	3.8 ± 1.8	0.42	0.03*
24 months	10.5 ± 3.1	0.82	4.5 ± 1.5	0.38	0.02*

*$p < 0.05$; p_1: the comparison between two groups; p_2: the comparison with last follow-up; AVHr: anterior vertebra height; CA: Cobb angle.

et al. reported a finite element study about the comparison of percutaneous kyphoplasty with or without pedicle screws and found that PKP had larger range of motion (ROM) than PKPF, but PKPF showed a higher level of support to vertebras [21].

In this study, VAS, ODI, AVHr, and CA were all significantly improved in the PKPF group than those in the PKP group at follow-up visits. Although there were significant improvements in vertebral body height, CA, and VAS in both two groups compared with those of the preoperative data, patients treated with PKPF yielded significantly better improvements than those with PKP [22]. As for radiological outcomes, all patients have achieved restoration at 1-month followed up visit compared with preoperative conditions, but there were significantly worse findings in AVHr at 6-month followed up visit than that at 1 month in patients treated with PKP. In contrast, there was significantly better improvement in AVHr and CA at each followed up visit in

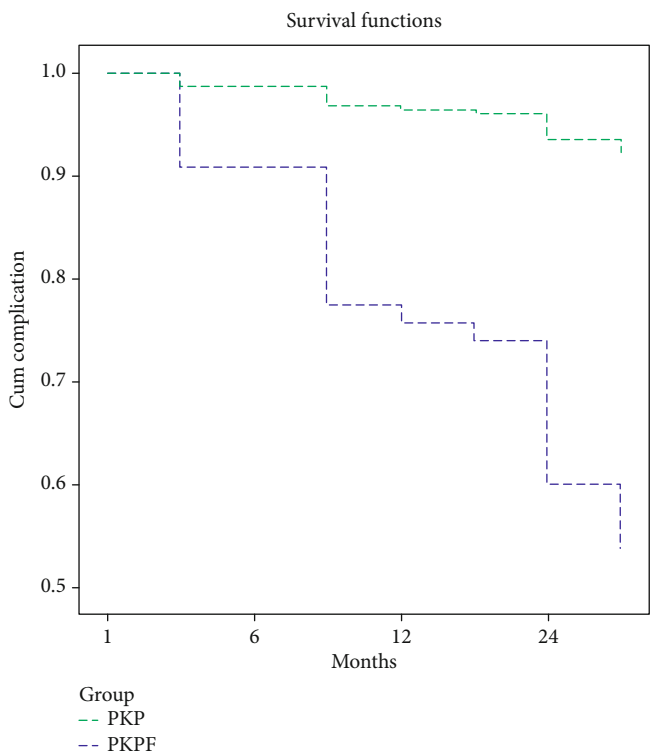

Figure 3: The survival analysis of complications between two groups.

the PKPF group than those in the PKP group, with longer correction maintained. Li et al. reported the same outcomes that all of the 50 patients with OVCF treated with PKP had yielded initial improvement in VAS, ODI, vertebral body height, and kyphosis angle, but significant loss of correction in vertebral body height and kyphosis angle at the final follow-up visit, with VAS score and ODI showing similarly patterns [23]. The possible reason maybe that PKP can initially restore the height of the vertebral body and local kyphosis, but there is a subsequence height loss due to intravertebral cleft [24] and osteoporosis [25]. The areas of intravertebral cleft consisted with necrotic cancellous bone, hyaline cartilage, and fractured callus that commonly associated with avascular necrosis [26]. That may induce instability, back pain, and recollapse, so patients may show the loss of vertebral body height, CA, and recurrence of back pain without strong support provided by pedicle screw fixation.

Other researches had documented similarly results. Lee et al. reported that 31 patients with OVCF received PKP, and all of them achieved significant postoperative improvements in the clinical and radiological findings during early follow-up, but 26 (78.8%) presented vertebral cement leakage, 5 (15.2%) were recollapse, and 6 (18.2%) had refracture [27]. Although the reason of refracture is still controversial, many studies reported the possible reason maybe that cement leakage into disk [28, 29].

Although there were many studies about comparison of the two procedures, this study is the first to show PKPF can achieve a longer correction period and stronger support of the vertebra 1 year after surgery in OVCF patients than PKP. Second, all cases were performed by a single experienced spine surgeon in our hospital with the same protocol; thus, the procedure has been highly consistent and comparable. Some limitations include a retrospective study design with a relatively small number of cases, and whether patients had used antiosteoporosis medication was not taken into account [30–33].

In conclusion, PKPF for patients with osteoporotic thoracolumbar fractures can not only achieve favorable outcomes but also maintain longer correction and stronger support of the vertebra than PKP. However, more randomized controlled trials are still needed to confirm these findings.

Data Availability

Data is available via a request to the corresponding author.

Conflicts of Interest

The authors declare that they have no conflicts of interest.

Authors' Contributions

The co-first author is Jichong Ying.

References

[1] O. Johnell and J. A. Kanis, "An estimate of the worldwide prevalence and disability associated with osteoporotic fractures," *Osteoporosis International*, vol. 17, no. 12, pp. 1726–1733, 2006.

[2] A. Lamanna, J. Maingard, H. K. Kok et al., "Vertebroplasty for acute painful osteoporotic vertebral compression fractures: an

update," *Journal of Medical Imaging and Radiation Oncology*, vol. 63, no. 6, pp. 779–785, 2019.

[3] K. Z. Hu, S. C. Chen, and L. Xu, "Comparison of percutaneous balloon dilation kyphoplasty and percutaneous vertebroplasty in treatment for thoracolumbar vertebral compression fractures," *European Review for Medical and Pharmacological Sciences*, vol. 22, 1 Suppl, pp. 96–102, 2018.

[4] L. Feng, C. Feng, J. Chen, Y. Wu, and J. M. Shen, "The risk factors of vertebral refracture after kyphoplasty in patients with osteoporotic vertebral compression fractures: a study protocol for a prospective cohort study," *BMC Musculoskeletal Disorders*, vol. 19, no. 1, p. 195, 2018.

[5] Y. X. Li, D. Q. Guo, S. C. Zhang et al., "Risk factor analysis for re-collapse of cemented vertebrae after percutaneous vertebroplasty (PVP) or percutaneous kyphoplasty (PKP)," *International Orthopaedics*, vol. 42, no. 9, pp. 2131–2139, 2018.

[6] X. Yi, H. Lu, F. Tian et al., "Recompression in new levels after percutaneous vertebroplasty and kyphoplasty compared with conservative treatment," *Archives of Orthopaedic and Trauma Surgery*, vol. 134, no. 1, pp. 21–30, 2014.

[7] P. Korovessis, E. Mpountogianni, and V. Syrimpeis, "Percutaneous pedicle screw fixation plus kyphoplasty for thoracolumbar fractures A2, A3 and B2," *European Spine Journal*, vol. 26, no. 5, pp. 1492–1498, 2017.

[8] J. Tang, W. C. Guo, J. F. Hu, and L. Yu, "Unilateral and bilateral percutaneous kyphoplasty for thoracolumbar osteoporotic compression fractures," *Journal of the College of Physicians and Surgeons Pakistan*, vol. 29, no. 10, pp. 946–950, 2019.

[9] A. Chiarotto, L. J. Maxwell, R. W. Ostelo, M. Boers, P. Tugwell, and C. B. Terwee, "Measurement properties of visual analogue scale, numeric rating scale, and pain severity subscale of the brief pain inventory in patients with low Back pain: a systematic review," *The Journal of Pain*, vol. 20, no. 3, pp. 245–263, 2019.

[10] D. S. Brodke, V. Goz, B. D. Lawrence, W. R. Spiker, A. Neese, and M. Hung, "Oswestry Disability Index: a psychometric analysis with 1,610 patients," *The Spine Journal*, vol. 17, no. 3, pp. 321–327, 2017.

[11] Y.-T. Gu, D.-H. Zhu, H.-F. Liu, F. Zhang, and R. McGuire, "Minimally invasive pedicle screw fixation combined with percutaneous vertebroplasty for preventing secondary fracture after vertebroplasty," *Journal of Orthopaedic Surgery and Research*, vol. 10, no. 1, p. 31, 2015.

[12] J. Niu, H. Zhou, Q. Meng, J. Shi, B. Meng, and H. Yang, "Factors affecting recompression of augmented vertebrae after successful percutaneous balloon kyphoplasty: a retrospective analysis," *Acta Radiologica*, vol. 56, pp. 1380–1387, 2015.

[13] J. McCarthy and A. Davis, "Diagnosis and management of vertebral compression fractures," *American Family Physician*, vol. 94, no. 1, pp. 44–50, 2016.

[14] F. Wang, L. F. Wang, D. C. Miao, Z. Dong, and Y. Shen, "Which one is more effective for the treatment of very severe osteoporotic vertebral compression fractures: PVP or PKP?," *Journal of Pain Research*, vol. Volume 11, pp. 2625–2631, 2018.

[15] J. W. Park, S. M. Park, H. J. Lee, C. K. Lee, B. S. Chang, and H. Kim, "Infection following percutaneous vertebral augmentation with polymethylmethacrylate," *Archives of Osteoporosis*, vol. 13, no. 1, p. 47, 2018.

[16] E. Wang, H. Yi, M. Wang, and C. Huang, "Treatment of osteoporotic vertebral compression fractures with percutaneous kyphoplasty: a report of 196 cases," *European Journal of Orthopaedic Surgery & Traumatology*, vol. 23, Suppl 1, pp. 71–75, 2013.

[17] P. Wei, Q. Yao, Y. Xu, H. Zhang, Y. Gu, and L. Wang, "Percutaneous kyphoplasty assisted with/without mixed reality technology in treatment of OVCF with IVC: a prospective study," *Journal of Orthopaedic Surgery and Research*, vol. 14, no. 1, p. 255, 2019.

[18] C. Wang, X. Zhang, J. Liu, Z. Shan, S. Li, and F. Zhao, "Percutaneous kyphoplasty: risk factors for recollapse of cemented vertebrae," *World Neurosurgery*, vol. 130, pp. e307–e315, 2019.

[19] A. Pingel, F. Kandziora, and C. H. Hoffmann, "Osteoporotic L1 burst fracture treated by short-segment percutaneous stabilization with cement-augmented screws and kyphoplasty (hybrid technique)," *European Spine Journal*, vol. 23, no. 9, pp. 2022-2023, 2014.

[20] J. Wu, Y. Q. Xu, H. F. Chen, Y. Y. Su, M. Zhu, and C. T. Zhu, "Percutaneous kyphoplasty combined with the posterior screw-rod system in treatment of osteoporotic thoracolumbar fractures," *Indian Journal of Orthopaedics*, vol. 47, no. 3, pp. 230–233, 2013.

[21] S. S. Elmasry, S. S. Asfour, and F. Travascio, "Finite element study to evaluate the biomechanical performance of the spine after augmenting percutaneous pedicle screw fixation with kyphoplasty in the treatment of burst fractures," *Journal of Biomechanical Engineering*, vol. 140, no. 6, 2018.

[22] Y. Qi, Y. Zeng, D. Wang, J. Sui, and Q. Wang, "Clinical application of the pedicle in vitro restorer in percutaneous kyphoplasty," *Journal of Orthopaedic Surgery and Research.*, vol. 13, no. 1, p. 268, 2018.

[23] Z. Li, T. Liu, P. Yin et al., "The therapeutic effects of percutaneous kyphoplasty on osteoporotic vertebral compression fractures with or without intravertebral cleft," *International Orthopaedics*, vol. 43, no. 2, pp. 359–365, 2019.

[24] W. Chongyan, X. Zhang, S. Li et al., "Mechanism of formation of intravertebral clefts in osteoporotic vertebral compression fractures: an in vitro biomechanical study," *The Spine Journal*, vol. 18, no. 12, pp. 2297–2301, 2018.

[25] T. T. Borgen, Å. Bjørnerem, L. B. Solberg et al., "High prevalence of vertebral fractures and low trabecular bone score in patients with fragility fractures: a cross-sectional sub-study of NoFRACT," *Bone*, vol. 122, pp. 14–21, 2019.

[26] D. E. Dupuy, W. E. Palmer, and D. I. Rosenthal, "Vertebral fluid collection associated with vertebral collapse," *American Journal of Roentgenology*, vol. 167, no. 6, pp. 1535–1538, 1996.

[27] J. K. Lee, H. W. Jeong, I. H. Joo, Y. I. Ko, and C. N. Kang, "Percutaneous balloon kyphoplasty for the treatment of very severe osteoporotic vertebral compression fractures: a case-control study," *The Spine Journal*, vol. 18, no. 6, pp. 962–969, 2018.

[28] A. S. Mudano, J. Bian, J. U. Cope et al., "Vertebroplasty and kyphoplasty are associated with an increased risk of secondary vertebral compression fractures: a population-based cohort study," *Osteoporosis International*, vol. 20, no. 5, pp. 819–826, 2009.

[29] C. Meyer, K. van Gaalen, T. Leschinger et al., "Kyphoplasty of osteoporotic fractured vertebrae: a finite element analysis about two types of cement," *BioMed Research International*, vol. 2019, Article ID 9232813, 7 pages, 2019.

[30] Q. Wang, C. Tang, J. Jia, G. Zhang, and Z. Liu, "Associations of IDUA and PTCH1 with bone mineral density, bone turnover markers, and fractures in Chinese elderly patients with

osteoporosis," *Disease Markers*, vol. 2019, Article ID 9503762, 8 pages, 2019.

[31] F. Lei, W. He, X. Tian et al., "Prophylactic percutaneous kyphoplasty treatment for nonfractured vertebral bodies in thoracolumbar for osteoporotic patients," *BioMed Research International*, vol. 2020, Article ID 8593516, 7 pages, 2020.

[32] L. Shi, N. Min, F. Wang, and Q. Y. Xue, "Bisphosphonates for secondary prevention of osteoporotic fractures: a Bayesian network meta-analysis of randomized controlled trials," *BioMed Research International*, vol. 2019, Article ID 2594149, 10 pages, 2019.

[33] H. F. Lu, P. H. Chou, G. H. Lin et al., "Pharmacogenomics Study for Raloxifene in Postmenopausal Female with Osteoporosis," *Disease Markers*, vol. 2020, Article ID 8855423, 8 pages, 2020.

Hindawi
Disease Markers
Volume 2023, Article ID 9861901, 1 page
https://doi.org/10.1155/2023/9861901

Retraction

Retracted: Pathogenic Characterization of a Porcine Circovirus Type 3 Isolate from Heilongjiang, China

Disease Markers

Received 11 July 2023; Accepted 11 July 2023; Published 12 July 2023

This article has been retracted by Hindawi following an investigation undertaken by the publisher [1]. This investigation has uncovered evidence of one or more of the following indicators of systematic manipulation of the publication process:

(1) Discrepancies in scope
(2) Discrepancies in the description of the research reported
(3) Discrepancies between the availability of data and the research described
(4) Inappropriate citations
(5) Incoherent, meaningless and/or irrelevant content included in the article
(6) Peer-review manipulation

The presence of these indicators undermines our confidence in the integrity of the article's content and we cannot, therefore, vouch for its reliability. Please note that this notice is intended solely to alert readers that the content of this article is unreliable. We have not investigated whether authors were aware of or involved in the systematic manipulation of the publication process.

Wiley and Hindawi regrets that the usual quality checks did not identify these issues before publication and have since put additional measures in place to safeguard research integrity.

We wish to credit our own Research Integrity and Research Publishing teams and anonymous and named external researchers and research integrity experts for contributing to this investigation.

The corresponding author, as the representative of all authors, has been given the opportunity to register their agreement or disagreement to this retraction. We have kept a record of any response received.

References

[1] M. Wang, Y. Yu, J. Wu et al., "Pathogenic Characterization of a Porcine Circovirus Type 3 Isolate from Heilongjiang, China," *Disease Markers*, vol. 2021, Article ID 9434944, 8 pages, 2021.

Hindawi
Disease Markers
Volume 2021, Article ID 9434944, 8 pages
https://doi.org/10.1155/2021/9434944

Research Article

Pathogenic Characterization of a Porcine Circovirus Type 3 Isolate from Heilongjiang, China

Menghang Wang,[1] Ying Yu,[2] Jianan Wu,[1] Fandan Meng,[1] Yandong Tang,[1] Shujie Wang,[1] Yu Wang,[1] Hongliang Cui,[1] Xijun He,[1] Yabin Tu,[1] Gang Wang,[1] and Xuehui Cai[1]

[1]*State Key Laboratory of Veterinary Biotechnology, Harbin Veterinary Research Institute, Chinese Academy of Agricultural Sciences, Harbin, China*
[2]*College of Veterinary Medicine, Qingdao Agricultural University, Qingdao 266109, China*

Correspondence should be addressed to Yabin Tu; tuyabin@caas.cn, Gang Wang; wanggang@caas.cn, and Xuehui Cai; caixuehui@caas.cn

Received 6 April 2021; Accepted 30 May 2021; Published 25 June 2021

Academic Editor: Zhongjie Shi

The clinical outcome of porcine circovirus 3 (PCV3) infection is still controversial. Herein, a novel PCV3 isolate (PCV3-China/DB-1/2017) with the molecular characterization of 24A and 27K in the Cap protein was used to inoculate three-week-old cesarean-derived, colostrum-deprived piglets. The nine PCV3 DB-1 inoculated piglets exhibited no obvious clinical symptoms or macroscopic lesions. PCV3 displayed a broad histotropism, including the heart, liver, spleen, lung, kidney, brain, lymph nodes, and tonsil, and the lungs and lymph nodes contained a higher quantity of viral genomes compared to that of the other organs. From 7 days after PCV3 DB-1 inoculation, the piglets showed obvious IgG antibody responses against PCV3 rCap-VLPs. The cumulative results demonstrated that PCV3 trend to low pathogenicity.

1. Introduction

Porcine circovirus (PCV) is currently recognized as four types (i.e., PCV1, PCV2, PCV3, and PCV4) [1–7], and PCV3 was recently recognized from a swine farm experiencing reproductive failure and porcine dermatitis and nephropathy syndrome- (PDNS-) like clinical signs in the United States in 2015 [3]. The metagenomic sequencing analysis showed that PCV3 has only 48% amino acid identity in the Rep protein and 26% amino acid identity in the Cap protein compared with PCV2 [3].

Since the first report of PCV3 in 2015, almost swine-producing countries in Asia, Europe, and America reported the same disease but highly variable clinical presentations ranging from inapparent to severe respiratory and enteric disease, as well as neurological disorders, multisystemic inflammation, and reproductive failure [8–15]. In China, more than 10 provinces have reported the appearance of this pathogen, and mostly focused on the pathogen appear and cycle through the swine herds [16–19]. Limited by viral isolation and prevalence in both diseased and healthy swine herds, the clinical relevance of PCV3 has being not clear and needs further study.

To investigate the pathogenicity of PCV3 in piglets, in this study, we used a PCV3 isolate (PCV3-China/DB-1/2017, MH286898) to inoculate three-week-old cesarean-derived, colostrum-deprived (CDCD) piglets. Clinical signs, pathological changes, viral load, viral mRNA in the tissue, and antibodies against PCV3 rCap-VLPs were investigated. These results showed that piglets infected with PCV3 DB-1 developed no obvious clinical symptoms or macroscopic lesions. Histological pathological observation showed lymphocyte reduction and a few inflammatory cells infiltration in the lymph nodes, as well as thickened alveolar septum in the lungs. PCV3 replication was detected in the lungs and lymph nodes of piglets using RNA in situ hybridization (RNAscope). The obvious IgG antibody responses trending against the PCV3 rCap-VLPs appeared in five out of nine

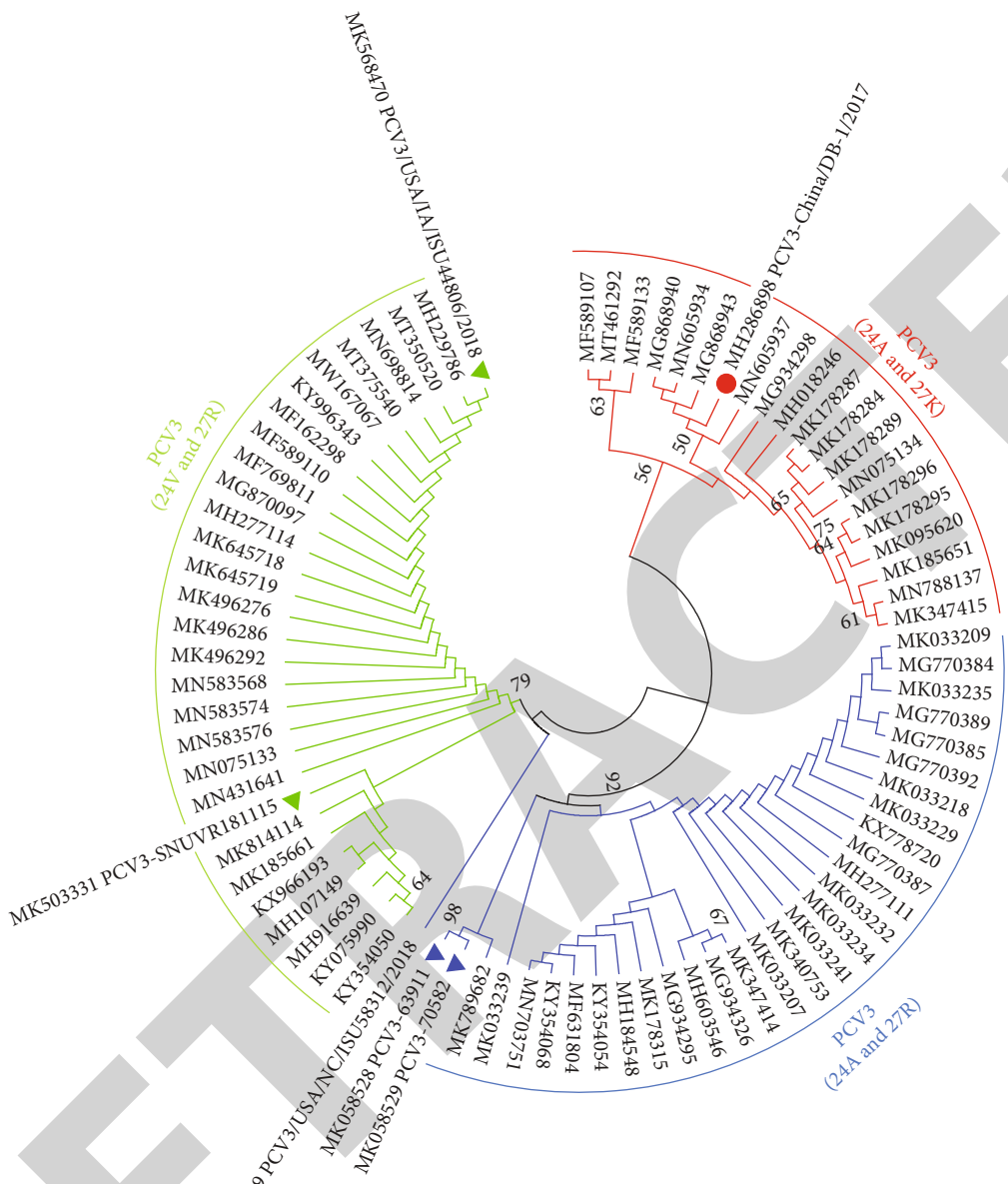

(a)

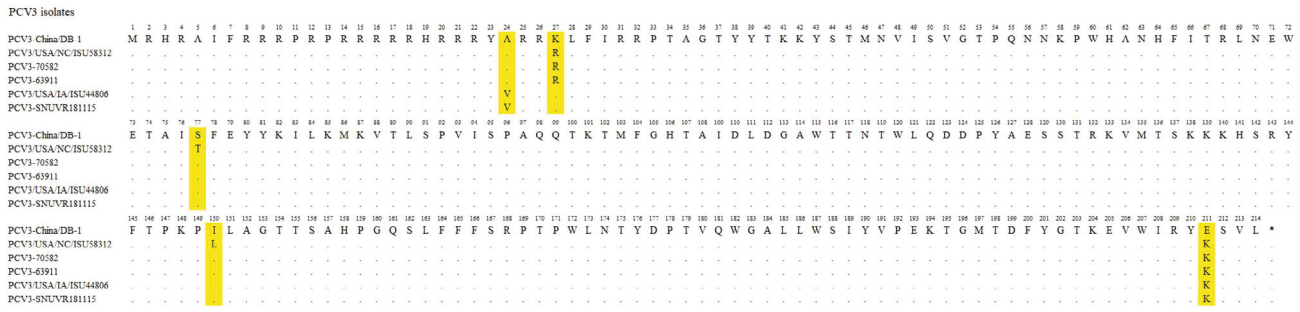

(b)

Figure 1: Phylogenetic analysis based on the ORF2 sequences of the PCV3 representative sequences (a). The ML tree was reconstructed using MEGA 5.0 with 1,000 bootstrap trials. The values along the branches represent bootstrap values. Difference analysis of the amino acid sequences of Cap protein of the PCV3 isolates (b). Yellow-shaded amino acids represent a difference in amino acid sequence of the PCV3 isolates.

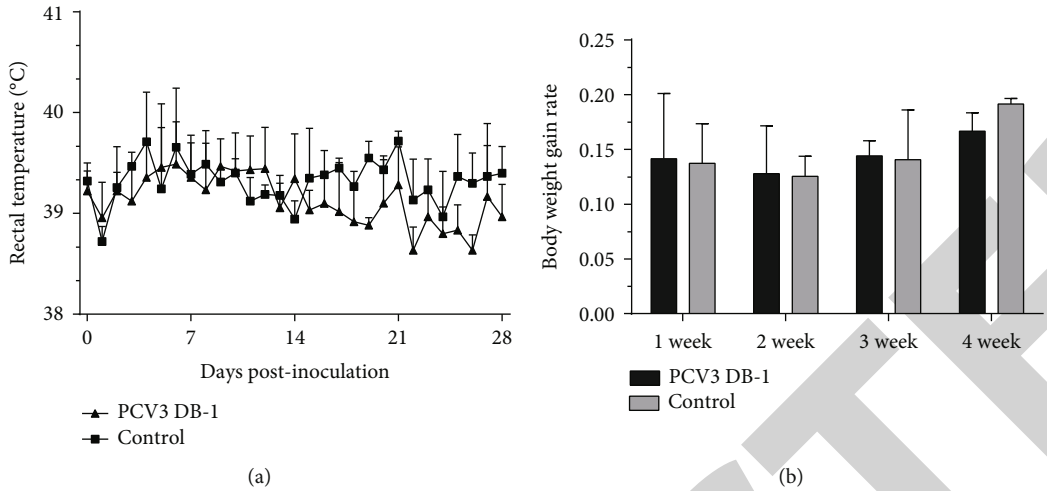

Figure 2: Rectal temperatures (a) and body weight gains (b) of the PCV3-inoculated and mock-inoculated piglets. No significant differences in rectal temperatures and body weight gains of the piglets were found between the PCV3-inoculated and mock-inoculated groups during the four weeks of the experiment. Mean ± SD (error bars) temperatures or body weight gain are shown.

DB-1 inoculated piglets. In conclusion, our results provide a further explanation for the debatable clinical relevance of PCV3 infection.

2. Materials and Methods

2.1. Virus. The PCV3 DB-1 isolate (PCV3-China/DB-1/2017, MH286898) used in this study was isolated from the lungs of two 10-day-old piglets in a commercial swine production system in Heilongjiang Province, Northeast China, by passaged three times in PK-15 cells refer to previously [20]. The ORF2 sequences of 80 representative PCV3 complete genomes originated from *Sus scrofa* (provided by NCBI) were downloaded for phylogenetic analysis. The consistent mutations in amino acids 24 and 27 of the cap protein are potential molecular markers for the classification of PCV3 [21]. Sequences were aligned using the Clustal X program with preset parameters in Clustal W (Lynnon Co., DNAMAN software). A phylogenic tree was deduced based on ORF2 by an ML method with 1,000 bootstrap replicates by MEGA 5.0.

2.2. Animal Challenge. A total of 18 three-week-old CDCD piglets (free of porcine circovirus type 2/3, porcine parvovirus, classical swine fever virus, or pseudorabies virus, confirmed by real-time PCR) were obtained from the Experimental Animal Center at the Veterinary Research Institute (Harbin, China). The piglets were randomly divided into two groups (nine piglets for PCV3 inoculation and another nine piglets for mock infection). Piglets were housed separately in two rooms and kept under biosafety level 2 conditions throughout the experiment. Piglets in the virus-inoculation group were intranasally (i.n.) and intramuscularly (i.m.) challenged with the PCV3 isolate DB-1at 1.18×10^5 genomic copies, respectively. The other nine piglets were used as control and received DMEM with the same manner. The piglets were monitored daily for clinical symptoms and rectal temperatures. Blood samples were periodically collected (0, 7, 10, 14, 17, 21, and 28 DPI) from piglets for PCV3 and serological detection. Three piglets from the PCV3-infected group and negative control group were humanely euthanized at 14, 21, and 28 DPI, respectively. At necropsy, the tissue sections (heart, liver, spleen, lung, kidney, lymph nodes, tonsil, and brain) were fixed in 10% phosphate-buffered formalin for hematoxylin and eosin (H&E), and RNAscope detection or stored at -70°C for virus quantitation.

Table 1: The dynamics of virus distribution in the organs of PCV3- and mock-inoculated piglets.

Ct values (copies/g)		14 DPI	21 DPI	28 DPI	Control
Tissue	Heart	32.2 ($10^{2.65}$)	29.7 ($10^{3.51}$)	31.0 ($10^{3.09}$)	—
	Liver	32.4 ($10^{2.64}$)	27.2 ($10^{4.29}$)	28.9 ($10^{3.79}$)	—
	Spleen	32.2 ($10^{2.65}$)	26.6 ($10^{4.51}$)	27.7 ($10^{4.14}$)	—
	Lung	32.1 ($10^{2.67}$)	23.3 ($10^{5.41}$)	26.3 ($10^{4.53}$)	—
	Kidney	33.1 ($10^{2.40}$)	29.7 ($10^{3.51}$)	30.3 ($10^{3.38}$)	—
	Brain	32.4 ($10^{2.64}$)	30.4 ($10^{3.37}$)	30.2 ($10^{3.39}$)	—
	ILN	33.6 ($10^{2.36}$)	25.8 ($10^{4.86}$)	26.0 ($10^{4.81}$)	—
	SLN	33.2 ($10^{2.40}$)	27.5 ($10^{4.19}$)	26.6 ($10^{4.51}$)	—
	MLN	33.6 ($10^{2.37}$)	28.3 ($10^{3.94}$)	27.9 ($10^{4.10}$)	—
	Tonsil	33.1 ($10^{2.40}$)	31.3 ($10^{3.01}$)	30.4 ($10^{3.37}$)	—

MLN: mesenteric lymph nodes, ILN: inguinal lymph nodes, SLN: submandibular lymph nodes; —: higher than Ct cut-off value; each number represents the average Ct values (copies/g) generated from at least three times detection.

2.3. Real-Time PCR Quantitation of the Viral Load in the Tissues. The total DNA was isolated from each tissue using a Dneasy Blood & Tissue Mini kit (Qiagen) in accordance with the manufacturer's instructions. TaqMan fluorescent quantitative PCR (q-PCR) was performed to determine the PCV3 viral loads in tissues collected at 14, 21, and 28 DPI according to a previous study [22].

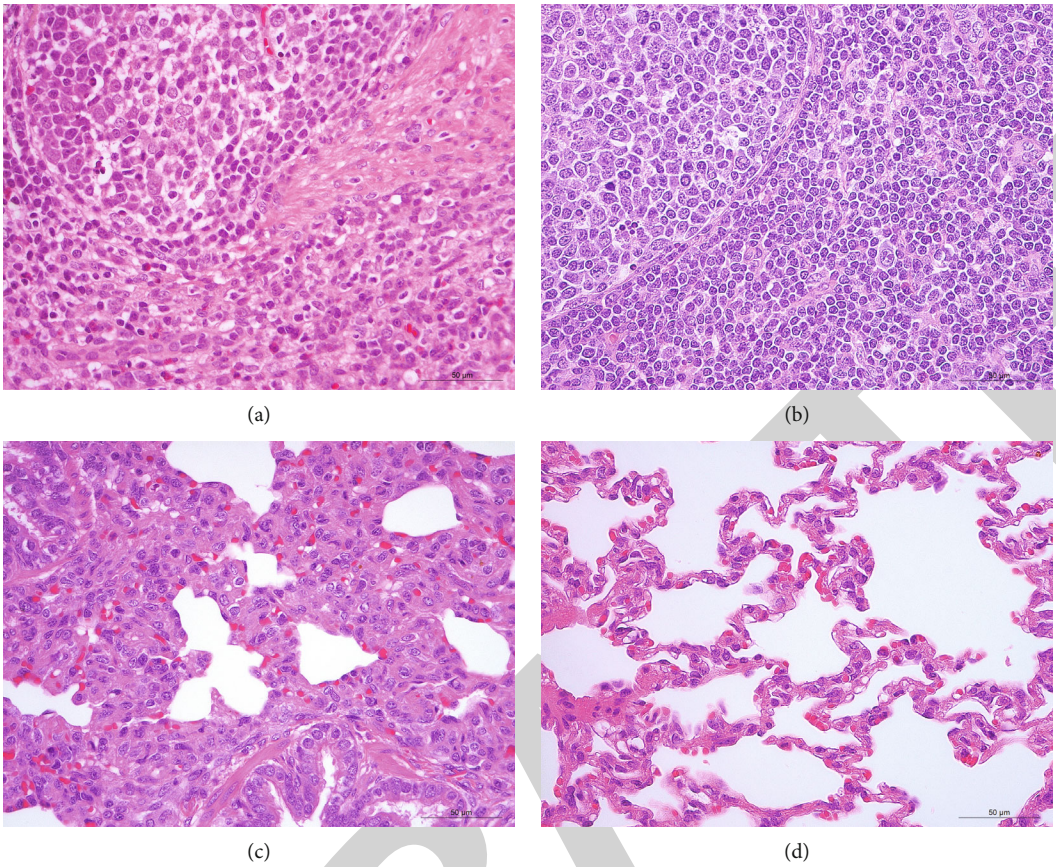

Figure 3: Histopathological lesions of the lymph nodes (a, b) and lungs (c, d) from PCV3- and mock-inoculated piglets. The piglets infected with the PCV3 DB-1 isolate showed a small number of lymphocyte reduction and inflammatory cell infiltration in the lymph nodes (a), and epithelial cell proliferation, inflammatory cells infiltration, and thickened alveolar septum in the lungs (c). No obvious pathological lesions were observed in the lymph nodes (b) and lungs (d) of the mock-inoculated piglets.

2.4. Histopathology Examinations and RNA Detection In Situ Hybridization (ISH). Tissue samples were fixed in 10% phosphate-buffered formalin, embedded in paraffin, cut into 4 μm sections, and stained with H&E according to the standard procedure. ISH-RNA was performed using RNAscope® 2.5 HD Reagent Kit (Advanced Cell Diagnostics Inc.), targeting the specific nucleotide sequence of the PCV3 viral mRNA (RNAscope® probes, catalog no. 463961 or 530431) for formalin-fixed paraffin-embedded samples. The samples were visualized using an Olympus BX43 bright-field microscope (Olympus Corporation, Tokyo, Japan).

2.5. Serology. Serum antibodies against PCV3 were detected using a modified indirect enzyme-linked immunosorbent assay (ELISA) based on PCV3 recombinant virus-like particles (VLPs) [23]. The optical density (OD) was read at 450 nm using an ELISA plate reader (PE, USA). The serum with an OD450 greater than or equal to the cut-off value was considered to be PCV3 antibody positive.

3. Results and Discussion

Phylogenetic characterization of ORF2 sequences showed that PCV3 DB-1 is the first isolation of alanine (A) and lysine (K) at positions 24 and 27 within the Cap protein in NCBI database of PCV3 so far. PCV3 DB-1 shared a nucleotide identity of ~98.3-99.8% with PCV3 ORF2 sequences deposited in GenBank® (including 80 representative sequences) (Figure 1(a)). The ORF2 sequence of PCV3 DB-1 exhibited the highest (99.8%) nucleotide identities with MG868940/MN605934/MN605937 and the lowest nucleotide identity (98.3%) with MK033235/MK033209/MG770384/MK568469. Difference analysis of Cap protein amino acid sequences among PCV3 DB-1 and other PCV3 isolates showed five specific amino acid sites, 24 (A/V), 27 (K/R), 77 (S/T), 150 (I/L), and 211 (E/K), respectively (Figure 1(b)). PCV3 is a newly discovered virus, but has been detected retrospectively since 1966 in China [21], 1967 in Brazil [24], 1996 in Spain [13], and 2006 in Thailand [25]. PCV3 has been reported in cases of reproductive failure [26, 27], PDNS, and porcine circovirus-associated disease (PCVAD) in clinical cases [28]. Thus, further studies are necessary to evaluate if the PCV3 DB-1 isolate with A24 and K27 within the Cap might have unique phenotypic traits that can be associated with specific clinical presentations.

In the animal experiment study, the clinical course of the PCV3 DB-1 and mock inoculation in three-week-old cesarean-derived, colostrum-deprived piglets was monitored. During the four weeks of the experiment, there was no significant differences in the rectal temperatures (Figure 2(a)), and

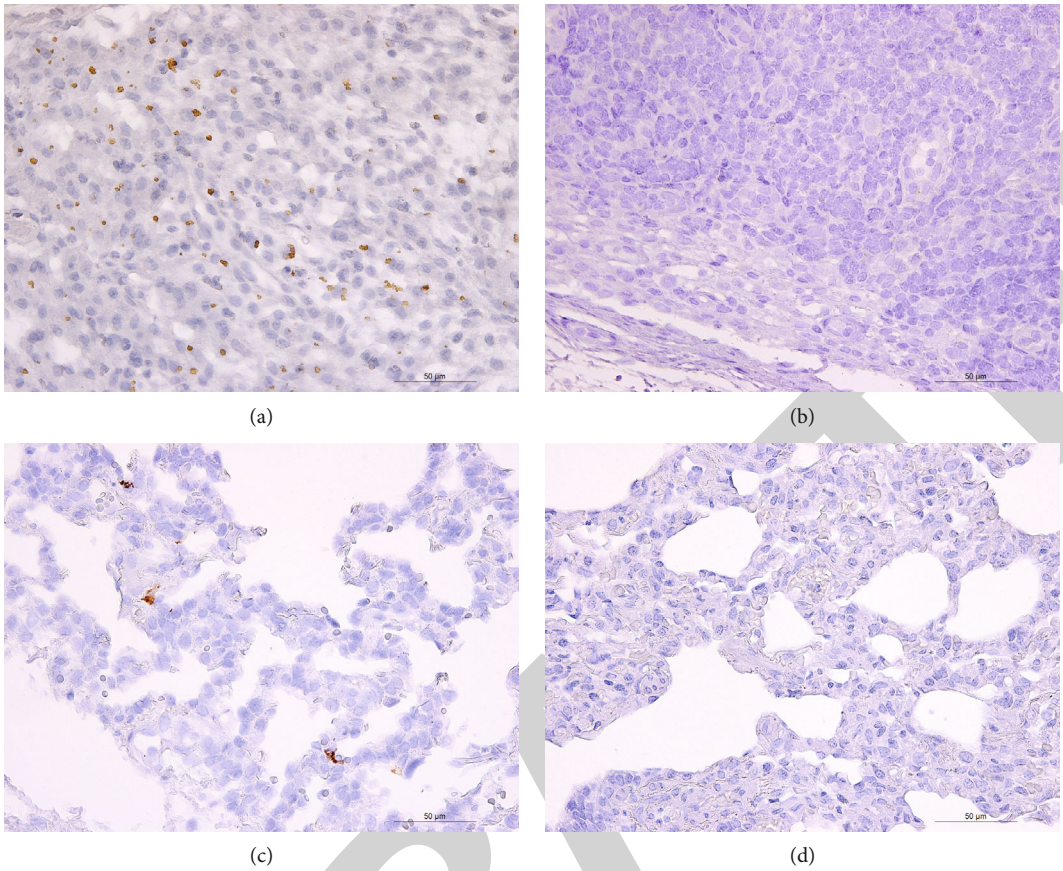

Figure 4: RNAscope in situ hybridization of the lymph nodes (a, b) and lungs (c, d) from PCV3- and mock-inoculated piglets. The PCV3 DB-1 infected piglets showed positive signals in the lymph nodes (a) and lungs (c). No obvious positive signals were observed in the lymph nodes (b) or lungs (d) of the mock-inoculated piglets.

body weight gains (Figure 2(b)) between the PCV3 DB-1 and mock inoculated piglets. No obvious macroscopic lesions were found in the lungs, spleens, lymph nodes (mesenteric lymph nodes, inguinal lymph nodes, and submandibular lymph nodes), tonsils, hearts, livers, kidneys, and brains during necropsy at 14, 21, and 28 DPI, respectively.

TaqMan fluorescent quantitative PCR (q-PCR) was performed to determine the viral load in the organs from PCV3-inoculated piglets as previously described [22, 29]. The accurate Ct cut-off was 37 for the detection limit of PCV3 that was positive in the diagnostic samples [22]. The PCV3 viral genome was detected in all of the relevant tissues, including the lung, spleen, lymph nodes (mesenteric lymph nodes, inguinal lymph nodes, and submandibular lymph nodes), tonsil, heart, liver, kidney, and brain; the results demonstrated that PCV3 has a wide range of histotropism (Table 1). Among these tissues, the highest level of the PCV3 viral genome was detected in the lung (Ct 32.1, $10^{2.67}$ copies/g), lung (Ct 23.3, $10^{5.41}$ copies/g), and inguinal lymph node (Ct 26.0, $10^{4.81}$ copies/g) at 14 DPI, 21 DPI, and 28 DPI, respectively. This finding demonstrated that PCV3 can replicate its viral genome more efficiently in the lungs and lymph nodes compared to that of the other tissues. However, PCV3 could not be passaged continuously in PK-15 cells [20], whether PCV3 can be passaged continuously in other cell lines is worth to further investigation.

To further characterize the organ lesions induced by PCV3 DB-1 infection, the lungs and lymph nodes were examined on a microscopic level for histopathological damage. H&E staining of PCV3 DB-1-infected piglets showed lymphocyte reduction, companying by inflammatory cell infiltration in the lymph nodes (Figure 3(a)), as well as epithelial cell proliferation, inflammatory cells infiltration, and thickened alveolar septum in the lungs (Figure 3(c)). Correspondingly, PCV3 replication was detected in the lymph nodes (Figure 4(a)) and lungs (Figure 4(c)) by ISH detection. No obvious pathological damage appeared in the mock-infected piglets (Figures 3(b) and 3(d)), as well as the negative signals in the lymph nodes (Figure 4(b)) and lungs (Figure 4(d)) of the mock-inoculated piglets.

To better understand the humoral immune response elicited by PCV3 DB-1 challenge, the anti-PCV3 antibody titer in the serum samples was assessed by an indirect ELISA based on PCV3 recombinant rCap-VLPs [23]. Throughout the experiment, the IgG antibody response varied among the individuals (Figure 5). Four out of nine PCV3 DB-1-inoculated piglets showed an obvious IgG antibody response from 7 (3/4) or 10 (1/4) DPI. One piglet (1/9) from 14 DPI and the other four piglets (4/9) showed either an absence or mild IgG seroconversion within the 28 days of experimental period. The humoral immune response elicited by PCV3 DB-1 is different from that of PCV3 63911 isolate, which

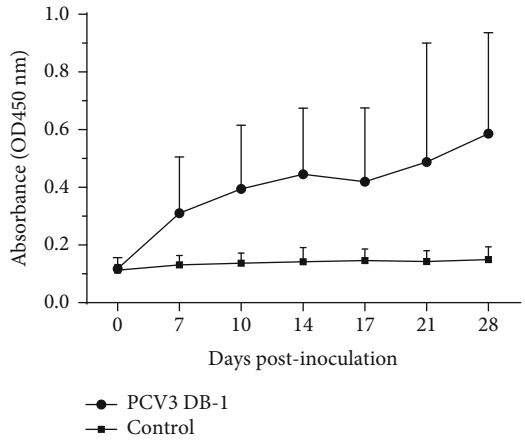

Figure 5: Detection of IgG antibodies against PCV3 rCap-VLPs antigens. IgG antibody responses (mean OD450 values) detected by PCV3 rCap-VLPs indirect ELISA in three-week-old CDCD piglets ($n = 18$) following experimental inoculation with PCV3 isolate DB-1 or negative control (0-14 dpi, $n = 9$; 14-21 dpi, $n = 6$; 21-28 dpi, $n = 3$) over the course of the infection. Mean ± SD (error bars) of the specific antibodies are shown.

inoculation induced more than one-half of cesarean-derived, colostrum-deprived piglets (5/8) and increased IgM antibody response against the PCV3 Cap protein between 7 and 14 DPI; however, no significant IgG seroconversion was detected in any infected piglet throughout the 28-day study period [20]. The difference between our study and the aforementioned study [20] is that there was a trend in the IgG antibody response against the PCV3 Cap protein. In our study, 5 of nine PCV3 DB-1 inoculated piglets showed an obvious trend in the IgG antibody response. The indirect ELISA method used in our study based on PCV3 recombinant rCap-VLPs [23, 30] might conserve the conformational epitopes and had the ability to detect IgG antibodies against the conformational epitope of the PCV3. Antibodies against rCap-VLPs of PCV3 that appeared in piglets with a specific immune status may be inflammatory factors that alert immune cells to respond to the viral infection; however, whether these antibodies can neutralize PCV3 requires further investigation.

Since the porcine circovirus (PCV3) was first reported from a swine farm in United States, PCV3 has been detected in swine farms throughout the world. Among those reports, clinical signs produced by PCV3 infection appear to be highly variable: sows characterized by reproductive failure and PDNS-like clinical signs [3]; clinical cases from 3 to 10 week piglets show multisystemic and cardiac inflammation [31]; 4-week-old piglets infected with PCV3 DNA clone develop PDNS-like disease and 40% mortality [32]; 6-week-old CDCD pigs with unremarkable visual clinical performance under experimental conditions [20]; and wild boar infection with PCV3 naturally showed nonpathogenic but highly prevalent (30%) [33]. Since there is an abundance of data indicating that a PCV3 infection can cause different clinical outcomes (different clinical syndromes) or subclinical (absence of symptoms) symptoms in domestic pigs [10, 12, 16, 17, 28, 34–37], PCV3 pathogenicity has become controversial and requires experimental data to reduce this controversial academic issue. In our study, the outcome of PCV3 inoculation to CDCD piglets indicates PCV3 infection cannot induce obvious clinical symptoms and pathological changes. The appearance of clinical symptoms and the severity of the disease may be affected by the immune status of pigs [38, 39], stress factors that cause systemic inflammation [40, 41], or coinfection with other pig pathogens [42, 43]. The cumulative results in our study demonstrated that PCV3 trend to low pathogenicity. Whether the synergy between PCV3 and bacterial/viral coinfections warrants further investigation [44, 45].

In conclusion, piglets inoculated by PCV3 DB-1 isolate with the molecular characterization of 24A and 27K exhibited no obvious clinical symptoms or macroscopic lesions. However, this isolate showed a broad histotropism, and the lungs and lymph nodes contained a higher quantity of viral genomes among the detected organs, as well as the infection induced obvious IgG antibody against PCV3 rCap-VLPs. These results imply that PCV3 DB-1 isolate trends to low pathogenicity to the piglets.

Data Availability

The datasets used and/or analyzed during the current study are available from the corresponding author on reasonable request.

Ethical Approval

The animal experiment protocols were approved by the Animal Ethics Committee of Harbin Veterinary Research Institute of the Chinese Academy of Agricultural Sciences (CAAS) with approval number SY-2018-SW-003.

Conflicts of Interest

The authors declared no conflict of interest.

Authors' Contributions

Menghang Wang, Ying Yu, and Jianan Wu contributed equally to this work.

Acknowledgments

This work was supported by a grant from the State Key Laboratory of Veterinary Biotechnology Foundation (grant number SKLVBP2018002) and the Ph.D. Foundation of Qingdao Agricultural University, China (6631120019).

References

[1] I. Tischer, R. Rasch, and G. Tochtermann, "Characterization of papovavirus-and picornavirus-like particles in permanent pig kidney cell lines," *Zentralbl Bakteriol Orig A*, vol. 226, no. 2, pp. 153–167, 1974.

[2] G. M. Allan, F. Mc Neilly, B. M. Meehan et al., "Isolation and characterisation of circoviruses from pigs with wasting

syndromes in Spain, Denmark and Northern Ireland," *Veterinary Microbiology*, vol. 66, no. 2, pp. 115–123, 1999.

[3] R. Palinski, P. Pineyro, P. Shang et al., "A novel porcine circovirus distantly related to known circoviruses is associated with porcine dermatitis and nephropathy syndrome and reproductive failure," *Journal of Virology*, vol. 91, no. 1, article e01879, 2017.

[4] K. Rosario, M. Breitbart, B. Harrach et al., "Revisiting the taxonomy of the family Circoviridae: establishment of the genus Cyclovirus and removal of the genus Gyrovirus," *Archives of Virology*, vol. 162, no. 5, pp. 1447–1463, 2017.

[5] H. H. Zhang, W. Q. Hu, J. Y. Li et al., "Novel circovirus species identified in farmed pigs designated as Porcine circovirus 4, Hunan province, China," *Transboundary and Emerging Diseases*, vol. 67, no. 3, pp. 1057–1061, 2020.

[6] U. Molini, G. Franzo, L. Gous et al., "Three different genotypes of porcine circovirus 2 (PCV-2) identified in pigs and warthogs in Namibia," *Archives of Virology*, vol. 166, no. 6, pp. 1723–1728, 2021.

[7] K. Yang, Z. Jiao, D. Zhou, R. Guo, Z. Duan, and Y. Tian, "Development of a multiplex PCR to detect and discriminate porcine circoviruses in clinical specimens," *BMC Infectious Diseases*, vol. 19, no. 1, p. 778, 2019.

[8] H. Shen, X. Liu, P. Zhang et al., "Genome characterization of a porcine circovirus type 3 in South China," *Transboundary and Emerging Diseases*, vol. 65, no. 1, pp. 264–266, 2018.

[9] T. Stadejek, A. Wozniak, D. Milek, and K. Biernacka, "First detection of porcine circovirus type 3 on commercial pig farms in Poland," *Transboundary and Emerging Diseases*, vol. 64, no. 5, pp. 1350–1353, 2017.

[10] T. Kwon, S. J. Yoo, C. K. Park, and Y. S. Lyoo, "Prevalence of novel porcine circovirus 3 in Korean pig populations," *Veterinary Microbiology*, vol. 207, pp. 178–180, 2017.

[11] C. Tochetto, D. A. Lima, A. P. M. Varela et al., "Full-genome sequence of Porcine circovirus type 3 recovered from serum of sows with stillbirths in Brazil," *Transboundary and Emerging Diseases*, vol. 65, no. 1, pp. 5–9, 2018.

[12] G. Franzo, M. Legnardi, C. K. Hjulsager et al., "Full-genome sequencing of porcine circovirus 3 field strains from Denmark, Italy and Spain demonstrates a high within-Europe genetic heterogeneity," *Transboundary and Emerging Diseases*, vol. 65, no. 3, pp. 602–606, 2018.

[13] F. Klaumann, G. Franzo, M. Sohrmann et al., "Retrospective detection of Porcine circovirus 3 (PCV-3) in pig serum samples from Spain," *Transboundary and Emerging Diseases*, vol. 65, no. 5, pp. 1290–1296, 2018.

[14] S. Faccini, I. Barbieri, A. Gilioli et al., "Detection and genetic characterization of Porcine circovirus type 3 in Italy," *Transboundary and Emerging Diseases*, vol. 64, no. 6, pp. 1661–1664, 2017.

[15] B. Savic, V. Milicevic, O. Radanovic et al., "Identification and genetic characterization of Porcine circovirus 3 on pig farms in Serbia," *Archives of Virology*, vol. 165, no. 1, pp. 193–199, 2020.

[16] G. H. Chen, K. J. Mai, L. Zhou et al., "Detection and genome sequencing of Porcine circovirus 3 in neonatal pigs with congenital tremors in South China," *Transboundary and Emerging Diseases*, vol. 64, no. 6, pp. 1650–1654, 2017.

[17] X. Ku, F. Chen, P. Li et al., "Identification and genetic characterization of Porcine circovirus type 3 in China," *Transboundary and Emerging Diseases*, vol. 64, no. 3, pp. 703–708, 2017.

[18] S. L. Zhai, X. Zhou, H. Zhang et al., "Comparative epidemiology of Porcine circovirus type 3 in pigs with different clinical presentations," *Virology Journal*, vol. 14, no. 1, p. 222, 2017.

[19] S. Wen, W. Sun, Z. Li et al., "The detection of Porcine circovirus 3 in Guangxi, China," *Transboundary and Emerging Diseases*, vol. 65, no. 1, pp. 27–31, 2018.

[20] J. Mora-Diaz, P. Pineyro, H. Shen et al., "Isolation of PCV3 from perinatal and reproductive cases of PCV3-associated disease and in vivo characterization of PCV3 replication in CD/CD growing pigs," *Viruses*, vol. 12, no. 2, p. 219, 2020.

[21] X. Fu, B. Fang, J. Ma et al., "Insights into the epidemic characteristics and evolutionary history of the novel porcine circovirus type 3 in southern China," *Transboundary and Emerging Diseases*, vol. 65, no. 2, pp. e296–e303, 2018.

[22] Y. Wang, Y. Feng, W. Zheng et al., "A multiplex real-time PCR assay for the detection and differentiation of the newly emerged Porcine circovirus type 3 and continuously evolving type 2 strains in the United States," *Journal of Virological Methods*, vol. 269, pp. 7–12, 2019.

[23] Y. Wang, G. Wang, W. T. Duan et al., "Self-assembly into virus-like particles of the recombinant capsid protein of Porcine circovirus type 3 and its application on antibodies detection," *AMB Express*, vol. 10, no. 1, p. 3, 2020.

[24] I. L. F. Rodrigues, A. C. M. Cruz, A. E. Souza et al., "Retrospective study of Porcine circovirus 3 (PCV3) in swine tissue from Brazil (1967-2018)," *Brazilian Journal of Microbiology*, vol. 51, no. 3, pp. 1391–1397, 2020.

[25] M. Sukmak, N. Thanantong, P. Poolperm et al., "The retrospective identification and molecular epidemiology of Porcine circovirus type 3 (PCV3) in swine in Thailand from 2006 to 2017," *Transboundary and Emerging Diseases*, vol. 66, no. 1, pp. 611–616, 2019.

[26] B. C. Bera, M. Choudhary, T. Anand et al., "Detection and genetic characterization of Porcine circovirus 3 (PCV3) in pigs in India," *Transboundary and Emerging Diseases*, vol. 67, no. 3, pp. 1062–1067, 2020.

[27] M. S. Serena, J. A. Cappuccio, H. Barrales et al., "First detection and genetic characterization of porcine circovirus type 3 (PCV3) in Argentina and Its association with reproductive failure," *Transboundary and Emerging Diseases*, 2020.

[28] D. S. Vargas-Bermudez, F. S. Campos, L. Bonil, D. Mogollon, and J. Jaime, "First detection of Porcine circovirus type 3 in Colombia and the complete genome sequence demonstrates the circulation of PCV3a1 and PCV3a2," *Veterinary Medicine and Science*, vol. 5, no. 2, pp. 182–188, 2019.

[29] C. Mio, A. Cifu, S. Marzinotto et al., "Validation of a one-step reverse transcription-droplet digital PCR (RT-ddPCR) approach to detect and quantify SARS-CoV-2 RNA in nasopharyngeal swabs," *Disease Markers*, vol. 2021, Article ID 8890221, 6 pages, 2021.

[30] M. C. Weber, M. Risch, S. L. Thiel et al., "Characteristics of three different chemiluminescence assays for testing for SARS-CoV-2 antibodies," *Disease Markers*, vol. 2021, Article ID 8810196, 13 pages, 2021.

[31] T. G. Phan, F. Giannitti, S. Rossow et al., "Detection of a novel circovirus PCV3 in pigs with cardiac and multi-systemic inflammation," *Virology Journal*, vol. 13, no. 1, p. 184, 2016.

[32] H. Jiang, D. Wang, J. Wang et al., "Induction of porcine dermatitis and nephropathy syndrome in piglets by infection with porcine circovirus type 3," *Journal of Virology*, vol. 93, no. 4, article e02045, 2019.

Hindawi
Disease Markers
Volume 2021, Article ID 9931690, 9 pages
https://doi.org/10.1155/2021/9931690

Research Article

Diaphragm Thickening Fraction as a Prognostic Imaging Marker for Postoperative Pulmonary Complications in Robot-Assisted Laparoscopic Prostatectomy Requiring the Trendelenburg Position and Pneumoperitoneum

Jihion Yu,[1] Yongsoo Lee,[2] Jun-Young Park,[1] Jai-Hyun Hwang,[1] and Young-Kug Kim[1]

[1]*Department of Anesthesiology and Pain Medicine, Asan Medical Center, University of Ulsan College of Medicine, Seoul, Republic of Korea*
[2]*Department of Anesthesiology and Pain Medicine, Uijeongbu Eulji Medical Center, Eulji University School of Medicine, Gyeonggi-do, Republic of Korea*

Correspondence should be addressed to Young-Kug Kim; kyk@amc.seoul.kr

Received 2 April 2021; Accepted 9 June 2021; Published 23 June 2021

Academic Editor: Zhongjie Shi

Background. Robot-assisted laparoscopic prostatectomy (RALP) frequently entails postoperative pulmonary complications (PPCs) due to the Trendelenburg position and pneumoperitoneum. Diaphragm thickening fraction (TF) as an imaging marker can offer the advantage of predicting respiratory outcomes. Therefore, we evaluated the effect of diaphragm TF on the occurrence of PPCs in RALP. *Methods*. We measured the preoperative thickness of the diaphragm at peak inspiration (T_{pi}) and end expiration (T_{ee}) using ultrasonography. Diaphragm TF was calculated as $TF = (T_{pi} - T_{ee})/T_{ee}$. A receiver operating characteristic (ROC) curve analysis of TF was performed. After dividing patients into two groups according to the optimal TF cut-off value, we compared the occurrence of PPCs between the groups. The predictivity of diaphragm TF for the occurrence of PPCs was evaluated. *Results*. Of 145 patients, 40 patients (27.6%) developed PPCs. Patients with PPCs had a significantly lower TF than those without PPCs (0.31 ± 0.09 vs. 0.39 ± 0.11, $P < 0.001$). In the ROC curve analysis, the optimal TF cut-off value was 0.28. The patients were divided into $TF \geq 0.28$ group ($n = 114$) and $TF < 0.28$ group ($n = 31$). The incidence of PPCs was significantly higher in the $TF < 0.28$ group than in the $TF \geq 0.28$ group (51.6% vs. 21.1%, $P = 0.001$). Diaphragm $TF < 0.28$ was associated with a higher incidence of PPCs than diaphragm $TF \geq 0.28$ (odds ratio = 4.534, 95% confidence interval [1.763–11.658], $P = 0.002$). *Conclusion*. Preoperative diaphragm $TF < 0.28$ was associated with an increased incidence of PPCs, suggesting that diaphragm TF as a prognostic imaging marker provides useful information on PPCs in RALP requiring the Trendelenburg position and pneumoperitoneum. *Trial Registry Number*. This trial is registered with KCT0005028.

1. Introduction

Robot-assisted laparoscopic prostatectomy (RALP) has been primarily adopted for prostate cancer due to its several advantages over open prostatectomy, including lower intraoperative blood loss, fewer blood transfusions, fewer anastomotic strictures, and shorter hospital stay [1]. However, RALP requires the steep Trendelenburg position and carbon dioxide pneumoperitoneum to maintain a good surgical condition. These specific surgical conditions reduce the functional residual capacity, vital capacity, and lung compliance [2, 3]. Consequently, in patients undergoing RALP, these conditions can adversely affect the respiratory system and lead to postoperative pulmonary complications (PPCs) [2, 3]. Furthermore, PPCs are associated with increased morbidity and mortality rates, even mild PPCs, such as atelectasis [4–6]. Therefore, meticulous preoperative evaluation and perioperative management are required to reduce PPCs in RALP.

The diaphragm is a principal muscle of respiration, and its function can be evaluated by diaphragm thickening fraction (TF) during respiration at the zone of apposition, which is the area of the diaphragm where it begins to peel away from the lower rib cage [7]. Diaphragm TF, which can be simply measured at bedside by ultrasonography, can precisely reflect the invasive gold standard measure of diaphragm function (i.e., transdiaphragmatic pressure measurement) [8, 9]. In particular, a low diaphragm TF can be a predictor of the failure of mechanical ventilation weaning in the intensive care unit and is associated with PPCs in cardiac surgery [10, 11]. However, little is known about the association between diaphragm TF and PPCs in surgeries requiring the steep Trendelenburg position and carbon dioxide pneumoperitoneum that adversely affect the respiratory system.

In this study, we hypothesized that low diaphragm TF can predict PPCs in RALP, which requires carbon dioxide pneumoperitoneum and the steep Trendelenburg position. To this end, after dividing the patients into two groups according to the optimal TF cut-off value for predicting PPCs, we evaluated the effect of low diaphragm TF as an imaging marker on the occurrence of PPCs in RALP.

2. Patients and Methods

2.1. Methods. This prospective observational study was conducted at a tertiary referral center. Prior to patient enrollment, the study protocol was registered at the Clinical Research Information Service (KCT 0005028, principal investigator: Young-Kug Kim, registration date: May 18, 2020). All patients provided written informed consent prior to study participation. The institutional review board of Asan Medical Center (Seoul, South Korea) approved the study protocol (approval number: 2020-0761, approval date: May 15, 2020).

2.2. Study Population. The study patients were enrolled between May 2020 and September 2020. The inclusion criteria were age 20–79 years, scheduled RALP, American Society of Anesthesiologists (ASA) physical status I–III, and voluntary participation in this study. Patients who underwent pneumonectomy and those who were converted to open prostatectomy were excluded.

2.3. Study Protocol. All patients were monitored with pulse oximetry, electrocardiography, end-tidal carbon dioxide concentration, noninvasive blood pressure, and bispectral index (A-1050 Monitor; Aspect Medical Systems, Newton, MA, USA). Anesthesia was induced using thiopental sodium (4–5 mg/kg) and rocuronium (0.5–0.8 mg/kg) and maintained with sevoflurane (1–2 vol%), medical air containing 50% oxygen, and 1.0–4.0 ng/mL remifentanil. The ventilation setting was a tidal volume of 6–8 mL/kg of the ideal body weight and an inspiratory-to-expiratory ratio of 1 : 2. Respiratory rate of 10–16 cycles/min was adjusted to achieve an end-tidal carbon dioxide partial pressure of 35–45 cmH_2O but not to exceed the maximum peak airway pressure of 30 cmH_2O. Positive end-expiratory pressure was applied at 6 cmH_2O with a recruitment maneuver (40 cmH_2O airway pressure for 30 seconds). The depth of anesthesia was maintained with the bispectral index of 40–60. Fluids and vasopressors, such as ephedrine and phenylephrine, were administered to maintain systolic blood pressure above 80 mmHg. Patients were administered crystalloid fluid at 2–4 mL/kg/h. Train-of-four monitoring was used to measure the degree of neuromuscular blockade. Rocuronium bromide was intermittently administered to maintain train-of-four count ≤ 2 throughout surgery. RALP was performed using the standard techniques of our institution [12, 13]. Pneumoperitoneum was induced with carbon dioxide gas at 15 mmHg abdominal pressure. Patients were positioned in the steep Trendelenburg position (45 degrees) during RALP. After skin closure, 2 mg/kg sugammadex (Bridion®; MSD, Oss, the Netherlands) was used to reverse the neuromuscular blockade if the train-of-four count was ≥ 2 at the end of surgery.

2.4. Measurements. Diaphragm TF was measured using a 13-6 MHz linear transducer (Sonosite X-Porte; Fujifilm SonoSite, Bothell, WA, USA) before anesthesia induction by two investigators highly experienced in lung and diaphragm ultrasonography. Patients were placed in a semirecumbent position with the head of the bed tilted downward at 45 degrees. The probe was placed on the ninth or tenth intercostal space in the left and right midaxillary line and perpendicularly angled to the chest wall. A 2D-clip (B-mode) was acquired while the patient performed a maximal inspiration and expiration. The diaphragm thicknesses at peak inspiration (T_{pi}) and end expiration (T_{ee}) were measured on the clip. Diaphragm TF was calculated as $TF = (T_{pi} - T_{ee})/T_{ee}$ (Figure 1) [8]. We acquired the measurements twice for both left and right sides and used the average of all four values in the analysis. Interobserver variability was calculated by evaluating a random sample of approximately 25% (i.e., 37/145 patients) of diaphragm TF twice by two investigators. Intraobserver variability was calculated by evaluating a random sample of approximately 25% of diaphragm TF twice by one investigator. The interobserver and intraobserver variabilities were determined as the mean absolute difference between the two values divided by their mean and presented as a percentage.

2.5. Assessments. Preoperative data included age, body mass index, ASA physical status, hypertension, diabetes mellitus, cerebrovascular disease, coronary artery disease, interstitial lung disease, chronic obstructive pulmonary disease, pulmonary tuberculosis, and preoperative pulmonary function test findings. Intraoperative data included preinduction hemodynamics, such as mean blood pressure, systolic blood pressure, diastolic blood pressure, body temperature, heart rate, and peripheral oxygen saturation, arterial blood gas analyses before induction and at skin closure, anesthesia duration, operation duration, and crystalloid amount. Arterial blood gas analysis included arterial hydrogen ion concentration (pH), arterial oxygen partial pressure (PaO_2), arterial carbon dioxide partial pressure ($PaCO_2$), bicarbonate (HCO_3^-), base excess, and arterial oxygen saturation.

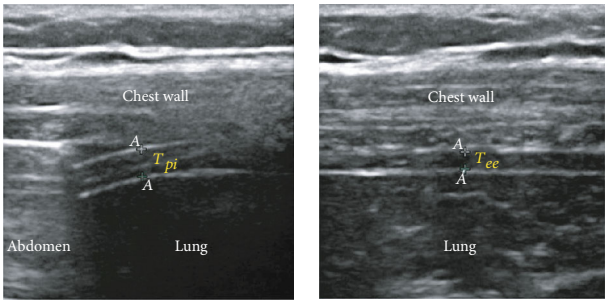

(a) (b)

Figure 1: Measurement of diaphragm thickening fraction (TF) by ultrasonography. The diaphragm thicknesses at peak inspiration (T_{pi}) (a) and end expiration (T_{ee}) (b) were measured. Diaphragm TF was calculated as follows: TF = $(T_{pi} - T_{ee})/T_{ee}$.

Table 1: Diagnostic criteria for postoperative pulmonary complications in robot-assisted laparoscopic prostatectomy.

Complication	Definition
Atelectasis	Atelectasis was defined as lung opacification with a shift of the hilum, hemidiaphragm, or mediastinum toward the affected side and compensatory overinflation in the adjacent nonatelectatic lung.
Pleural effusion	Pleural effusion was defined as chest X-ray showing loss of the sharp silhouette of the ipsilateral hemidiaphragm in the upright position, evidence of displacement of adjacent anatomical structures, blunting of the costophrenic angle, or a hazy opacity in one hemithorax with preserved vascular shadows.
Bronchospasm	Bronchospasm was defined as newly developed expiratory wheezing that needed treatment with bronchodilators.
Pneumothorax	Pneumothorax was defined as air in the pleural space without vascular bed surrounding the visceral pleura.
Respiratory infection	Respiratory infection was diagnosed as the need of treatment with antibiotics for suspected respiratory infection and as the occurrence of one or more of the following symptoms: new or changed sputum, fever, new or changed lung opacities, or leukocyte count more than 12,000/mm^3.
Aspiration pneumonitis	Aspiration pneumonitis was defined as an acute lung injury due to aspiration of gastric contents.
Respiratory failure	Respiratory failure was defined as a partial arterial oxygen pressure/fractional inspired oxygen concentration < 300 mmHg, partial arterial oxygen pressure < 60 mmHg in room air, or arterial oxygen saturation measured with pulse oximeter < 90% and requiring oxygen therapy.

Atelectasis, pleural effusion, and pneumothorax were diagnosed with radiologist's description of chest X-rays.

Postoperative variables included PPCs and the duration of hospitalization defined as the period from the day of surgery to the day of discharge. PPCs were diagnosed as the occurrence of the following within seven days after RALP [14–20]: atelectasis, pleural effusion, bronchospasm, pneumothorax, respiratory infection, aspiration pneumonitis, and respiratory failure (Table 1).

2.6. Statistical Analysis. By referring to our previous study [15], we assumed a normal distribution, correlation of 0.2 with other variables, and 30% occurrence of PPCs in RALP. Accordingly, it was calculated that 145 patients were needed to detect an odds ratio of 2.0 for a low diaphragm TF with 90% power, a two-sided $\alpha = 0.05$, and a 10% dropout rate. Categorical variables were compared using the Fisher's exact test or the chi-squared test as appropriate and are presented as number (percentage). Continuous variables were compared using the Mann–Whitney U test or unpaired t-test as appropriate and are presented as mean ± standard deviation.

To determine the prognostic ability of preoperative diaphragm TF for the occurrence of PPCs in RALP, the receiver operator characteristic (ROC) curve analysis was performed.

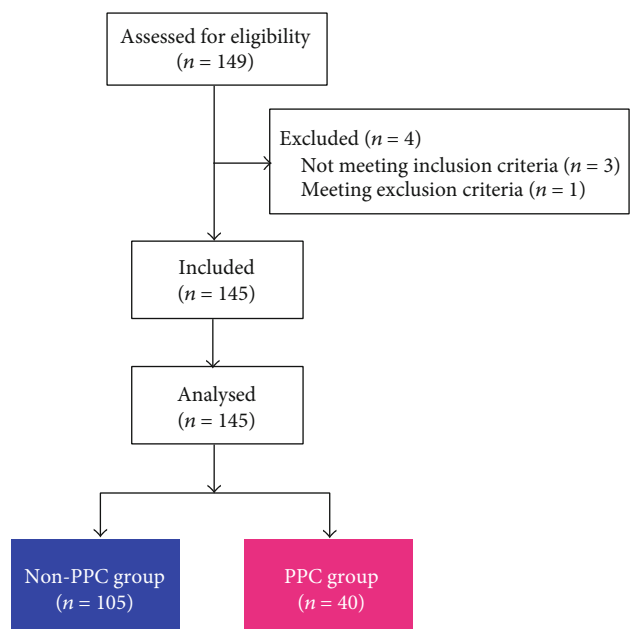

Figure 2: Study flow diagram of patients. PPC: postoperative pulmonary complication.

Table 2: Preoperative and intraoperative data.

Variables	All patients (n = 145)	Non-PPC group (n = 105)	PPC group (n = 40)	P value*
Age (years)	67.2 ± 6.3	67.0 ± 6.7	67.9 ± 5.2	0.418
Body mass index (kg/m^2)	24.8 ± 2.6	24.8 ± 2.7	24.9 ± 2.4	0.912
ASA physical status				0.637
2	119 (82.1)	85 (81.0)	34 (85.0)	
3	26 (17.9)	20 (19.0)	6 (15.0)	
Hypertension	61 (42.1)	46 (43.8)	15 (37.5)	0.492
Diabetes mellitus	20 (13.8)	15 (14.3)	5 (12.5)	0.800
Cerebrovascular disease	10 (6.9)	9 (8.6)	1 (2.5)	0.285
Coronary artery disease	14 (9.7)	9 (8.6)	5 (12.5)	0.532
COPD	19 (13.1)	14 (13.3)	5 (12.5)	>0.999
Interstitial lung disease	0 (0)	0 (0)	0 (0)	>0.999
Pulmonary tuberculosis	0 (0)	0 (0)	0 (0)	>0.999
Pulmonary function test				
FVC (L)	3.8 ± 0.6	3.8 ± 0.6	3.6 ± 0.6	0.104
FEV_1 (L)	2.8 ± 0.5	2.8 ± 0.5	2.6 ± 0.5	0.051
FEV_1/FVC ratio (%)	73.2 ± 11.2	73.6 ± 11.7	72.2 ± 10.1	0.477
Pre-induction hemodynamics				
Mean blood pressure (mmHg)	90 ± 11	90 ± 10	90 ± 12	0.743
Systolic blood pressure (mmHg)	137 ± 18	136 ± 18	138 ± 19	0.437
Diastolic blood pressure (mmHg)	75 ± 11	75 ± 10	75 ± 13	0.728
Body temperature (°C)	36.6 ± 0.3	36.6 ± 0.3	36.6 ± 0.3	0.850
Heart rate (beats/min)	71 ± 13	70 ± 13	71 ±12	0.642
SpO_2 (%)	97.9 ± 1.8	98.0 ± 1.8	97.7 ± 1.8	0.343
Arterial blood gas analysis after induction				
pH	7.46 ± 0.03	7.46 ± 0.03	7.46 ± 0.03	0.722
PaO_2 (mmHg)	288.4 ± 72.8	287.5 ± 70.9	290.6 ±78.6	0.822
$PaCO_2$ (mmHg)	39.1 ± 4.8	39.2 ± 5.0	38.9 ± 4.1	0.713
HCO_3^- (mmol/L)	28.1 ± 2.3	28.2 ± 2.3	27.7 ± 2.3	0.248
Base excess (mmol/L)	4.0 ± 2.1	4.1 ± 2.1	3.7 ± 2.1	0.236
SaO_2 (%)	99.9 ± 0.5	99.9 ± 0.4	99.9 ± 0.6	0.566
Arterial blood gas analysis at skin closure				
pH	7.42 ± 0.03	7.42 ± 0.03	7.41 ± 0.04	0.055
PaO_2 (mmHg)	189.0 ± 45.0	191.8 ± 43.4	181.7 ± 48.8	0.230
$PaCO_2$ (mmHg)	40.5 ± 3.3	40.2 ± 3.2	41.3 ± 3.3	0.071
HCO_3^- (mmol/L)	26.1 ± 1.9	26.1 ± 1.9	26.2 ± 2.2	0.934
Base excess (mmol/L)	1.5 ± 2.0	1.6 ± 1.9	1.3 ± 2.4	0.408
SaO_2 (%)	99.6 ± 0.8	99.7 ± 0.6	99.4 ± 1.0	0.051
Anesthesia duration (min)	160.9 ± 25.8	160.9 ± 24.6	160.9 ± 28.9	0.988
Operation duration (min)	120.8 ± 25.6	120.8 ± 24.5	121.0 ± 28.8	0.963
Crystalloid amount (mL)	838.7 ± 540.5	848.2 ± 596.9	813.8 ± 357.3	0.733

Continuous variables are presented as mean ± standard deviation, and categorical variables are presented as number (percentage). * For comparisons between the PPC and non-PPC groups. ASA, American Society of Anesthesiologists; COPD, chronic obstructive pulmonary disease; FEV_1, forced expiratory volume in the first second; FVC, forced vital capacity; SpO_2, peripheral oxygen saturation; pH, hydrogen ion concentration; $PaCO_2$, arterial carbon dioxide partial pressure; PaO_2, arterial oxygen partial pressure; HCO_3^-, bicarbonate; SaO_2, arterial oxygen saturation.

The value with the highest specificity and sensitivity was designated as the optimal cut-off value. After dividing into two groups according to the optimal diaphragm TF cut-off value for predicting PPCs (i.e., low TF vs. high TF), we compared the occurrence of PPCs between high and low TFs in RALP. The predictive ability of low diaphragm TF for the occurrence of PPCs was evaluated by a multivariate-adjusted odds ratio. A P value of < 0.05 was considered to denote statistical significance. IBM SPSS version 21.0.0 for Windows (IBM Corp., Armonk, NY, USA) and MedCalc version 11.3.3.0 (MedCalc Software bvba, Mariakerke, Belgium) were used for statistical analyses.

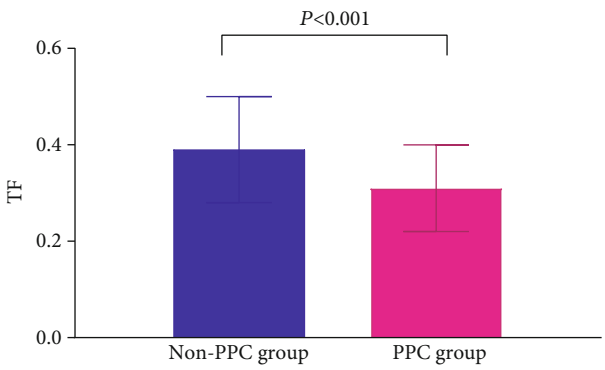

Figure 3: Comparison of the preoperative diaphragm TF between the PPC group and non-PPC group in patients undergoing RALP. Note that diaphragm TF is significantly lower in the PPC group than in the non-PPC group. TF: thickening fraction; PPC: postoperative pulmonary complication; RALP: robot-assisted laparoscopic prostatectomy.

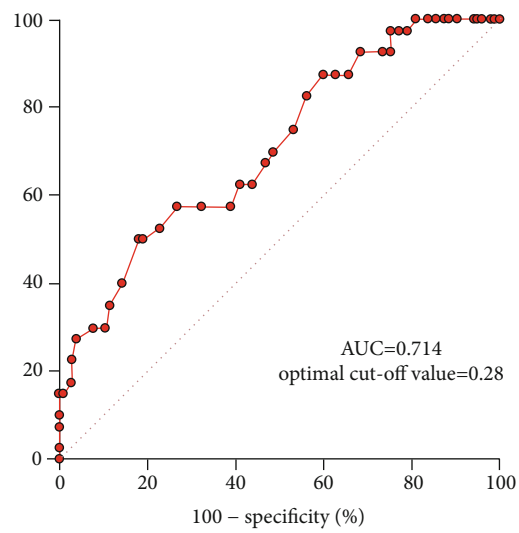

Figure 4: Receiver operating characteristic curve analysis of diaphragm TF for predicting PPCs in patients undergoing RALP. The AUC is 0.714, with an optimal cut-off value of 0.28. TF: thickening fraction; PPCs: postoperative pulmonary complications; RALP: robot-assisted laparoscopic prostatectomy; AUC: area under the curve.

3. Results

A total of 149 patients were preoperatively assessed for eligibility, of whom 145 patients were finally included in the analysis after excluding four patients (Figure 2). Forty patients (27.6%) developed PPCs. One patient developed pneumonia, 22 patients developed pleural effusion, and 27 patients developed atelectasis. Table 2 enlists the preoperative and intraoperative data. The PPC group and the non-PPC group did not show significant differences in preoperative and intraoperative data (Table 2).

Preoperative diaphragm TF was significantly lower in the PPC group than in the non-PPC group (0.31 ± 0.09 vs. 0.39 ± 0.11, $P < 0.001$) (Figure 3). No significant differences were found between TFs in the right and left diaphragm (0.36 ± 0.14 vs. 0.38 ± 0.13, $P = 0.167$). The interobserver and intraobserver variabilities of diaphragm TF measurements were 2.2% and 2.4%, respectively. In ROC curve analysis, the area under the curve of diaphragm TF for predicting PPCs was 0.714 (Figure 4). The optimal diaphragm TF cut-off value for predicting the occurrence of PPCs was 0.28. The patients were then categorized according to the optimal diaphragm TF cut-off value: TF ≥ 0.28 group ($n = 114$) and TF < 0.28 group ($n = 31$). Table 3 enlists preoperative and intraoperative data of the two groups. There were no significant differences in preoperative and intraoperative data between TF ≥ 0.28 and TF < 0.28 groups (Table 3). The incidence of PPCs was significantly higher in the TF < 0.28 group than in the TF ≥ 0.28 group (51.6% [16/31] vs. 21.1% [24/114], $P = 0.001$; Figure 5). Compared with the TF ≥ 0.28 group, the TF < 0.28 group had higher incidences of PPCs in unadjusted (odds ratio = 4.000, 95% confidence interval [1.734–9.229], $P = 0.001$) and multivariate-adjusted analyses (odds ratio = 4.534, 95% confidence interval [1.763–11.658], $P = 0.002$; Figure 6). The duration of hospitalization was not significantly different between the PPC group and the non-PPC group (7.9 ± 4.4 days vs. 7.3 ± 1.8 days, $P = 0.304$).

4. Discussion

In this prospective study, 40/145 patients (27.6%) developed PPCs in RALP. We found that the patients who developed PPCs had a significantly lower preoperative diaphragm TF than those who did not develop PPCs in RALP performed with specific conditions of the Trendelenburg position and pneumoperitoneum. The optimal cut-off value of preoperative diaphragm TF for predicting PPCs in RALP was 0.28. The incidence of PPCs was significantly higher in the TF < 0.28 group than in the TF ≥ 0.28 group, and diaphragm TF < 0.28 was associated with increased incidence of PPCs in RALP. To our knowledge, our study is the first to present the empirical evidence that preoperative low diaphragm TF as a prognostic imaging marker is associated with a high occurrence of PPCs when RALP is performed with specific intraoperative conditions of the Trendelenburg position and pneumoperitoneum, which confer unfavorable effects on the respiratory system.

In this large prospective observational study, the incidence of PPCs in prostate cancer patients who underwent RALP was 27.6%. Previous studies have reported PPC occurrence rates of 2.7%–33.4% in noncardiac surgeries [5, 21, 22]. Our findings may have been influenced by the aforementioned special surgical conditions and patient characteristics. RALP warrants the surgical conditions of carbon dioxide pneumoperitoneum and the steep Trendelenburg position, which adversely affect the respiratory system [15]. The steep Trendelenburg position can reduce lung compliance and lung volume parameters, such as functional residual capacity and vital capacity; furthermore, it can cause edema of the upper airway and elevation in ventilation–perfusion mismatch and peak airway pressure. These conditions may be aggravated further by carbon dioxide pneumoperitoneum,

Table 3: Preoperative and intraoperative data of the two groups categorized according to the optimal diaphragm TF cut-off value.

Variables	TF ≥ 0.28 group (n = 114)	TF < 0.28 group (n = 31)	P value
Age (years)	67.5 ± 6.1	66.3 ± 7.0	0.349
Body mass index (kg/m^2)	24.8 ± 2.6	24.9 ± 2.5	0.926
ASA physical status			0.598
2	92 (80.7)	27 (87.1)	
3	22 (19.3)	4 (12.9)	
Hypertension	42 (43.0)	12 (38.7)	0.838
Diabetes mellitus	16 (14.0)	4 (12.9)	>0.999
Cerebrovascular disease	8 (7.0)	2 (6.5)	>0.999
Coronary artery disease	12 (10.5)	2 (6.5)	0.388
COPD	14 (12.3)	5 (16.1)	0.765
Interstitial lung disease	0 (0)	0 (0)	>0.999
Pulmonary tuberculosis	0 (0)	0 (0)	>0.999
Pulmonary function test			
FVC (L)	3.8 ± 0.6	3.8 ± 0.7	0.731
FEV_1 (L)	2.8 ± 0.5	2.8 ± 0.7	0.549
FEV_1/FVC ratio (%)	73.1 ± 11.2	73.7 ± 11.5	0.796
Preinduction hemodynamics			
Mean blood pressure (mmHg)	90.5 ± 10.3	87.6 ± 12.1	0.173
Systolic blood pressure (mmHg)	137.0 ± 18.2	134.7 ± 17.6	0.538
Diastolic blood pressure (mmHg)	76.0 ± 10.4	72.0 ± 12.2	0.075
Body temperature (°C)	36.6 ± 0.3	36.6 ± 0.3	0.943
Heart rate (beats/min)	70.6 ± 12.9	70.4 ± 12.1	0.931
SpO_2 (%)	98.0 ± 1.8	97.5 ± 1.6	0.140
Arterial blood gas analysis after induction			
pH	7.5 ± 0.03	7.5 ± 0.03	0.472
PaO_2 (mmHg)	283.9 ± 70.6	304.7 ± 79.4	0.193
$PaCO_2$ (mmHg)	38.9 ± 4.9	40.0 ± 4.5	0.235
HCO_3^- (mmol/L)	28.0 ± 2.2	28.4 ± 2.7	0.442
Base excess (mmol/L)	4.0 ± 2.0	4.2 ± 2.4	0.648
SaO_2 (%)	99.9 ± 0.4	99.9 ± 0.7	0.709
Arterial blood gas analysis at skin closure			
pH	7.4 ± 0.04	7.4 ± 0.05	0.460
PaO_2 (mmHg)	188.9 ± 43.6	189.6 ± 50.5	0.939
$PaCO_2$ (mmHg)	40.2 ± 3.3	41.3 ± 3.0	0.093
HCO_3^- (mmol/L)	26.2 ± 1.9	26.0 ± 2.2	0.625
Base excess (mmol/L)	1.6 ± 1.9	1.2 ± 2.4	0.412
SaO_2 (%)	99.6 ± 0.7	99.4 ± 1.0	0.070
Anesthesia duration (min)	159.3 ± 24.8	166.7 ± 28.6	0.200
Operation duration (min)	119.4 ± 24.9	126.2 ± 28.0	0.192
Crystalloid amount (mL)	845.7 ± 577.3	812.9 ± 382.1	0.766

Continuous variables are presented as mean ± standard deviation, and categorical variables are presented as number (percentage). TF: thickening fraction; ASA: American Society of Anesthesiologists; COPD: chronic obstructive pulmonary disease; FEV_1: forced expiratory volume in the first second; FVC: forced vital capacity; SpO_2: peripheral oxygen saturation; pH: hydrogen ion concentration; $PaCO_2$: arterial carbon dioxide partial pressure; PaO_2: arterial oxygen partial pressure; HCO_3^-: bicarbonate; SaO_2: arterial oxygen saturation.

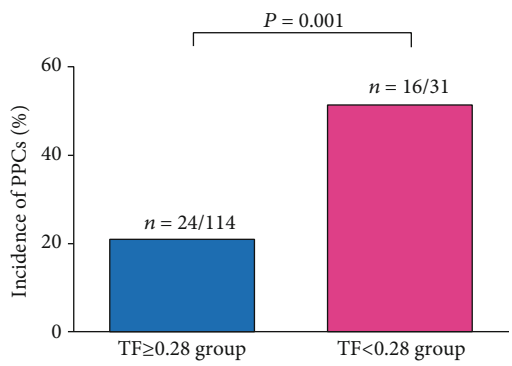

Figure 5: Comparison of the incidence of PPCs between the TF ≥ 0.28 group and TF < 0.28 group. Note that the TF < 0.28 group has a higher incidence of PPCs than TF ≥ 0.28 group. PPCs: postoperative pulmonary complications; TF: thickening fraction.

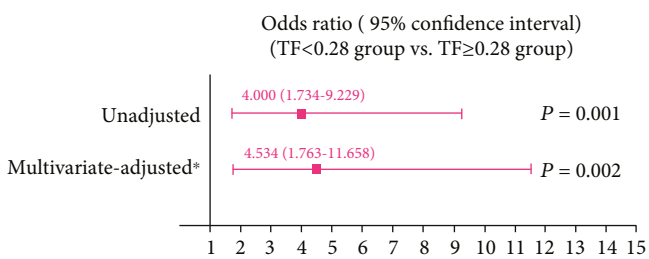

Figure 6: Predictive ability of diaphragm TF ≥ 0.28 for the occurrence of PPCs in patients undergoing RALP. ∗The multivariate-adjusted odds ratio was adjusted using the variables shown in Table 2. TF: thickening fraction; PPCs: postoperative pulmonary complications; RALP: robot-assisted laparoscopic prostatectomy.

which causes hypercapnia and respiratory acidosis [23]. Moreover, most patients undergoing RALP are elderly and are thus even more vulnerable under the specific surgical conditions due to decreased lung compliance and pulmonary function [24]. Therefore, patients undergoing RALP show relatively a higher incidence of PPCs compared with those undergoing other noncardiac surgeries [15].

We found that low diaphragm TF was associated with high occurrence of PPCs in RALP requiring the steep Trendelenburg position and pneumoperitoneum. Diaphragm TF at the zone of apposition allows for direct visualization of the diaphragm muscle; as such, the diaphragm TF depends on the activity of the diaphragm and reflects the work of breathing of the diaphragm [7]. In addition, it could be well correlated with overall respiratory function and offers valuable information, such as ventilator-induced diaphragmatic dysfunction and the prediction of difficult weaning in ventilated patients [10, 25]. Moreover, unlike other tools for evaluating the diaphragm function, such as diaphragmatic electromyography, transdiaphragmatic pressure measurement, magnetic resonance imaging, phrenic nerve stimulation, and computed tomography, the ultrasonographic assessment of diaphragm function as an imaging marker is a real-time and noninvasive method with high feasibility and reproducibility and can be done at bedside in awake patients [8, 9].

Importantly, the strength of respiratory muscles is associated with lung reexpansion after surgery [11]. It is known that evaluating the diaphragm function reflects the strength of the inspiratory muscle [26]. Therefore, diaphragmatic dysfunction could contribute to the etiology of PPCs after noncardiac surgery. In particular, the function of the diaphragm could be characterized by diaphragm TF [11, 26, 27]. In agreement with our results, in several previous studies, diaphragm TF was measured using ultrasonography for evaluating diaphragm function in different clinical settings, such as cardiac surgery and intensive care unit setting [11, 27]. Vivier et al. reported that ultrasonographic assessment of diaphragm TF could evaluate the diaphragmatic function and respiratory workload in critically ill patients with noninvasive ventilation [27]. In addition, Cavayas et al. reported that low diaphragm TF was a risk factor for PPCs after cardiac surgery [11, 27]. Therefore, to minimize the risk of PPCs in patients undergoing RALP under carbon dioxide pneumoperitoneum and the steep Trendelenburg position, special attention should be given to patients with low preoperative diaphragm TF.

In our analysis, the optimal cut-off value of the preoperative diaphragm TF in terms of the prediction of PPCs in RALP was 0.28. In line with the results of our study, Dubé et al. demonstrated that a diaphragm TF of less than 0.29 was significantly associated with poor diaphragm strength and could predict prolonged mechanical ventilation and higher intensive care unit and hospital deaths [28]. However, the optimal cut-off value of diaphragm TF for predicting PPCs in RALP is yet to be evaluated, and our current study is the first to report that patients with TF < 0.28 are at a higher risk of PPCs in RALP performed under the Trendelenburg position and pneumoperitoneum.

Respiratory muscles include expiratory muscles (e.g., diaphragm and internal intercostal muscles) and inspiratory muscles (e.g., diaphragm and external intercostal muscles) [8]. The reduced respiratory muscle capacity contributes to pulmonary complications in critically ill patients [29]. In particular, the diaphragm is the main respiratory muscle that has a key role in pulmonary complications [8]. Therefore, measuring diaphragm TF using ultrasonography can properly reflect the active contraction of respiratory muscle bundles and help assess the diaphragm activity and function [30, 31]. Furthermore, ultrasonography could be simply and noninvasively performed at bedside. Taken together, our study has its strengths because we evaluated the ultrasonographic diaphragm TF for predicting PPCs in a large number of patients undergoing RALP under the Trendelenburg position and pneumoperitoneum.

Our study is limited in that it was conducted in a single center and may have limited generalizability; therefore, multicenter studies are needed for further validation of the results. In addition, our study did not specifically evaluate the relationship between PPCs and diaphragm TF in patients undergoing other types of surgeries, which should be investigated in further targeted studies.

5. Conclusions

PPCs occurred in 27.6% of patients who underwent RALP requiring carbon dioxide pneumoperitoneum and the steep Trendelenburg position. Diaphragm TF < 0.28 was associated with a higher likelihood of PPCs in RALP. These results suggest that the evaluation of preoperative diaphragm TF as an imaging marker should be recommended in prostate cancer patients undergoing RALP for predicting the risk of PPCs.

Data Availability

The data used in the present study are available from the corresponding author upon reasonable request.

Conflicts of Interest

All authors declared no competing interests.

References

[1] J. C. Hu, X. Gu, S. R. Lipsitz et al., "Comparative effectiveness of minimally invasive vs open radical prostatectomy," *JAMA*, vol. 302, no. 14, pp. 1557–1564, 2009.

[2] H. Awad, C. M. Walker, M. Shaikh, G. T. Dimitrova, R. Abaza, and J. O'Hara, "Anesthetic considerations for robotic prostatectomy: a review of the literature," *Journal of Clinical Anesthesia*, vol. 24, no. 6, pp. 494–504, 2012.

[3] D. M. Gainsburg, "Anesthetic concerns for robotic-assisted laparoscopic radical prostatectomy," *Minerva Anestesiologica*, vol. 78, no. 5, pp. 596–604, 2012.

[4] A. Shander, L. A. Fleisher, P. S. Barie, L. M. Bigatello, R. N. Sladen, and C. B. Watson, "Clinical and economic burden of postoperative pulmonary complications: patient safety summit on definition, risk-reducing interventions, and preventive strategies," *Critical Care Medicine*, vol. 39, no. 9, pp. 2163–2172, 2011.

[5] A. Fernandez-Bustamante, G. Frendl, J. Sprung et al., "Postoperative pulmonary complications, early mortality, and hospital stay following noncardiothoracic surgery: a multicenter study by the perioperative research network investigators," *JAMA Surgery*, vol. 152, no. 2, pp. 157–166, 2017.

[6] E. H. Lawson, B. L. Hall, R. Louie et al., "Association between occurrence of a postoperative complication and readmission: implications for quality improvement and cost savings," *Annals of Surgery*, vol. 258, no. 1, pp. 10–18, 2013.

[7] F. D. McCool and G. E. Tzelepis, "Dysfunction of the diaphragm," *The New England Journal of Medicine*, vol. 366, no. 10, pp. 932–942, 2012.

[8] D. Matamis, E. Soilemezi, M. Tsagourias et al., "Sonographic evaluation of the diaphragm in critically ill patients. Technique and clinical applications," *Intensive Care Medicine*, vol. 39, no. 5, pp. 801–810, 2013.

[9] E. C. Goligher, F. Laghi, M. E. Detsky et al., "Measuring diaphragm thickness with ultrasound in mechanically ventilated patients: feasibility, reproducibility and validity," *Intensive Care Medicine*, vol. 41, no. 4, pp. 642–649, 2015.

[10] M. Dres, B. P. Dube, J. Mayaux et al., "Coexistence and impact of limb muscle and diaphragm weakness at time of liberation from mechanical ventilation in medical intensive care unit patients," *American Journal of Respiratory and Critical Care Medicine*, vol. 195, no. 1, pp. 57–66, 2017.

[11] Y. A. Cavayas, R. Eljaiek, E. Rodrigue et al., "Preoperative diaphragm function is associated with postoperative pulmonary complications after cardiac surgery," *Critical Care Medicine*, vol. 47, no. 12, pp. e966–e974, 2019.

[12] E. Y. Joo, Y. J. Moon, S. H. Yoon, J. H. Chin, J. H. Hwang, and Y. K. Kim, "Comparison of acute kidney injury after robot-assisted laparoscopic radical prostatectomy versus retropubic radical prostatectomy: a propensity score matching analysis," *Medicine*, vol. 95, no. 5, article e2650, 2016.

[13] J. Y. Park, J. H. Hong, J. Yu et al., "Effect of ketorolac on the prevention of postoperative catheter-related bladder discomfort in patients undergoing robot-assisted laparoscopic radical prostatectomy: a randomized, double-blinded, placebo-controlled study," *Journal of clinical medicine*, vol. 8, no. 6, 2019.

[14] J. Canet, L. Gallart, C. Gomar et al., "Prediction of postoperative pulmonary complications in a population-based surgical cohort," *Anesthesiology*, vol. 113, no. 6, pp. 1338–1350, 2010.

[15] J. Yu, J. Y. Park, D. H. Kim et al., "Incidence and risk factors of pulmonary complications after robot-assisted laparoscopic prostatectomy: a retrospective observational analysis of 2208 patients at a large single center," *Journal of clinical medicine*, vol. 8, no. 10, 2019.

[16] J. Yu, B. Hong, J. Y. Park, J. H. Hwang, and Y. K. Kim, "ASO author reflections: prognostic nutritional index—a simple evaluation that may help reduce the risk of postoperative pulmonary complications in radical cystectomy," *Annals of Surgical Oncology*, vol. 27, no. S3, pp. 880-881, 2020.

[17] J. A. Brooks-Brunn, "Postoperative atelectasis and pneumonia," *Heart & Lung*, vol. 24, no. 2, pp. 94–115, 1995.

[18] M. Duggan and B. P. Kavanagh, "Pulmonary atelectasis: a pathogenic perioperative entity," *Anesthesiology*, vol. 102, no. 4, pp. 838–854, 2005.

[19] N. Maskell and R. Butland, "BTS guidelines for the investigation of a unilateral pleural effusion in adults," *Thorax*, vol. 58, Suppl 2, pp. ii8–i17, 2003.

[20] M. Henry, T. Arnold, and J. Harvey, "BTS guidelines for the management of spontaneous pneumothorax," *Thorax*, vol. 58, Suppl 2, pp. ii39–ii52, 2003.

[21] F. A. McAlister, K. Bertsch, J. Man, J. Bradley, and M. Jacka, "Incidence of and risk factors for pulmonary complications after nonthoracic surgery," *American Journal of Respiratory and Critical Care Medicine*, vol. 171, no. 5, pp. 514–517, 2005.

[22] A. Miskovic and A. B. Lumb, "Postoperative pulmonary complications," *British Journal of Anaesthesia*, vol. 118, no. 3, pp. 317–334, 2017.

[23] O. F. Kilic, A. Börgers, W. Köhne, M. Musch, D. Kröpfl, and H. Groeben, "Effects of steep Trendelenburg position for robotic-assisted prostatectomies on intra- and extrathoracic airways in patients with or without chronic obstructive pulmonary disease," *British Journal of Anaesthesia*, vol. 114, no. 1, pp. 70–76, 2015.

[24] K. J. Pienta and P. S. Esper, "Risk factors for prostate cancer," *Annals of Internal Medicine*, vol. 118, no. 10, pp. 793–803, 1993.

[25] N. S. Arora and D. F. Rochester, "Effect of body weight and muscularity on human diaphragm muscle mass, thickness, and area," *Journal of Applied Physiology: Respiratory, Environmental and Exercise Physiology*, vol. 52, no. 1, pp. 64–70, 1982.

[26] M. Dres and A. Demoule, "Monitoring diaphragm function in the ICU," *Current Opinion in Critical Care*, vol. 26, no. 1, pp. 18–25, 2020.

[27] E. Vivier, A. Mekontso Dessap, S. Dimassi et al., "Diaphragm ultrasonography to estimate the work of breathing during non-invasive ventilation," *Intensive Care Medicine*, vol. 38, no. 5, pp. 796–803, 2012.

[28] B. P. Dube, M. Dres, J. Mayaux, S. Demiri, T. Similowski, and A. Demoule, "Ultrasound evaluation of diaphragm function in mechanically ventilated patients: comparison to phrenic stimulation and prognostic implications," *Thorax*, vol. 72, no. 9, pp. 811–818, 2017.

[29] T. Vassilakopoulos, S. Zakynthinos, and C. Roussos, "The tension-time index and the frequency/tidal volume ratio are the major pathophysiologic determinants of weaning failure and success," *American Journal of Respiratory and Critical Care Medicine*, vol. 158, no. 2, pp. 378–385, 1998.

[30] E. DiNino, E. J. Gartman, J. M. Sethi, and F. D. McCool, "Diaphragm ultrasound as a predictor of successful extubation from mechanical ventilation," *Thorax*, vol. 69, no. 5, pp. 423–427, 2014.

[31] A. Sarwal, F. O. Walker, and M. S. Cartwright, "Neuromuscular ultrasound for evaluation of the diaphragm," *Muscle & Nerve*, vol. 47, no. 3, pp. 319–329, 2013.

Hindawi
Disease Markers
Volume 2021, Article ID 9186056, 10 pages
https://doi.org/10.1155/2021/9186056

Research Article

Clinicopathological, Radiological, and Molecular Features of Primary Lung Adenocarcinoma with Morule-Like Components

Li-Li Wang,[1] Li Ding,[2] Peng Zhao,[1] Jing-Jing Guan,[1] Xiao-Bin Ji,[1] Xiao-Li Zhou,[1] Shi-Hong Shao,[1] Yu-Wei Zou,[1] Wei-Wei Fu,[1] and Dong-Liang Lin[1]

[1]*Department of Pathology, The Affiliated Hospital of Qingdao University, Qingdao, China*
[2]*Medical Affairs Department, The Affiliated Hospital of Qingdao University, Qingdao, China*

Correspondence should be addressed to Wei-Wei Fu; eer-df@163.com and Dong-Liang Lin; lindongliang@outlook.com

Received 21 April 2021; Accepted 5 June 2021; Published 14 June 2021

Academic Editor: Dong Pan

Background. Morule-like component (MLC) was a rare structure in primary lung adenocarcinoma. We aimed to reveal the clinicopathological, radiological, immunohistochemical, and molecular features of lung adenocarcinoma with MLCs. *Methods*. Twenty lung adenocarcinomas with MLCs were collected, and computed tomographic and histological documents were reviewed. Immunohistochemistry, targeted next-generation sequencing, and Sanger sequencing for *β-catenin* gene were performed. *Results*. There were 9 lepidic adenocarcinomas, 8 acinar adenocarcinomas, 2 papillary adenocarcinomas, and 1 minimally invasive adenocarcinoma. Most patients (16/17) were shown a pure solid nodule, and 1 patient was shown a partly solid nodule on chest computed tomography (CT). Nine cases were accompanied with micropapillary components, and 3 were with cribriform components in which 2 suffered a worse prognosis. No significant association was found between the MCLs and the overall survival of lung adenocarcinoma ($P = 0.109$). The MLCs were often arranged in whorled or streaming patterns. The cells in MLCs showed syncytial and mild appearance. The MLCs were positive for E-cadherin, CK7, TTF-1, napsin-A, vimentin, and β-catenin (membrane), and negative for CK5/6, p40, p63, Synaptophysin, chromogranin A, and Cdx-2. *EGFR* mutation, *ALK-EML4* fusion, *HER*2 amplification, and *PIK3CA* mutation were detected in 16 cases, 2 cases, 1 case, and 1 case, respectively. *EGFR* mutation was more frequent in adenocarcinomas with MLCs than those without MLCs ($P = 0.040$). *β-catenin* gene mutation was not detected in any patients. *Conclusions*. MLC is often observed in the background of acinar, lepidic, and papillary adenocarcinomas. Lung adenocarcinomas with MLCs tend to appear as a solid mass on CT and harbor *EGFR* gene mutations. The micropapillary components and cribriform components may cause poor prognosis of lung adenocarcinomas with MLCs. Vimentin is always positive in MLCs, and it is a useful marker for the identification of MLCs.

1. Introduction

In the recent World Health Organization (WHO) classification of primary lung neoplasm, primary lung adenocarcinomas were subdivided into five subtypes (lepidic adenocarcinoma, papillary adenocarcinoma, micropapillary adenocarcinoma, acinar adenocarcinoma, and solid adenocarcinoma) and four uncommon variants (mucinous adenocarcinoma, colloid adenocarcinoma, fetal adenocarcinoma, and enteric adenocarcinoma) depending on their architectural and cellular features [1]. However, lung adenocarcinoma combined with morule-like components (MLCs) is not mentioned in this edition. Fornelli et al. first released a case of lung adenocarcinoma with MLCs in 2003 [2]. Until now, there have been only 35 cases reported in the English literature [2–8]. Traditional morules often demonstrated refined cell clusters composed of spindle- to oval-shaped cells, and they lack cellular atypia or mitotic figures, which have been reported in endometrial and ovarian lesions [9–11], papillary thyroid carcinoma (cribriform/morular variant) [12], and some colonic adenomas [13]. In lung tumors, the morule is one of the most important histological characteristics of pulmonary blastoma and low-grade fetal adenocarcinoma [1]. The signal pathway of Wnt/beta-catenin is usually activated in the above-mentioned morule-related tumors, in which abnormal nuclear/cytoplasmic β-catenin

Table 1: Clinicopathologic characteristics of lung adenocarcinomas with MLCs.

Case no.	Age (years)/sex/smoking	Location	Size (cm)	Proportion of MLCs (%)	Histologic findings				Treatment	TNM stage	Follow-up (months)
					Predominant component	Other components	STAS	Visceral pleural invasion			
1	50/F/no	LLL	2.2	10	Acinar	Micropapillary	—	—	Lobectomy	T1N1M0	AWT (45)
2	46/F/no	RLL	2.5	15	Acinar	Micropapillary	+	—	Lobectomy	T1N0M0	NET (38)
3	68/F/no	LUL	3.0	20	Acinar	Micropapillary	—	+	Lobectomy	T2N0M0	NET (37)
4	46/F/no	RUL	2.5	5	Acinar	Lepidic/micropapillary	—	—	Lobectomy	T1N0M0	NET (37)
5	48/M/yes	LUL	2.0	5	Lepidic	Acinar	+	—	Lobectomy	T1N1M0	NET (34)
6	66/M/yes	LLL	3.2	15	Lepidic	Papillary/cribriform	—	—	Lobectomy	T2N1M0	DOT(22)
7	55/F/no	RLL	3.1	10	Lepidic	Papillary	—	—	Lobectomy	T2N0M0	NET (33)
8*	51/M/no	RLL	1.2	15	Lepidic	Acinar	—	—	Lobectomy	T1N1M0	NET (32)
9	56/F/no	LUL	1.0	20	Papillary	Lepidic	—	—	Lobectomy	T1N0M0	NET (32)
10	53/M/yes	LLL	2.0	15	Lepidic	Cribriform	—	+	Lobectomy	T2N1M0	DOT (3)
11	68/F/no	LUL	2.5	25	Lepidic	Acinar	—	—	Lobectomy	T1N0M0	NET (30)
12	60/M/no	LLL	2.0	5	Lepidic	Acinar/micropapillary	—	—	Wedge resection	T1N0M0	NET (30)
13	56/M/yes	LLL	3.4	15	Lepidic	Papillary/micropapillary/acinar	+	+	Lobectomy	T2N1M0	NET (29)
14	68/F/yes	RML	1.3	5	Lepidic	Cribriform/micropapillary	+	—	Lobectomy	T1N0M0	NET (28)
15	55/F/no	LUL	2.5	35	Acinar	Micropapillary	+	—	Lobectomy	T1N0M0	Lost to follow-up
16	70/F/no	RUL	2.3	50	Acinar	None	—	+	Wedge resection	T2N0M0	NET (28)
17	61/M/no	RUL	3.0	10	Acinar	Micropapillary	—	—	Lobectomy	T1N1M0	NET (27)
18	48/F/no	LUL	2.8	5	Lepidic	Acinar	—	+	Lobectomy	T2N0M0	NET (27)
19	66/F/yes	LUL	2.5	10	Acinar	Lepidic	—	+	Lobectomy	T2N0M0	NET (27)
20	68/F/no	RLL	1.7	5	Papillary	Lepidic	—	—	Lobectomy	T1N0M0	NET (26)

AWT: alive with tumor (recurrence); DOT: died of tumor; F: female; LLL: left lower lobe; LUL: left upper lobe; M: male; NET: no evidence of tumor; RLL: right lower lobe; RML: right middle lobe; RUL: right upper lobe; STAS: spread through air spaces. *This case was a minimally invasive adenocarcinoma.

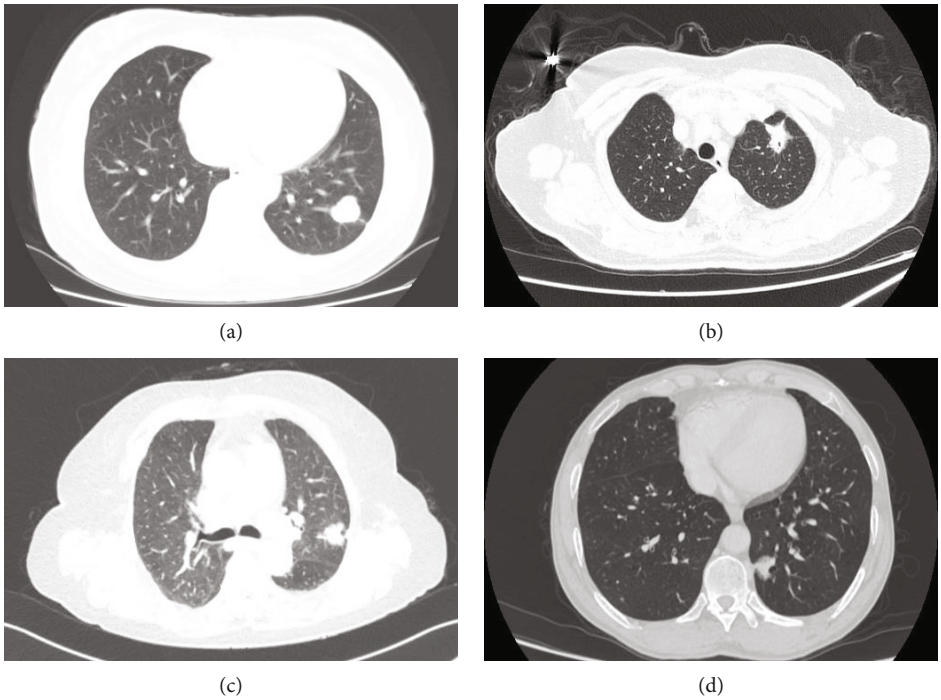

Figure 1: CT imaging of lung adenocarcinomas with MLCs. CT scans showed a solid mass in almost all patients (a–c). A well-defined solid mass in case 1 (a). A spiculated solid mass in case 3 (b). A lobular solid mass in case 16 (c). A mass composed of the central solid component and peripheral ground-glass opacity in case 12 (d).

expression is often seen. Interestingly, lung adenocarcinoma with MLCs usually had no mutation in the *β-catenin* (*CTNNB1*) gene or any aberrant β-catenin expression [5]. Here, we report 20 cases of lung adenocarcinoma with MLCs. We attempt to reveal the clinicopathological, radiological, immunohistochemical, and molecular features of primary lung adenocarcinoma with MLCs.

2. Materials and Methods

2.1. Clinicopathological and Radiological Data. A total of 721 patients, who underwent initial surgical resection dating from 2016 to 2018, were reviewed in our study. The patients involved in our work had never received chemotherapy or radiotherapy before surgery. The median time of follow-up was 34.1 months (range from 1 to 45 months). The cases with MLCs of more than 5% were included in this study. According to this criterion, twenty patients with MLCs were selected in our work. The clinical documents and computed tomographic (CT) imaging were reviewed. This work was approved by the Ethics Committee in our Hospital on Dec. 20, 2019 (No. 25849), and all patients signed informed consent.

2.2. Immunohistochemistry. Immunohistochemical stainings were carried out on paraffin-embedded tissue fixed by formalin. The following antibodies were involved in our work: cytokeratin (CK) 7 (clone: OV-TL12/30), thyroid transcription factor-1 (TTF-1) (clone: SPT24), p40 (clone: BC28), CK5/6 (clone: D5/16B4), p63 (clone: 4A4), ALK (clone: D5F3), Synaptophysin (clone: SP11), chromogranin A (clone: MX018), CD56 (clone: MX039), vimentin (clone: V9), vimentin (clone: EP21), E-cadherin (clone:4A2C7), β-catenin (clone: 17C2), Cdx-2 (clone: EPR2764Y), napsin-A (clone: 1P64), and Ki-67 (clone: MIB1). ALK (D5F3) and vimentin were performed on an automated platform (Benchmark® XT, Ventana). The other stainings were performed on the platform of BOND-MAXTM. Immunohistochemical staining was individually evaluated by two independent pathologists. Both MLCs and the adjacent tumor area of the adenocarcinoma were assessed in the wholes slide.

2.3. Targeted Next-Generation Sequencing and Mutation Analysis of β-Catenin Gene. All hematoxylin and eosin (H&E) stained slides containing adenocarcinoma components were evaluated. Targeted next-generation sequencing was performed in all 721 patients. The lung cancer-associated targeted genes included *EGFR*, *HER2*, *BRAF*, *KRAS*, *NRAS*, *ALK*, *PIK3CA*, *MET*, *RET*, and *ROS1*. The paraffin blocks with the most abundant morule-like components were sorted out for molecular analysis. The nontumorous components were removed as much as possible based on the morphological examination. The method of DNA extraction, DNA concentration, next-generation sequencing, and data analysis was identical to our previous study [14]. The *β-catenin* gene (*CTNNB1*) exon 3 was amplified by polymerase chain reaction (PCR). The primer pairs were as follows: 5′-GATTTGATG GAGTTGGACATGG-3′(F) and 5′-GCTACTTGTTCTTG AGTGAAGG-3′ (R). PCR amplification conditions were as

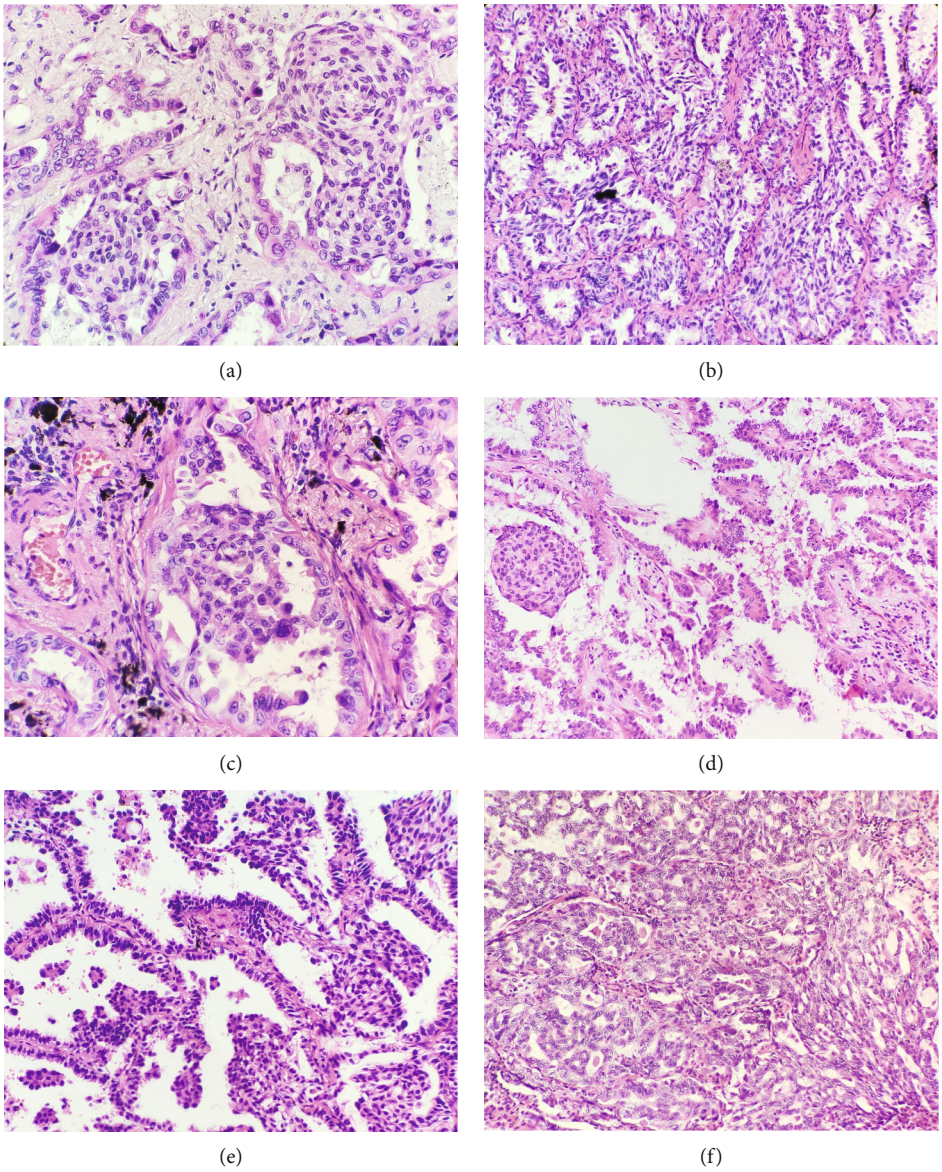

Figure 2: Histological findings of lung adenocarcinomas with MLCs. The MLCs were composed of spindle cells showing a whorled growth pattern, and the spindle cells in the MLCs had a syncytial appearance (a). The MLCs showed a streaming growth pattern with fenestration which was similar to the usual ductal hyperplasia in the breast (b). A few MLCs were epithelioid (c). An MLC in a papillary adenocarcinoma (d). MLCs and micropapillary components in a lepidic adenocarcinoma (e). The transitional region between the cribriform component and the MLC (f).

follows: predenaturation at 98°C for 5 min, 35 cycles of 95°C for 30 s, 55°C for 30 s, and extension at 72°C for 30 s. The PCR data were analyzed using the 3730xl DNA Analyzer (Applied Biosystems, Foster City, USA). Chromas 2.6.6 software were used for analysing the mutations/variations (Technelysium, South Brisbane, Australia).

2.4. Statistical Analysis. Statistical procedures were run using the IBM SPSS 20.0 statistical software package for Microsoft Windows. Pearson's χ^2 test was used to assess the association between MLC and EGFR mutation. We used Kaplan-Meier survival analysis to draw the survival curves. The statistical differences between curves were tested by the log-rank test.

3. Results

3.1. Clinical and Radiological Findings. All clinicopathological records were reviewed, and the relevant results are listed in Table 1. All 721 patients were Chinese people. Of the 20 patients with MLCs, there were 13 women and 7 men. The median age of the 20 patients was 56 years (range from 46 to 70 years). Six patients had a history of smoking. The mean size of the tumor was 2.3 cm (range from 1.0 to 3.4 cm). The patients could manifest chest pain (4 cases) and cough (2 cases). The other 14 patients were asymptomatic. The patients underwent lobectomy (18 cases) or wedge resection (2 cases). The median time of follow-up was 29.3 months (range from 3 to 45 months). CT scans showed a pure solid

Table 2: Immunohistochemical features of adenocarcinoma with MLCs.

Antibody	MLC	Adjacent tumour area
CK7	20 (100%)	20 (100%)
TTF-1	20 (100%)	20 (100%)
Napsin-A	20 (100%)	20 (100%)
E-cadherin	20 (100%)	20 (100%)
Vimentin (V9)	20 (100%)	6 (30%)
Vimentin (EP21)	20 (100%)	6 (30%)
β-Catenin		
Membranous	20 (100%)	20 (100%)
Cytoplasmic and nuclear	0	0
CK5/6	0	0
p40	0	0
p63	0	0
Synaptophysin	0	0
Chromogranin A	0	0
Cdx-2	0	0
Ki-67 index	1%-10%	1%-10%

mass in almost all patients (16/17) (Figures 1(a)–1(c)). In case 12, the mass showed a central solid portion accompanied by peripheral ground-glass opacity and on CT (Figure 1(d)).

3.2. Histological Findings. The morule-like structures were located in the glandular lumens of adenocarcinoma. Most MLCs showed a whorled or streaming growth pattern (Figures 2(a) and 2(b)), and the cells were usually spindle-shaped. Cytoplasmic keratinization and intercellular bridge were not detected in the MLCs. In some cases, the lumens involved by MLC demonstrated a fenestrated growth pattern which was similar to the usual ductal hyperplasia in the breast (Figures 2(a) and 2(b)). A few MLCs demonstrated epithelioid rather than spindle nodules (Figure 2(c)). The cells in MLCs often had a syncytial appearance. The background adenocarcinoma cells frequently demonstrated apical snouting in all cases. Nuclei in most MLCs resembled their adenocarcinoma counterparts. However, in some MLCs, the nuclei appeared slightly smaller and milder than the non-MLC components. The epithelioid cells in MLCs usually showed more atypia than the spindle ones (Figure 2(c)). The mitosis is almost absent in MLCs. Among the 20 cases, 9 were lepidic adenocarcinomas, 8 were acinar adenocarcinomas, 2 were papillary adenocarcinomas (Figure 2(d)), and 1 was a minimally invasive adenocarcinoma. The proportion of MLCs varied from 5% to 50%. A focal micropapillary component (accounting for 5–20%) was observed in 9 cases (45%, Figure 2(e)). A cribriform component (accounting for 10–30%) was observed in 3 cases (15%), and a transitional region between the cribriform component and the MLC could be observed in these cases (Figure 2(f)). Spread through air spaces (STAS) was observed in 5 cases (25%). Six cases (30%) showed a visceral pleural invasion which was demonstrated by elastic staining.

3.3. Immunohistochemistry. The immunohistochemical staining result was listed in Table 2. Both MLCs and the adjacent tumor area of the adenocarcinoma were positive for CK7, TTF-1, napsin-A, and E-cadherin (Figures 3(a)–3(d)). Vimentins (V9 and EP21) were positive in the MLCs in all cases and a few non-MLC components (especially in cribriform and micropapillary components) (Figure 3(e)), but abnormal expression (cytoplasmic and nuclear staining) of β-catenin was not detected (all showed membranous staining) (Figure 3(f)). The MLCs always showed negative immunoreactivities for CK5/6, p40, p63 (Figure 3(g)), Synaptophysin, chromogranin A, and Cdx-2. The 2 cases with *ALK-EML4* fusion and the case with *HER2* amplification were also positive for ALK and Her-2 (Figures 3(h) and 3(i)), respectively. Ki-67 proliferative index in MLCs ranged from 1% to 10%, which was similar to the adjacent tumor areas.

3.4. NGS and Sequencing Analysis of β-Catenin Gene. *EGFR* mutation was detected in 16 patients (80.0%), in which 8 patients showed an exon 21 L858R mutation (1 had a synchronous exon 20 T790M and 1 had a synchronous *PIK3CA* mutation). Exon 19-del was found in 7 patients (1 had a synchronous *HER2* amplification). One patient had synchronous point mutations both in exon 18 and exon 20 (exon18 p.G719C and exon20 p.S768I). *EGFR* mutation was more common in the lung adenocarcinomas accompanied with MLCs than lung adenocarcinomas without MLCs ($\chi^2 = 4.339$, $P = 0.040$). *ALK-EML4* fusion was detected in two patients (Figure 4). β-Catenin gene mutation was not detected in all patients (see Figure S1 in the Supplementary Material).

3.5. Impact of MLC on the Prognosis of Lung Adenocarcinoma. Kaplan-Meier survival curves showed that there was no significant difference between lung adenocarcinomas with MLCs and lung adenocarcinomas without MLCs in overall survival (OS) (Figure 5, $P = 0.109$).

4. Discussion

MLC, also called nonsarcomatous spindle cell morphology, is a rare architecture in lung adenocarcinoma, accounting for about 0.5%–4.0% of all reported lung adenocarcinomas in the literature [4, 5, 8]. It usually presents in middle-aged to elderly people, and only one case occurred in a patient under 40 [2–8]. MLC accounted for 2.8% of all adenocarcinomas in the present series, with a 1.86 : 1 female/male ratio.

The cells in MLCs usually have a whorled or streaming growth pattern, with a squamoid or sarcomatoid pattern, but no definite squamous differentiation, such as cytoplasmic keratinization or intercellular bridges, has ever been observed. MLCs often arise in well-differentiated adenocarcinomas, such as papillary, lepidic, and acinar patterns [5, 8]. In our study, there were 10 cases of lepidic predominant adenocarcinomas. As we know, lepidic predominant lung adenocarcinoma can appear as a mixed ground-glass opacity on CT [15]. However, only one case in our study appeared as a part-solid mass. This may be related to the MLCs that

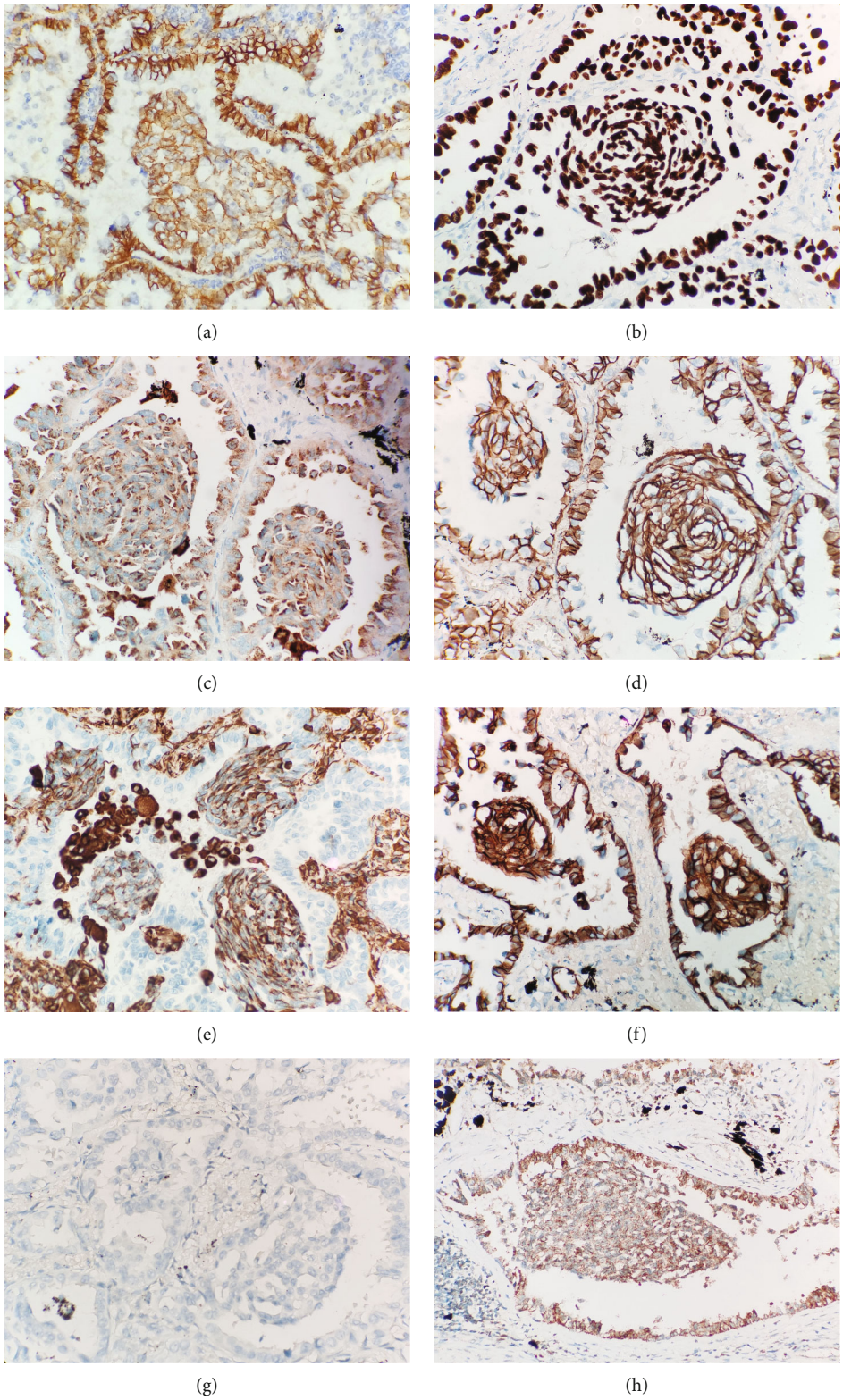

Figure 3: Continued.

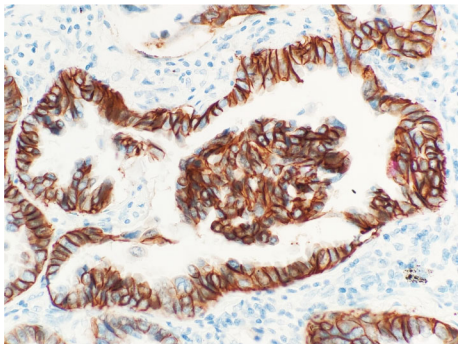

(i)

Figure 3: The MLCs were positive for CK7, TTF-1, napsin-A, and E-cadherin (a–d). Vimentin was always positive in the MLCs (e). β-Catenin showed membranous staining in all cases (f). The MLCs were negative for p63 (g). ALK immunopositivity showed cytoplasmic granular staining in a case harboring ALK-EML4 fusion (h). Her-2 immunopositivity showed membranous staining in the case harboring HER2 amplification (i).

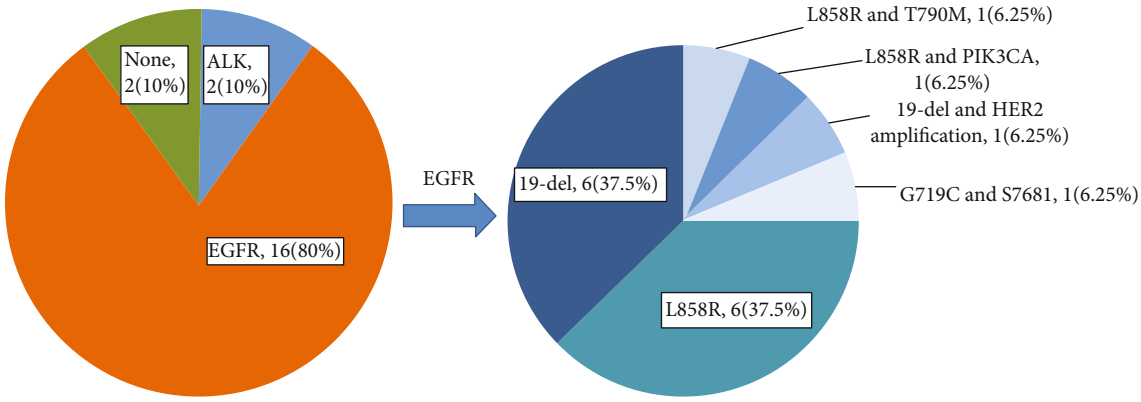

Figure 4: The driver mutation status in lung adenocarcinomas with MLCs.

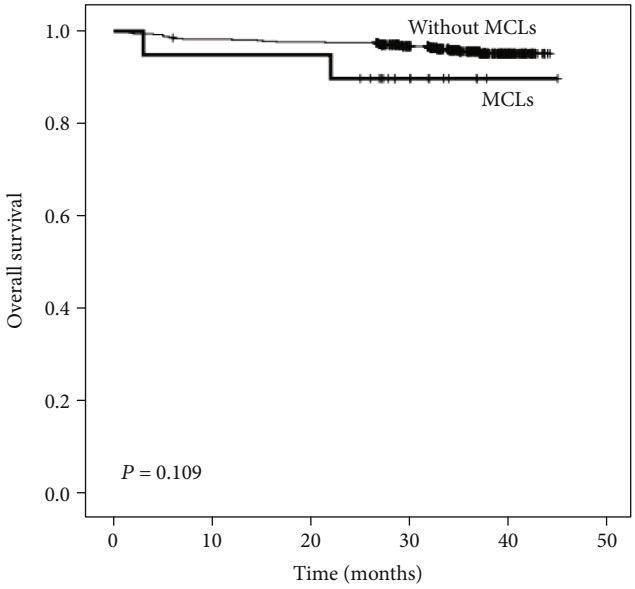

Figure 5: Kaplan-Meier analysis showing the role of MCLs in the prognosis of lung adenocarcinoma. No significant difference in OS was detected between the lung adenocarcinoma with MCLs and without MCL.

occupy the alveolar space associated with lepidic adenocarcinoma. A micropapillary component was observed in 50% (10 cases) in our study in contrast to 88% in Tsuta's study [5], although it was usually not a predominant component [5, 8]. As we know, lung adenocarcinomas with micropapillary components tend to have poor prognosis even if the micropapillary component is not predominant [16, 17]. Some lumens involved with MLC showed a fenestrated pattern, which was similar to the usual ductal hyperplasia in the breast. We identified the fenestrated structures from published illustrations, although they were not mentioned in those reports [5, 8]. The fenestrations were peripherally located and tended to be slit-like, in contrast to cribriform adenocarcinoma. A transitional region between the cribriform component and the MLC with a fenestrated pattern was always observed locally in the three cases with cribriform components, and sometimes, it was difficult to distinguish these two components. Two of them showed a worse prognosis (cases 6 and 10). Although lung adenocarcinoma with a cribriform pattern is not a subtype or variant in the WHO classification [1], recent studies have shown that those lung adenocarcinomas involving cribriform components had a worse outcome [18–21]. Chang et al. contended that the MLC was a histological hallmark of aggressive behavior in

lung adenocarcinomas. However, many cases (15/17, 88%) showed a micropapillary component in their study [5]. This poor prognosis is probably due to the micropapillary component or cribriform component rather than the MLCs. In our study, we did not find a significant relationship between the MCLs and overall survival of lung adenocarcinoma patients. We do not recommend classifying the MLC as a solid component because of their mild appearance and uncertain indication for aggressive behavior. Pathologists should pay more attention to the micropapillary components and cribriform components in lung adenocarcinoma with MLCs.

Immunohistochemically, MLCs always express alveolar epithelial markers such as TTF-1, CK7, and napsin-A, indicating that the MLCs may originate from alveolar pneumocytes. The neuroendocrine markers and squamous epithelial markers were usually negative, showing that they did not represent a neuroendocrine component, a squamous cell component in an adenosquamous carcinoma or squamous metaplasia. Traditional morules always showed aberrant nuclear/cytoplasmic expression of β-catenin due to the activation of the Wnt/beta-catenin signaling pathway [1, 9–13]. In our study, neither *β-catenin* (*CTNNB1*) gene mutation nor aberrant β-catenin expression was detected, which indicated that the Wnt/beta-catenin signaling pathway was not involved. Cdx-2, a marker frequently positive in traditional morules in various lesions [22], was always negative in our study. Thus, we believe that MLCs in lung adenocarcinomas and the traditional morules have different etiology. Vimentin was positive in all 20 cases, which contradicted the results reported by Matsukuma et al. [8]. Two different clones of vimentin were made to verify our results, and they were both positive in MLCs. This discrepancy might be ascribed to different experimental conditions. The spindle syncytial appearance and the expression of vimentin make us think of epithelial-mesenchymal transformation. However, epithelial-mesenchymal transformation often arose in poorly differentiated lung cancer, and it usually showed reduced E-cadherin expression [23–25]. These things were not observed in the MLCs. The formation of MLCs may involve an unrevealed molecular process that needs further study.

Lung adenocarcinoma with MLCs has a high rate of *EGFR* mutation, and some researchers believe that the MLCs are a predictor for *EGFR* mutation in lung adenocarcinoma [5]. In our study, 80% (16/20) of lung adenocarcinomas with MLCs harbored an *EGFR* mutation, higher than those adenocarcinomas without MLCs, which was similar to previous research [5]. However, the *EGFR* mutation is not the only genetic alteration in lung adenocarcinomas with MLCs. At present, among all the cases reported including our cases, three cases were associated with *ALK-EML4* fusion [5], and one case was associated with *KRAS* mutation (substitution mutation at codon 12: G12C) [6]. One case harboring coalteration of exon 19 del and *HER2* amplification and one case harboring coalteration exon 21 L858R mutation and *PIK3CA* point mutation were also detected in the current study. Usually, lepidic, acinar, or papillary components are the predominant components in lung adenocarcinomas with MLCs. As we know, *EGFR* mutations were very common in these subtypes of lung adenocarcinomas [26–32]. In our recently published data, among 814 patients with lung adenocarcinoma, *EGFR* gene alteration was observed in 503 (61.8%) patients, and the *EGFR* gene alteration was frequently found in papillary adenocarcinoma (79.8%), acinar adenocarcinoma (72.4%), and lepidic adenocarcinoma (55.3%) [33]. In this way, the frequent *EGFR* mutation in lung adenocarcinomas with MLCs may be due to the lung adenocarcinoma itself rather than the MLCs. Histologically, lung adenocarcinoma with MLCs must be distinguished from low-grade fetal lung adenocarcinoma. The glandular tumor cells in low-grade fetal adenocarcinoma are columnar with clear cytoplasm and lack apical snouting cytoplasm. Due to the activation of the Wnt/beta-catenin signaling pathway by *β-catenin* gene mutation, low-grade fetal adenocarcinoma usually showed nuclear/cytoplasmic β-catenin expression.

5. Conclusion

The MLCs are usually accompanied by lepidic, acinar, and papillary predominant lung adenocarcinomas. Lung adenocarcinoma with MLCs tend to appear as a solid mass on CT images. The frequent *EGFR* mutation may be due to the lung adenocarcinoma itself rather than the MLCs. In addition to *EGFR*, *ALK-EML4* fusion, *KRAS* mutation, *HER2* amplification, and *PIK3CA* mutation were also found in lung adenocarcinomas with MLCs. The micropapillary components and cribriform components may cause poor prognosis of lung adenocarcinomas with MLCs. Vimentin is always positive in MLCs and is a useful marker to identify the MLCs.

Data Availability

The data in this paper which were used to support the study analysis are available upon request from the corresponding authors.

Conflicts of Interest

The authors have no conflicts of interest to declare.

Authors' Contributions

DLL and WWF conceived and designed this experiment. LLW and LD acquired data and drafted the manuscript. PZ, JJG, and SHS interpreted data and performed statistical analysis. XBJ and XLZ design some parts of the work. YWZ edited figures and tables for publication.

Supplementary Materials

Supplementary 1. Figure S1: *β-catenin* gene mutation was not detected. *(Supplementary Materials)*

References

[1] W. Travis, E. Brambilla, and A. Burke, *WHO classification of tumours of the lung, pleura, thymus and heart*, Lyon: IARC Press, 4th edition, 2015.

[2] A. Fornelli, A. Cavazza, A. Cancellieri, G. Rossi, and L. de Marco, "Bronchioloalveolar carcinoma with nodular

("morule-like") features," *Virchows Archiv : an international journal of pathology*, vol. 442, no. 4, pp. 407-408, 2003.

[3] C. A. Moran, J. Jagirdar, and S. Suster, "Papillary lung carcinoma with prominent "morular" component," *American journal of clinical pathology*, vol. 122, no. 1, pp. 106–109, 2004.

[4] S. Makishi, T. Kinjo, S. Sawada et al., "Morules and morule-like features associated with carcinomas in various organs: report with immunohistochemical and molecular studies," *Journal of Clinical Pathology*, vol. 59, no. 1, pp. 95–100, 2006.

[5] K. Tsuta, M. Kawago, A. Yoshida et al., "Primary lung adenocarcinoma with morule-like components: a unique histologic hallmark of aggressive behavior and _EGFR_ mutation," *Lung cancer (Amsterdam, Netherlands)*, vol. 85, no. 1, pp. 12–18, 2014.

[6] S. Tajima and K. Koda, "Transition between morule-like and solid components may occur in solid-predominant adenocarcinoma of the lung: report of 2 cases with EGFR and KRAS mutations," *International Journal of Clinical and Experimental Pathology*, vol. 8, no. 6, pp. 7475–7481, 2015.

[7] Y. J. Lee, H. Oh, E. Kim et al., "Morule-like features in pulmonary adenocarcinoma associated with epidermal growth factor receptor mutations: two case reports with targeted next-generation sequencing analysis," *Journal of pathology and translational medicine*, vol. 54, no. 1, pp. 119–122, 2020.

[8] S. Matsukuma, K. Obara, K. Kato et al., "Non-sarcomatous spindle cell morphology in conventional lung adenocarcinoma: a clinicopathological study," *Virchows Archiv : an international journal of pathology*, vol. 465, no. 2, pp. 165–172, 2014.

[9] H. Takahashi, T. Yoshida, T. Matsumoto et al., "Frequent _β-catenin_ gene mutations in atypical polypoid adenomyoma of the uterus," *Human Pathology*, vol. 45, no. 1, pp. 33–40, 2014.

[10] E. F. Brachtel, C. Sánchez-Estevez, G. Moreno-Bueno, J. Prat, J. Palacios, and E. Oliva, "Distinct molecular alterations in complex endometrial hyperplasia (CEH) with and without immature squamous metaplasia (squamous morules)," *The American Journal of Surgical Pathology*, vol. 29, no. 10, pp. 1322–1329, 2005.

[11] M. Saegusa and I. Okayasu, "Frequent nuclear beta-catenin accumulation and associated mutations in endometrioid-type endometrial and ovarian carcinomas with squamous differentiation," *The Journal of Pathology*, vol. 194, no. 1, pp. 59–67, 2001.

[12] J. M. Cameselle-Teijeiro, D. Peteiro-González, J. Caneiro-Gómez et al., "Cribriform-morular variant of thyroid carcinoma: a neoplasm with distinctive phenotype associated with the activation of the WNT/β-catenin pathway," *Modern pathology : an official journal of the United States and Canadian Academy of Pathology, Inc*, vol. 31, no. 8, pp. 1168–1179, 2018.

[13] T. Ueo, K. Kashima, T. Daa, Y. Kondo, A. Sasaki, and S. Yokoyama, "Immunohistochemical analysis of morules in colonic neoplasms: morules are morphologically and qualitatively different from squamous metaplasia," *Pathobiology : journal of immunopathology, molecular and cellular biology*, vol. 72, no. 5, pp. 269–278, 2005.

[14] D. L. Lin, X. M. Xing, W. W. Ran et al., "Pulmonary peripheral glandular papilloma and mixed squamous cell and glandular papilloma frequently harbour the BRAF V600E mutation," *Histopathology*, vol. 76, no. 7, pp. 997–1004, 2020.

[15] H. J. Lee, C. H. Lee, Y. J. Jeong et al., "IASLC/ATS/ERS international multidisciplinary classification of lung adenocarcinoma: novel concepts and radiologic implications," *Journal of Thoracic Imaging*, vol. 27, no. 6, pp. 340–353, 2012.

[16] N. Yanagawa, S. Shiono, M. Abiko, M. Katahira, M. Osakabe, and S.-y. Ogata, "The clinical impact of solid and micropapillary patterns in resected lung adenocarcinoma," *Journal of Thoracic Oncology*, vol. 11, no. 11, pp. 1976–1983, 2016.

[17] Y. Zhao, R. Wang, X. Shen et al., "Minor components of micropapillary and solid subtypes in lung adenocarcinoma are predictors of lymph node metastasis and poor prognosis," *Annals of Surgical Oncology*, vol. 23, no. 6, pp. 2099–2105, 2016.

[18] Q. Ding, D. Chen, X. Wang et al., "Characterization of lung adenocarcinoma with a cribriform component reveals its association with spread through air spaces and poor outcomes," *Lung cancer (Amsterdam, Netherlands)*, vol. 134, pp. 238–244, 2019.

[19] K. Kadota, Y. Kushida, S. Kagawa et al., "Cribriform subtype is an independent predictor of recurrence and survival after adjustment for the eighth edition of TNM staging system in patients with resected lung adenocarcinoma," *Journal of thoracic oncology : official publication of the International Association for the Study of Lung Cancer*, vol. 14, no. 2, pp. 245–254, 2019.

[20] Y. Qu, H. Lin, C. Zhang, K. Li, and H. Zhang, "Cribriform pattern in lung invasive adenocarcinoma correlates with poor prognosis in a Chinese cohort," *Pathology, Research and Practice*, vol. 215, no. 2, pp. 347–353, 2019.

[21] R. Zhang, G. Hu, J. Qiu et al., "Clinical significance of the cribriform pattern in invasive adenocarcinoma of the lung," *Journal of Clinical Pathology*, vol. 72, no. 10, pp. 682–688, 2019.

[22] Y. Wani, K. Notohara, Y. Nakatani, and A. Matsuzaki, "Aberrant nuclear Cdx2 expression in morule-forming tumours in different organs, accompanied by cytoplasmic reactivity," *Histopathology*, vol. 55, no. 4, pp. 465–468, 2009.

[23] M. Dauphin, C. Barbe, S. Lemaire et al., "Vimentin expression predicts the occurrence of metastases in non small cell lung carcinomas," *Lung cancer (Amsterdam, Netherlands)*, vol. 81, no. 1, pp. 117–122, 2013.

[24] N. Tsoukalas, E. Aravantinou-Fatorou, M. Tolia et al., "Epithelial-mesenchymal transition in non small-cell lung cancer," *Anticancer Research*, vol. 37, no. 4, pp. 1773–1778, 2017.

[25] Y. Lin, H. Yang, Q. Cai et al., "Characteristics and prognostic analysis of 69 patients with pulmonary sarcomatoid carcinoma," *American Journal of Clinical Oncology*, vol. 39, no. 3, pp. 215–222, 2016.

[26] C. Villa, P. T. Cagle, M. Johnson et al., "Correlation of EGFR mutation status with predominant histologic subtype of adenocarcinoma according to the new lung adenocarcinoma classification of the International Association for the Study of Lung Cancer/American Thoracic Society/European Respiratory Society," *Archives of Pathology & Laboratory Medicine*, vol. 138, no. 10, pp. 1353–1357, 2014.

[27] N. Yanagawa, S. Shiono, M. Abiko, S. Y. Ogata, T. Sato, and G. Tamura, "The correlation of the International Association for the Study of Lung Cancer (IASLC)/American Thoracic Society (ATS)/European Respiratory Society (ERS) classification with prognosis and EGFR mutation in lung adenocarcinoma," *The Annals of Thoracic Surgery*, vol. 98, no. 2, pp. 453–458, 2014.

[28] Z. Chen, X. Liu, J. Zhao, H. Yang, and X. Teng, "Correlation of EGFR mutation and histological subtype according to the IASLC/ATS/ERS classification of lung adenocarcinoma," *International Journal of Clinical and Experimental Pathology*, vol. 7, no. 11, pp. 8039–8045, 2014.

[29] P. A. Russell, S. A. Barnett, M. Walkiewicz et al., "Correlation of mutation status and survival with predominant histologic subtype according to the new IASLC/ATS/ERS lung adenocarcinoma classification in stage III (N2) patients," *Journal of thoracic oncology : official publication of the International Association for the Study of Lung Cancer*, vol. 8, no. 4, pp. 461–468, 2013.

[30] Y. Zhang, Y. Sun, Y. Pan et al., "Frequency of driver mutations in lung adenocarcinoma from female never-smokers varies with histologic subtypes and age at diagnosis," *Clinical cancer research : an official journal of the American Association for Cancer Research*, vol. 18, no. 7, pp. 1947–1953, 2012.

[31] H. Hu, Y. Pan, Y. Li et al., "Oncogenic mutations are associated with histological subtypes but do not have an independent prognostic value in lung adenocarcinoma," *Oncotargets and Therapy*, vol. 7, pp. 1423–1437, 2014.

[32] K. Tsuta, M. Kawago, E. Inoue et al., "The utility of the proposed IASLC/ATS/ERS lung adenocarcinoma subtypes for disease prognosis and correlation of driver gene alterations," *Lung cancer (Amsterdam, Netherlands)*, vol. 81, no. 3, pp. 371–376, 2013.

[33] D. Li, L. Ding, W. Ran et al., "Status of 10 targeted genes of non-small cell lung cancer in eastern China: a study of 884 patients based on NGS in a single institution," *Thoracic cancer*, vol. 11, no. 9, pp. 2580–2589, 2020.

Hindawi
Disease Markers
Volume 2021, Article ID 6640254, 10 pages
https://doi.org/10.1155/2021/6640254

Research Article

A Scoring System for Outpatient Orthopedist to Preliminarily Distinguish Spinal Metastasis from Spinal Tuberculosis: A Retrospective Analysis of 141 Patients

Xing Du, Yuxiao She, Yunsheng Ou, Yong Zhu, Wei Luo, and Dianming Jiang

Department of Orthopedics, The First Affiliated Hospital of Chongqing Medical University, Chongqing 400016, China

Correspondence should be addressed to Yunsheng Ou; ouyunsheng2001@163.com

Received 30 December 2020; Revised 22 April 2021; Accepted 13 May 2021; Published 29 May 2021

Academic Editor: Ioannis Kosmas

Objective. Spinal tuberculosis (TB) misdiagnosed of spinal metastasis was not rarely reported, especially in outpatients department. This study was aimed to establish an outpatient scoring system to preliminarily distinguish spinal metastasis from spinal TB. *Methods*. We retrospectively reviewed consecutive 141 patients with a pathological diagnosis of spinal metastasis (82 cases) or spinal TB (59 cases) in our hospital from January 2017 to June 2018. The following clinical characteristics which can be obtained by outpatient orthopedist were recorded and analyzed: age, gender, malignant tumor history, erythrocyte sedimentation rate (ESR), C-reactive protein (CRP), and imaging features including distribution characteristics of vertebral lesions, subligamentous spread, paravertebral or psoas abscess, involved vertebral element, intervertebral disc, and sequestra formation. The prevalence of clinical characteristics in spinal metastasis was evaluated, and the scoring system was established using logistic regression analysis. The performance of the scoring system was also prospectively validated. *Results*. The outpatient scoring system was based on five clinical characteristics confirmed as significant predictors of spinal metastasis, namely, malignant tumor history, subligamentous spread, posterior element lesions, preserved discs, and no sequestra formation. Spinal metastasis showed a significant higher score than spinal TB (8.17 points *vs.* 1.97 points, $t = 18.621$, $P < 0.001$), and the optimal cut-off value for the scoring system was 5 points. The sensitivity and specificity of the scoring system for predicting spinal metastasis were 97.85% and 88.33%, respectively, in the validation set. *Conclusion*. Spinal lesions with the score of 5 to 10 would be considered a diagnosis of spinal metastasis, while the score of 0 to 4 may be spinal TB. Because the scoring system is mainly based on the clinical characteristics that can be obtained by an outpatient orthopedist, it is suitable to be used as a diagnostic tool in the outpatient department.

1. Introduction

Spinal metastasis and spinal TB are both common spinal lesions [1, 2], but the treatment of them are quite different. Spinal metastasis is a malignant lesion and surgery might be an optimal therapy [3], while spinal TB is a benign disease and effective anti-TB chemotherapy is of great importance [4]. So distinguishing spinal metastasis from spinal TB is essential to reduce pain, prevent neurological disability, minimize spinal deformity, and improve prognosis [5, 6].

However, spinal metastasis and spinal TB show similar clinical manifestations and imaging features such as back pain, weakness, weight loss, vertebrae destruction, pathological fracture, kyphosis deformity, and even neurological dysfunction [7], so it is difficult to distinguish the two accurately, especially in the outpatient department because of the limited consultation time and examination condition [8]. Although biopsy has been proved as the gold standard to distinguish spinal metastasis from spinal TB [9], it cannot be conducted in the outpatient department, so in actual outpatient work, the diagnosis was mainly dependent on the combination of clinical findings and auxiliary examination [3, 10]. However, because not everyone shows the typical clinical characteristics of spinal metastasis or spinal TB, spinal TB misdiagnosed of spinal metastasis was not rarely reported, even during the hospitalization [11–14]. What

was worse, incorrect outpatient diagnosis may give a negative effect on the patients' treatment choice [15, 16]. For example, misdiagnosis of spinal TB as spinal metastasis may result in patient's giving up of hospitalization, missing the best opportunity for treatment, and wasting medical resources, especially for the poor patients [17]. Therefore, it is important to establish a new method to improve the accuracy of distinguishing spinal metastasis from spinal TB in the outpatient department to help the outpatients receive optimal therapy.

In this study, we retrospectively analyzed the clinical characteristics of spinal metastasis and spinal TB and confirmed five characteristics which can be obtained by outpatient orthopedist as significant predictors of spinal metastasis and developed an outpatient scoring system. We also validated the performance of this scoring system and confirmed that it can improve the ability to distinguish spinal metastasis from spinal TB.

2. Materials and Methods

This study was approved by the Ethics Committee of the First Affiliated Hospital of Chongqing Medical University (2017-99). All of the participants provided their written informed consent to participate in this study. The work has been reported in line with the STARD criteria.

2.1. Patients Selection. We retrospectively reviewed the medical records of hospitalized patients diagnosed of spinal metastasis or spinal TB in our department from January 2017 to June 2018 to form the derivation set.

2.1.1. Inclusion Criteria. (1) The medical records were complete, including the general information of the patient, preoperative laboratory examination, and imaging results (MRI and CT were both performed). (2) Patients who were preliminarily diagnosed with spinal metastasis or spinal TB according to clinical symptoms and results of auxiliary examinations before surgery. (3) Patients who underwent surgical treatment (including minimally invasive surgery or open surgery). (4) Lesion tissues were taken during the surgery, and postoperative pathological diagnosis was spinal metastasis or spinal TB

2.1.2. Exclusion Criteria. (1) Patients with suspected spinal metastasis or spinal TB who were not been confirmed by pathological examination. (2) Patients with preliminary and pathological diagnosis of other diseases other than spinal metastasis or spinal TB. (3) Patients with a previous history of spinal metastasis or spinal TB.

2.2. Data Collection. Based on the results of previous studies and our experience, we included the possible predictors for differential diagnosis of spinal metastasis and spinal TB, which mainly included patients' general conditions, laboratory examination indexes, and imaging examination indexes.

(1) General conditions: age, gender, and malignant tumor history

(2) Laboratory examination indexes: ESR and CRP

(3) Imaging examination indexes: two spinal surgeons with more than five years of experiences and who were blinded as to the patients' diagnosis independently reviewed all MRI and CT images and recorded the lesion characteristics (Figure 1): distribution characteristics of vertebral lesions (such as isolated, skipped or contiguous), subligamentous spread, paravertebral or psoas abscess, and involved vertebral elements (vertebral body or posterior elements such as lamina, pedicle, or spinous process); whether the intervertebral disc was destroyed or not and whether sequestra was formed. If there was any disagreement between the two surgeons, the consensus decision was made after a discussion with the third surgeon

2.3. Development of the Scoring System. Firstly, all the included patients were divided into two groups, namely, spinal metastasis or spinal TB according to their pathological diagnosis.

Secondly, we converted the continuous variables (age, ESR, and CRP) to dichotomous variables. The threshold values of continuous variables for predicting spinal metastasis were obtained using receiver operating characteristic (ROC) curves analysis.

Thirdly, univariate analysis was conducted on the general conditions, laboratory examination indexes, and imaging examination indexes of patients in the two groups. Based on the results of univariate analysis, the index with a P value less than 0.05 was considered a possible predictor for differential diagnosis between spinal metastasis and spinal TB.

Next, multivariate logistic regression analysis was performed for the indexes with P values less than 0.05 in univariate analysis. According to the results of multivariate logistic regression analysis, the indexes with P values less than 0.05 were considered the final predictors for differential diagnosis between spinal metastasis and spinal TB and, thus, determined as the items of the scoring system.

Then, we established the weighted score of each item based on the relative size of the β-coefficient according to the method reported by Kharbanda et al. [18] and Zhou et al. [19].

Finally, we made the appropriate cut-off points for the scoring system using ROC curves corresponding to the point on the curve nearest the upper left corner of the ROC graph.

2.4. Validation of the Scoring System. From July 2018 to December 2020, we prospectively included outpatients to validate the accuracy of the scoring system. The following criteria were used to determine whether an outpatient should be prospectively included in the validation set.

Inclusion criteria: (1) the outpatients' general information and preoperative imaging examination results were all accessible for the outpatient orthopedist. (2) According to the scoring system, outpatients were preliminarily diagnosed with spinal metastasis or spinal TB. (3) Outpatients were willing to be hospitalized for surgical treatment.

Exclusion criteria: (1) outpatients with a preliminary diagnosis of other diseases other than spinal metastasis or

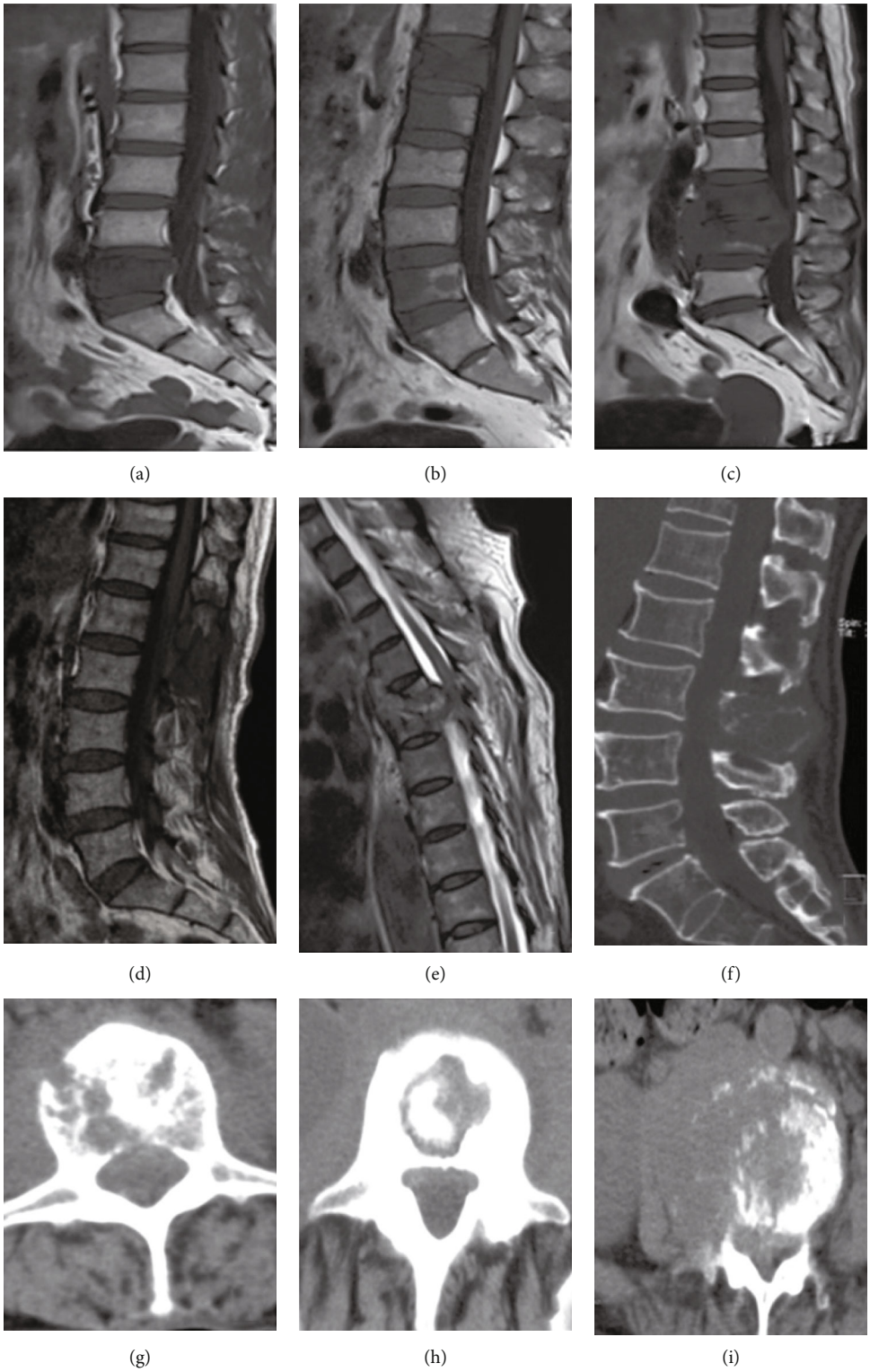

Figure 1: Included imaging features. (a) Isolated vertebral lesion. (b) Skipped vertebral lesions. (c) Contiguous vertebral lesions and subligamentous spread of abscess. (d) Preserved intervertebral disc. (e) Destroyed intervertebral disc and subligamentous spread of abscess. (f) Destroyed vertebral posterior elements. (g) Destroyed vertebral body. (h) Sequestra formation. (i) Paravertebral abscess.

spinal TB. (2) Outpatients had no enough preoperative data and the outpatient orthopedist could hardly make a diagnosis based on the scoring system.

After surgery, the final pathological diagnosis of the included patients was recorded. The accuracy of the scoring system was evaluated by comparing the consistency

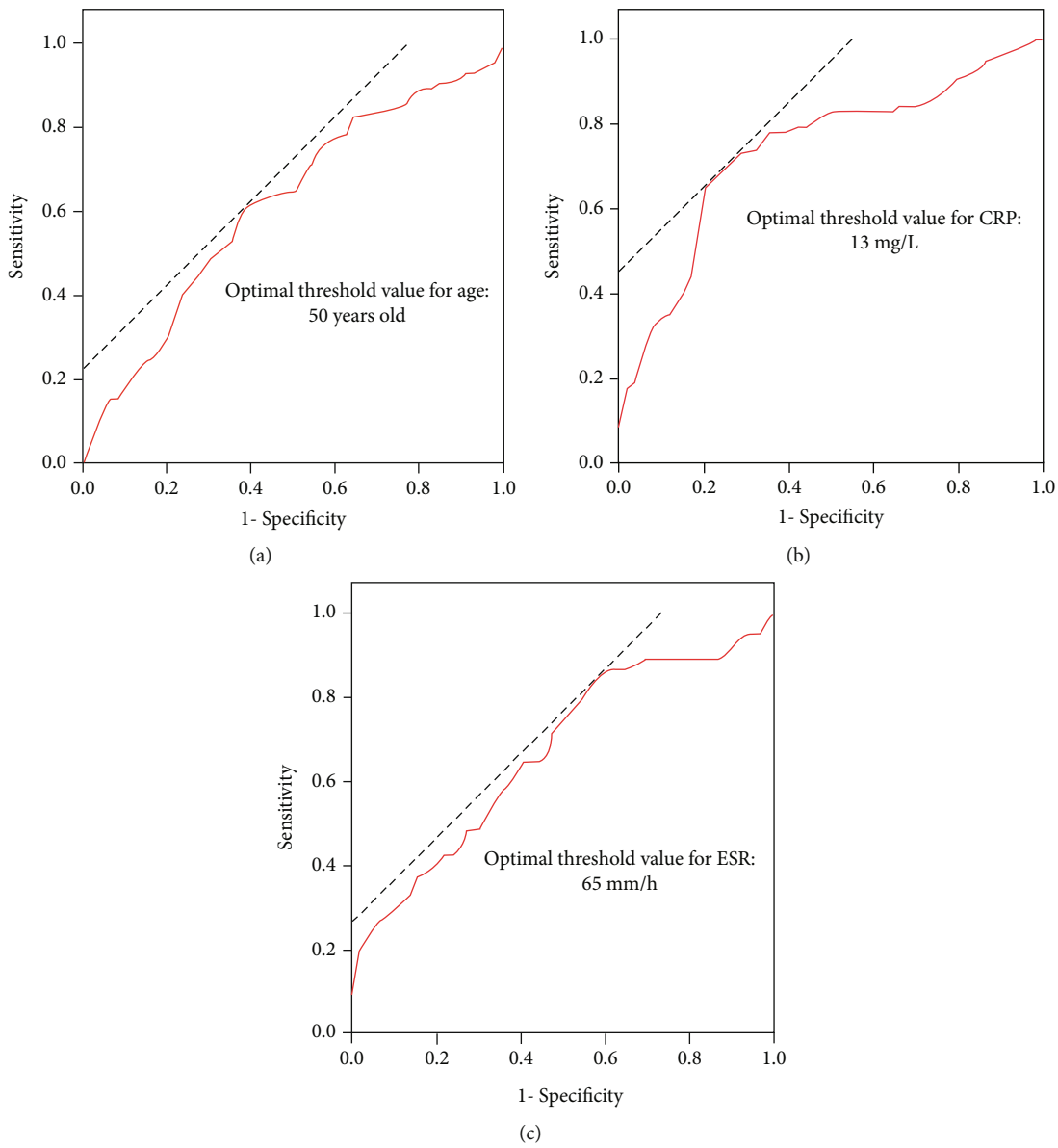

Figure 2: Threshold values for continuous variables. ROC curve analysis showed that the optimal threshold values for age (a), CRP (b), and ESR (c) were 50 years old, 65 mm/h, and 13 mg/L, respectively.

between the preliminary diagnosis and the final pathological diagnosis.

2.5. Statistical Analysis. Both the threshold values for continuous variables and the appropriate cut-off points for the scoring system were determined by the ROC curves analysis. The prevalences of included clinical characteristics were evaluated by calculating the sensitivity and specificity for each factor. The clinical characteristics were also subjected to univariate logistic regression analysis, and the significant factors were evaluated by multivariate logistic regression analysis. The items of the scoring system were determined by multivariate logistic regression, and the weighted score of each item was based on the relative size of the β-coefficient. $P < 0.05$ was set of statistical significance. The SPSS version 10.0 software was used for statistical analysis.

3. Results

3.1. Patients Population. Finally, a total of 141 patients were included in the derivation set, including 82 cases of spinal metastasis and 59 cases of spinal TB, according to the pathological examination. The primary lesions of 82 spinal metastases were as follows: 28 cases with lung cancer, 13 cases with breast cancer, 10 cases with prostate cancer, 7 cases with liver cancer, 6 cases with cervical cancer, 5 cases with kidney cancer, 4 cases with gastrointestinal cancer, 3 cases with ovary cancer, 2 cases with bladder cancer, 2 cases with thyroid gland cancer, 1 case with nasopharynx cancer, and 1 case with parotid gland cancer. 48 men and 34 women were diagnosed with spinal metastasis, and 36 men and 23 women were spinal TB. The mean ages of spinal metastasis and spinal TB groups were 54.09 ± 15.71 years and 48.25 ± 15.65 years, respectively.

Table 1: Prevalence and univariate analysis of clinical characteristics of spinal metastasis.

Clinical characteristic	Pathological diagnosis		Sensitivity (%)	Specificity (%)	*P* value
	Spinal metastasis	Spinal TB			
Gender = male	48/82	36/59	58.53	38.98	0.767
Age >50 years	53/82	26/59	64.63	55.93	0.015
Malignant tumor history	29/82	6/53	30.49	88.68	0.004
ESR <65 mm/h	68/82	33/53	82.93	37.74	<0.001
CRP <13 mg/L	54/82	14/53	65.85	73.58	<0.001
No subligamentous spread	72/82	6/53	87.80	88.67	<0.001
No paravertebral or psoas abscess	67/82	11/53	81.70	79.25	<0.001
Isolated or skipped vertebral lesions	68/82	8/59	82.93	86.44	<0.001
Vertebral posterior elements destroyed	61/82	14/59	71.76	76.27	<0.001
Preserved intervertebral discs	74/82	8/59	90.24	86.44	<0.001
No sequestra formation	74/82	23/59	90.24	60.02	<0.001

Table 2: Multivariate analysis of clinical characteristics of spinal metastasis.

Clinical characteristics	Regression coefficient (β)	*P* value	Odds ratio (OR)
Malignant tumor history	2.362	0.007	10.615
No subligamentous spread	1.617	0.029	5.040
Vertebral posterior elements destroyed	2.199	0.004	9.018
Preserved intervertebral discs	2.779	0.001	16.102
No sequestra formation	2.183	0.014	8.871

3.2. Derivation of the Scoring System: Univariate Analysis. ROC curve analysis showed that (1) the best threshold value for age was 50 years old, the area under curve (AUC) was 0.614 (95% CI: 0.520-0.728, $P = 0.021$), and the diagnostic accuracy was low (Figure 2(a)). (2) The best threshold value for CRP was 13 mg/L, the AUC was 0.739 (95% CI: 0.656-0.823, $P < 0.001$), and the diagnostic accuracy was moderate (Figure 2(b)). (3) The best threshold value for ESR was 65 mm/h, the AUC was 0.670 (95% CI: 0.581-0.759, $P = 0.001$), and the diagnostic accuracy was low (Figure 2(c)). These continuous variables were converted to categorical variables on the basis of these threshold value. The relationship between each categorical variable and spinal metastasis was evaluated with chi-square analysis (Table 1).

3.3. Development of the Scoring System. Multivariate logistic regression analysis was carried out on the significant findings in univariate analysis and showed five clinical characteristics, namely, malignant tumor history, no subligamentous spread, and posterior elements of vertebrae were involved, and intervertebral disc was normal were significant predictors of spinal metastasis (Table 2).

In order to distinguish spinal metastasis from spinal TB, we developed a scoring system based on five clinical characteristics that were conformed significant predictors of spinal metastasis. The variables with significant predictive value for spinal metastasis were given the weighted scores according to the relative value of the β-coefficient in multivariate logistic regression analysis: malignant tumor history, no subligamentous spread, vertebral posterior elements destroyed, no sequestra formation, and preserved intervertebral discs were weighted as 2 points, 1 point, 2 points, 3 points, and 2 points, respectively. The score was then calculated by determining the total number of points, ranging from 0 to 10 (Table 3).

Table 3: The outpatient scoring system for distinguishing spinal metastasis from spinal TB.

Predictors	Points
Malignant tumor history	
Yes	2
No	0
No subligamentous spread	
Yes	1
No	0
Vertebral posterior elements destroyed	
Yes	2
No	0
Preserved intervertebral disc	
Yes	3
No	0
No sequestra formation	
Yes	2
No	0

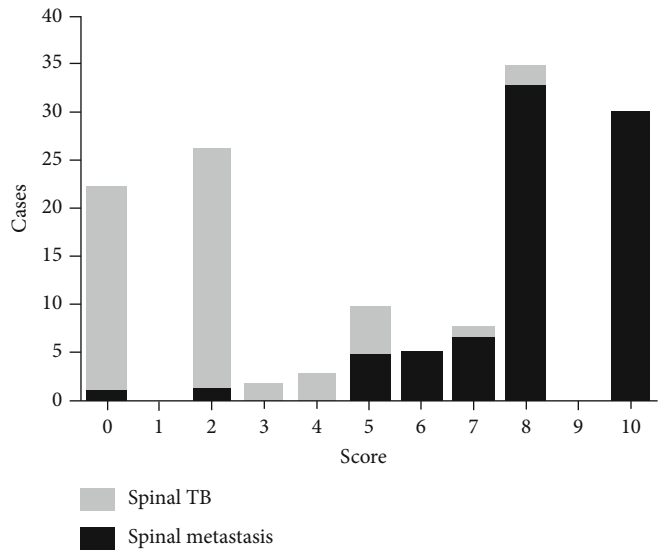

Figure 3: Histogram distribution of spinal metastasis and spinal TB for each score.

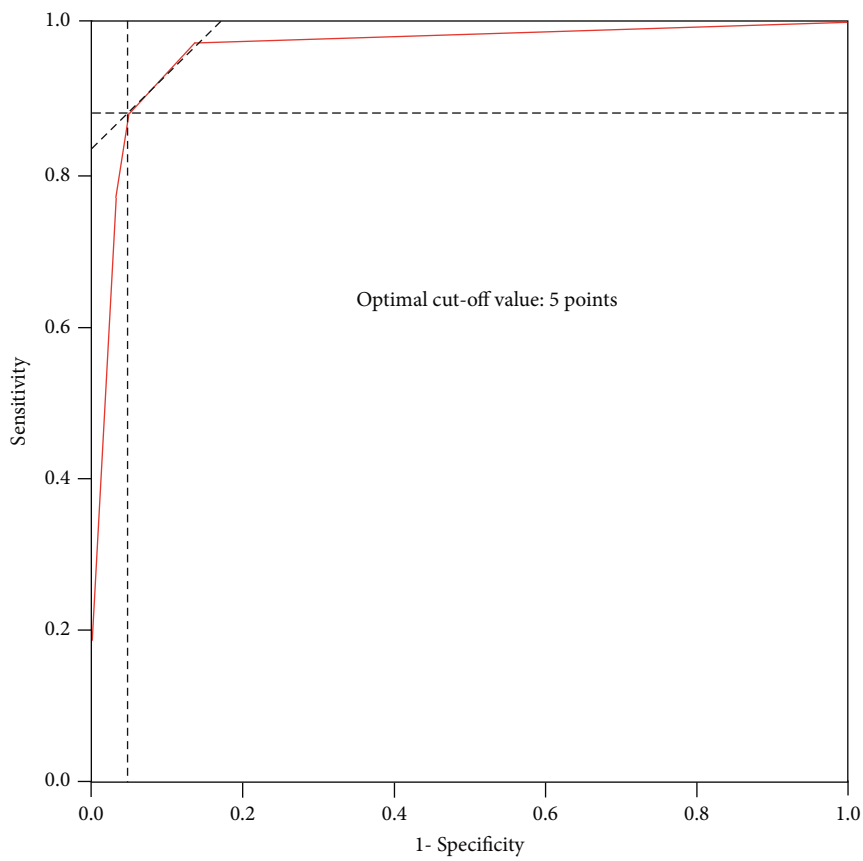

Figure 4: ROC curve analysis of the outpatient scoring system. The optimal cut-off point based on the ROC curve analysis of scores was 5 points.

A histogram distribution of the score values was shown in Figure 3. Remarkably, spinal metastasis showed a significant higher score than spinal TB (8.17 points *vs.* 1.97 points, $t = 18.621$, $P < 0.001$). The optimal cut-off value of the scoring system was 5 points, and the AUG was 0.965 (95% CI: 0.935-0.996, $P < 0.001$) (Figure 4).

3.4. Validation of the Scoring System. Finally, a total of 153 patients were prospectively included in the validation set, including 98 cases of spinal metastasis and 55 cases of spinal TB according to the pathological examination.

Comparison of the performance of the score system on derivation set and validation set was shown in Table 4. Based

Table 4: Comparison of performance of the outpatient scoring system on derivation set and validation set.

		Derivation set			Validation set		
		Spinal metastasis	Spinal TB	Total	Spinal metastasis	Spinal TB	Total
Pathological diagnosis	Spinal metastasis	80	2	82	91	2	93
	Spinal TB	8	51	59	7	53	60
	Total	88	53	141	98	55	153
Sensitivity (%)		97.56			97.85		
Specificity (%)		86.44			88.33		

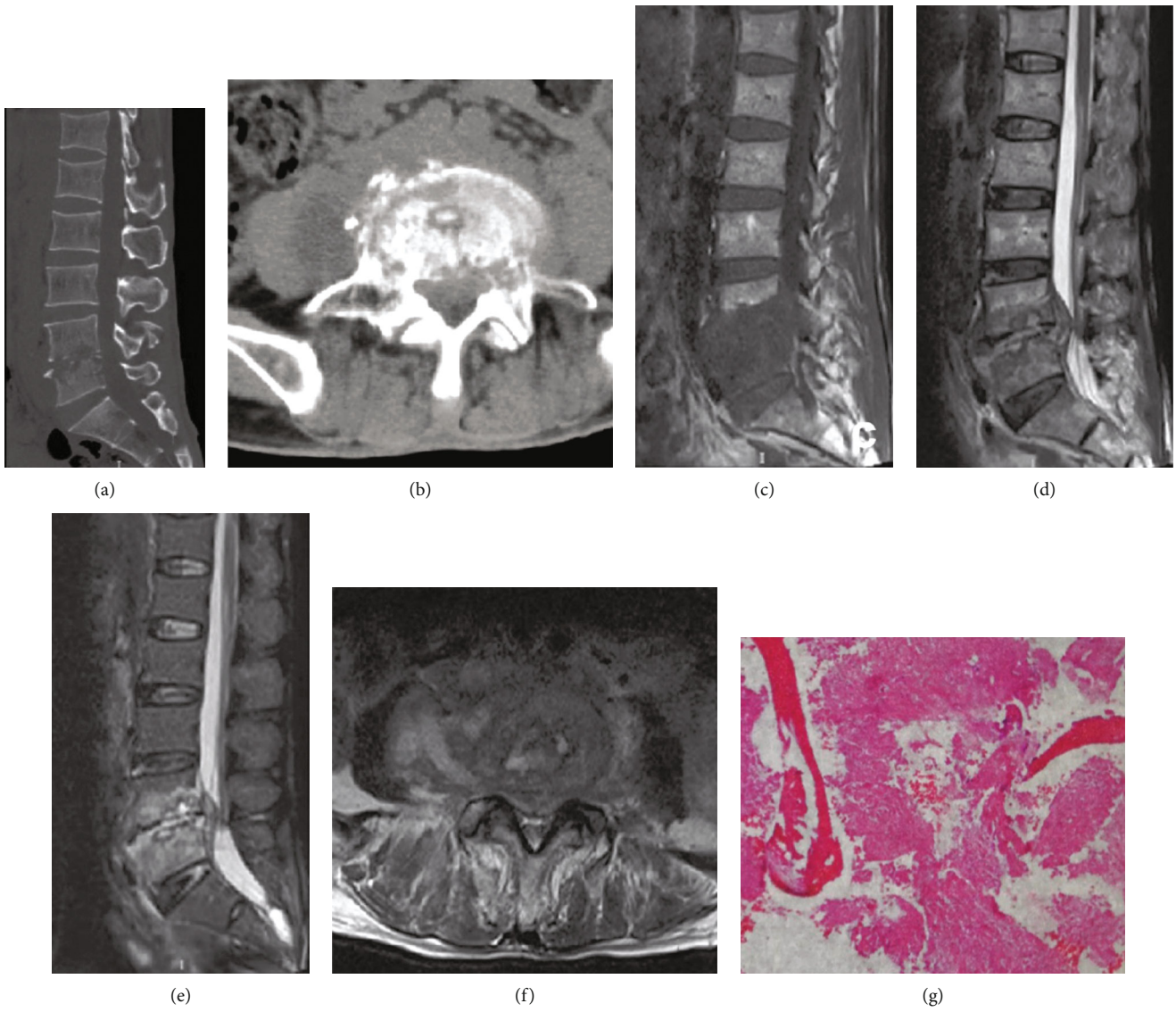

Figure 5: A 56-year-old male suffered from back pain for 4 months with no malignant tumor history. (a, b) lumbar CT showed L4 and L5 vertebral body bone destruction, narrow intervertebral disc, and sequestra formation. (c–f) Lumbar MRI indicated that L4 and L5 vertebral body destruction, subligamentous spread of abscess, and intervertebral disc were involved. (g) The score was 0 points and the preoperative diagnosis was spinal TB which was consistent with the postoperative pathological diagnosis (granulomatous inflammation).

on the cut-off value of 5 points, the sensitivity and specificity of the score for predicting spinal metastasis were 97.56% and 86.44%, respectively, in derivation set and 97.85% and 88.33% in validation set.

Typical cases are shown in Figures 5 and 6.

4. Discussion

4.1. Clinical Findings. Previous study suggested that the onset age of spinal metastasis was higher than that of spinal TB. But in our study, age was found no contribution to the differential

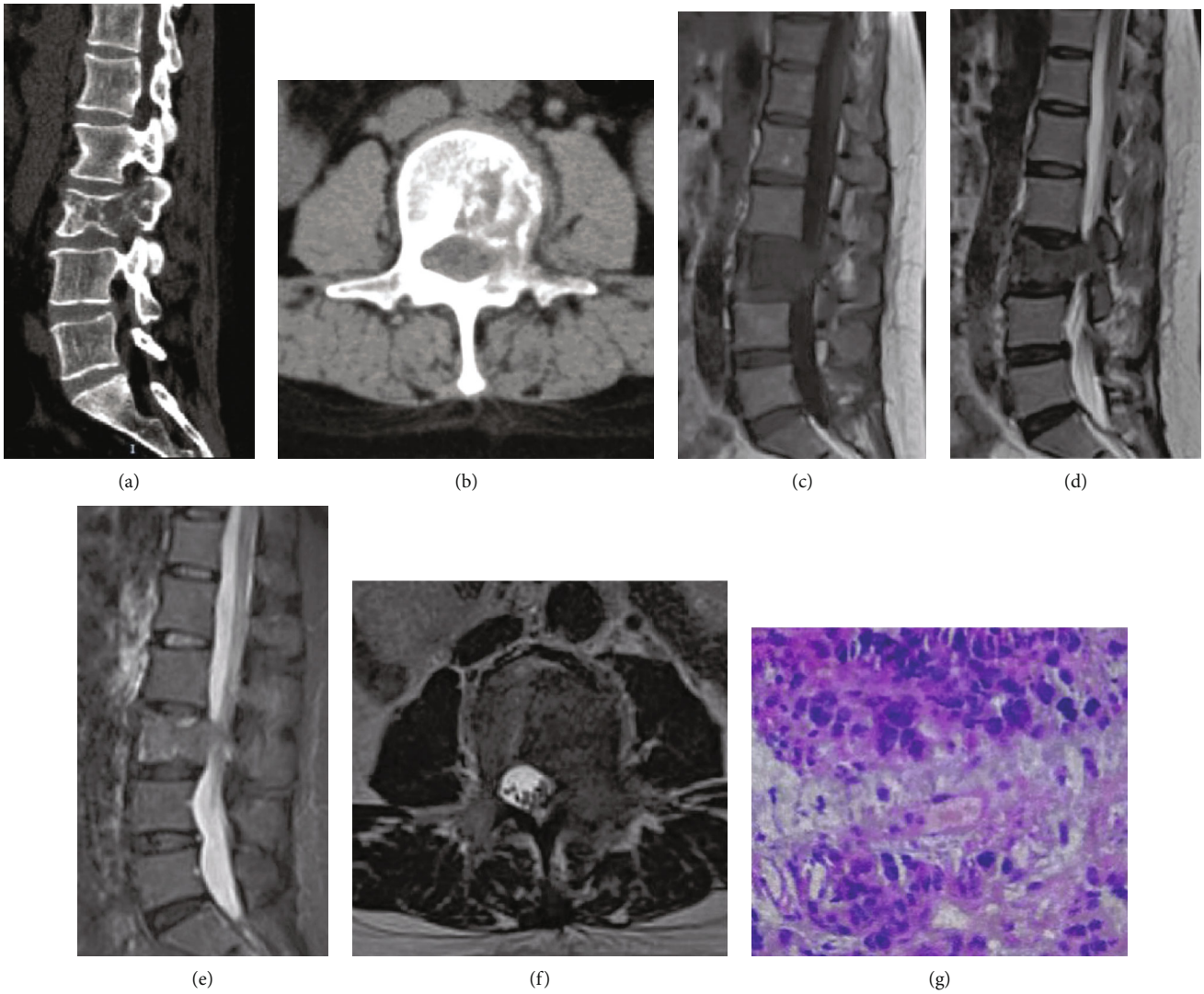

Figure 6: A 42-year-old female suffered from back pain for 6 months and double lower limbs weakness for 10 days with a breast cancer history. (a, b) Lumbar CT showed L3 vertebral body and attachment bone destruction, no subligamentous spread of abscess, no obvious narrow intervertebral space, and sequestra formation. (c–f) Lumbar MRI indicated that L3 vertebral body and attachment bone destruction, but intervertebral disc was normal. (g) The score was 10 points and the preoperative diagnosis was spinal metastasis which was consistent with the postoperative pathological diagnosis (metastatic adenocarcinoma).

diagnosis, this may due to the expansion of the overlap of the onset age of two diseases [2]. A male predominance in spinal metastasis was also reported [5], but no significant difference in gender was found, and this may because more breast cancer than prostate cancer was included in our study (13 and 10 cases, respectively). Sciubba et al. [20] found that 90% of malignant tumor patients had spinal metastasis, and about 30% of them were admitted to the hospital because of symptomatic spinal metastases. And our study also found that malignant tumor history is an important predictor for spinal metastasis. Momjian et al. reported that more than 50% of spinal TB patients could not find evidence of lung TB [21], which may be why we can hardly found the pulmonary TB history of suspected spinal TB patients at the outpatient department. Thus, in this study, we did not include the TB history for analyzing.

4.2. Laboratory Test. Both ESR and CRP were thought helpful for the differential diagnosis of spinal metastasis and spinal TB [10]. However, in our study, the diagnostic specificity of neither ESR nor CRP was satisfactory. We think this may be related to the anti-TB drug treatment before outpatient [22]. All patients included in this study were admitted to our hospital for surgical treatment and most of them had received at least 2 weeks of anti-TB chemotherapy before they went for outpatient, so ESR and CRP might be not high or even normal.

4.3. Imaging Examination. Because mycobacterium TB lacks the proteolytic enzymes and cannot destroy the ligaments [23], so once a spinal TB begins as a destructive lesion in one of the anterior margins of the body of a vertebra, it will spread under the anterior longitudinal ligament.

Subligamentous spread of a TB abscess under the anterior longitudinal ligament seems to be a unique feature of spinal TB with strong diagnostic accuracy. Jain et al. found that 92% of spinal TB patients had subligamentous spread of abscess [24]. In Kanna et al.'s study, 85% of spinal TB patients had subligamentous spread [25], which is similar with our results (88.67%).

Spinal TB mainly spreads via the anterior vertebral arterial; thus, the TB lesions generally began in the anterior superior border of the vertebra. With the progress of the disease, spinal TB can spread to the posterior part of vertebra causing the infection of the whole vertebra [26]. While spinal metastasis is mainly caused by primary tumor spread through Batson venous plexus [27]. Batson venous plexus match with each other and form a traffic branch on the surface of lamina, process, and articular process [28], and this may be the reason why posterior vertebral elements are involved in most spinal metastases.

Because the mycobacterium TB cannot produce proteolytic enzyme and directly destroy the intervertebral disc structure [23], so in the early stage of spinal TB, intervertebral disc may appear normal or only with mildly signal change [29]. But as a result of that disc nutrition is mainly provided by adjacent vertebra, when both sides of the endplate are destroyed, intervertebral disc loses nutrition supply and thus be damaged [30]. Our study found 8 cases of spinal TB appeared with disc preserved; this may be due to the early stage of the disease. While for spinal metastasis, the intervertebral disc is of poor blood supply, so it is rarely affected [31].

Jain et al. reported four patterns of bone destruction in spinal TB, namely, fragmentary, osteolytic, subperiosteal, and well-defined lytic with sclerotic margins, and the fragmentary type was the most common [32]. Fragmentary type imaged as multiple points and platelet high-density bone in bone destruction zone on CT and they were named sequestra. Sequestra were the bone tissue that loses blood supply, and the growth metabolism was broken off. It is assumed that sequestra formation may be related to that TB inflammatory exudate cannot destroy the bone tissue that loses blood supply due to lack of protein enzyme [23]. While the bone destruction of spinal metastases included osteolytic, osteogenic, and osteolytic-osteogenic mixed [33]. And spinal tumor mainly imaged as osteolytic bone destruction, and sequestra were rare.

Due to the combination of clinical characteristics rather than based on any single feature, there is no doubt that the outpatient scoring system can also improve the accuracy of distinguishing spinal metastasis from atypical spinal TB. For example, Shen et al. [34] reported an atypical spinal TB which was misdiagnosed of spinal metastasis with multilevel and noncontiguous lesions, CT showed that the intervertebral spaces between affected vertebra are narrowed and isolated, small sand-like sequestra can also be seen, and MRI showed that the intervertebral discs were involved, but no paraspinal soft tissues. According to the outpatient scoring system, the score was 1 point, which suggested that the lesion should be spinal TB which was consistent with the pathological diagnosis.

Our study also has limitations. First, certain MRI findings of spinal TB or spinal metastasis can be confused with pyogenic infections and other noninfective disorders, but in this study, we just studied the two with higher incidence (spinal TB and spinal metastasis). Second, the sample size was small and it was impossible to further explore the differential diagnosis of atypical spinal lesions. Third, the clinical symptoms and tumor markers were not analyzed.

5. Conclusion

The outpatient scoring system seems to achieve high sensitivity and specificity in distinguishing spinal metastasis from spinal TB. Spinal lesions with the score of 5 to 10 would be considered spinal metastasis, while the score of 0 to 4 is spinal TB. Because the scoring system is mainly based on the clinical characteristics that can be obtained by an outpatient orthopedist, it is suitable to be used as a diagnostic tool in the outpatient department.

Abbreviations

TB: Tuberculosis
ESR: Erythrocyte sedimentation rate
CRP: C-reactive protein
CT: Computed tomography
MRI: Magnetic resonance imaging
ROC: Receiver operating characteristic
AUC: Area under curve.

Data Availability

The clinical data in this study is available from the corresponding author on reasonable request.

Conflicts of Interest

The authors declare that they have no competing interests.

Authors' Contributions

Xing Du and Yunsheng Ou performed the conception and design; Xing Du, Yuxiao She, and Yong Zhu performed the data analysis and interpretation; Xing Du, Yuxiao She, Wei Luo, and Dianming Jiang performed the data collection and management; all authors performed the manuscript writing and critical revisions; Xing Du and Yunsheng Ou did the overall responsibility.

Acknowledgments

This work was supported by the Basic Research and Frontiers Exploration Project of Yuzhong District, Chongqing, (2018114) and the Science and Technology Innovation Project for Postgraduate of Chongqing Municipal Education Commission (CYS18200).

References

[1] M. Ciftdemir, M. Kaya, E. Selcuk, and E. Yalniz, "Tumors of the spine," *World Journal of Orthopedics*, vol. 7, no. 2, pp. 109–116, 2016.

[2] K. Dheda and G. Maartens, "Tuberculosis," *The Lancet*, vol. 387, no. 10024, pp. 1211–1226, 2016.

[3] R. Harel and L. Angelov, "Spine metastases: current treatments and future directions," *European Journal of Cancer*, vol. 46, no. 15, pp. 2696–2707, 2010.

[4] R. N. Dunn and H. M. Ben, "Spinal tuberculosis," *The Bone & Joint Journal*, vol. 100-B, no. 4, pp. 425–431, 2018.

[5] A. K. Jain and J. Kumar, "Tuberculosis of spine: neurological deficit," *European Spine Journal*, vol. 22, no. S4, pp. 624–633, 2013.

[6] V. Eslami and V. Rahimi-Movaghar, "Early diagnosis of tuberculosis in Afghanistan is the best available strategy to prevent spinal cord injury," *Spinal Cord*, vol. 51, no. 4, p. 343, 2013.

[7] B. Paus, "Tumour, tuberculosis and osteomyelitis of the spine. Differential diagnostic aspects," *Acta Orthopaedica Scandinavica*, vol. 44, no. 4, pp. 372–382, 1973.

[8] C. S. Wang, S. W. Feng, L. J. Huang et al., "Atypical mycobacterial spondylitis as a challenging differential diagnosis to metastatic disease of the spine: a case report," *European Journal of Orthopaedic Surgery and Traumatology*, vol. 23, no. S2, pp. 135–139, 2013.

[9] J. Rehm, S. Veith, M. Akbar, H. U. Kauczor, and M. A. Weber, "Ct-guided percutaneous spine biopsy in suspected infection or malignancy: a study of 214 patients," *Rofo.*, vol. 188, no. 12, pp. 1156–1162, 2016.

[10] C. H. Chen, Y. M. Chen, C. W. Lee, Y. J. Chang, C. Y. Cheng, and J. K. Hung, "Early diagnosis of spinal tuberculosis," *Journal of the Formosan Medical Association*, vol. 115, no. 10, pp. 825–836, 2016.

[11] M. Ye, J. Huang, J. Wang et al., "Multifocal musculoskeletal tuberculosis mimicking multiple bone metastases: a case report," *BMC Infectious Diseases*, vol. 16, no. 1, p. 34, 2016.

[12] A. Osmanagic, A. Emamifar, J. Christian Bang, and I. M. Jensen Hansen, "A rare case of Pott's disease (spinal tuberculosis) mimicking metastatic disease in the southern region of Denmark," *Am J Case Rep.*, vol. 17, pp. 384–388, 2016.

[13] Y. Meng, Q. Gong, and H. Liu, "A case of atypical spinal tuberculosis mimicking metastatic tumor," *The Spine Journal*, vol. 16, no. 4, pp. e267–e270, 2016.

[14] C. Y. Zheng, D. X. Liu, S. W. Luo, and S. X. Du, "Imaging presentation highly manifested as tuberculosis in a case of spinal metastatic carcinoma," *Orthopedics*, vol. 34, no. 8, pp. e436–e438, 2011.

[15] J. Flais, G. Coiffier, E. Brillet, A. Perdriger, and P. Guggenbuhl, "Atypical presentation of spine bone metastasis in prostate cancer mimicking Pott's disease," *Clinical Cases in Mineral and Bone Metabolism*, vol. 14, no. 2, pp. 239-240, 2017.

[16] S. Emir, A. Y. Erdem, H. A. Demir, A. Kaçar, and B. Tunç, "Spinal tuberculosis (Pott's disease) mimicking paravertebral malignant tumor in a child presenting with spinal cord compression," *J Lab Physicians.*, vol. 4, no. 2, pp. 98–100, 2012.

[17] F. C. Ringshausen, A. Tannapfel, V. Nicolas et al., "A fatal case of spinal tuberculosis mistaken for metastatic lung cancer: recalling ancient pott's disease," *Annals of Clinical Microbiology and Antimicrobials*, vol. 8, no. 1, p. 32, 2009.

[18] A. B. Kharbanda, G. A. Taylor, S. J. Fishman, and R. G. Bachur, "A clinical decision rule to identify children at low risk for appendicitis," *Pediatrics*, vol. 116, no. 3, pp. 709–716, 2005.

[19] X. Zhou, Q. Qiao, L. Ji et al., "Nonlaboratory-based risk assessment algorithm for undiagnosed type 2 diabetes developed on a nation-wide diabetes survey," *Diabetes Care*, vol. 36, no. 12, pp. 3944–3952, 2013.

[20] D. M. Sciubba, R. J. Petteys, M. B. Dekutoski et al., "Diagnosis and management of metastatic spine disease," *Journal of Neurosurgery: Spine*, vol. 13, no. 1, pp. 94–108, 2010.

[21] R. Momjian and M. George, "Atypical imaging features of tuberculous spondylitis: case report with literature review," *J Radiol Case Rep.*, vol. 8, no. 11, pp. 1–14, 2014.

[22] S. Rajasekaran and G. Khandelwal, "Drug therapy in spinal tuberculosis," *European Spine Journal*, vol. 22, Suppl 4, pp. 587–593, 2013.

[23] M. S. Moon, S. S. Kim, H. L. Moon, and D. H. Kim, "Mycobacterium tuberculosis in spinal tuberculosis," *Asian Spine J.*, vol. 11, no. 1, pp. 138–149, 2017.

[24] A. K. Jain, R. Sreenivasan, N. S. Saini, S. Kumar, S. Jain, and I. K. Dhammi, "Magnetic resonance evaluation of tubercular lesion in spine," *International Orthopaedics*, vol. 36, no. 2, pp. 261–269, 2012.

[25] R. M. Kanna, N. Babu, M. Kannan, A. P. Shetty, and S. Rajasekaran, "Diagnostic accuracy of whole spine magnetic resonance imaging in spinal tuberculosis validated through tissue studies," *Eur Spine J*, vol. 28, no. 12, pp. 3003–3010, 2019.

[26] T. Kilborn, P. J. van Rensburg, and S. Candy, "Pediatric and Adult Spinal Tuberculosis," *Neuroimaging Clinics of North America*, vol. 25, no. 2, pp. 209–231, 2015.

[27] D. Cossigny and G. M. Quan, "In vivo animal models of spinal metastasis," *Cancer Metastasis Reviews*, vol. 31, no. 1-2, pp. 99–108, 2012.

[28] M. M. LaBan, J. C. Wilkins, B. Szappanyos, A. N. Shetty, and A. M. Wang, "Paravertebral plexus of veins (Batson's)–potential route of paraspinal muscle metastases as imaged by magnetic venous angiography. A commentary," *American Journal of Physical Medicine & Rehabilitation*, vol. 76, no. 6, pp. 517–519, 1997.

[29] A. K. Jain and I. K. Dhammi, "Tuberculosis of the spine: a review," *Clinical Orthopaedics and Related Research*, vol. 460, pp. 39–49, 2007.

[30] K. Kumar, "Spinal tuberculosis, natural history of disease, classifications and principles of management with historical perspective," *European Journal of Orthopaedic Surgery and Traumatology*, vol. 26, no. 6, pp. 551–558, 2016.

[31] M. D. Switlyk, K. H. Hole, S. Skjeldal et al., "MRI and neurological findings in patients with spinal metastases," *Acta Radiologica*, vol. 53, no. 10, pp. 1164–1172, 2012.

[32] R. Jain, S. Sawhney, and M. Berry, "Computed tomography of vertebral tuberculosis: patterns of bone destruction," *Clinical Radiology*, vol. 47, no. 3, pp. 196–199, 1993.

[33] J. Redmond 3rd, D. B. Spring, S. H. Munderloh, C. B. George, R. P. Mansour, and S. A. Volk, "Spinal computed tomography scanning in the evaluation of metastatic disease," *Cancer*, vol. 54, no. 2, pp. 253–258, 1984.

[34] Y. Shen, W. Zhong, D. Peng et al., "Atypical, multilevel and noncontiguous tuberculous spondylitis that affected the vertebrae of thoracic, lumbar and sacrum: a case report," *International Journal of Clinical and Experimental Medicine*, vol. 8, no. 2, pp. 3006–3009, 2015.

Hindawi
Disease Markers
Volume 2021, Article ID 9990382, 7 pages
https://doi.org/10.1155/2021/9990382

Research Article

Anti-N-Methyl-D-Aspartate Receptor Encephalitis Associated with Ovarian Teratoma in South China-Clinical Features, Treatment, Immunopathology, and Surgical Outcomes of 21 Cases

Huiyun Jiang,[1] Huixia Ye,[1] Yifeng Wang,[2] Yunhui Li,[1] Ying Wang,[2] and Xiaomao Li[1]

[1]*Department of Gynecology, Third Affiliated Hospital, Sun Yat-sen University, Guangzhou 510630, China*
[2]*Department of Gynecology and Obstetrics, Zhujiang Hospital, Southern Medical University, Guangzhou 510000, China*

Correspondence should be addressed to Xiaomao Li; lixmao@mail.sysu.edu.cn

Received 30 March 2021; Accepted 8 May 2021; Published 21 May 2021

Academic Editor: Zhongjie Shi

Objective. To study the clinical characteristics and surgical outcomes of anti-NMDAR encephalitis and the immunopathology of associated teratomas. *Methods*. Twenty-one patients were enrolled in this retrospective study, who were diagnosed with anti-NMDAR encephalitis with ovarian teratoma and admitted to two tertiary hospitals in South China from July 2014 to December 2019. The clinical data of patients were reviewed. Comparisons were made between the patients with different outcomes after surgery. Immunohistochemical analyses of associated ovarian teratomas were performed. *Results*. The mean age of the patients was 24.33 ± 5.12 years. The peak seasons of disease onset were autumn and winter (30.61% and 32.65%). The symptoms could be divided into 8 categories, including psychiatric abnormalities, seizures, movement dysfunction, consciousness disorders, autonomic dysregulation, speech disturbance, central hypoventilation, and memory deficits. All patients developed four or more categories of symptoms within the first four weeks. Twelve patients (57.1%) had a maximum mRS of 5, and 11 patients (52.4%) were admitted to ICU. Twenty patients received surgery, and only 3 patients were diagnosed pathologically with immature ovarian teratomas, while the other 17 patients had mature ovarian teratomas. After surgery, 17 patients (85.0%) got clinical improvement. The central hypoventilation symptom and mature ovarian teratomas were associated with surgical outcome. Immunohistochemical analysis revealed that there were NMDAR-positive neural tissues in all 8 teratomas and in which 3 cases also contained large numbers of NMDAR-positive sebaceous glands and squamous epithelial tissues. *Conclusion*. The disease is of high prevalence in autumn and winter. The central hypoventilation symptom and mature ovarian teratomas were associated with surgical outcome. NMDAR-positive neural tissue is not the only etiological factor of encephalitis. We speculate that encephalitis development in some patients may result from NMDAR expression in sebaceous glands and squamous epithelial tissues.

1. Introduction

Anti-N-methyl-D-aspartate receptor (NMDAR) encephalitis belongs to immune-mediated disorder with prominent neuropsychiatric symptoms, which is serious and potentially lethal. It was firstly identified by Dalmau et al. [1]. Along with the progress of anti-NMDAR antibody detection and the growing attention paid to the disease, related researches began to rise rapidly. Several autoimmune diseases are known to have well-established seasonal variation. However, there is still little knowledge about the anti-NDMAR encephalitis's onset season.

Teratoma is a confirmed trigger of anti-NMDAR encephalitis [2]. About 50% of the female patients with anti-NMDAR encephalitis were identified to have teratoma [3]. And Dalmau et al. [1] founded neural tissue with strong expression of NR2 subunits in the patients' teratoma, which could react with patients' antibodies. Thus, autoimmune factor is widely considered to be an important etiology of anti-NMDAR encephalitis. However, some patients' teratomas

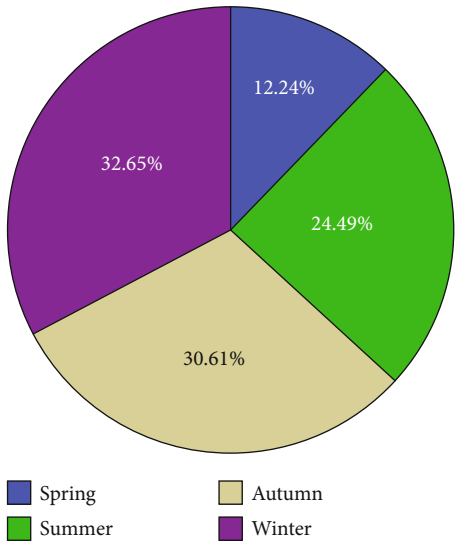

Figure 1: Seasonal variation of the incidence of anti-NMDAR encephalitis with ovarian teratoma.

lack neural tissue, and the immunopathology of the associated teratomas needs to be further studied.

The therapeutic methods of anti-NMDAR encephalitis involve immunotherapy and tumor section. First-line immunotherapy is the first choice, including corticosteroids, intravenous immunoglobulins, and plasma exchange. Second-line immunotherapy includes rituximab, cyclophosphamide, and mycophenolate mofetil [4]. Tumor section is usually recommended for patients with ovarian tumors, as studies reported that tumor section was associated with a lower rate of relapse in patients with teratoma compared to patients without teratoma [5]. But it is still lack of study focusing on the influence factors of surgical outcome.

This study is aimed at characterizing the onset season, clinical presentations, auxiliary examinations, treatment experience, immunopathology of teratomas, and prognosis of anti-NMDAR encephalitis with ovarian teratoma and comparing the difference in clinical features of patients with or without clinical improvement after surgery.

2. Materials and Methods

2.1. Patients. Patients diagnosed with anti-NDAMR encephalitis with ovarian teratoma, who were admitted into the Third Affiliated Hospital, Sun Yat-sen University, and Zhujiang Hospital, Southern Medical University, Guangzhou, China, from July 1, 2014 to December 30, 2019, were enrolled in this study, which was approved by the ethics committee of the Third Affiliated Hospital, Sun Yat-sen University (No. [2017]2-198). Written consent was provided by the patients or their representatives.

The inclusion criteria were as follows: (1) at least one of the symptoms, including psychiatric abnormalities, seizures, speech disturbance, dyskinesias, disturbance of consciousness, autonomic dysfunction, or central hypoventilation; (2) positive anti-NMDAR antibody in cerebrospinal fluid (CSF); (3) imaging findings of ovarian teratoma. All patients were diagnosed with anti-NMDAR encephalitis according to the criteria suggested by Dalmau et al. [2]. The fixed cell-based indirect immunofluorescence test (OUMENG FA 112d-51) was used to detect the anti-NMDAR antibodies in CSF or serum samples.

2.2. Data Collection. We collected demographic details, clinical features, auxiliary examinations and imaging examinations, treatments, and prognosis of patients included. Clinical features were divided into eight categories: psychiatric abnormalities, seizures, memory deficits, movement dysfunction, autonomic dysregulation, speech disorder, central hypoventilation, and loss of consciousness.

2.3. Outcome Evaluation. The modified Rankin Scale (mRS) was used to evaluate the severity of illness and outcome of patients [4, 6]. An mRS score of 0-2 was considered as good outcome.

A decrease in mRS ≥ 1 was defined as clinical improvement. No change in mRS or mRS ≥ 4 for 1 month after surgery was defined as having no clinical improvement. The new onset or worsening of symptoms occurring after two months of stabilization was considered as disease relapse [5]. Patients received prognosis evaluation at defined time points (1 week, 1 month, 3 months, 6 months, and 12 months after surgery).

2.4. Immunohistochemistry. Immunohistochemistry was performed on formalin-fixed, paraffin-embedded specimens. Slides of paraffin-embedded tumors were deparaffinized in xylene for 5 min and rehydrated in ethanol (4 min for 100%, 4 min for 95%, 4 min for 85%, and 4 min for 70%) and then washed by PBS for 2 min. Sections were pretreated with EDTA buffer pH 8.0 to retrieve antigens and washed three times with PBS. Sections were serially incubated with 3% H_2O_2 for 10 min and blocked with goat serum (Boster, AR0009) for 30 min. Sections were incubated at 4°C overnight with primary antibodies as follows: anti-NDMAR1 antibody (1 : 200; Abcam ab52177), anti-NMDAR2A (1 : 25; Abcam ab118587), anti-NMDAR2B (1 : 25; Novus NB100-74475), and anti-MAP2(1 : 250; Abcam, ab183093). Then, sections were washed with PBS for three times and incubated with rabbit or mouse normal serum for 30 min and labeled polymer-HRP anti-rabbit or anti-mouse. DAB was used to stain the sections.

2.5. Statistical Analysis. SPSS version 20.0 was used to perform Statistical analyses. p values <0.05 (two-sided) were considered significant. Baseline parameters were presented using descriptive statistics. Continuous variables were analyzed with an independent sample t-test. Contingency tables were analyzed using Pearson's chi-square test or Fisher's two-sided exact test when appropriate. Factors influencing surgical outcome were assessed by multivariable binary logistic regression.

3. Results

Twenty-one patients were reviewed, of which 15 patients were admitted to the Third Affiliated Hospital, Sun Yat-sen

Table 1: General and clinical characteristics in patients having clinical improvement after surgery and patients having no improvement after surgery ($N = 20$).

Parameters	Patients having improvement after surgery ($n = 17$)[§]	Patients having no improvement after surgery ($n = 3$)[€]	t	p
Age (y)	23.53 ± 5.03	28.00 ± 5.56	-1.403	0.178
Fertilized women	3 (17.6%)	2 (66.7%)		0.140*
History of ovarian surgery	2 (11.8%)	0 (0.0%)		0.716*
Clinical features [5]				
Prodromal symptoms				
Fever ($T > 37.5^{\circ}$C)	4 (23.5%)	1 (33.3%)		0.601*
Headache	6 (35.3%)	2 (66.7%)		0.620*
Initial symptoms				0.579*
Psychiatric abnormalities	9 (52.9%)	2 (66.7%)		
Seizures	8 (47.1%)	1 (33.3%)		
Psychiatric abnormalities	17 (100.0%)	3 (100.0%)		-
Seizures	12 (70.6%)	2 (66.7%)		0.681*
Movement dysfunction	10 (58.8%)	2 (66.7%)		0.656*
Loss of consciousness	8 (47.1%)	3 (100.0%)		0.218*
Autonomic dysregulation	10 (58.8%)	1 (33.3%)		0.566*
Speech disturbance	6 (35.3%)	2 (66.7%)		0.537*
Central hypoventilation	5 (29.4%)	3 (100.0%)		0.049*
Memory deficits	2 (11.8%)	0 (0.0%)		0.716*
Number of symptoms[#] [4]	3.94 ± 1.39	5.33 ± 1.15	-1.627	0.121
ICU admission [4]	8 (47.1%)	3 (100.0%)		0.218*
mRS at onset [4]	4.23 ± 0.90	5.00 ± 0.00	-3.490	0.003
Diameter of the ovarian teratoma (mm)	48.47 ± 35.31	49.00 ± 13.53	-0.025	0.980*
Pathological type				0.284*
Mature ovarian teratoma	16 (94.1%)	2 (66.7%)		
Immature ovarian teratoma	1 (5.9%)	1 (33.3%)		
Time until surgery initiation (d)	36.10 ± 13.22	45.67 ± 21.22	-0.969	0.353*

[§]A decrease in mRS ≥ 1 was defined as having clinical improvement after surgery. [€]No change in mRS or mRS ≥ 4 for 1 month after surgery was defined as having no clinical improvement. [#]The eight symptom categories are as follows: psychiatric abnormalities, seizures, movement dysfunction, loss of consciousness, autonomic dysregulation, speech disturbance, central hypoventilation, and memory deficits. *Fisher's exact test. mRS: modified Rankin Scale; ICU: intensive care unit.

University, and the other 6 patients were admitted to the Zhujiang Hospital, Southern Medical University, Guangzhou, China. All 21 patients were female. The mean age of patients was 24.33 ± 5.12 years (ranging from 15 to 33 years old). The disease could occur all year round, and the peak seasons focused in autumn and winter (30.61% and 32.65%) (Figure 1).

3.1. Clinical Features. Thirteen patients (61.9%) had prodromal symptoms, including fever and headache, and the mean duration was 7.15 ± 5.92 d, ranging from 1 d to 20 d. And 20 patients (95.2%) had psychiatric abnormalities, 14 (66.7%) patients had seizures, 12 (57.1%) patients had movement dysfunction, 11 (52.4%) patients had loss of consciousness, 11 (52.4%) patients had autonomic dysregulation, 9 (42.9%) patients had speech disturbance, 8 (38.1%) patients had central hypoventilation, and 2 (9.5%) patients had memory deficits. For all patients, 12 of them (57.1%) developed psychiatric symptoms as initial manifestations, and the other 9 cases (42.9%) presented with seizures initially. All patients developed four or more categories of symptoms within the first four weeks. Twelve of 21 patients (57.1%) had a maximum mRS of 5, and 11 of 21 patients (52.4%) were admitted to ICU.

Only one patient (4.8%) had lower abdominal pain during the onset period, as a result of acute torsion of ovarian teratoma. Other patients did not present any gynecological symptoms.

3.2. Ancillary Examinations. Ten of 21 patients (47.6%) had lymphocytic pleocytosis of cerebrospinal fluid. Seropositive anti-thyroid autoimmune antibodies were detected in 10 of 21 patients (47.6%). Seven of 21 patients (33.3%) had

Table 2: Factors associated with clinical improvement after surgery (multivariable analysis).

Factor	p	OR	95% CI
Age	0.160		
Fertilized women	0.718		
Loss of consciousness	0.089		
Central hypoventilation	0.021	0.89	0.60-1.45
Number of symptoms	0.109		
ICU admission	0.089		
mRS at onset	0.152		
Pathological type			
Mature ovarian teratoma	0.007	1.39	0.89-1.93

OR: odds ratio; CI: confidence interval; mRS: modified Rankin Scale; ICU: intensive care unit.

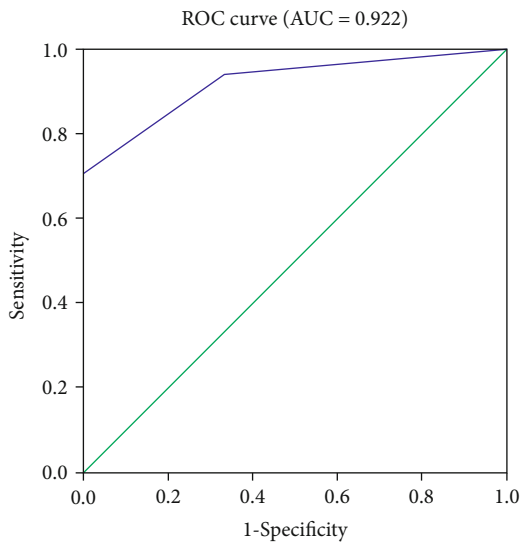

Figure 2: ROC curves showed the predictive efficiency of the model for the surgical outcome.

abnormalities in thyroid function test. In addition, 8 patients underwent 25-hydroxyvitamin D detection, and 7 of them (87.5%) had a lower level than normal, ranging from 18.9 to 44.0 nmol/L.

We detected serum cancer antigen 125 (CA 125), carbohydrate antigen 19-9 (CA 19-9), and serum alpha protein (AFP). And 8 of 21 patients' (38.1%) CA 125 level was higher than normal, and the maximum value was 218.6 KU/L. Three of the 21 patients (14.3%) had elevated AFP levels, and the maximum value was 34.9 ng/ml. All patients' CA19-9 values were in the normal range.

All patients received intensive oncological assessments routinely, including pelvic ultrasound and/or abdominal-pelvis CT/MRI. The diameters of the ovarian teratoma ranged from 10 to 160 mm. Nineteen of the 21 patients' (90.5%) ovarian teratomas were unilateral, and only 2 of the 21 patients' (9.5%) ovarian teratomas were bilateral.

3.3. Treatment and Outcomes. All patients received immunotherapy. Eight patients (38.1%) were treated only with single or multiple first-line immunotherapies, and the other 13 patients (61.9%) received first-line immunotherapies and second-line immunotherapy subsequently.

Twenty patients underwent surgery during the initial episode. Only one patient did not receive surgery because of the rejection of her family. Of the 20 patients with surgical treatment, 6 patients (30.0%) received ovarian cystectomy, and the other 14 patients (70.0%) received affected unilateral adnexectomy. The mean mRS score of patients receiving ovarian cystectomy was 3.50 ± 0.84, which was lower than that of patients receiving affected unilateral adnexectomy (4.71 ± 0.61) ($p = 0.006$). The mean duration between disease onset and surgery was 36.92 ± 14.72 d, ranging from 16 d to 63 d. Of the 20 patients who underwent surgery, 17 patients (85.0%) got clinical improvement after surgery, and the other 3 patients (15.0%) had no improvement of the mRS scores for 4 weeks after surgery.

Table 1 summarized the difference of general and clinical characteristics of patients having clinical improvement and patients having no clinical improvement after surgery. There was no significant difference in age, gravidity, history of ovarian surgery, prodromal symptoms, type of initial symptoms, incidence of all other symptoms except central hypoventilation, number of symptoms, ICU admission, diameter of the ovarian teratoma, pathological type of ovarian teratoma, or duration between surgery and onset between patients having no clinical improvement after surgery and patients having clinical improvement after surgery. The incidence of central hypoventilation in patients having no clinical improvement after surgery was significantly higher than those in patients having clinical improvement after surgery (100.0% vs. 29.4%, $p = 0.049$). Additionally, the mRS score at acute onset in patients having no improvement after surgery was 5.00 ± 0.00, which was higher than that in patients having clinical improvement after surgery (4.23 ± 0.90), and the difference was statistically significant ($p = 0.003$). In multivariable analysis, the factors associated with surgical outcome included central hypoventilation (OR 0.89, 95% CI 0.60-1.45, and $p = 0.021$) and mature ovarian teratoma (OR 1.39, 95% CI 0.89-1.93, and $p = 0.007$) (Table 2). The estimated regression coefficients were as follows: $\text{logit}(p) = -19.817^{*}A + 2.079^{*}B + 19.123$, where A represented the symptom of central hypoventilation, and B represented the pathological type of mature ovarian teratoma. The ROC curve revealed that the model was reliable in predicting the surgical outcome (Figure 2).

At 12-month follow-up, all of the 17 patients having clinical improvement after surgery had a good outcome (mRS ≤ 2) and no one died or relapsed. Among 3 patients having no improvement after surgery, no one had a good outcome (mRS ≤ 2). No relapse of ovarian tumor or significant changes in menstrual pattern was observed in the 20 patients who underwent surgery.

3.4. Pathological Findings. Seventeen of the 20 patients' (85.0%) histological types were reported to be mature ovarian teratoma, and the other 3 (15.0%) were reported to be immature ovarian teratoma. We performed immunohistochemical tests for 8 of the 20 patients' teratoma tissues. The result revealed that all 8 samples were positive for MAP2, a specific

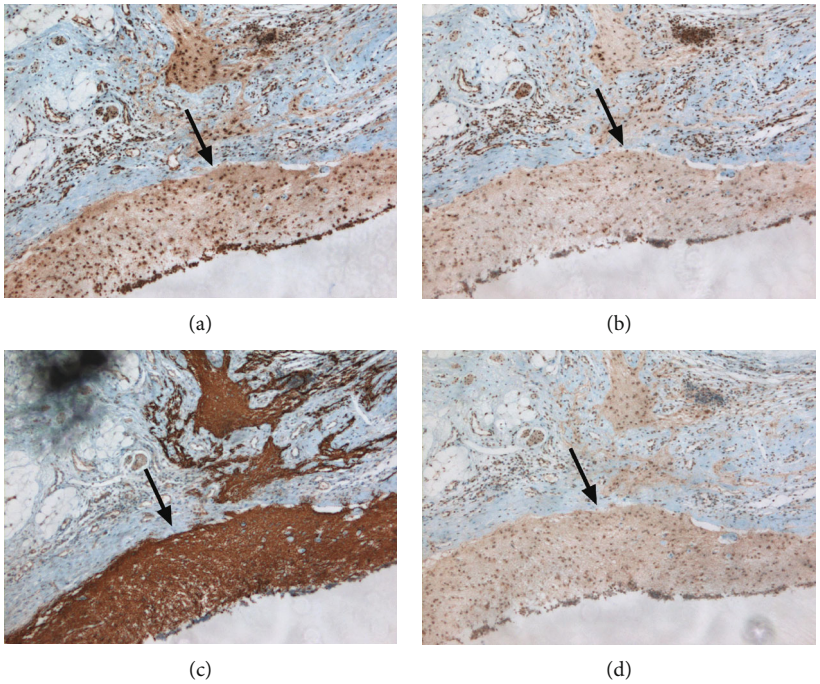

Figure 3: Representative immunohistochemical features. Densely aggregated neurons (the black arrow) were positive for (a) MAP2, (b) NDMAR1, (c) NDMAR2A, and (d) NDMAR2B (a–d, ×40).

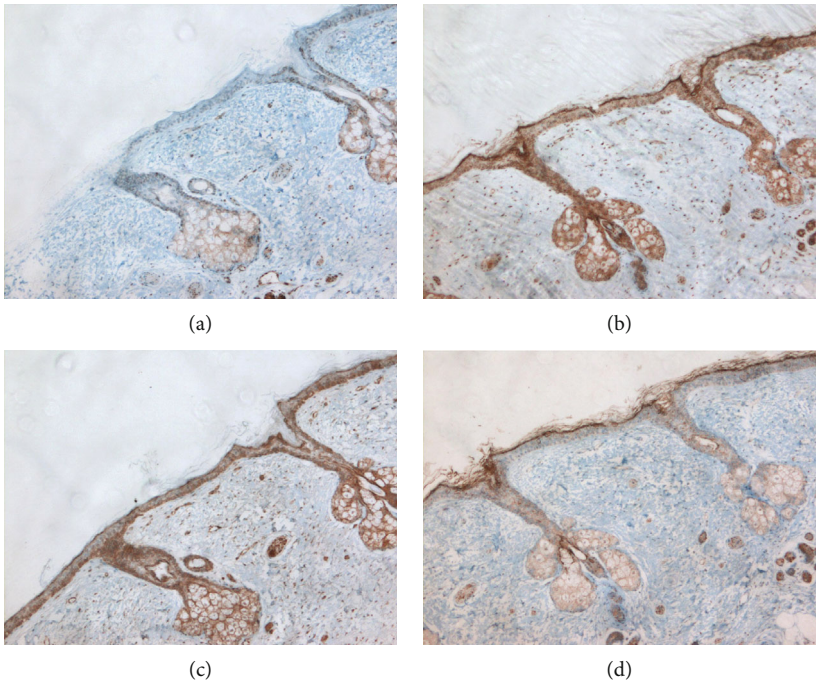

Figure 4: Representative immunohistochemical features. Sebaceous glands and squamous epithelial tissue were found in the tissue and were negative for (a) MAP2, strongly positive for (b) NMDAR1 and (c) NDMAR2A, and weakly positive for (d) NMDAR2B (a–d, ×40).

marker of mature neurons, and the same areas were also positive for NDMAR1, NMDAR2A, and NMDAR2B (Figure 3). Among which, 3 patients' ovarian teratomas also showed positive for NDMAR1, NMDAR2A, and NMDAR2B in the sebaceous glands and squamous tissues (Figure 4).

4. Discussion

This retrospective study demonstrates that patients with anti-NMDAR encephalitis with ovarian teratoma tend to present more neuropsychiatric symptoms than gynecological

symptoms. The disease incidence is higher during autumn and winter. Most patients get clinical improvement after surgery. The central hypoventilation symptom and mature ovarian teratomas are associated with surgical outcome. Partial cases also contain large number of NMDAR-positive sebaceous glands and squamous tissues.

The mean age of the patients in this study was consistent with other studies [5]. The youngest patient in our study was 15 years old. Leel et al. reported the youngest patient with anti-NDMAR encephalitis with ovarian teratoma, who was just 7 years old [7]. So it suggests that there is a need to conduct ovarian tumors screening for female patients of all ages.

Several autoimmune diseases are known to have well-established seasonal variation. The incidence of acute gouty attacks is highest in the spring. The onset or exacerbation of rheumatoid arthritis and Wegener's granulomatosis are all seen more commonly in the winter [8]. However, there were few studies focused on the onset season of anti-NDMAR encephalitis. Adang et al. [9] revealed that anti-NDMAR encephalitis without tumor were more common in warm months (April-September) (18/23, 78%), whereas anti-NDMAR encephalitis with tumors presented during cold months (6/6,100%). Our study revealed that the onset of anti-NMDAR encephalitis with ovarian teratoma was more commonly in autumn and winter, which was the same with the current study. As the samples of both studies are limited, we still need a larger-scale study to determine whether anti-NMDAR encephalitis has seasonal variation or not.

Our data revealed that most patients presented psychiatric abnormalities as initial symptom, which was consistent with previous studies [10–12]. As to the gynecological symptoms, only one patient had lower abdominal pain. It revealed that it is important to screen tumors with imaging methods for all anti-NMDAR encephalitis patients. Ultrasound is the first choice to screen ovarian teratoma, and transvaginal ultrasound is more sensitive than transabdomial ultrasound [13]. CT or MRI has a higher sensitivity in detecting teratomas, compared to that of ultrasound [14]. However, ultrasound has many advantages, like the lower cost, shorter examination time, and convenience for the patients with serious conditions. In some cases of anti-NMDAR encephalitis, whose screening revealed no specific clue for ovarian teratoma, an occult teratoma was found by histological examination after laparoscopy examination and ovariectomy [15]. However, we could only conduct laparoscopic exploration for patients with detection of ovarian teratoma by imaging examination, because of ethical considerations.

The seropositive rate of anti-thyroid autoimmune antibodies in our study was 47.6%, which was higher than that of limbic encephalitis patients (33%) and the general population(10-15%) [16, 17]. Study found that anti-NMDAR encephalitis patients with seropositive anti-thyroid antibodies had a higher mRS score [18], but the relevant mechanism remains to be studied.

The role of B cells in the autoimmunity of anti-NMDAR encephalitis has become increasingly prominent [19–21]. Recently, the effect of vitamin D on immune cells has gradually gained attention [22, 23]. Vitamin D suppresses the proliferation and differentiation of B cells, resulting in a reduction of immunoglobulin secretion [24]. Our data found that the levels of 25-hydroxyvitamin D of most patients with anti-NMDAR encephalitis with teratoma were significantly lower than normal. It suggests that 25-hydroxyvitamin D may be an index to reflect the disease severity, which needs further study to confirm.

Early treatment and a lack of ICU admission are reported predictors of good outcome [4]. In our studies, the proportion of ICU admission was higher for patients having clinical improvement after surgery than that of the patients having improvement after surgery, but the difference had no statistical significance. Our findings suggested that the central hypoventilation symptom and mature ovarian teratomas were associated with surgical outcome of patients with anti-NMDAR encephalitis and ovarian teratoma.

Teratoma may contain tissues from all three germ layers, including ectoderm, mesoderm, and endoderm, and it can be either mature or immature. Bost et al. [25] reported that 11.8% of ovarian teratoma was immature in patients with anti-NMDAR encephalitis, which was associated with a higher risk of death. Patients with immature ovarian teratoma accounted for 10.0% in our study, but they did not present a higher mRS score or worse prognosis. In our study, all teratomas contained neural tissue, and immunohistochemical analysis confirmed that NMDAR expressed in the neural tissues, besides that NMDAR also expressed in the sebaceous glands and squamous tissue. As some patients' teratomas lack neural tissue and the majority of the teratomas are composed of skin, we speculate that encephalitis development in some patients may result from NMDAR expression in sebaceous glands and squamous epithelial tissues.

There were a few limitations in this study. First, this was a retrospective study and bias was inevitable. Second, our data only focused on the pathological results of ovarian teratoma in patients with anti-NMDAR encephalitis. Next, we plan to explore and compare the pathological features of teratomas in patients without anti-NDMAR encephalitis.

5. Conclusion

In summary, this study confirms that the disease incidence is higher during autumn and winter. Most patients get clinical improvement after surgery. The central hypoventilation symptom and mature ovarian teratomas are associated with surgical outcome. Systemic complications, such as pulmonary infection and respiration failure, should not be looked as surgical contraindications. We hope that our study can attract gynecologists and anesthesiologists' attention to the importance and necessity of early resection of tumors.

Data Availability

The data used to support the findings of this study are included within the article.

Conflicts of Interest

The authors declare that there is no conflict of interest regarding the publication of this paper.

Acknowledgments

This work was supported by Wu Jieping Fund Medical Association (No. 320.6755.15012).

References

[1] J. Dalmau, E. Tüzün, H. Y. Wu et al., "Paraneoplastic anti-N-methyl-D-aspartate receptor encephalitis associated with ovarian teratoma," *Annals of Neurology*, vol. 61, no. 1, pp. 25–36, 2007.

[2] J. Dalmau, T. Armangué, J. Planagumà et al., "An update on anti-NMDA receptor encephalitis for neurologists and psychiatrists: mechanisms and models," *Lancet Neurology*, vol. 18, no. 11, pp. 1045–1057, 2019.

[3] J. Dalmau, E. Lancaster, E. Martinez-Hernandez, M. R. Rosenfeld, and R. Balice-Gordon, "Clinical experience and laboratory investigations in patients with anti-NMDAR encephalitis," *Lancet Neurology*, vol. 10, no. 1, pp. 63–74, 2011.

[4] M. J. Titulaer, L. McCracken, I. Gabilondo et al., "Treatment and prognostic factors for long-term outcome in patients with anti- NMDA receptor encephalitis: an observational cohort study," *Lancet Neurology*, vol. 12, no. 2, pp. 157–165, 2013.

[5] Y. Dai, J. Zhang, H. Ren et al., "Surgical outcomes in patients with anti-N-methyl D-aspartate receptor encephalitis with ovarian teratoma," *American Journal of Obstetrics and Gynecology*, vol. 221, no. 5, pp. 485.e1–485.e10, 2019.

[6] N. Gresa-Arribas, M. J. Titulaer, A. Torrents et al., "Antibody titres at diagnosis and during follow-up of anti-NMDA receptor encephalitis: a retrospective study," *Lancet Neurology*, vol. 13, no. 2, pp. 167–177, 2014.

[7] N. Leel, H. S. Thakkar, D. Drake, and N. Bouhadiba, "Ovarian teratoma associated with anti-NMDA (N-methyl D-aspartate) receptor encephalitis," *BMJ Case Reports*, vol. 2018, p. 3, 2018.

[8] N. Schlesinger and M. Schlesinger, "Seasonal variation of rheumatic diseases," *Discovery Medicine*, vol. 5, no. 25, pp. 64–69, 2005.

[9] L. A. Adang, D. R. Lynch, and J. A. Panzer, "Pediatric anti-NMDA receptor encephalitis is seasonal," *Annals of Clinical Translational Neurology*, vol. 1, no. 11, pp. 921–925, 2014.

[10] X. Liu, B. Yan, R. Wang et al., "Seizure outcomes in patients with anti-NMDAR encephalitis: a follow-up study," *Epilepsia*, vol. 58, no. 12, pp. 2104–2111, 2017.

[11] S. Sartori, M. Nosadini, E. Cesaroni et al., "Paediatric anti-N-methyl-D-aspartate receptor encephalitis: the first Italian multicenter case series," *European Journal of Paediatric Neurology*, vol. 19, no. 4, pp. 453–463, 2015.

[12] M. J. Titulaer and J. Dalmau, "Seizures as first symptom of anti-NMDA receptor encephalitis are more common in men," *Neurology*, vol. 82, no. 7, pp. 550-551, 2014.

[13] S. Campbell and A. Gentry-Maharaj, "The role of transvaginal ultrasound in screening for ovarian cancer," *Climacteric*, vol. 21, no. 3, pp. 221–226, 2018.

[14] M. Saleh, P. Bhosale, C. O. Menias et al., "Ovarian teratomas: clinical features, imaging findings and management," *Abdominal Radiology*, 2021.

[15] A.-L. Boeck, F. Logemann, T. Krauß et al., "Ovarectomy despite negative imaging in anti-NMDA receptor encephalitis: effective even late," *Case Rep Neurol Med*, vol. 2013, article 843192, 3 pages, 2013.

[16] H. Pruss, J. Dalmau, L. Harms et al., "Retrospective analysis of NMDA receptor antibodies in encephalitis of unknown origin," *Neurology*, vol. 75, no. 19, pp. 1735–1739, 2010.

[17] C.-L. Xu, L. Liu, W.-Q. Zhao et al., "Anti-N-methyl-D-aspartate receptor encephalitis with serum anti-thyroid antibodies and IgM antibodies against Epstein-Barr virus viral capsid antigen: a case report and one year follow-up," *BMC Neurology*, vol. 11, 2011.

[18] Y. Lin, S. Tan, Y. Wang et al., "Anti-thyroid antibodies and thyroid function in anti-N-methyl-d-aspartate receptor encephalitis," *Neurochemistry International*, vol. 113, pp. 107–111, 2018.

[19] J.-P. Camdessanché, N. Streichenberger, G. Cavillon et al., "Brain immunohistopathological study in a patient with anti-NMDAR encephalitis," *European Journal of Neurology*, vol. 18, no. 6, pp. 929–931, 2011.

[20] Y. Hachiya, A. Uruha, E. Kasai-Yoshida et al., "Rituximab ameliorates anti-N-methyl-D-aspartate receptor encephalitis by removal of short-lived plasmablasts," *Journal of Neuroimmunology*, vol. 265, no. 1-2, pp. 128–130, 2013.

[21] E. Martinez-Hernandez, J. Horvath, Y. Shiloh-Malawsky, N. Sangha, M. Martinez-Lage, and J. Dalmau, "Analysis of complement and plasma cells in the brain of patients with anti-NMDAR encephalitis," *Neurology*, vol. 77, no. 6, pp. 589–593, 2011.

[22] A. Caraba, V. Crişan, I. Romoşan, I. Mozoş, and M. Murariu, "Vitamin D status, disease activity, and endothelial dysfunction in early rheumatoid arthritis patients," *Disease Markers*, vol. 2017, Article ID 5241012, 7 pages, 2017.

[23] M. G. Petruzzelli, L. Marzulli, F. Margari et al., "Vitamin D deficiency in autism spectrum disorder: a cross-sectional study," *Disease Markers*, vol. 2020, Article ID 9292560, 5 pages, 2020.

[24] A. Boonstra, F. J. Barrat, C. Crain, V. L. Heath, H. F. J. Savelkoul, and A. O'Garra, "1alpha,25-dihydroxyvitamin d3 has a direct effect on naive $CD4^+$ T cells to enhance the development of Th2 cells," *Journal of Immunology*, vol. 167, no. 9, pp. 4974–4980, 2001.

[25] C. Bost, E. Chanson, G. Picard et al., "Malignant tumors in autoimmune encephalitis with anti-NMDA receptor antibodies," *Journal of Neurology*, vol. 265, no. 10, pp. 2190–2200, 2018.

Hindawi
Disease Markers
Volume 2021, Article ID 6662938, 5 pages
https://doi.org/10.1155/2021/6662938

Research Article

Personalized Prechemotherapy Education Reduces Peri-Chemotherapy Anxiety in Colorectal Cancer Patients

Shasha Li,[1] Lihong Li,[2] Xin Shi,[1] Mingshu Wang,[1] Xiaoli Song,[1] and Feng Cui[1]

[1]*Department of Oncology, 2nd Affiliated Hospital of Harbin Medical University, No. 246 Xuefu Rd, Harbin 150086, China*
[2]*Department of Urology, 2nd Affiliated Hospital of Harbin Medical University, China*

Correspondence should be addressed to Shasha Li; lishasha2727@163.com

Received 29 December 2020; Revised 26 February 2021; Accepted 6 March 2021; Published 3 May 2021

Academic Editor: Zhongjie Shi

Objective. To evaluate the effect of personalized prechemotherapy education in the reduction of peri-chemotherapy anxiety in patients with colorectal cancer. *Methods*. Patients admitted to the Department of Oncology with a diagnosis of stage III or IV colorectal cancer and scheduled for initial chemotherapy from January 1, 2017, to June 30, 2019, were retrieved. Patients in the educated group completed the GAD-7 form to evaluate their anxiety level at admission and 14 days after personalized prechemotherapy education, the educator team of which included both physician and nurse staff. Patients in the control group only completed GAD-7 forms at admission and 14 days thereafter without personalized education. *Results*. Three hundred and sixty-four patients were enrolled for analysis, including 127 patients who received personalized prechemotherapy education and 237 patients who did not receive education. There were no significant differences in age, gender, education level, or pretreatment GAD-7 scores between the two groups, but significantly lower posttreatment GAD-7 score, and fewer medium to severe posttreatment anxiety patients in the educated group. *Conclusion*. Personalized prechemotherapy education involving physician for medical treatment and nursing staff for peri-treatment care, in contrast to traditional brief discussion with physicians during clinic visits and unified informed consent before treatments, may reduce peri-chemotherapy anxiety more efficiently.

1. Introduction

According to data from 2012 to 2016, the new cases of colorectal cancer (CRC) were 38.6 per 100,000 men and women per year [1]. The overall percent of CRC patients surviving 5 years is 64%, ranging from an early stage of 90% to a late stage of 14% [2]. While the incidence rate of CRC had been dropping by 3.6% each year from 2007 to 2016 in population aged 55 and above, it rose by 2% each year in the younger population [2]. The prolonged 5-year survival and extended younger age of incidence make it important to keep the surviving CRC patients healthy both physically and psychologically.

Anxiety is a commonly seen psychological response to stressful situations including diseases. The existence of peri-treatment anxiety in CRC patients receiving surgeries and/or chemotherapies and the influence of peri-treatment anxiety on life quality, as well as factors in the development of peri-treatment anxiety have been shown [3].

Chemotherapy is a major treatment for patients with advanced colorectal cancer [4]. However, only one study showed reduction of peri-treatment anxiety by pretreatment education with a controlled design, which mixed different treatment methods and patients with different stages of CRC [5]. In the present study, we evaluated the effect of personalized prechemotherapy education in the reduction of peri-chemotherapy anxiety in late stage CRC patients.

2. Methods

The study protocol was approved by the institutional ethical committee. Informed consent for anonymous participation in this study and future publication was obtained from patients.

Starting from January 1st, 2017, our institution has been advocating for personalized patient education. However, there were still quite a lot of admitted patients who did not receive such education due to the availability of clinical staff. Patients admitted to the Department of Oncology with a diagnosis of CRC [6] and scheduled for initial chemotherapy from December 1, 2017, to November 30, 2019, were retrieved. Exclusion criteria were cases received any previous chemotherapy treatment or cases complicated with other cancers or cases with clinically diagnosed psychological problems before the diagnosis of CRC or concurrent medications such as benzodiazepines, serotonin reuptake inhibitors, or other antidepressants or neuropathic pain medication.

The Chinese version of generalized anxiety disorder 7-item scale (GAD-7) [7] was employed to evaluate patients' anxiety level at admission and 14 days after personalized prechemotherapy education during follow-up visits. Individual personalized prechemotherapy education was given by a team consisted of both physician and nurse staff and covered the development, diagnosis, treatment choices, and prognosis of CRC in plain language, as well as the prechemotherapy preparation and postchemotherapy care based on previous studies [8–10]. Useful experience from anonymous previous patients who received similar chemotherapy was discussed. Patients' specific concerns were also discussed during the education session. Patients in the control group completed GAD-7 forms at admission and the 14 days follow-up visits but did not receive dedicated personalized prechemotherapy education. Patients in both groups were free to discuss their disease with physicians during clinic visits and after admission and had informed consent about their treatment plans.

2.1. Statistics. Categorical data were expressed as number of cases and analyzed using χ^2-test. Continuous data were shown as mean ± standard deviation (SD) and were analyzed using Student's t-test. Prediction equations for preeducational and postchemotherapy anxiety were obtained using logistic regression. SPSS24.0 (IBM Corp, Armonk, NY) was used for statistical analysis. A two-tailed $p < 0.05$ was considered significantly different.

3. Results

There were 1044 patients admitted to the Department of Oncology due to CRC during the study period, and complete data were available from 364 patients who met the inclusion criteria (Figure 1). One hundred and twenty-seven CRC patients received personalized prechemotherapy education, while the rest 237 patients did not. There were no significant differences in age, gender, or education level between the two groups (Table 1, $p > 0.05$). There were no differences in preeducational GAD-7 score or the number of medium to severe anxiety (GAD-7 score above 9) patients before education between the prechemotherapy educated and noneducated groups (Table 1, $p > 0.05$), but significantly lower postchemotherapy GAD-7 score, and fewer medium to severe anxiety patients after chemotherapy in the prechemotherapy educated group (Table 1, $p < 0.01$). There was a significant reduction in postchemotherapy GAD-7 score in the prechemotherapy educated group (Table 1, $p < 0.01$).

A prediction equation for preeducational anxiety was obtained using logistic regression based on the gender, age, and educational level of all 364 patients, with gender and education level showing significant contribution ($p < 0.05$ for both):

$$\log\left[\frac{p}{(1-p)}\right] = 0.537 + 0.338\,\text{gender} - 0.11\,\text{age} + 0.45\,\text{education level}, \tag{1}$$

where p is the probability of having moderate to severe anxiety, gender = 1 if male and =2 if female, and education level =2 if lower than secondary education and =1 if equal to or above secondary education.

A prediction equation for postchemotherapy anxiety was obtained using logistic regression based on the gender, age, and educational level of the 127 patients who received prechemotherapy education, with education level showing significant contribution ($p < 0.05$):

$$\log\left[\frac{p}{(1-p)}\right] = 0.26 + 0.422\,\text{gender} - 0.042\,\text{age} + 0.303\,\text{education level}, \tag{2}$$

where p is the probability of having moderate to severe anxiety, gender =1 if male and =2 if female, and education level = 2 if lower than secondary education and =1 if equal to or above secondary education.

Another prediction equation for postchemotherapy anxiety was obtained using logistic regression based on the gender, age, and educational level of the 237 patients who did not receive prechemotherapy education:

$$\log\left[\frac{p}{(1-p)}\right] = 1.094 + 0.132\,\text{gender} - 0.018\,\text{age} + 0.015\,\text{education level}, \tag{3}$$

where p is the probability of having moderate to severe anxiety, gender =1 if male and =2 if female, and education level =2 if lower than secondary education and =1 if equal to or above secondary education.

4. Discussion

Anxiety in CRC patients concerning treatment might arises from treatment side effects, treatment costs, time away from family, time away from work, and transportation to treatment sites [11]. Therefore, the provision of comprehensive, useful, timely, and personalized information to CRC patients is needed [12]. Nowadays, all kinds of information related to CRC therapies may come from different sources. Some may even be exaggerated advertisements. Others may be experience from specific cases that are not suitable for the general CRC population. A comprehensive personalized prechemotherapy education by doctors and nurses may systematically improve the overview of CRC patients about how to

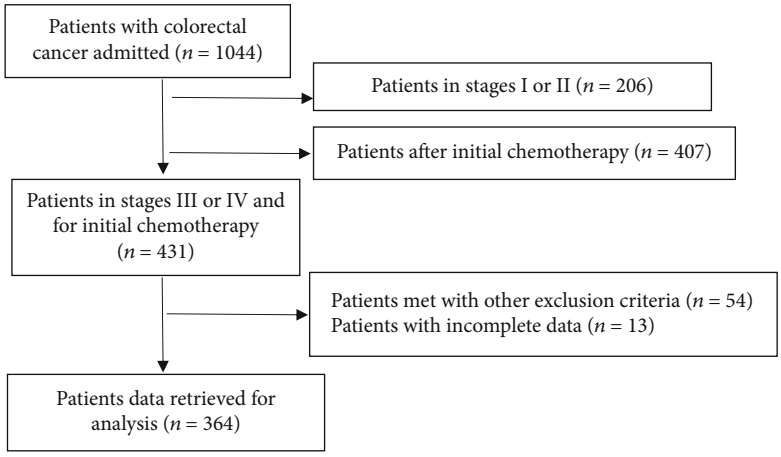

Figure 1: Flow chart of the present study.

Table 1: Clinical characteristics of enrolled patients.

Characteristics	Prechemotherapy educated (127 cases)	Not educated (237 cases)	p value (between groups)	Relative risk	95% CI
Age[&]	69.28 ± 6.68	68.09 ± 6.92	0.12*	—	—
Male[$]	84	145	0.74**	1.08	(0.92, 1.27)
Education level (≥ secondary education)[$]	46	68	0.14**	0.89	(0.77, 1.04)
Prechemotherapy GAD-7[&]	9.88 ± 3.01	10.07 ± 2.70	0.55*	—	—
Moderate to severe anxiety[$]	58	128	0.13**	0.85	(0.68, 1.06)
Postchemotherapy GAD-7[&]	6.85 ± 2.90	9.70 ± 2.16	<0.01*	—	—
Moderate to severe anxiety[$]	26	121	<0.01**	0.40	(0.28, 0.58)
p value (before vs. after education)	<0.01*	0.10*	—	—	—
Change in GAD-7[&]	−2.19 ± 1.60	−1.43 ± 0.95	<0.01*	—	—

[$]Number of patients. [&]Mean ± SD. *t-test. **χ^2 test.

deal with those potential problems, set realistic expectations, and be prepared for potential chemotherapy and postchemotherapy issues. It has been shown that anxiety begins at treatment planning and increases to high level on admission to hospital [13]. According to the modified Roy Adaptation Model in Figure 2 [14], more effort is needed in the pre- or early hospitalization of CRC patients to minimize anxiety level as well as the potential need for extra medical and care resources [15].

The involvement of nursing staff in personalized prechemotherapy patient education to reduce patients' anxiety has not been adequately reported. A literature search on February 20, 2020, using the key words of "colon rectal cancer anxiety" in PubMed produced 654 papers, whereas addition of extra key words of "nurse OR nursing" only produced 94 papers. Concerning CRC patients receiving chemotherapy, some studies have reported pretreatment education and follow-up without control groups or details of education [16], some employed web-based education with small number of patients without controls [17], some used tailored information pack according to the treatment plan [5], and some had telephone sessions nearing or after the completion of chemotherapy [18–21]. However, conversation in person might be the best option to reduce anxiety [22]. In our present study, in collaboration with physicians who concentrated on medical aspect, the nursing staff who gave instructions on chemotherapy and postchemotherapy care greatly benefited the CRC patients and effectively reduced peri-chemotherapy anxiety.

Generalized anxiety disorder (GAD) is among the most common anxiety disorders in general medical practice as well as in the general population [23]. The GAD-7 form was among the most popular scales for the measurement of GAD [24]. Other scales have been used to measure anxiety, including Hospital Anxiety and Depression Scale (HADS) [5, 16, 25]. The HADS has been used to identify both anxiety and depression in nonpsychiatric clinics and contains an Anxiety (HADS-A) and a Depression subscale (HADS-D). It has been shown that both GAD-7 and HADS-A showed AUC of adequate diagnostic accuracy and hence are applicable for GAD screening in cancer patients [26].

There are potential personal factors contributing to the level of anxiety, such as gender [23] or education level [27]. In this study, we found significant contribution of gender of female and low education level to prechemotherapy anxiety but not age. CRC patients are generally older (the mean age

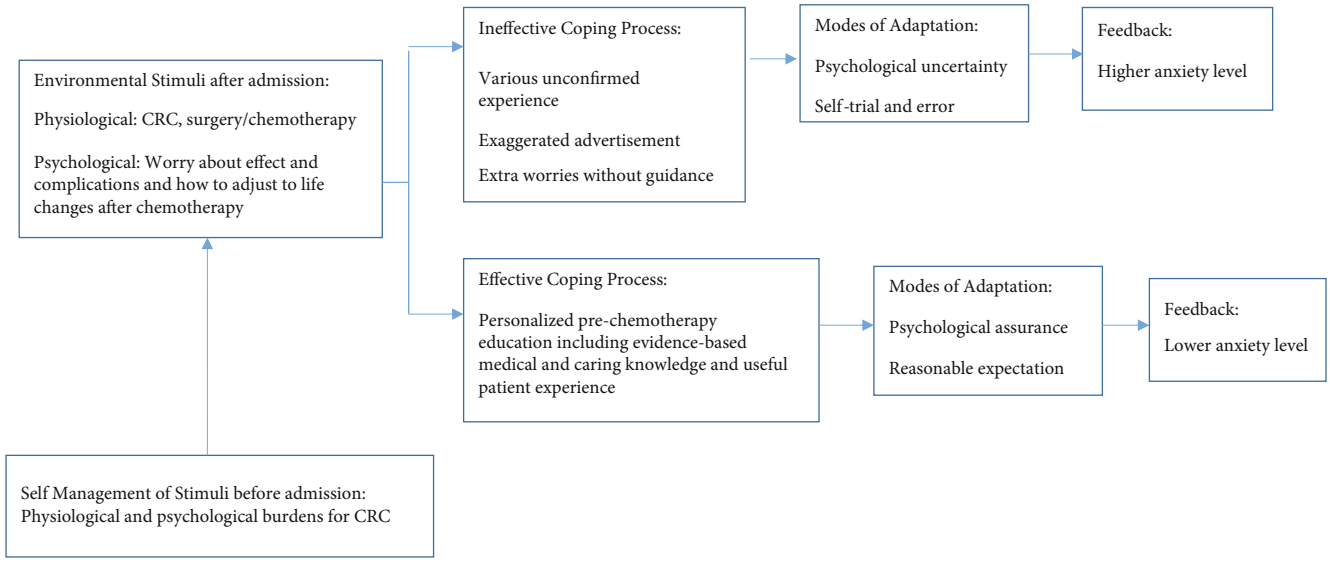

Figure 2: A revised Roy Adaptation Model in the present study.

was 68.36 years old in our study) and are more likely to miss the details of chemotherapy by brief discussions with physicians. A personalized prechemotherapy education session might be helpful for those patients to comprehensively understand and systematically memorize the chemotherapy procedures and care tips so that anxiety levels could be reduced [28].

5. Conclusions

This study was the first one to explore the effect of personalized prechemotherapy education in reducing peri-chemotherapy anxiety in CRC patients. Personalized prechemotherapy education provided in collaboration by physician and nursing staff, as well valuable experience from previous patients was beneficial in reducing peri-chemotherapy anxiety in CRC patients. Education level has an important role in the development and severity of peri-chemotherapy anxiety.

Data Availability

The data used to support the findings of this study are available from the corresponding author upon request.

Ethical Approval

This study was approved by the research ethics committee of the Second Affiliated Hospital of Harbin Medical University. This study was performed in accordance with the ethical standards as laid down in the 1964 Declaration of Helsinki and its later amendments or comparable ethical standards.

Consent

Informed consent for anonymous participation in medical study and publication was obtained from patients at admission.

Conflicts of Interest

The authors declare that they have no conflicts of interest.

Authors' Contributions

Shasha Li and Lihong Li co-first authors.

References

[1] *Cancer stat facts: colorectal cancer*March 2020, https://seer.cancer.gov/statfacts/html/colorect.html.

[2] *Colorectal cancer: statistics*March 2020, https://www.cancer.net/cancer-types/colorectal-cancer/statistics.

[3] L. S. Hoon, C. W. Chi Sally, and H. Hong-Gu, "Effect of psychosocial interventions on outcomes of patients with colorectal cancer: a review of the literature," *European Journal of Oncology Nursing*, vol. 17, no. 6, pp. 883–891, 2013.

[4] J. Jia, P. Zhang, M. Gou, F. Yang, N. Qian, and G. Dai, "The role of serum CEA and CA19-9 in efficacy evaluations and progression-free survival predictions for patients treated with cetuximab combined with FOLFOX4 or FOLFIRI as a first-line treatment for advanced colorectal cancer," *Disease Markers*, vol. 2019, Article ID 6812045, 8 pages, 2019.

[5] G. O'Connor, V. Coates, and S. O'Neill, "Randomised controlled trial of a tailored information pack for patients undergoing surgery and treatment for rectal cancer," *European Journal of Oncology Nursing*, vol. 18, no. 2, pp. 183–191, 2014.

[6] M. B. Amin, S. B. Edge, F. L. Greene et al., *AJCC Cancer Staging Manual. 8th Edition*, Springer, NewYork, NY, USA, 2017.

[7] X. Tong, D. An, A. McGonigal, S. P. Park, and D. Zhou, "Validation of the Generalized Anxiety Disorder-7 (GAD-7) among Chinese people with epilepsy," *Epilepsy Research*, vol. 120, pp. 31–36, 2016.

[8] S. Bryan and S. Dukes, "The enhanced recovery programme for stoma patients: an audit," *British Journal of Nursing*, vol. 19, no. 13, pp. 831–834, 2010.

[9] S. Chaudhri, L. Brown, I. Hassan, and A. F. Horgan, "Preoperative intensive, community-based vs. traditional stoma

education: a randomized, controlled trial," *Diseases of the Colon & Rectum*, vol. 48, no. 3, pp. 504–509, 2005.

[10] M. Jefford, K. Lotfi-Jam, C. Baravelli et al., "Development and pilot testing of a nurse-led posttreatment support package for bowel cancer survivors," *Cancer Nursing*, vol. 34, no. 3, pp. E1–E10, 2011.

[11] M. Y. Martin, M. N. Fouad, R. A. Oster et al., "What do cancer patients worry about when making decisions about treatment? Variation across racial/ethnic groups," *Supportive Care in Cancer*, vol. 22, no. 1, pp. 233–244, 2014.

[12] C. van Mossel, L. Leitz, S. Scott et al., "Information needs across the colorectal cancer care continuum: scoping the literature," *European Journal of Cancer Care*, vol. 21, no. 3, pp. 296–320, 2012.

[13] M. J. Pritchard, "Identifying and assessing anxiety in preoperative patients," *Nursing Standard*, vol. 23, no. 51, pp. 35–40, 2009.

[14] C. Roy, *The Roy Adaptation Model*, Prentice Hall Health, Upper Saddle River, NJ, 2009.

[15] D. M. Stamenkovic, N. K. Rancic, M. B. Latas et al., "Preoperative anxiety and implications on postoperative recovery: what can we do to change our history," *Minerva Anestesiologica*, vol. 84, no. 11, pp. 1307–1317, 2018.

[16] U. Polat, A. Arpacı, S. Demir, S. Erdal, and S. Yalcin, "Evaluation of quality of life and anxiety and depression levels in patients receiving chemotherapy for colorectal cancer: impact of patient education before treatment initiation," *Journal of Gastrointestinal Oncology*, vol. 5, no. 4, pp. 270–275, 2014.

[17] L. Northouse, A. Schafenacker, K. L. C. Barr et al., "A tailored web-based psychoeducational intervention for cancer patients and their family caregivers," *Cancer Nursing*, vol. 37, no. 5, pp. 321–330, 2014.

[18] P. M. Livingston, M. J. Craike, V. M. White et al., "A nurse-assisted screening and referral program for depression among survivors of colorectal cancer: feasibility study," *Medical Journal of Australia*, vol. 193, no. S5, pp. S83–S87, 2010.

[19] J. Young, J. Harrison, M. Solomon et al., "Development and feasibility assessment of telephone-delivered supportive care to improve outcomes for patients with colorectal cancer: pilot study of the CONNECT intervention," *Supportive Care in Cancer*, vol. 18, no. 4, pp. 461–470, 2010.

[20] A. L. Hawkes, S. Gollschewski, B. M. Lynch, and S. Chambers, "A telephone delivered lifestyle intervention for colorectal cancer survivors 'CanChange': a pilot study," *Psychooncology*, vol. 18, no. 4, pp. 449–455, 2009.

[21] C. L. Alter, S. B. Fleishman, A. B. Kornblith et al., "Supportive telephone intervention for patients receiving chemotherapy: a pilot study," *Psychosomatics*, vol. 37, no. 5, pp. 425–431, 1996.

[22] V. Kuzminskaitė, J. Kaklauskaitė, and J. Petkevičiūtė, "Incidence and features of preoperative anxiety in patients undergoing elective non-cardiac surgery," *Acta Medica Lituanica*, vol. 26, no. 1, pp. 93–100, 2019.

[23] R. C. Kessler, N. Brandenburg, M. Lane et al., "rethinking the duration requirement for generalized anxiety disorder: evidence from the national comorbidity survey replication," *psychological medicine*, vol. 35, no. 7, pp. 1073–1082, 2005.

[24] R. L. Spitzer, K. Kroenke, J. B. W. Williams, and B. Lowe, "A brief measure for assessing generalized anxiety disorder," *Archives of Internal Medicine*, vol. 166, no. 10, pp. 1092–1097, 2006.

[25] A. S. Zigmond and R. P. Snaith, "The hospital anxiety and depression scale," *Acta Psychiatrica Scandinavica*, vol. 67, no. 6, pp. 361–370, 1983.

[26] P. Esser, T. J. Hartung, M. Friedrich et al., "The Generalized Anxiety Disorder Screener (GAD-7) and the anxiety module of the Hospital and Depression Scale (HADS-A) as screening tools for generalized anxiety disorder among cancer patients," *Psychooncology*, vol. 27, no. 6, pp. 1509–1516, 2018.

[27] I. Bjelland, S. Krokstad, A. Mykletun, A. A. Dahl, G. S. Tell, and K. Tambs, "Does a higher educational level protect against anxiety and depression? The HUNT study," *Social Science & Medicine*, vol. 66, no. 6, pp. 1334–1345, 2008.

[28] L. Li, S. Li, Y. Sun, S. Zhang, X. Zhang, and H. Qu, "Personalized preoperative education reduces perioperative anxiety in old men with benign prostatic hyperplasia: a retrospective cohort study," *Gerontology*, pp. 1–7, 2021.

Hindawi
Disease Markers
Volume 2023, Article ID 9759372, 1 page
https://doi.org/10.1155/2023/9759372

Retraction

Retracted: Environmental and Genetic Factors in the Pathogenesis of COPD in the Road-Working Population

Disease Markers

Received 11 July 2023; Accepted 11 July 2023; Published 12 July 2023

This article has been retracted by Hindawi following an investigation undertaken by the publisher [1]. This investigation has uncovered evidence of one or more of the following indicators of systematic manipulation of the publication process:

(1) Discrepancies in scope
(2) Discrepancies in the description of the research reported
(3) Discrepancies between the availability of data and the research described
(4) Inappropriate citations
(5) Incoherent, meaningless and/or irrelevant content included in the article
(6) Peer-review manipulation

The presence of these indicators undermines our confidence in the integrity of the article's content and we cannot, therefore, vouch for its reliability. Please note that this notice is intended solely to alert readers that the content of this article is unreliable. We have not investigated whether authors were aware of or involved in the systematic manipulation of the publication process.

Wiley and Hindawi regrets that the usual quality checks did not identify these issues before publication and have since put additional measures in place to safeguard research integrity.

We wish to credit our own Research Integrity and Research Publishing teams and anonymous and named external researchers and research integrity experts for contributing to this investigation.

The corresponding author, as the representative of all authors, has been given the opportunity to register their agreement or disagreement to this retraction. We have kept a record of any response received.

References

[1] Y. Zhou, M. Wang, W. Yang et al., "Environmental and Genetic Factors in the Pathogenesis of COPD in the Road-Working Population," *Disease Markers*, vol. 2021, Article ID 9953234, 10 pages, 2021.

Hindawi
Disease Markers
Volume 2021, Article ID 9953234, 10 pages
https://doi.org/10.1155/2021/9953234

Research Article

Environmental and Genetic Factors in the Pathogenesis of COPD in the Road-Working Population

Yumin Zhou,[1] Man Wang,[2] Weiyan Yang,[2] Jianjun Li,[2] Jialin Li,[3] Yueying Hu,[2] Wei Wang,[2] Chunli Che,[2] and Hong Qi[4]

[1]*State Key Laboratory of Respiratory Disease, National Center for Respiratory Diseases, Guangzhou Institute of Respiratory Diseases, The First Affiliated Hospital of Guangzhou Medical University, Guangzhou 510120, China*
[2]*Harbin Medical University, Harbin 150010, China*
[3]*Department of Respiratory Medicine, Southern University of Science & Technology Hospital, Shenzhen 518012, China*
[4]*State Key Laboratory of Urban Water Resource and Environment, Harbin Institute of Technology, Harbin 150090, China*

Correspondence should be addressed to Chunli Che; 118402@hrbmu.edu.cn and Hong Qi; hongqi@hit.edu.cn

Received 5 March 2021; Revised 11 April 2021; Accepted 16 April 2021; Published 30 April 2021

Academic Editor: Zhongjie Shi

Background. Chronic obstructive pulmonary disease (COPD) is a typical heterogeneous condition caused by environmental and genetic risk factors. *Objectives*. We investigated extrinsic (environmental) and intrinsic (genetic) factors contributing to the development of COPD in a nonsmoker road-working population in Northeast China. *Method*. The target population was divided into a COPD group and an exposed control group. Another healthy nonroad working nonsmoker control group was also included for environmental factor comparison. Peripheral blood was collected and analyzed using inductively coupled plasma mass spectrometry for inorganic elements of PM2.5, and microarray, rt-PCR, and Multiplex ELISA for genetic factors. *Results*. Forty-three COPD road workers, thirty-nine non-COPD road workers, and 52 age and gender-matched healthy nonroad workers were enrolled. There were significantly higher levels in all 24 inorganic elements in the COPD group compared with the healthy control group except potassium and manganese, while the majority of inorganic elements were similar between the COPD group and the exposed control group except in aluminum and cobalt. There were 39 genes showing significant differences between the COPD group and the exposed control group. Collagen, type XV, alpha 1 (COL15A1), Meis homeobox 1 (MEIS1), carbonyl reductase 3 (CBR3), and amine oxidase, copper containing 3 (AOC3) were confirmed by rt-PCR to be differentially expressed. Their correlations with blood cytokines were also evaluated. *Conclusions*. Aluminum might contribute to the development of COPD in the road-working population. CBR3 and AOC3 seem expressed in different patterns than previously reported, evidenced by their correlation with proinflammatory and anti-inflammatory cytokines.

1. Introduction

Chronic obstructive pulmonary disease (COPD) is characterized by exacerbation episodes and is frequently associated with comorbid conditions [1]. The incidence, prevalence, and mortality rates of COPD remain high [2]; therefore, it is very important to identify the causes and pathogenesis of COPD. It is now clear that COPD is a typical heterogeneous condition [3]. The development and acute exacerbation of COPD are related to the short-term heavy exposure and/or long-term chronic exposure of atmospheric fine particulate matter (PM2.5) [4, 5]. We have shown that in COPD patients, the levels of components of PM2.5 in the bronchoalveolar lavage fluid (BALF) are higher than those in the blood [6]. However, it is still unclear which components of PM2.5 in the blood contribute to the pathogenesis of COPD.

Inorganic components have always been considered as the main pollutants in toxic PM, which are stable in nature, slower to decompose in the body, and the detection methods are more accurate [7]. Although our previous study detected PM2.5 in the BALF of COPD patients [6], the detection of PM2.5 component in blood samples, considering its easy access and as a confirmation of direct accumulation of PM2.5 in blood, is still rarely reported. In this study, we

Table 1: Characteristics of enrolled participants.

	Group A (43 total)	Group B (39 total)	Group C (52 total)	*P* value (A vs. B)	*P* value (A vs. C)
Age	47.2 ± 8.8	49.1 ± 8.0	46.9 ± 8.2	0.31	0.86
Gender (male)	40	35	43	0.60	0.13
Years of road work	14 ± 5.9	13 ± 5.1	—	0.42	—

investigated intrinsic (genes) and extrinsic (environmental) factors contributing to the development and exacerbation of COPD in a road-working traffic police population in Northeast China.

2. Materials and Methods

All experimental protocols in this study were approved by the Institutional Ethics Committee of the First Affiliated Hospital of Harbin Medical University, and all procedures involving human were carried out in accordance with the World Medical Association Declaration of Helsinki. Written informed consent was obtained from enrolled participants.

2.1. Sample Collection. The target population was road-working traffic police in the region who received physical examination in October 2019. Healthy volunteers engaged in nonoutdoor work who received physical examination and agreed to participate at the same time were enrolled as healthy controls (group C). The road-working participants were divided into a COPD study group (group A, the traffic police population diagnosed as COPD) and an exposed control group (group B, the traffic police population not diagnosed as COPD). Participants in groups A and B met all the following criteria: (1) continuous work as traffic police on the road for more than 5 years; (2) nonsmoking (smoking was defined as >400 cigar/year, and >1 year before the time of physical exam); (3) aged over 30 years old; and (4) no other complicated diseases, such as infection, cancer, endocrine disease, and hypertension. COPD was diagnosed according to the 2019 GOLD criteria [8]. Five ml of fasting peripheral blood samples was collected during physical examination, aliquoted, and stored in a -80°C freezer before analyses.

2.2. Determination of Inorganic Elements of PM2.5 in Blood Samples. Inorganic elements in blood samples were determined as described before [6]. Briefly, 0.5 ml of blood sample was transferred into a colorimetric tube incubated with 10% nitric acid and, sequentially, added with 1 ml of concentrated nitric acid (MOS grade), 0.5 ml of 30% hydrogen peroxide of MOS grade, and digested in water bath at 100°C for 3 h, followed by addition of 2% nitric acid of MOS grade for a total volume of 2 ml. The prepared sample was filtered, transferred to a 5 ml disposable centrifugal tube, and analyzed in an inductively coupled plasma mass spectrometry (ICP-MS, Thermo Fisher Inc., US) according to the manufacturer's manual [9].

2.3. Microarray Analysis. Half ml of blood sample from each participant in the COPD group was randomized into three subgroups ($n = 14, 14$, and 15, respectively) and, similarly, subgrouped in the exposed control group ($n = 13, 13$, and 13, respectively). Blood samples in each subgroup were mixed together and treated with Trizol (Invitrogen) for total RNA extraction, which was quantified using NanoDrop-2000 (Thermo Scientific), and the integrity was checked by Agilent Bioanalyzer 2100 (Agilent Technologies). QIAGEN RNeasy Kit was used to further purify total RNA, out of which 250 ng was used for microarray using a human Gene expression chip (LC Biotech Human lncRNA Microarray 4 × 180 K) [10, 11]. Chips were then scanned on an Agilent Scanner G5761A (Agilent Technologies), and images were analyzed with the Feature Extraction software version 12.0.3.1 (Agilent Technologies) using default parameters. Raw data were normalized in a quantile algorithm with Genespring version 14.8 (Agilent Technologies). Genes with a P value < 0.05 between the exposed COPD group and the exposed control group using t-test were candidates for Gene Ontology (GO) and Kyoto Encyclopedia of Genes and Genomes (KEGG) analyses for biological function and pathway analysis.

2.4. qRT-PCR Verification of Genes. One ml of blood sample from each participant was treated with Trizol (Invitrogen) for RNA extraction, and 50 ng of the extracted total RNA was reverse transcribed into cDNA using a reverse transcriptase cDNA synthesis kit (Toyobo, Osaka, Japan), and qPCR was performed using an Entrans 2X qPCR Probe Master Mix (ABclonal) in a CFX96 Real-Time System (BIO-RAD) according to the manufacturer's manual. Comparative quantification was assessed based on the $2^{-\Delta Ct}$ method using β-actin as control. Primers are listed in Supplementary Table 1.

2.5. Multiplex ELISA. Serum cytokine levels were measured using the Milliplex Luminex Magpix high-sensitivity immunoassay (EMD Millipore, Burlington, MA) with the human Cytokine Autoantibody panel and analyzed using Milliplex Analyst (Millipore) [12].

2.6. Statistical Analysis. Categorical variables are presented as n (%), and continuous variables as the mean ± SD. Student's t-test or Fisher's exact probability test were used to compare differences between the COPD group and the exposed control group or the healthy control group. Pearson correlation coefficient was calculated to show the correlation between genes and cytokines, where a coefficient above 0.7 or below -0.7 was considered as having a strong positive or negative correlation, respectively [13]. All statistical analyses were performed using SPSS 26.0 (Chicago, IL, USA). A two-tailed $P < 0.05$ was considered to be statistically significant.

Table 2: Inorganic component of PM2.5 in the blood of participants by ICP-MS tests.

Elements	Normal range	Measured blood elements value					No. of participants above normal range (%)				
		Group A ($n = 43$)	Group B ($n = 39$)	Group C ($n = 52$)	P (A vs. B)	P (A vs. C)	Group A ($n = 43$)	Group B ($n = 39$)	Group C ($n = 52$)	P (A vs. B)	P (A vs. C)
K (mg/mL)	3.50-5.30	3.80 ± 0.36	3.74 ± 0.33	3.77 ± 0.35	0.44	0.68	0	0	0	1	1
Al (μg/mL)	0.005-0.465	4.19 ± 0.33	3.85 ± 0.28	0.0027 ± 0.002	**<0.001**	<0.001	43 (100)	39 (100)	6 (11.54)	1	<0.001
Mg (μg/mL)	3.31-5.02	4.34 ± 1.56	4.32 ± 1.45	3.17 ± 1.54	0.95	<0.001	10 (23.26)	0	1 (1.92)	**0.001**	<0.01
Fe (mg/mL)	3.72 -6.46	4.49 ± 0.85	4.70 ± 0.69	3.07 ± 1.19	0.23	<0.001	0	0	0	1	1
Ca (μg/mL)	4.57-7.58	8.21 ± 5.81	7.79 ± 3.83	6.01 ± 2.68	0.70	0.02	25 (58.14)	15 (38.46)	3 (5.77)	0.07	<0.001
Pb (μg/mL)	0.0225-0.13	2.53 ± 2.98	2.49 ± 2.45	0.13 ± 0.11	0.94	<0.001	43 (100)	39 (100)	10 (19.23)	1	<0.001
Zn (ug/mL)	6.32-22.57	11.57 ± 7.88	11.30 ± 6.98	8.40 ± 3.29	0.87	<0.01	5 (11.62)	6 (15.38)	1 (1.92)	0.62	0.09
Ba (μg/mL)	0.002-0.218	0.49 ± 0.55	0.39 ± 0.35	0.15 ± 0.15	0.33	<0.001	43 (100)	26 (66.67)	5 (9.61)	**<0.001**	<0.001
Cu (μg/mL)	0.66-1.05	0.92 ± 0.26	0.91 ± 0.18	0.30 ± 0.02	0.84	<0.001	10 (23.26)	6 (15.38)	0	0.37	<0.001
Cr (μg/mL)	0.003-0.025	1.088 ± 0.8	0.89 ± 0.63	0.04 ± 0.01	0.22	<0.001	43 (100)	39 (100)	52 (100)	1	1
Ti (μg/mL)	0.105-0.292	4.32 ± 3.26	3.88 ± 3.03	0.032 ± 0.039	0.53	<0.001	43 (100)	39 (100)	0	1	<0.001
Mn (μg/mL)	0.008 -0.028	0.187 ± 0.35	0.13 ± 0.08	0.102 ± 0.04	0.32	0.09	43 (100)	39 (100)	6 (11.54)	1	<0.001
Rb (μg/mL)	2.12-4.46	2.45 ± 0.56	2.58 ± 0.48	2.51 ± 0.65	0.26	0.48	0	0	0	1	1
Cd (μg/mL)	0.0007-0.002	0.067 ± 0.08	0.069 ± 0.06	0.009 ± 0.02	0.90	<0.001	43 (100)	39 (100)	14 (26.92)	1	<0.001
Sr (μg/mL)	0.012-0.05	0.076 ± 0.04	0.072 ± 0.036	0.014 ± 0.037	0.64	<0.001	21 (48.83)	23 (58.85)	2 (3.85)	0.36	<0.001
Ni (μg/mL)	0.009-0.036	0.081 ± 0.074	0.062 ± 0.048	0.004 ± 0.005	0.18	<0.001	30 (69.76)	28 (71.79)	1 (1.92)	0.97	<0.001
V (μg/mL)	0.0006-0.005	0.056 ± 0.05	0.046 ± 0.04	0.001 ± 0.0006	0.32	<0.001	43 (100)	39 (100)	0	1	<0.001
Ag (μg/mL)	0.00005-0.002	0.009 ± 0.02	0.006 ± 0.007	0.0017 ± 0.001	0.38	0.01	43 (100)	39 (100)	13 (25)	1	<0.001
Se (μg/mL)	0.171-0.310	0.129 ± 0.12	0.110 ± 0.02	0.0008 ± 0.001	0.33	<0.001	1 (2.32)	0	0	1	0.45
Mo (μg/mL)	0.0005-0.004	0.008 ± 0.008	0.006 ± 0.006	0.0008 ± 0.001	0.21	<0.001	5 (11.62)	3 (7.69)	3 (5.77)	0.72	0.46
Co (μg/mL)	0.005-0.89	0.003 ± 0.002	0.002 ± 0.001	0.0002 ± 0.0001	**<0.01**	<0.001	0	0	0	1	1
Sb (μg/mL)	0.01-29.5	0.013 ± 0.007	0.013 ± 0.006	0.0002 ± 0.0001	1	<0.001	1 (2.32)	0	0	1	0.45
Tl (μg/mL)	0.001-0.50	0.001 ± 0.007	0.001 ± 0.001	0.02 ± 0.014	1	<0.001	0	0	0	1	1
As (μg/mL)	0.002-0.017	0.132 ± 0.10	0.109 ± 0.06	0.006 ± 0.006	0.22	<0.001	43 (100)	39 (100)	6 (11.54)	1	<0.001

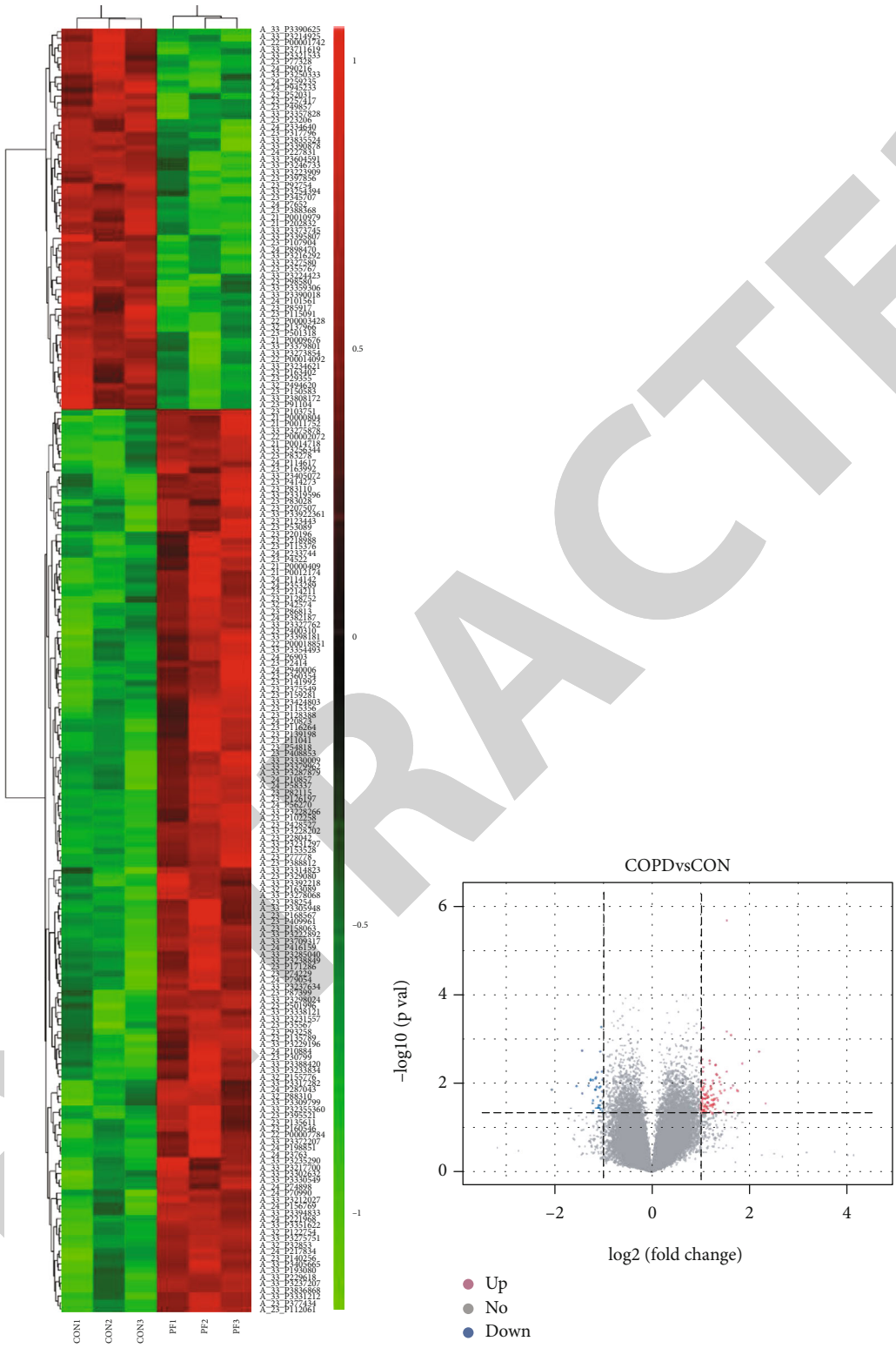

(a) (b)

Figure 1: Continued.

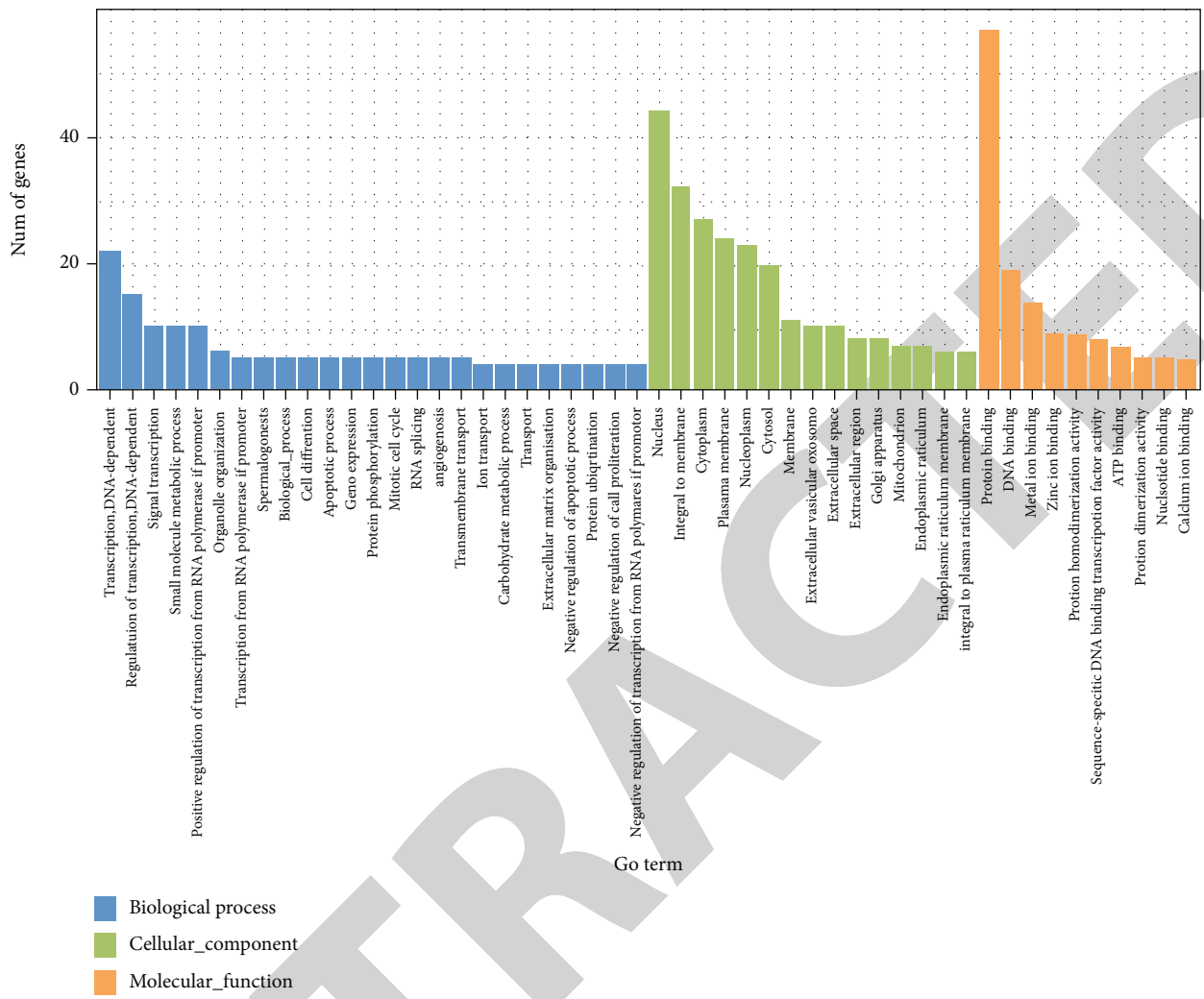

(c)

Figure 1: Continued.

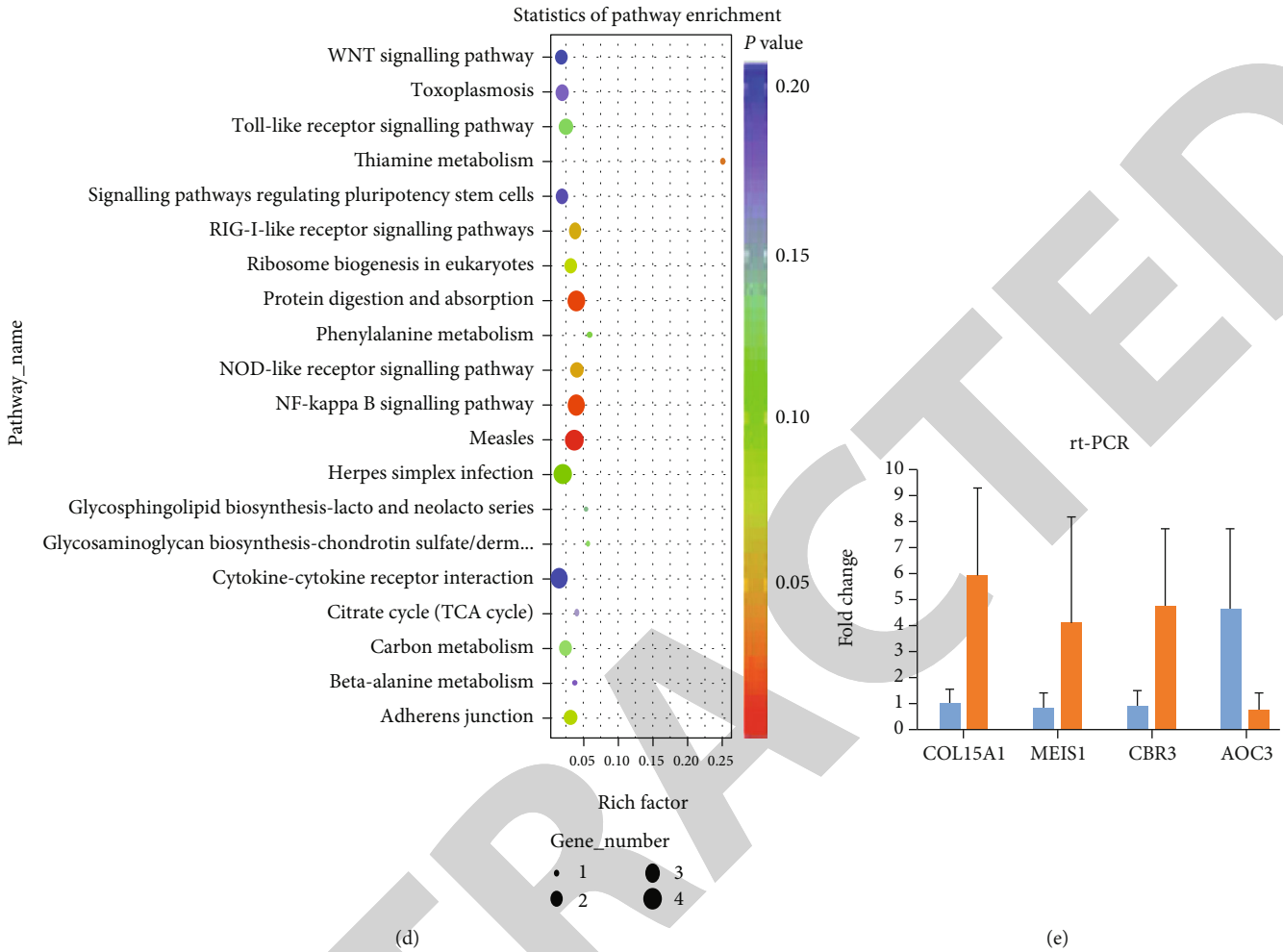

Figure 1: Microarray analysis. (a) Heatmap of sequencing result (top 200 genes). Red: increased gene level; green: decreased gene level. (b) Volcano plot of microarray results. (Blue dots were significantly decreased genes, while red dots were significantly increased genes, $P < 0.05$, respectively). (c) Bar plot of GO analysis. (d) ggplot of KEGG analysis. (e) Validation of gene expression by rt-PCR. Blue bars represent exposure control, and orange bars represent COPD cases ($n = 35$ in each group, $P < 0.05$ in all comparisons).

3. Results

There were 309 traffic police who received annual physical exam at the outpatient department of our hospital, out of which 82 participants met the inclusion criteria. Forty-three were diagnosed with COPD (group A), and 39 were without (group B). Another 52 age and gender-matched healthy non-smokers (determined by annual physical exam) who received annual physical exam and had careers unrelated to outdoor working, mining, chemical industry, or professional driver were selected as healthy controls (group C). The characteristics were shown in Table 1.

3.1. Inorganic Components of PM2.5 in Peripheral Blood. There were significantly higher levels in all 24 inorganic elements in the COPD group compared with the healthy control group except potassium and manganese, while the majority of inorganic elements were similar between the COPD group and the exposed control group except in aluminum and cobalt (Table 2), with aluminum above normal blood level.

3.2. Different Gene Expression in Peripheral Blood of COPD Patients by Microarray. The top 200 most differentially expressed genes between the COPD group and the exposed control group were shown in Figures 1(a)–1(d), and the involved pathways were also presented. There were 39 genes showing significant difference between the COPD group and the exposed control group ($P < 0.05$, Table 3).

3.3. Genes Validated by Rt-PCR. Out of the 39 genes, we found through KEGG analysis that collagen, type XV, alpha 1 (COL15A1), Meis homeobox 1 (MEIS1), carbonyl reductase 3 (CBR3), and amine oxidase, copper containing 3 (AOC3) could be candidates involved in the development of or exacerbation of COPD. We then did rt-PCR using β-actin as an internal control and confirmed that the first 3 genes were significantly upregulated and AOC3 was

Table 3: Genes showing significant changes between the COPD group and the exposure control group by microarray analysis.

Gene name	Average fold change*	SD	*P* value
ESD	5.04	1.68	2.79E-02
PRKRIR	4.60	1.67	1.90E-03
RAB3IP	3.62	1.68	3.50E-03
ARHGAP26	3.35	1.85	1.41E-02
CBR3	3.23	1.79	4.80E-02
MEIS1	3.17	1.79	1.09E-02
CEMP1	3.08	1.87	8.00E-04
TTC13	3.08	1.80	1.25E-02
EDEM3	2.95	1.80	2.71E-02
ZNF737	2.90	1.80	2.10E-06
PCDH15	2.90	1.79	6.65E-04
CARD8	2.90	1.79	5.36E-03
ZNF799	2.87	1.85	4.91E-02
SLC35F4	2.82	1.85	1.41E-02
C8orf48	2.77	1.85	4.47E-02
TMTC2	2.68	1.84	1.65E-02
NPR3	2.68	1.84	1.04E-02
LAMA1	2.63	1.89	1.47E-02
FBXW2	2.62	1.89	7.30E-03
BCKDHB	2.62	1.89	9.00E-03
SYNE1	2.59	2.04	4.71E-02
SPEF2	2.56	2.32	2.37E-02
COL15A1	2.52	2.08	2.10E-02
CDK17	2.51	2.10	6.06E-03
ZNF461	0.45	3.43	7.22E-03
TFEC	0.45	3.45	3.68E-02
NTNG1	0.45	3.49	7.70E-03
ZNF789	0.45	3.53	1.38E-02
FAM83G	0.45	3.55	1.36E-02
SCNM1	0.44	3.25	4.41E-02
TP53I11	0.44	3.07	2.38E-02
TMEM63A	0.43	2.95	8.30E-03
AOC3	0.43	2.96	2.78E-02
HAND2	0.42	1.97	8.06E-03
ZCCHC16	0.42	1.90	8.40E-03
B3GNT4	0.41	2.05	1.10E-02
FBXO25	0.37	2.12	1.80E-03
C1orf220	0.35	2.32	1.13E-02
OFD1	0.24	3.83	1.37E-02

*Compared with the exposed control group.

significantly downregulated in the COPD group compared with those of the exposed control group (Figure 1(e)).

3.4. Analysis of Different Cytokine Levels in Peripheral Blood of COPD Patients. Serum cytokine levels were measured using ELISA-based Multiplex, and the correlation between the 39 genes and 16 cytokines was shown in Figure 2. Using a coefficient above 0.7 or below -0.7 as thresholds for strong correlation, COL15A1 was positively correlated with proinflammatory cytokines IL-2 ($r = 0.86$), IL-5 ($r = 0.88$), and IFN-γ ($r = 0.74$), and conditional proinflammatory cytokine IL-6 ($r = 0.88$), while negatively correlated with proinflammatory cytokine IL-1α ($r = -0.71$). MEIS1 was positively correlated with proinflammatory cytokines IL-2 ($r = 0.85$), IL-5 ($r = 0.79$), TNF-β ($r = 0.80$), and IFN-γ ($r = 0.97$); conditional proinflammatory cytokine IL-6 ($r = 0.71$); and anti-inflammatory cytokine IL-10 ($r = 0.71$). CBR3 was positively correlated with proinflammatory cytokines IL-2 ($r = 0.78$), TNF-β ($r = 0.70$), and IFN-γ ($r = 0.71$). AOC3 was negatively correlated with proinflammatory cytokines IL-2 ($r = -0.70$), IL-12p40 ($r = -0.73$), TNF-β ($r = -0.71$), and IFN-γ ($r = -0.73$).

4. Discussion/Conclusion

Aluminum has been reported to be involved in the development of COPD [14]. In our study, there was a significantly higher level of aluminum in the blood of COPD patients compared with that of the exposed controls, suggesting that the blood level of aluminum could be a cause leading to COPD. Some studies have shown that certain components in PM2.5, such as metals and polycyclic aromatic hydrocarbons, stimulate the release of reactive oxygen species (ROS) from lung epithelial cells, which can damage cilia, increase mucus production, block airway, and lead to difficulty in breathing [15, 16].

The inflammatory response is one of the important pathogenesis of COPD. With the development of high-throughput sequencing technology, PM2.5 has been shown to affect the expression of genes. In bronchial epithelial cells collected from COPD patients, maternally expressed gene 3 (Meg3), a long noncoding RNA, is upregulated after exposure to fine PM and is negatively correlated with FEV1% [17]. It has been reported that PM2.5 can inhibit RhoA activity by overactivating PI3Kδ, causing abnormal cytoskeletal rearrangement, weakening the defective phagocytic ability of alveolar macrophages, and aggravating oxidative stress in mice with COPD [18]. Li et al. showed that after healthy young people were exposed to PM2.5 for a short period of time, genes regulating inflammation and oxidative stress were methylated [19]. The triple motif methylation of 45 (TRIM45) gene is significantly higher under high PM2.5 exposure. The target protein of this gene regulates the MAPK and NF-κB signaling pathways, which play an important role in the inflammatory response [20]. Therefore, exposure to atmospheric fine particles may affect the expression of COPD genes, and abnormal gene expression will also affect COPD, forming a vicious circle that affects the progress of COPD.

Through microarray analysis, we found 39 differentially expressed genes between the COPD and exposed control groups. Among the four rt-PCR validated genes, COL15A1 is involved in protein digestion and absorption and is identified in asthma-idiopathic pulmonary fibrosis [21]. MEIS1 is involved in signaling pathways regulating pluripotency of stem cells as well as transcriptional misregulation in cancers and is hypermethylated in COPD smokers [22]. CBR3 is

Genes\Cytokines	IL-1alpha	IL-1beta	IL-2	IL-4	IL-5	IL-6	IL-8	IL-9	IL-10	IL-12p40	IL-13	IL-17F	IL-18	TNF-alpha	TNF-beta	IFN-r
AOC3	0.47	−0.39	−0.70	−0.33	−0.61	−0.52	0.25	−0.01	t0.46	−0.73	−0.50	0.12	0.33	−0.63	−0.71	−0.73
ARHGAP26	−0.62	0.41	0.74	0.22	0.77	0.73	−0.20	0.03	0.47	0.89	0.42	−0.37	−0.10	0.75	0.62	0.70
B3GNT4	0.72	−0.42	−0.79	−0.17	−0.86	−0.82	0.01	−0.04	−0.50	−0.86	−0.31	0.39	−0.10	−0.75	−0.62	−0.71
BCKDHB	−0.65	0.30	0.89	0.21	0.76	0.73	0.28	0.04	0.49	0.61	0.18	−0.16	0.13	0.56	0.71	0.80
C1orf220	0.62	−0.40	−0.86	−0.27	−0.88	−0.82	−0.28	−0.21	−0.61	−0.67	−0.21	0.25	−0.23	−0.67	−0.72	−0.84
C8orf48	−0.51	0.41	0.78	0.33	0.77	0.66	0.34	0.19	0.60	0.48	0.21	−0.02	0.15	0.55	0.77	0.81
CARD8	−0.45	0.13	0.96	0.26	0.75	0.81	0.24	0.31	0.52	0.69	0.16	−0.41	0.13	0.57	0.63	0.88
CBR3	−0.63	0.29	0.78	0.18	0.63	0.57	0.32	−0.08	0.41	0.43	0.16	0.05	0.09	0.42	0.70	0.71
CDK17	−0.78	0.08	0.94	−0.04	0.77	0.92	0.21	0.00	0.32	0.83	0.04	−0.62	0.30	0.59	0.42	0.67
CEMP1	−0.65	0.37	0.91	0.25	0.89	0.87	0.16	0.19	0.59	0.80	0.25	−0.37	0.16	0.73	0.70	0.85
COL15A1	−0.71	0.33	0.86	0.13	0.88	0.88	0.35	0.14	0.52	0.68	0.09	−0.36	0.38	0.64	0.60	0.74
EDEM3	−0.21	0.57	0.70	0.65	0.76	0.54	−0.10	0.42	0.79	0.62	0.59	0.04	−0.30	0.72	0.94	0.96
ESD	−0.43	0.56	0.73	0.49	0.79	0.60	0.08	0.24	0.70	0.57	0.44	0.06	−0.09	0.67	0.89	0.88
FAM83G	0.46	−0.30	−0.81	−0.34	−0.62	−0.57	−0.01	−0.07	−0.49	−0.62	−0.38	0.07	0.20	−0.55	−0.76	−0.82
FBXO25	0.54	−0.43	−0.87	−0.38	−0.85	−0.76	−0.10	−0.23	−0.65	−0.73	−0.36	0.20	−0.01	−0.71	−0.81	−0.90
FBXW2	−0.38	0.19	0.90	0.35	0.68	0.68	0.10	0.26	0.53	0.66	0.29	−0.27	−0.08	0.56	0.70	0.89
HAND2	0.64	−0.25	−0.83	−0.16	−0.67	−0.69	0.05	0.05	−0.38	−0.79	−0.31	0.32	0.08	−0.61	−0.60	−0.72
LAMA1	−0.73	−0.01	0.97	−0.06	0.78	0.97	0.38	0.10	0.32	0.76	−0.09	−0.68	0.46	0.53	0.36	0.68
MEIS1	−0.27	0.36	0.85	0.51	0.79	0.71	0.08	0.47	0.71	0.67	0.38	−0.23	−0.07	0.68	0.80	0.97
NPR3	−0.54	0.42	0.86	0.35	0.86	0.77	0.24	0.25	0.65	0.64	0.26	−0.17	0.13	0.66	0.78	0.88
NTNG1	0.40	−0.57	−0.75	−0.53	−0.81	−0.63	0.15	−0.28	−0.72	−0.75	−0.57	0.08	0.25	−0.78	−0.89	−0.91
OFD1	0.35	−0.70	−0.69	−0.59	−0.92	−0.71	0.25	−0.43	−0.83	−0.85	−0.64	0.20	0.21	−0.92	−0.88	−0.91
PCDH15	−0.66	0.22	0.93	0.14	0.84	0.91	0.08	0.15	0.47	0.89	0.20	−0.57	0.16	0.71	0.56	0.79
PRKRIR	−0.69	0.11	0.96	0.08	0.72	0.82	0.22	0.01	0.37	0.74	0.11	−0.42	0.15	0.54	0.56	0.77
RAB3IP	−0.54	0.41	0.81	0.33	0.76	0.69	−0.13	0.11	0.54	0.82	0.45	−0.25	−0.17	0.72	0.74	0.82
SCNM1	0.51	−0.34	−0.66	−0.26	−0.56	−0.50	0.26	0.07	−0.38	−0.73	−0.47	0.15	0.32	−0.59	−0.63	−0.65
SLC35F4	−0.65	0.04	0.97	0.02	0.81	0.96	0.39	0.20	0.40	0.73	−0.06	−0.63	0.44	0.55	0.42	0.74
SPEF2	−0.17	0.44	0.75	0.61	0.70	0.55	−0.10	0.43	0.72	0.63	0.54	−0.05	−0.30	0.67	0.87	0.96
SYNE1	−0.68	0.29	0.83	0.13	0.79	0.78	0.46	0.09	0.49	0.52	0.03	−0.20	0.38	0.52	0.61	0.72
TFEC	0.71	−0.41	−0.85	−0.21	−0.85	−0.80	−0.17	−0.06	−0.54	−0.73	−0.25	0.25	−0.15	−0.68	−0.70	−0.78
TMEM63A	0.51	−0.15	−0.95	−0.24	−0.73	−0.76	−0.32	−0.20	−0.50	−0.60	−0.13	0.28	−0.15	−0.51	−0.66	−0.86
TMTC2	−0.50	0.36	0.82	0.35	0.69	0.60	0.15	0.10	0.55	0.55	0.32	0.00	−0.07	0.55	0.80	0.85
TP53I11	0.56	−0.35	−0.72	−0.25	−0.63	−0.58	0.20	0.05	−0.41	−0.76	−0.44	0.19	0.24	−0.63	−0.66	−0.69
TTC13	−0.33	0.12	0.91	0.31	0.75	0.82	0.08	0.44	0.55	0.77	0.23	−0.55	0.06	0.63	0.56	0.87
ZCCHC16	0.69	−0.05	−0.91	0.00	−0.68	−0.82	−0.08	0.03	−0.28	−0.83	−0.12	0.58	−0.13	−0.56	−0.42	−0.67
ZNF461	0.60	−0.35	−0.80	−0.25	−0.71	−0.67	0.11	−0.01	−0.46	−0.79	−0.40	0.25	0.15	−0.67	−0.68	−0.76
ZNF737	−0.58	0.33	0.93	0.29	0.86	0.85	0.09	0.22	0.59	0.82	0.30	−0.38	0.06	0.72	0.71	0.89
ZNF789	0.45	−0.34	−0.88	−0.34	−0.91	−0.88	−0.25	−0.44	−0.68	−0.71	−0.21	0.41	−0.25	−0.71	−0.68	−0.89
ZNF799	−0.71	0.31	0.80	0.11	0.73	0.70	0.41	−0.04	0.44	0.48	0.07	−0.09	0.28	0.48	0.64	0.69

Figure 2: Correlation between 39 genes and 16 cytokines in COPD cases by Pearson correlation coefficient ($n = 43$). On the top, anti-inflammatory cytokines were labeled in orange, while conditional anti-inflammatory cytokines were in green.

involved in the metabolism of arachidonic acid and xenobiotics by cytochrome P450 and is highly expressed in Keap knockout mice that protected Clara cells against oxidative stress ex vivo and attenuated oxidative stress and cigarette smoke-induced inflammation in vivo [23]. AOC3 is involved in the metabolism of glycine, serine, threonine, tyrosine, phenylalanine, and beta-alanine, as well as in leukocyte recirculation by oxidizes primary amines to produce hydrogen peroxide, aldehyde, and ammonia, contributing to leukocyte adhesion [24]. Thus, the increase in CBR3 and decrease of AOC3 at RNA level in the COPD group participants in our study hinted their extra roles in COPD and need further validation by proteomic studies.

Serum cytokines are involved in the development of non-smoking COPD after exposure to PM2.5 [25]. Major anti-inflammatory cytokines include IL-4, IL-10, and IL-13, whereas IL-6 is either anti-inflammatory or proinflammatory, under various conditions [26–28]. In the COPD participants in our study, CBR3 was positively correlated with proinflammatory cytokines, and AOC3 was negatively correlated with proinflammatory cytokines, which are consistent with their differentiated expression level. Although none of the participants in the present study received influenza and pneumonia vaccines during their annual physical exam, it is still interesting to note that those vaccines might not be associated with COPD [29]. Single-nucleotide polymorphisms [30, 31] and ambient PM2.5-bound organic and inorganic chemicals [32] might also be involved in the pathogenesis of COPD that warrants further investigations.

In conclusion, we found that aluminum might contribute to the development of COPD in the road-working population. CBR3 and AOC3 seem expressed in different pattern than previously reported, supported by their correlation with cytokines. Our findings provided novel insights into future studies in the development of COPD.

Data Availability

After publication, the data will be made available to others on reasonable requests to the corresponding author. Availability of data and material also need to be approved by the Institutional Ethics Committee of the First Affiliated Hospital of Harbin Medical University.

Additional Points

What is Already Known about This Subject? Chronic obstructive pulmonary disease (COPD) is a typical heterogeneous condition caused by environmental and genetic risk factors. *What Are the New Findings?* For the first time, inorganic components of PM2.5 are measured in peripheral blood. Environmental factors, such as PM2.5, and genetic factors, such as COL15A1, MEIS1, CBR3, and AOC3 genes, are involved in COPD. *How Might This Impact on Policy or Clinical Practice in the Foreseeable Future?* Regular physical examination with blood test of inorganic components of PM2.5 and occupational disease protection measures are needed in road-working population.

Ethical Approval

All experimental protocols in this study were approved by the Institutional Ethics Committee of the First Affiliated Hospital of Harbin Medical University, and all procedures

involving human were carried out in accordance with the World Medical Association Declaration of Helsinki. Written informed consent was obtained from enrolled participants.

Disclosure

The above funding sources were not involved in study design, or the collection, analysis or interpretation of data, or in the writing of the report, or in the decision to submit the article for publication.

Conflicts of Interest

The authors have no conflicts of interest to declare.

Authors' Contributions

Yumin Zhou performed the conceptualization, funding acquisition, data curation, formal analysis, methodology, and writing—original draft. Man Wang performed the conceptualization, data curation, formal analysis, methodology, and writing—review and editing. Weiyan Yang performed the data curation, formal analysis, and writing—review and editing. Jianjun Li performed the data curation, formal analysis, and writing—review and editing. Jialin Li performed the data curation, formal analysis, and writing—review and editing. Yueying Hu performed the methodology, software, and writing—review and editing. Wei Wang performed the methodology, software, and writing—review and editing. Chunli Che performed the conceptualization, funding acquisition, supervision, and writing—review and editing. Hong Qi performed the conceptualization, funding acquisition, supervision, and writing—review and editing. Yumin Zhou and Man Wang are the co-first authors.

Acknowledgments

This study was supported by the National Key Laboratory of Urban Water Resources and Water Environment Full Funds (ESK201602) and National Key Laboratory of Respiratory Diseases Fully Funds Open Project Fund (SKLRD-OP-201902).

Supplementary Materials

Sequence of primers for rt-PCR is listed in Table S1. *(Supplementary Materials)*

References

[1] C. F. Vogelmeier, G. J. Criner, F. J. Martinez et al., "Global strategy for the diagnosis, management, and prevention of chronic obstructive lung disease 2017 report. GOLD executive summary," *American Journal of Respiratory and Critical Care Medicine*, vol. 195, no. 5, pp. 557–582, 2017.

[2] "Chronic obstructive pulmonary disease," 2018, https://www.cdc.gov/copd/data.html.

[3] S. I. Rennard, "COPD heterogeneity: what this will mean in practice," *Respiratory Care*, vol. 56, no. 8, pp. 1181–1187, 2011.

[4] R. Chen, P. Yin, X. Menget al. et al., "Fine Particulate Air Pollution and Daily Mortality. A Nationwide Analysis in 272 Chinese Cities," *American Journal of Respiratory and Critical Care Medicine*, vol. 196, no. 1, pp. 73–81, 2017.

[5] M. Wang, C. P. Aaron, J. Madrigano et al., "Association between long-term exposure to ambient air pollution and change in quantitatively assessed emphysema and lung function," *JAMA*, vol. 322, no. 6, pp. 546–556, 2019.

[6] C. Che, J. Li, F. Dong et al., "Seasonal characteristic composition of inorganic elements and polycyclic aromatic hydrocarbons in atmospheric fine particulate matter and bronchoalveolar lavage fluid of COPD patients in Northeast China," *Respiratory Medicine*, vol. 171, p. 106082, 2020.

[7] Y. Y. Jia, Q. Wang, and T. Liu, "Toxicity research of PM2.5 compositions in vitro," *International Journal of Environmental Research and Public Health*, vol. 14, no. 3, p. 232, 2017.

[8] "Global initiative for chronic obstructive lung disease," https://goldcopd.org/wp-content/uploads/2018/11/GOLD-2019-v1.7-FINAL-14Nov2018-WMS.pdf.

[9] T. Cantlay, D. J. Bain, J. Curet et al., "Determining conventional and unconventional oil and gas well brines in natural sample II: cation analyses with ICP-MS and ICP-OES," *Journal of Environmental Science and Health. Part A, Toxic/Hazardous Substances & Environmental Engineering*, vol. 55, no. 1, pp. 11–23, 2020.

[10] C. Ni, Q. Fang, W. Chen et al., "Breast cancer-derived exosomes transmit lncRNA SNHG16 to induce CD73+$\gamma\delta$1 Treg cells," *Signal Transduction and Targeted Therapy*, vol. 5, no. 1, p. 41, 2020.

[11] Q. Guo, J. Wang, R. Sun et al., "Identification of circulating hub long noncoding RNAs associated with hypertrophic cardiomyopathy using weighted correlation network analysis," *Molecular Medicine Reports*, vol. 22, no. 6, pp. 4637–4644, 2020.

[12] K. B. Gordon, A. W. Armstrong, P. Foley et al., "Guselkumab efficacy after withdrawal is associated with suppression of serum IL-23-regulated IL-17 and IL-22 in psoriasis: VOYAGE 2 study," *Journal of Investigative Dermatology*, vol. 139, no. 12, pp. 2437–2446.e1, 2019.

[13] M. M. Mukaka, "Statistics corner: a guide to appropriate use of correlation coefficient in medical research," *Malawi Medical Journal*, vol. 24, no. 3, pp. 69–71, 2012.

[14] P. D. Blanc, I. Annesi-Maesano, J. R. Balmes et al., "The occupational burden of nonmalignant respiratory diseases. An official American Thoracic Society and European Respiratory Society statement," *American Journal of Respiratory and Critical Care Medicine*, vol. 199, no. 11, pp. 1312–1334, 2019.

[15] M. Figliuzzi, M. Tironi, L. Longaretti et al., "Copper-dependent biological effects of particulate matter produced by brake systems on lung alveolar cells," *Archives of Toxicology*, vol. 94, no. 9, pp. 2965–2979, 2020.

[16] R. Xia, N. Fang, Y. Yang, F. Xu, L. Zhang, and S. Ji, "PM2.5 promotes apoptosis of alveolar epithelial cells via targeting ROS/p38 signaling pathway and thus leads to emphysema in mice," *Minerva Medica*, 2020.

[17] B. Song, L. Ye, S. Wu, and Z. Jing, "Long non-coding RNA MEG3 regulates CSE-induced apoptosis and inflammation via regulating miR-218 in 16HBE cells," *Biochemical and Biophysical Research Communications*, vol. 521, no. 2, pp. 368–374, 2020.

[18] Z. Xu, W. Ding, and X. Deng, "PM 2.5, fine particulate matter: a novel player in the epithelial-mesenchymal transition?," *Frontiers in Physiology*, vol. 10, p. 1404, 2019.

Hindawi
Disease Markers
Volume 2023, Article ID 9839325, 1 page
https://doi.org/10.1155/2023/9839325

Retraction

Retracted: Introducing V-Line as a New Strategy to Choose Surgical Corridor in Oblique Lumbar Interbody Fusion at the L5-S1 Segment

Disease Markers

Received 11 July 2023; Accepted 11 July 2023; Published 12 July 2023

This article has been retracted by Hindawi following an investigation undertaken by the publisher [1]. This investigation has uncovered evidence of one or more of the following indicators of systematic manipulation of the publication process:

(1) Discrepancies in scope
(2) Discrepancies in the description of the research reported
(3) Discrepancies between the availability of data and the research described
(4) Inappropriate citations
(5) Incoherent, meaningless and/or irrelevant content included in the article
(6) Peer-review manipulation

The presence of these indicators undermines our confidence in the integrity of the article's content and we cannot, therefore, vouch for its reliability. Please note that this notice is intended solely to alert readers that the content of this article is unreliable. We have not investigated whether authors were aware of or involved in the systematic manipulation of the publication process.

Wiley and Hindawi regrets that the usual quality checks did not identify these issues before publication and have since put additional measures in place to safeguard research integrity.

We wish to credit our own Research Integrity and Research Publishing teams and anonymous and named external researchers and research integrity experts for contributing to this investigation.

The corresponding author, as the representative of all authors, has been given the opportunity to register their agreement or disagreement to this retraction. We have kept a record of any response received.

References

[1] W. Zhang, X. Du, Y. Zhu et al., "Introducing V-Line as a New Strategy to Choose Surgical Corridor in Oblique Lumbar Interbody Fusion at the L5-S1 Segment," *Disease Markers*, vol. 2021, Article ID 5584372, 9 pages, 2021.

Hindawi
Disease Markers
Volume 2021, Article ID 5584372, 9 pages
https://doi.org/10.1155/2021/5584372

Research Article

Introducing V-Line as a New Strategy to Choose Surgical Corridor in Oblique Lumbar Interbody Fusion at the L5-S1 Segment

Wei Zhang, Xing Du, Yong Zhu, Wei Luo, Ben Wang, Guanyin Jiang, and Yunsheng Ou

Department of Orthopedics, The First Affiliated Hospital of Chongqing Medical University, YouYi Road 1#, YuZhong District, Chongqing 400016, China

Correspondence should be addressed to Yunsheng Ou; ouyunsheng2001@163.com

Received 7 January 2021; Revised 23 March 2021; Accepted 5 April 2021; Published 22 April 2021

Academic Editor: Dong Pan

Purpose. A retrospective imaging study assessing the availability of oblique lumbar interbody fusion at the level of L5-S1 (OLIF51) and to choose ideal surgical corridor in OLIF51 by introducing V-line. *Methods*. The axial views through the center of L5-S1 disc were reviewed. We adopt 18 mm as the width of the simulated surgical corridor. The midline of the surgical corridor is at the center of L5-S1 disc. According to the traction distance of the left iliac vein (LCIV) and psoas major (PM), we defined all the subjects as V (+) (traction-difficultly LCIV), V (-) (traction-friendly LCIV), P (+) (traction-difficultly PM), and P (-) (traction-friendly PM). V-line was defined as a straight line dividing equally the simulated surgical corridor. All cases were divided into 2 groups: The V-line (+) group, more than half of the LCIV region, is located in the ventral part of V-line; the V-line (-) group, more than half of the LCIV region, is located in the dorsal part of V-line. Multiple variables regressive analysis was conducted to analyze the independent risk factors of V-line (+). *Results*. V-line (+) was found in 36 (38.7%) patients and V-line (-) in 57 (61.3%). Incidence of V (+) and P (+) was 35.4% (33/93) and 30.1% (28/93), respectively. 16.1% (15/93) subjects processed V (+) and P (+) at the same time. The independent risk factor of V-line (+) were gender of male ($P = 0.034$, OR: 12.152) and medial position of LCIV ($P < 0.001$, OR: 265.085). High iliac crest was a significant independent protective factor ($P = 0.001$, OR: 0.750). *Conclusions*. Most patients were suitable for OLIF51. V-line could assess the injury risk of LCIV. For patients who are V-line (+), mainly among males having the LCIV near the midline or the iliac crest relatively low, a surgical corridor external to the LCIV should be taken into consideration.

1. Introduction

The oblique interbody fusion (OLIF), as a new type of minimally invasive technique, has good applicability at L2-L5. It has a wide range of indications including lumbar degenerative disease, spinal deformities, trauma, infections, and neoplasms [1]. This procedure has many advantages in comparison with traditional spinal posterior approach surgery. As with ALIF and LLIF, it also avoids iatrogenic injury to the paraspinal musculature and disruption of spinal canal [2]. Besides, this surgical technique allows access to the anterolateral margin of the vertebral body between the psoas major and abdominal aorta, thus reducing the lumbar plexus injury during LLIF and abdominal large vessel injury during ALIF [3]. However, its application is often impeded for severe canal stenosis, large disc herniation, or concomitant ruptured disc herniation by its characteristics of indirect decompression. Therefore, OLIF should be carefully chosen in clinical indications [4–6].

There were a few cases using OLIF of L5-S1 in recent literatures; however, it is still quite difficult to perform OLIF51 because of the risks associated with stretch of the iliac vessels and the presence of the iliac wing disturbing insertion of the cage. Silvestre et al. [7] reported 179 patients using miniopen

anterior retroperitoneal lumbar interbody fusion concluding that it is a safe approach for accessing the L2-L5 and advised using another approach for the L5-S1 due to the danger of injuring the iliac vessels.

Several studies have evaluated the size of OLIF51 surgical corridor. Capellades et al. [8] confirmed the great anatomic variability of vascular structures in the lumbosacral area, and the window is really small in 18.05% of the study population because of the venous structures overlapping the L5-S1 disc. To our knowledge, there is no study to analyze the anatomic structure at L5-S1 combined with OLIF surgical corridor, as the oblique operation channel will change many anatomical parameters.

The purpose of this study is to simulate the OLIF operation process at the L5-S1 level and then obtain anatomical data through CT image analysis, thus providing a way to evaluate the feasibility of OLIF51 and to minimize vascular complications in the preoperative planning stage.

2. Methods and Methods

2.1. Subject Characteristics. 120 consecutive patients undergoing lumbar CT examination at our hospital's Department of Radiology from 1 October 2019 to 31 December 2019 were reviewed. All subjects had a clear thin-slice CT scan. Patients who had abdominal vascular abnormalities or diseases (i.e., abdominal aortic aneurysms, Budd-Chiari syndrome, abdominal aortic dissection, and iliac artery occlusion), spinal deformity from any cause, lumbar spondylolisthesis, transitional anatomy (i.e., sacralisation of L5, or lumbarisation of S1), lumbar fracture, or a surgical history on lumbar or retroperitoneum were excluded. The CT images were obtained via PACS (Picture Archiving and Communication System) with the patient in supine position. All the radiological measurements were measured and recorded by two independent researchers, and the average value was taken as the final result. This study was approved by the institutional review board following the declaration of Helsinki principles, and informed consent was obtained from all individual participants. The whole research is being reported in line with the STROCSS criteria [9].

2.2. Surgical Simulation. The width of the OLIF cage is 18 mm (Medtronic, Inc, Minneapolis, Minnesota). As the actual operative window for OLIF is not less than the width of a cage, the author adopts 18 mm as the width of surgical corridor to simulate the operation process. The midline of surgical corridor is at the center of the L5-S1 disc, and the dorsal margin of surgical corridor is close to the left iliac crest. We assumed that the cage is inserted obliquely with the midline going through the center of the L5-S1 disc (Figure 1).

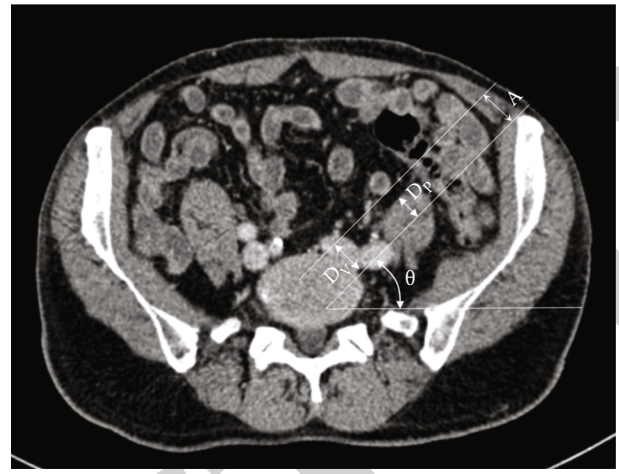

Figure 1: Illustration showing the simulated surgical corridor. The midline of surgical corridor is at the center of the L5-S1 disc and the dorsal margin of surgical corridor is close to left iliac crest. Distance A is the diameter of the surgical corridor (18 mm). D_V is the traction distance of the left iliac vein. D_P is the traction distance of the psoas major. $\boldsymbol{\theta}$ is the tilt angle of surgical corridor.

2.3. Evaluation of Vascular Parameters

2.3.1. The Left Iliac Vein Position (VP). On the axial plane of the L5-S1 disc, the area between the median line and the left edge of the intervertebral disc was equally divided into three zones. Patients were classified into three groups according to their right edge of the left iliac vein: lateral, intermediate, and medial (Figure 2).

2.3.2. The Iliocaval Junction Position (JP). We used the classification established by Capellades et al. [8]. A percentage of the distance between the inferior surface of the iliocaval junction and the center of the L4-L5 disc as well as the distance between the center of the L4-L5 disc and the center of the L5-S1 disc was calculated. Patients were classified into four groups according to their junction position: very high (iliocaval junction position less than -33.3%), high (iliocaval junction position between -33.3% and 33.3%), low (iliocaval junction position between 33.4% and 66.6%), or very low (iliocaval junction position greater than 66.7%) (Figure 3).

2.3.3. The V-Line. In the present study, we proposed a new index that can evaluate the traction distance of iliac vessels. We named this index the V-line. The "V" stands for "vessel" or "vein." We defined V-line as a straight line dividing equally the surgical corridor which we simulated before. According to the V-line, all cases were divided into 2 groups: V-line (+) group and V-line (-) group. In the V-line (+) group, more than half of the left iliac vein region is located in the ventral part of V-line, so the corridor external to the left iliac vessels leads to less traction. In the V-line (-) group, more than half of the left iliac vein region is located in the dorsal part of V-line, which indicates that a surgical corridor between the bifurcations of the iliac vessels is more optimal (Figure 4).

2.4. Quantitative Measurements. All the following parameters were analyzed and recorded in an axial plane of the center of the L5-S1 disc.

2.4.1. L5-S1 Disk Size. The anteroposterior diameter is defined as the maximal distance of the anterior and posterior border of the intervertebral disk; the left-right diameter is

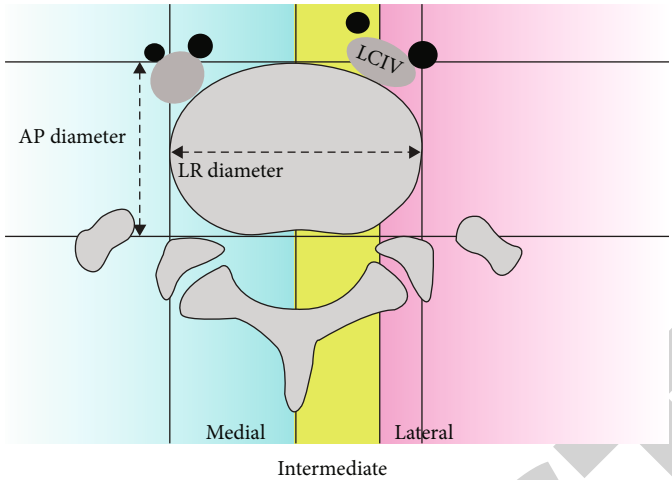

Figure 2: Diagram showing the anteroposterior diameter, the left-right diameter of L5-S1 disk, and the proposed classification for left common iliac vein positions. As shown in the figure, the left common iliac vein is classified into intermediate group.

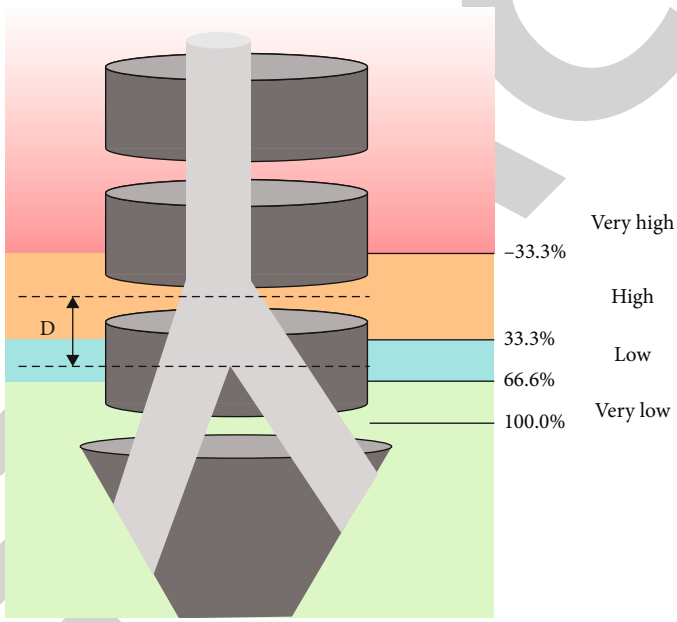

Figure 3: Diagram showing the proposed classification for iliocaval junction positions. *D* is the distance between the inferior surface of the iliocaval junction and the center of the L4-L5 disc.

defined as the maximal distance of the left and right border of the intervertebral disk (Figure 2).

2.4.2. Tilt Angle of Surgical Corridor. It is defined as the angle between the surgical corridor and the horizontal line. This parameter simulated the cage implantation angle when a patient was placed in the right lateral decubitus position (Figure 1).

2.4.3. Traction Distance of the Left Iliac Vein. It is defined as the minimum distance to retract the iliac vein out of the surgical corridor (Figure 1). The LCIV that needs to be stretched more than 9 mm were defined as V (+) (traction-difficultly LCIV) and that less than 9 mm as V (-) (traction-friendly LCIV).

2.4.4. Traction Distance of the Psoas Major. It is defined as the minimum distance to retract psoas major out of the surgical corridor. In all cases, psoas major was retracted dorsally (Figure 1). The psoas was defined as P (+) (traction-difficultly PM) and P (-) (traction-friendly PM) in the same way as LCIV.

2.5. Statistical Analysis. Continuous variables were presented as mean ± SD. χ^2 analysis was used to find a statistical difference in the left iliac vein position (VP) and the iliocaval junction position (JP) between men and women. Univariate analysis for all risk factors of V-line (+) was conducted using the 2-tailed independent Student *t*-tests for continuous variables and χ^2 or Fisher exact test for categorical variables. A multivariate logistic regression was conducted to find

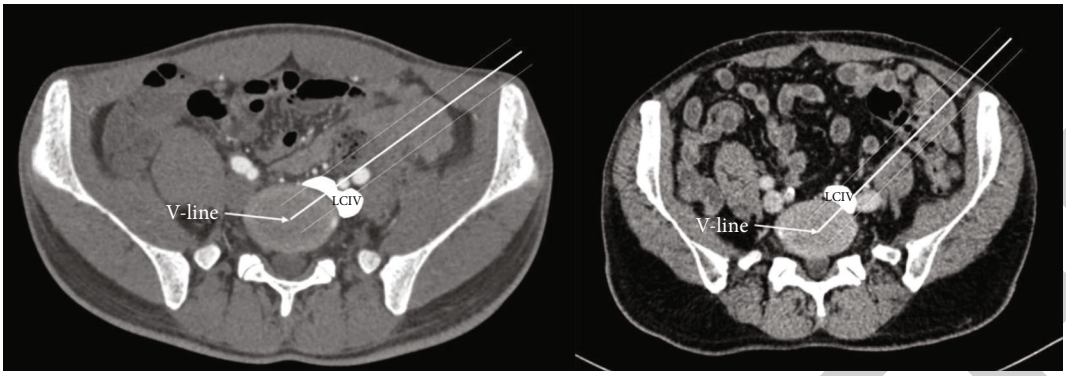

Figure 4: The diameter of the OLIF surgical corridor is 18 mm. The midline of the surgical corridor is at the center of the L5-S1 disc. Left, the V-line (-) group, more than half of the left iliac vein region is located in the dorsal part of V-line. In this situation, we could retract the LCIV dorsally. Right, the V-line (+) group, more than half of the left iliac vein region is located in ventral part of V-line. In this situation, we could retract the LCIV ventrally.

independent risk factors for V-line (+). Risk factors for V-line (+) with $P < 0.15$ by univariate analysis were included in the model. Using a forward (LR), variables with a $P < 0.10$ remained in the final model, with significant variables having $P < 0.05$. Odds ratios (OR) and 95% confidence intervals were calculated for all variables in the model. Statistical analysis was performed using SPSS 20.0 (IBM Corporation, Armonk, New York, USA).

3. Results

We accessed 93 CT data in this paper, consisting of 49 men and 44 women with a mean age of 55.80 ± 15.94 years. A total of 27 subjects were excluded—among them 10 with transitional anatomy, 7 with huge abdominal neoplasms, 5 with spinal deformity, 4 with surgical history on lumbar or retroperitoneum, and 1 with huge lumbosacral osteophyte. The subjects' other quantitative measurements are summarized in Table 1.

According to the VP classification, 35 patients (37.6%) were grouped in the lateral group, 33 patients (35.5%) in the intermediate group, and 25 patients (26.9%) in the medial group. Statistically significant difference was found between gender and the left iliac vein position. Males displayed a more medial position of LCIV.

According to the JP classification, 3 patients (3.2%) were grouped in the very high group, 39 patients (41.9%) in the high group, 38 patients (40.9%) in the low group, and 13 patients (14.0%) in the very low group. No statistically significant differences were found between gender and the iliocaval junction position (Table 2).

To evaluate precisely the ease of surgical exposure of OLIF51, the study population was classified into 4 configurations by combining traction distance of LCIV and psoas major. According to the four-configuration classification, 47 patients (50.5%) were included in P (-) V (-) group, 18 (19.4%) in P (-) V (+) group, 13 (14.0%) in P (+) V (-) group, and 15 (16.1%) in P (+) V (+) group. The P (+) V (+) group is considered not suitable for OLIF51 due to hard exposure. There were 61.3% (57/93) of the subjects that were defined as V-line (-) and 38.7% (36/93) as V-line (+) (Table 3).

Chi-square analysis or Student t-tests was used to compare gender, age, L5-S1 disk size, tilt angle of surgical corridor, sacral slope, the left iliac vein position (VP), and the iliocaval junction position (JP) in relation to the V-line. Differences were observed in tilt angle of surgical corridor, sacral slope, left iliac vein position (VP), and iliocaval junction position (JP); they were all statistically significant (tilt angle of surgical corridor, $P = 0.001$; sacral slope, $P = 0.002$; left iliac vein position, $P < 0.001$; iliocaval junction position, $P < 0.001$). The gender, age of the patient, and the L5-S1 disk size will not significantly influence the V-line (Table 1).

The multivariate analysis identified gender of male ($P = 0.034$, odds ratio [OR]: 12.152) and medial position of LCIV ($P < 0.001$, odds ratio [OR]: 265.085) as significant independent risk factors for V-line (+), while high iliac crest was a significant independent protective factor ($P = 0.001$, OR: 0.750) (Table 4).

4. Discussion

4.1. Application of OLIF51. OLIF51 is considered as minimally invasive ALIF through the oblique corridor in the lateral position [10]. It keeps the advantages of traditional ALIF with direct and extensive exposure of the intervertebral disc and avoidance of neural and muscular injury compared with the posterior approach. As a new surgical technique, OLIF51 could be described as laterally positioned ALIF, but the latter was superior to the former in many aspects [3, 11, 12]. First, it can be extended to upper levels in a single position with less mobilization of the great vessels, especially for ALIF at L4-5. Secondly, it can avoid rectus abdominis muscle injury, as well as minimize the mobilization of the peritoneal content [3]. Moreover, OLIF51 is advantageous in obese patients because gravity pulls the visceral fat away from the spine [13]. Even so, OLIF at L5-S1 is still difficult because of the risks associated with mobilization of the vessels and the presence of the iliac wing.

Many literatures have proved the practicability of OLIF51 [3, 10, 14–18]. Silvestre et al. [7] first reported OLIF51 through a retroperitoneal approach was performed successfully in 6 patients, but one patient had to be aborted

Table 1: Univariate analysis of risk factors for V-line (+) during OLIF51.

Risk factors	Patients with V-line (+), $n = 36$	Patients with V-line (-), $n = 57$	χ^2/t	P
Sex				
Female	14	30	1.672	0.196
Male	22	27		
Age	57.39 ± 14.07	54.79 ± 17.06	-0.764	0.447
L5-S1 disk AP diameter	37.66 ± 3.44	37.48 ± 3.80	-0.229	0.820
L5-S1 disk left-right diameter	55.95 ± 6.49	54.04 ± 5.21	-1.564	0.121
Tilt angle of surgical corridor	27.15 ± 10.20	34.05 ± 6.72	3.595	0.001*
Sacral slope	35.42 ± 5.34	39.44 ± 6.02	3.269	0.002*
Low iliac crest#	*22*	*21*	*5.228*	*0.022* *
High iliac crest	*14*	*36*		
The left iliac vein position (VP)				
Medial	22	3	44.570	<0.001*
Intermediate	13	20		
Lateral	1	34		
The iliocaval junction position (JP)				
Very high	8	31	23.263	<0.001*
High	16	22		
Low	0	3		
Very low	12	1		

*$P < 0.05$, #subjects were divided into low iliac crest group and high iliac crest group according to the average value of the tilt angle of surgical corridor.

Table 2: Gender differences of the left iliac vein position (VP) and the iliocaval junction position (JP).

The left iliac vein position (VP)	Female	Male	P
Medial	25 (26.9%)	5 (5.4%)	0.001*
Intermediate	33 (35.5%)	15 (16.1%)	20 (21.5%)
Lateral	35 (37.6%)	24 (25.8%)	18 (19.4%)
			11 (11.8%)
The iliocaval junction position (JP)			
Very high	3 (3.2%)	2 (2.2%)	1 (1.1%)
High	39 (41.9%)	21 (22.6%)	18 (19.4%)
Low	38 (40.9%)	17 (18.3%)	21 (22.6%)
Very low	13 (14.0%)	4 (4.3%)	9 (9.7%)

*$P < 0.05$.

Table 3: V-line and four-configuration classification system.

	P (-) V (-)	P (-) V (+)	P (+) V (-)	P (+) V (+)	Total
V-line (-)	25 (26.9%)	8 (8.6%)	9 (9.7%)	15 (16.1%)	57 (61.3%)
V-line (+)	22 (23.7%)	10 (10.8%)	4 (4.3%)	0 (0.0%)	36 (38.7%)
Total	47 (50.5%)	18 (19.4%)	13 (14.0%)	15 (16.1%)	93 (100.0%)

and switched to another operation. Woods et al. [3] retrospectively evaluated 137 patients who underwent the OLIF procedure, in which 10 patients who underwent OLIF51 only, and 84 patients who underwent OLIF25 combined with OLIF51; then, the author draws a conclusion that OLIF is a safe procedure at L1-5 as well as L5-S1. Mun et al. [19] retrospectively reviewed and compared 74 patients who underwent OLIF51 and 74 who underwent TLIF51 and concluded that OLIF51 was more effective for indirect decompression of foraminal stenosis, providing strong mechanical support. Zairi et al. [14] also showed the feasibility of accessing the L5-S1 level through the mini-open retroperitoneal approach without the need for ALIF.

4.2. OLIF51 Surgical Window. Similar to ALIF L5-S1, OLIF51 typically involves the corridor under the bifurcation of the great abdominal vessels [3]. Tribus and Belanger [20] performed a cadaveric study in 35 cadavers to examine the size

Table 4: Multivariate analysis of risk factors for V-line (+) during OLIF51.

Risk factor	Odds ratio	95% confidence interval	*P*
Sex	12.152	1.208-122.276	0.034
The left iliac vein position (VP)	265.085	16.629-4225.839	<0.001
Tilt angle of surgical corridor	0.750	0.632-0.890	0.001
Age	—	—	0.112
L5-S1 disk AP diameter	—	—	0.712
L5-S1 disk left-right diameter	—	—	0.970
Sacral slope	—	—	0.696
The iliocaval junction position (JP)	—	—	0.364

of the central window; the mean distance from the bifurcation to the top of the L5-S1 disc was 18 mm, and the mean width between the left common iliac vein and the right common iliac artery averaged 33.5 mm. In 2014, Davis et al. [21] defined the OLIF51 corridor through 2 measurements. The lateral window was the distance transversely from the midsagittal line of the inferior endplate of L-5 to the medial border of the left common iliac vessel, while the vertical window to the first vascular structure that crosses midline. The author measured the corridor diameters in 20 cadavers in a static state and with mild traction of the psoas and found that the L5-S1 corridor mean distance was 14.75 mm transversely and 23.85 mm vertically. Davis et al. concluded that the L5-S1 disc space can be accessed from an oblique angle. Oblique access to L5-S1 has also been studied through radiological measurement. Molinares et al. [22] measured that the L5-S1 corridor mean distance was 10 mm between midline and left common iliac vessel and 10.13 mm from the first midline vessel to the inferior endplate of L-5. The author found access to the L5-S1 disc established in 69% of the MR images analyzed. However, all these studies were just simple measurements of natural anatomic spaces, without considering the influence of oblique corridor on anatomical parameter. In addition, at the L5-S1 level, the psoas muscle is often lifted off the spine to leave the pelvis, which could also obstruct the surgical corridor. Our aim was to simulate the OLIF operation process at the L5-S1 level and then evaluate the feasibility of OLIF51 based on CT images. Similar studies have not been described in the literature.

4.3. Simulation of OLIF51. In our study, the author adopted 18 mm as the width of surgical corridor to simulate the operation process. We had reason to believe that traction-difficultly structure will obstruct the OLIF working corridor, and there will be excessive stretch of these structures during the procedure. More than 1/3 of the subjects (33/93, 35.5%) were grouped into traction-difficultly LCIV and nearly three in 10 (28/93, 30.1%) were grouped into traction-difficultly PM. Further analysis revealed that about one-sixth of the subjects (15/93, 16.1%) processed traction-difficultly LCIV and traction-difficultly PM at the same time. Because left common iliac vein and psoas major account for more than half of OLIF working corridor, causing difficulty in operating channel placement and increased injury risk of these structures. Therefore, we consider these subjects not suitable for OLIF51, while the P (-) V (-) group is obviously the most ideal situation. And as for the other two groups, namely, the P (-) V (+) group and P (+) V (-) group, the former gives us a large operation space for psoas major and the latter for vessel. This classification could help spine surgeons make preoperative planning and guide the surgical management.

The anatomical structure of the lumbosacral segment is complex and adjacent to the important structure. Damage to LCIV is the most threatening complication associated with OLIF51 which can be very difficult to control once injured, and mobilization of these vascular structures is often a technically demanding procedure [15, 23]. The injury to LCIV is also the most commonly complication observed in clinical practice [8, 19]. This phenomenon is caused by the low iliocaval junction positions and the medially located LCIV, reducing the size of the operating field. According to reports in the literature, the vascular injury in the early result of OLIF was 8.6%, and it increases when the L5-S1 segment is involved [3, 24]. Therefore, careful preoperative evaluation of the vascular structure is desperately needed during OLIF at L5-S1.

In 2017, Chung et al. [18] evaluated the configuration of LCIV and its risk of mobilization during anterior approach at the L5-S1 segment. They postulated the presence of perivascular adipose tissue under the LCIV, and they categorized the LCIV into three types: type I (no requirement for mobilization), type II (easy mobilization), and type III (potentially difficult mobilization). In their study, type I LCIV configuration was found in 32 (49.2%) patients, type II in 18 (27.7%), and type III in 15 (23.1%). There were 7 (10.8%) patients with LCIV injury (type I, $n = 0$; type II, $n = 2$; type III, $n = 5$) ($P = 0.003$). The result indicated that their LCIV classification system is valid for the evaluation of LCIV injury during its mobilization. However, we noted that there were still 2 patients of type II who had LCIV injury. In addition to improving surgical techniques, how could we further reduce the vascular injury at OLIF51?.

4.4. Assessment of V-Line. During the surgery, surgeons have to mobilize LCIV for surgical exposure when it obstructs the operative window on the L5-S1 disc. We could mobilize LCIV laterally choosing the central disk space between the bifurcations or stretch it medially choosing lateral disk space external to the left iliac vessels. However, which approach might reduce the risk of mobilization has not been

comprehensively studied. Previous work on the morphological characteristics of the LCIV cannot solve the problem properly. In this thesis, a new concept, V-line, is proposed for assessing the mobilization risk of these two approaches. By introducing the concept of V-line, we could qualitatively evaluate the extent of vascular traction of two approaches to guide surgical treatment.

In our work, there were 61.3% (57/93) of the subjects were defined as V-line (-). In this group, a surgical corridor between the bifurcations of the iliac vessels is more favorable which is exactly the mainstream approach in the world. One important concern with this approach is the injury to the SHP (superior hypogastric plexus), which overlies the L5-S1 disk between the bifurcations and supplies the sympathetic function for the urogenital system [25]. Consequently, damage to the SHP could result in retrograde ejaculation in male patients [26]. Careful unilateral blunt dissection of the SHP and avoidance of monopolar coagulation is recommended [3, 17]. Besides, middle sacral vessels are also important structures during this central approach; we could simply divide these vessels by the application of bipolar cautery or vascular clips.

Naturally, the rest of the subjects (36/93, 38.7%) were defined as V-line (+), in which the corridor external to the left iliac vessels is superior for less stretch of the LCIV. On this condition, particular attention should be paid to the identification and handling of the iliolumbar vein (ILV) [13]. The ILV travels laterally approximately 3-4 cm below the bifurcation and then traverses medially along the L5 vertebral body, coursing between the obturator nerve and lumbar trunks [27]. In exposing the L5-S1 level external to the LCIV, the ILV is easily avulsed due to medial traction of LCIV. Zairi et al. had gained access to the L5-S1 level by finding and clipping the ILV before retracting the iliac artery and vein anteriorly. This study considered this a safer and feasible approach [14]. Coagulation or ligation is recommended in case the ILV is identified. We could also take gentle dissection of the fat around the L5-S1 level lateral to the iliac vessels in order to obtain better recognition of the ILV.

Recently, many studies analyzing the venous anatomy in the lumbosacral area have been reported. Whether they are useful for predicting the surgical approach of OLIF51? Multiple variables regressive analysis demonstrated that gender of male, medial position of LCIV, and high iliac crest were predictive factors of V-line, while age of the patient, L5-S1 disk size, sacral slope, and iliocaval junction position (JP) were not. As to the left iliac vein position (VP), it is found that almost all subjects of the medial group were classified into the V-line (+) group and they accounted for nearly 2/3 of the V-line (+) group. In addition, the height of iliac crest is also crucial for the preoperative evaluation, there were more than half of low iliac crest group could choose an external corridor to decrease the stretch of the LCIV. However, the iliocaval junction position (JP) was not a crucial factor. A possible explanation for this is that although lower junction positions have more medial LCIV, it is not the only factor, the junction angle will affect the distribution pattern of iliac vein as well. Therefore, in the clinical practice of OLIF51, a comprehensive, detailed analysis and conventional CT examination is important to minimize the vascular injury. For patients who are V-line (+), mainly among males having the LCIV near the midline or the iliac crest relatively low, a surgical corridor external to the LCIV should be taken into consideration, and vice versa. Finally, it is worth noting that all the subjects in P (+) V (+) group were divided into V-line (-) taking almost a quarter of the V-line (-) group, indicating potential difficulties in operating procedure.

4.5. Limitations. The present research has several limitations. First, the study object of this article is patients undergoing lumbar CT examination, whose regional anatomical character in the lumbosacral area are different from those with lumbar degeneration disease. In addition, we did not include the disc height in the measurement which might change in different pathologies and impact the result of the iliocaval junction position. The second limitation concerns the patient's position, as CT images are obtained in the supine position, whereas OLIF is performed in the right lateral decubitus position, the location and configuration of LCIV and psoas major may vary [28]. Third, all the subjects in our study were Chinese; the positive rate of V-line might be different in other ethnic populations. Lastly, a high-quality prospective study is much needed to confirm the validity of this retrospective anatomical imaging study.

5. Conclusions

This study demonstrated that the majority of the patients were suitable for OLIF51 without excessive traction of the LCIV and the psoas major. There was a relatively high incidence of V-line (+) in the Asian population. Among male patients having the LCIV near the midline or the iliac crest relatively low, a surgical corridor external to the LCIV should be taken into consideration to minimize the risk of vascular injury.

6. Trial Registry Number

The study had been registered in chictr.org.cn (UIN = ChiCTR2000038598). Full detail can be accessed via http://www.chictr.org.cn/showprojen.aspx?proj=61903.

Abbreviations

LCIV: Left common iliac vein
OLIF: Oblique lumbar interbody fusion
ALIF: Anterior lumbar interbody fusion
LLIF: Lateral lumbar interbody fusion
VP: Left iliac vein position
JP: Iliocaval junction position.

Data Availability

The datasets used to support the findings of this study are available from the corresponding author upon request.

Ethical Approval

This study was approved by the institutional review board following the declaration of Helsinki principles.

Consent

Informed consent was obtained from all individual participants. The whole research is being reported in line with the STROCSS criteria.

Conflicts of Interest

The authors declare that they have no competing interests.

Acknowledgments

This article has been presented as preprint according to the following link: https://www.researchsquare.com/article/rs-118245/v1. This work was supported by the Basic Research and Frontiers Exploration Project of Yuzhong District, Chongqing (2018114) and the Science and Technology Innovation Project for Postgraduate of Chongqing Municipal Education Commission (CYS18200). All authors gratefully acknowledge the support of the subjects who participated in the present study.

References

[1] K. Phan, M. Maharaj, Y. Assem, and R. J. Mobbs, "Review of early clinical results and complications associated with oblique lumbar interbody fusion (OLIF)," *Journal of clinical neuroscience : official journal of the Neurosurgical Society of Australasia*, vol. 31, pp. 23–29, 2016.

[2] J. Allain and T. Dufour, "Anterior lumbar fusion techniques: ALIF, OLIF, DLIF, LLIF, IXLIF," *Orthopaedics & Traumatology: Surgery & Research*, vol. 106, no. 1, pp. S149–S157, 2020.

[3] K. R. Woods, J. B. Billys, and R. A. Hynes, "Technical description of oblique lateral interbody fusion at L1-L5 (OLIF25) and at L5-S1 (OLIF51) and evaluation of complication and fusion rates," *The Spine Journal*, vol. 17, no. 4, pp. 545–553, 2017.

[4] D. H. Heo and J. S. Kim, "Clinical and radiological outcomes of spinal endoscopic discectomy-assisted oblique lumbar interbody fusion: preliminary results," *Neurosurgical Focus*, vol. 43, no. 2, article E13, 2017.

[5] J. Quillo-Olvera, G. X. Lin, H. J. Jo, and J. S. Kim, "Complications on minimally invasive oblique lumbar interbody fusion at L2-L5 levels: a review of the literature and surgical strategies," *Annals of Translational Medicine*, vol. 6, no. 6, p. 101, 2018.

[6] D. S. Xu, C. T. Walker, J. Godzik, J. D. Turner, W. Smith, and J. S. Uribe, "Minimally invasive anterior, lateral, and oblique lumbar interbody fusion: a literature review," *Annals of Translational Medicine*, vol. 6, no. 6, p. 104, 2018.

[7] C. Silvestre, J. M. Mac-Thiong, R. Hilmi, and P. Roussouly, "Complications and morbidities of mini-open anterior retroperitoneal lumbar interbody fusion: oblique lumbar interbody fusion in 179 patients," *Asian spine journal*, vol. 6, no. 2, pp. 89–97, 2012.

[8] J. Capellades, F. Pellisé, A. Rovira, E. Grivé, S. Pedraza, and C. Villanueva, "Magnetic resonance anatomic study of iliocava junction and left iliac vein positions related to L5-S1 disc," *Spine (Phila Pa 1976)*, vol. 25, no. 13, pp. 1695–1700, 2000.

[9] R. Agha, A. Abdall-Razak, E. Crossley, N. Dowlut, C. Iosifidis, and G. Mathew, "STROCSS 2019 Guideline: strengthening the reporting of cohort studies in surgery," *International journal of surgery (London, England)*, vol. 72, pp. 156–165, 2019.

[10] N. Anand, A. Alayan, A. Agrawal, S. Kahwaty, E. Nomoto, and B. Khandehroo, "Analysis of spino-pelvic parameters and segmental lordosis with L5-S1 oblique lateral interbody fusion at the bottom of a long construct in circumferential minimally invasive surgical correction of adult spinal deformity," *World Neurosurgery*, vol. 130, pp. e1077–e1083, 2019.

[11] R. C. Sasso, J. Kenneth Burkus, and J. C. LeHuec, "Retrograde ejaculation after anterior lumbar interbody fusion: transperitoneal versus retroperitoneal exposure," *Spine (Phila Pa 1976)*, vol. 28, no. 10, pp. 1023–1026, 2003.

[12] B. K. Weiner, M. Walker, and R. D. Fraser, "Vascular anatomy anterior to lumbosacral transitional vertebrae and implications for anterior lumbar interbody fusion," *The Spine Journal*, vol. 1, no. 6, pp. 442–444, 2001.

[13] N. S. Chung, H. D. Lee, and C. H. Jeon, "Vascular anatomy and surgical approach in oblique lateral interbody fusion at lumbosacral transitional vertebrae," *Journal of orthopaedic science : official journal of the Japanese Orthopaedic Association*, 2020.

[14] F. Zairi, T. P. Sunna, H. J. Westwick et al., "Mini-open oblique lumbar interbody fusion (OLIF) approach for multi-level discectomy and fusion involving L5-S1: preliminary experience," *Orthopaedics & traumatology, surgery & research : OTSR.*, vol. 103, no. 2, pp. 295–299, 2017.

[15] N. S. Chung, C. H. Jeon, and H. D. Lee, "Use of an alternative surgical corridor in oblique lateral interbody fusion at the L5-S1 segment: a technical report," *Clinical Spine Surgery: A Spine Publication*, vol. 31, no. 7, pp. 293–296, 2018.

[16] K. Kanno, S. Ohtori, S. Orita et al., "Miniopen oblique lateral L5-s1 interbody fusion: a report of 2 cases," *Case reports in orthopedics*, vol. 2014, Article ID 603531, 5 pages, 2014.

[17] J. S. Kim and S. B. Sharma, "How I do it? Oblique lumbar interbody fusion at L5S1(OLIF51)," *Acta Neurochirurgica*, vol. 161, no. 6, pp. 1079–1083, 2019.

[18] N. S. Chung, C. H. Jeon, H. D. Lee, and H. J. Kweon, "Preoperative evaluation of left common iliac vein in oblique lateral interbody fusion at L5-S1," *European Spine Journal*, vol. 26, no. 11, pp. 2797–2803, 2017.

[19] H. Y. Mun, M. J. Ko, Y. B. Kim, and S. W. Park, "Usefulness of oblique lateral interbody fusion at L5-S1 level compared to transforaminal lumbar interbody fusion," *Journal of Korean Neurosurgical Society*, vol. 63, no. 6, pp. 723–729, 2020.

[20] C. B. Tribus and T. Belanger, "The vascular anatomy anterior to the L5-S1 disk space," *Spine (Phila Pa 1976)*, vol. 26, no. 11, pp. 1205–1208, 2001.

[21] T. T. Davis, R. A. Hynes, D. A. Fung et al., "Retroperitoneal oblique corridor to the L2-S1 intervertebral discs in the lateral position: an anatomic study," *Journal of Neurosurgery. Spine*, vol. 21, no. 5, pp. 785–793, 2014.

[22] D. M. Molinares, T. T. Davis, and D. A. Fung, "Retroperitoneal oblique corridor to the L2-S1 intervertebral discs: an MRI study," *Journal of Neurosurgery. Spine*, vol. 24, no. 2, pp. 248–255, 2016.

[23] N. A. Quraishi, M. Konig, S. J. Booker et al., "Access related complications in anterior lumbar surgery performed by spinal

Hindawi
Disease Markers
Volume 2021, Article ID 5522729, 15 pages
https://doi.org/10.1155/2021/5522729

Research Article

Prediction of COVID-19 with Computed Tomography Images using Hybrid Learning Techniques

Varalakshmi Perumal,[1] **Vasumathi Narayanan**,[1] **and Sakthi Jaya Sundar Rajasekar**[2]

[1]*Department of Computer Technology, MIT Campus, Anna University, Chennai, India*
[2]*Melmaruvathur Adhiparasakthi Institute of Medical Sciences and Research, Melmaruvathur, Chengalpattu District, India*

Correspondence should be addressed to Varalakshmi Perumal; varanip@gmail.com
and Sakthi Jaya Sundar Rajasekar; drsakthi03@gmail.com

Received 30 January 2021; Revised 18 March 2021; Accepted 31 March 2021; Published 22 April 2021

Academic Editor: Dong Pan

Reverse Transcription Polymerase Chain Reaction (RT-PCR) used for diagnosing COVID-19 has been found to give low detection rate during early stages of infection. Radiological analysis of CT images has given higher prediction rate when compared to RT-PCR technique. In this paper, hybrid learning models are used to classify COVID-19 CT images, Community-Acquired Pneumonia (CAP) CT images, and normal CT images with high specificity and sensitivity. The proposed system in this paper has been compared with various machine learning classifiers and other deep learning classifiers for better data analysis. The outcome of this study is also compared with other studies which were carried out recently on COVID-19 classification for further analysis. The proposed model has been found to outperform with an accuracy of 96.69%, sensitivity of 96%, and specificity of 98%.

1. Introduction

The COVID-19 virus, believed to have initially originated from the Phinolophus bat, transmitted to human beings in December 2019. Wuhan city's Huanan Seafood Market was the nerve center for the COVID-19 outbreak which spread rapidly all around the world [1] and was eventually announced as a pandemic by World Health Organization (WHO) during March 2020 [2]. COVID-19-infected individuals have experienced severe acute respiratory disorders, fever, continuous coughing, and other infections. The mortality rate of this pandemic reached its peak in a short span of time. Early detection of the COVID-19 virus is the best way in mortality reduction. The CT scan images of COVID-19-affected individuals show distinctive characteristics like patchy multifocal consolidation, ground-glass opacities, interlobular cavitation, lobular septum thickening, and clear indication of fibrotic lesions, peribronchovascular, pleural effusion, and thoracic lymphadenopathy. The evolution of consolidation and ground-glass opacities over a period of time of a COVID-19-affected patient from symptom commencement to the next 31 days is delineated in Figure 1 [2–4]. RT-PCR is known to be the standard testing tool but has produced false negative rates in recent studies [5, 6] at the early stages. Studies also postulated the importance of CT scan images to screen COVID-19 with better specificity and sensitivity [7].

The characteristics of COVID-19 are similar to other viral pneumonia [4]. Yet with help of deep learning techniques, one can predict the differences between types of viral pneumonia precisely. The main differences between pneumonia caused by different types of viruses including the Respiratory Syncytial Virus (RSV) and Human Metapneumovirus (HMPV) in terms of ground-glass opacity (GGO), consolidation, and pleural effusion are depicted in Table 1. +++ is 50% area of lungs being involved and + is 10% area of lungs being involved.

The large number of CT scan images opens up a research area for start-up companies. These techniques proposed by researchers aid radiologists and physicians for fast and early prediction of the disease.

RT-PCR which is used for diagnosing COVID-19 has a few limitations. Firstly, the test kits are not sufficiently available and consume more time for testing, and the sensitivity of

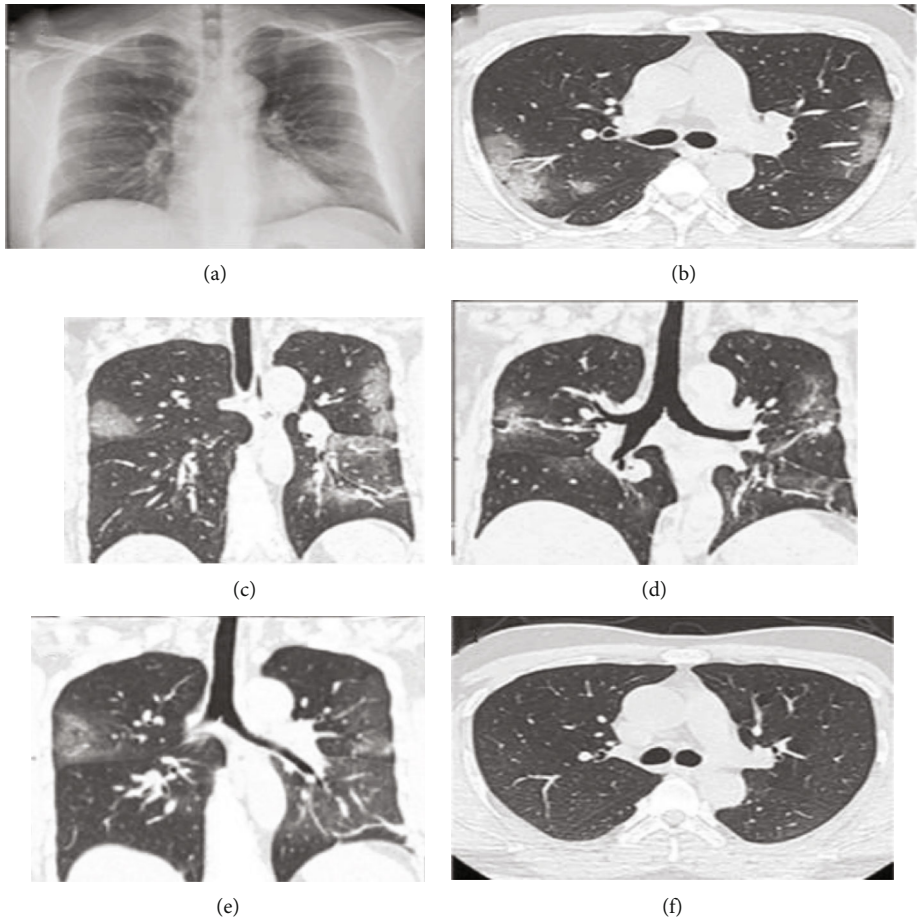

Figure 1: CT scan images of a COVID-19 patient as time goes by. (a) 7th Day (as soon as symptoms show up): CT scan presents opacities formed in left lower lobe and right upper lobe. (b, c) 9th Day: CT scan depicts ground-glass opacities which are bilateral and multifocal. (d) 15th Day: CT scan presents that virus has evolved into mixture of consolidations and opacities. (e) 19th Day: CT scan shows partial disappearance of ground-glass opacities and consolidations using antiviral treatments. (f) 31st Day: CT scan shows absence of pleural effusions, pulmonary cavitation, and lymphadenopathy [2–4].

Table 1: CT findings for major types of viral pneumonia.

Infections	Transmission	GGO	Consolidation	Nodule	Pleural effusion
Adenovirus	Respiratory, oral-fecal	+++	+++	Centro lobular	C
Influenza	Droplet, airborne	+	+	++	UC
RSV	Aerosol, contact	+	+	Centrilobular +++	C
SARS-CoV2	Airborne, contact	+	+++	Rare	Rare
HMPV	Contact, droplet	+	+	Centrilobular +++	UC

testing varies. Thus, using CT scan images for screening COVID-19 is important. CT scans images expose patchy ground-glass opacities which are hazy white spots in the lungs, which is the primary sign of COVID-19. In a recent study [8], with 1,014 patients, deep learning technique was able to predict (888/1014) positive cases using CT scan images of suspected COVID-19 patients, while RT-PCR was only able to predict (601/1014) positive cases of suspected COVID-19 patients. The results have shown that the CT scan images were able to diagnose COVID-19 effectively thus saving more lives. The mortality rates for different CoV viruses are discussed in Table 2. There is little knowledge on what will be the future of the outbreak. There are different manifestations of COVID-19 as discussed in a study [9]. In a study [10], it was found that CT scans had a high sensitivity while diagnosing for COVID-19. CT scan of the chest is considered to be an important tool for COVID-19 detection in endemic regions. As a result of the sensitivity and specificity of CT scans, a clinical detection threshold based upon ideal CT scan imaging manifestations is now utilized in China. So, CT scan images act as a better alternative to RT-PCR testing. Thus, chest CT scan images can be utilized as a primary resource for detecting COVID-19 in endemic regions which lack access to the testing kits.

Table 2: Severe Acute Respiratory Syndrome (SARS) versus Middle East Respiratory Syndrome (MERS) versus COVID-19.

CoV	Year	Origin	Mortality rate	Community attack rate	Incubation time
SARS	2002	Saudi Arabia	10%	30%-40%	4-14 days
MERS	2013	Saudi Arabia	34%	10-60%	7 days
COVID-19	2019	China	3.4%	4-13%	6 days

This also takes less time thereby saving radiologist's time for carrying out the further treatments. The following conclusions were arrived from the researchers carried out by many studies mentioned above:

(1) The sensitivity and specificity of chest CT scans to screen COVID-19 is high. Thus, in endemic regions one can use the automated system that detects COVID-19 precisely

(2) Chest CT scan images play a vital role in monitoring and evaluating COVID-19 patients with extreme and severe respiratory symptoms. Based on CT scans, the intensity of the lung infection and the time taken by the disease to evolve were assessed and discussions on treatments were made accordingly

(3) Patients infected with COVID-19 require multiple chest CT scan images during the treatment to find the progression of the disease. Analysing multiple CT images is a time-consuming task and it cannot be completed with greater precision manually. Thus, screening many images quickly is a priority which is achieved through deep learning techniques

(4) The prime abnormalities which are developed after the onset of symptoms in COVID-19-affected patients are ground-glass opacities (GGO), consolidations, and nodules. These features are easily recognizable through deep learning techniques

(5) Early detection of COVID-19 infection is critical for treatment mitigation and safety control. When compared with RT-PCR, testing with chest CT images are more dependable, rapid, and practical methodology to scan and monitor COVID-19 patients, specifically in the hotspot regions

(6) Even when the symptoms are not visible (asymptomatic), CT findings can detect visible changes and series of abnormalities in COVID-19-affected lungs using proposed model

So far, medical and clinical studies on chest CT scan findings have been discussed. In Table 3, the deep learning techniques which were carried out using images are presented.

The accuracy of the works is also shown along with the classification methods that were used. The predominant works delineated in Table 3 show 94.52% accuracy when model was built for CT images. It is also seen that most of the models are built for X-ray images [17–26]. Studies have shown instances where patient's chest X-ray showed no traces of lung nodules but then were later identified using CT scans [13, 15]. CT images play a major role in detecting the COVID-19 infection. Hence, for the above reasons, a hybrid learning model was proposed which scans the CT images and classifies them as COVID-19, CAP, and Normal images using machine learning and deep learning techniques.

Table 3: Comparison of studies on COVID-19 classification.

Author	Image	Accuracy	Classification
Wang [11]	CT	82.9%	Transfer learning
Zhao [12]	CT	85%	DenseNet
Vruddhi Shah [13]	CT	94.52%	VGG-19
He X [14]	CT	94%	Self-trans model
Michael J. Horry [15]	CT	84%	Fine-tuned VGG-19
Song Ying [16]	CT	93%	Deep CNN

2. Materials and Methods

Figure 2 shows the overall progression of the proposed hybrid learning model. The CT scan input images are collected from various sources like Google Images, RSNA, and Github, so they are different in resolution, size, and many other features. So, all the CT scan input images are preprocessed to standardize the images and given to the pretrained deep learning models for feature extraction. The extracted features are then given to machine learning classification models. The pretrained deep learning models used in the proposed work are VGG-16, Resnet50, InceptionV3, and AlexNet. The machine learning models used in the proposed work are Support Vector Machine (SVM), Random Forest, Decision Tree, Naive Bayes, and K-Nearest Neighbour (KNN).

2.1. Image Processing. Figure 3 shows the progression of image processing.

The histogram equalization is applied to enhance the quality of the image without losing the important features of the image. The histograms of the original and equalized image are shown in Figure 4. The Weiner filter is used to remove the noises from the image yet preserving fine details and edges of the lungs. The filter size is chosen to be 4×4 in order to prevent the image from getting over smooth. Weiner filter is typically based on estimation of variance and mean from the local adjacent of individual pixels. It then constructs pixel-based linear filters using the Eq (1).

$$\mathrm{WF}(i, j) = \mu + \frac{\sigma^2 - \nu^2}{\sigma^2}.(O(i, j) - \mu), \tag{1}$$

where $\mathrm{WF}(i, j)$ denotes the position of pixel in filtered image and $O(i, j)$ denotes the position of pixel in the original image.

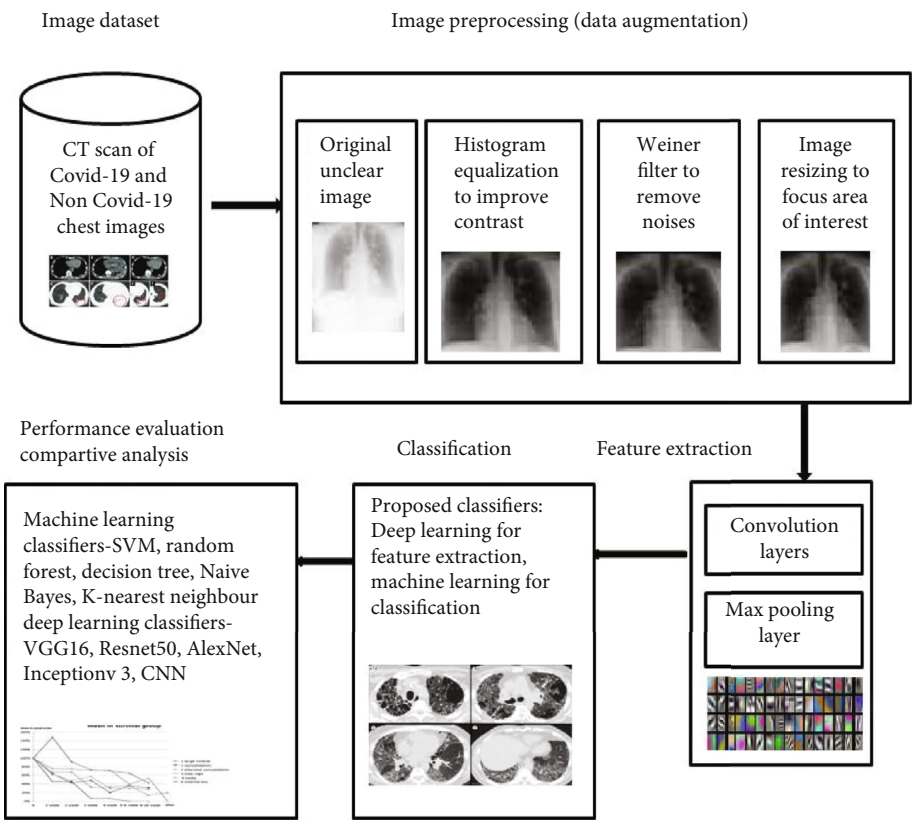

Figure 2: System architecture that was proposed for screening COVID-19 chest CT scans using feature extraction and classification.

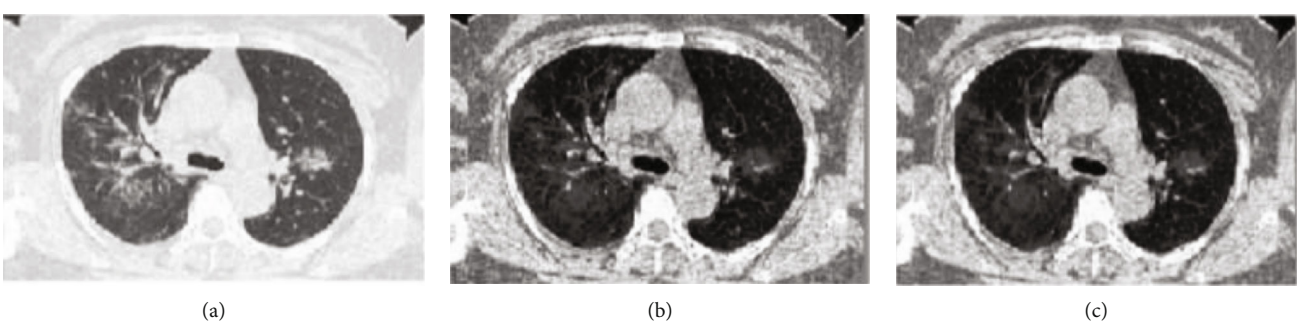

Figure 3: (a) Original COVID-19 CT scan image (b) Histogram equalized COVID-19 CT scan image (c) Weiner filtered COVID-19 CT scan image.

μ and σ are mean and variance of local adjacent pixels, respectively. v is called the noise variance. Images are then resized to focus on a specific area of interest in order to extract its features.

2.2. Feature Extraction. Feature extraction is achieved using pretrained CNN models such as VGG-16, Restnet50, InceptionV3, and AlexNet. CNN models are purposely used for image classification. An image is viewed as an array of pixel which also depends upon the resolution of an image. These CNN models consist series of convolutional and pooling layers. The data augmentation is achieved using a convolutional layer. The convolution operation is applied to a region of an image, sampling the values of the pixels in that particular region and converting them into a solitary value. This convolution operation is defined in Eq (2) and Figure 5.

$$E(i,j) = \sum_{a=-K}^{K} \sum_{b=-K}^{K} I(a,b) F(i-a, j-b), \tag{2}$$

where $E(j,j)$ is the value of pixel at (i,j) after convolution operation; $I(a,b)$ is the value of pixel at (a,b) in input matrix and $F(i-a, j-b)$ is the value of pixel at $(i-a, j-b)$ in filter (Kernel) matrix and K is the kernel size or size of the filter matrix.

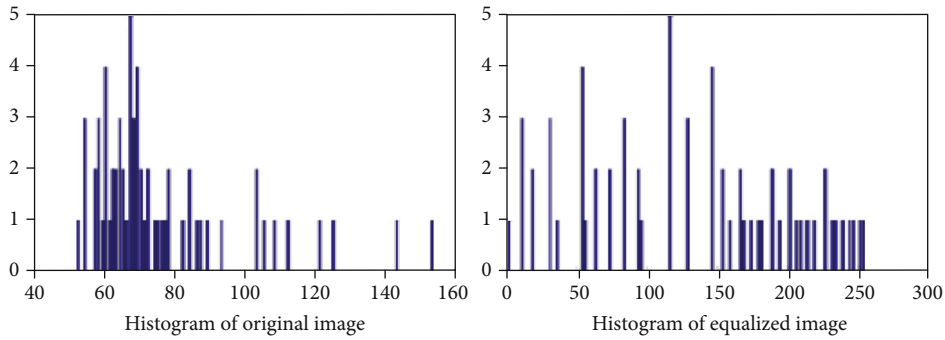

Figure 4: Histogram of original and equalized images.

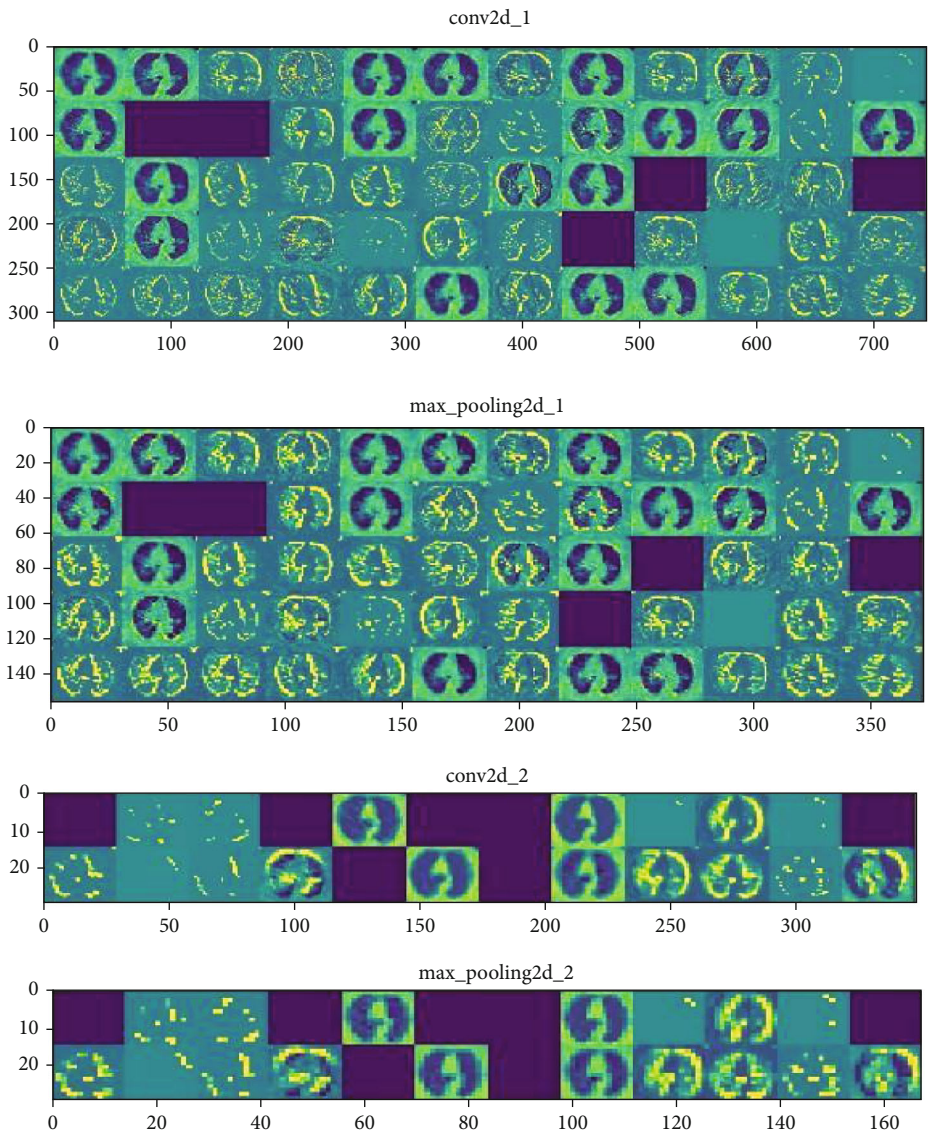

Figure 5: Convolutional and max-pooling layer intermediate image.

The output size of the convolution layer is given in Eq (3).

$$M = \frac{I - F + 2P}{S} + 1, \tag{3}$$

where M is the size of the output matrix, I is the size of the input matrix, F is the size of the convolution filter, P is padding, and S is stride value for convolution operation. The max-pooling layer performs dimensionality reduction.

Table 4: Model parameter comparison.

Model	Image size	Total parameters	Trainable parameters	Nontrainable parameters	Number of layers
VGG-16	14,882,883	1,66,403	14,716,480	16	224 × 224
InceptionV3	22,370,339	5,62,691	21,807,6487	48	299 × 299
Resnet50	24,155,267	5,62,691	23,592,576	50	224 × 224
AlexNet	62,378,344	2,29,123	62,149,221	8	227 × 227

This layer will downsample the value without losing any important information. It does max operation by finding the maximum valued neuron in a particular region for the output from the previous layer which is given in Eq (4) and Figure 5.

$$P(i,j) = \sum_{a=-M}^{a=M} \sum_{b=-M}^{b=M} \max(E(a,b)), \tag{4}$$

where $P(i,j)$ is the value of pixel at (i,j) after pooling operation is performed; $E(a,b)$ is the value of pixel at (a,b) of preceding layer's output and M is the size of previous layer's output grid. The output size of the max-pooling layer is given in Eq (5).

$$N = \frac{M-F}{S} + 1, \tag{5}$$

where N is the size of the output matrix, M is the size of the previous layer's matrix, F is the size of the pooling filter, and S is the stride value same as what was chosen for convolution operation. Relu acts as an activation for convolutional and max-pooling layer as given in Eq (6)

$$F(x) = \max\,(0, x), \tag{6}$$

where x is the input value provided to activate the neuron. Thus, all the parameters which were extracted from the series of convolution and pooling operations from all the pretrained models that were used for feature extraction only are shown in Table 4. One can notice that nontrainable parameters are less and only trainable parameters are used by the backpropagation algorithm to optimize and update the values of weight and bias. Thus, only the important features are utilized for training the model. The features are nonredundant and informative values are intended to facilitate precise diagnosis of classes.

2.3. Classification. Classification refers to a predictive modelling problem where a class label is predicted for an input image. The classification is performed using traditional machine learning classifiers by removing the fully connected layers from the pretrained deep learning models. The extracted features were utilized for the final classification using Support Vector Machine (SVM), Decision Tree, Naive Bayes, K-Nearest Neighbour (KNN), and Random Forest. In SVM, the input values are plotted in an n-dimensional space, and the optimal hyperplane that differentiates the classes is found. In Random Forest, a large number of decision trees are built to operate as an ensemble model where all decision trees predict the class label and eventually the class that gets more votes will be chosen as the predicted label. In Decision Tree, each node acts as a splitting criterion and the branches lead to the final node (leaf node) to provide the output. Naive Bayes is a conditional probability model which used the Bayes theorem for classification. KNN is a nonparametric classifier which classifies images based on its k-nearest neighbours.

Table 5: Multisource data assimilation for COVID-19, CAP, and normal CT scan images.

Categories	Source	Images
COVID-19	medRXiv, bioRxiv, NEJM, JAMA, Lancet Medical Segmentation	349
	Coronacases	100
	Radiopaedia	10
	Zenodo	9
Total		488
CAP	Google Images, RSNA	500
Normal	Google Images, Github	500

Table 6: Data for training, testing, and validation.

Class	Training	Validation	Testing	Total
COVID-19	340	37	111	488
CAP	340	49	111	500
Normal	340	49	111	500

3. Results and Discussion

In this section, datasets that have been utilized for carrying out the experiments are discussed. Further, the comparative analysis of results is discussed.

3.1. Data Formulation. The dataset used here contains CT scan images for COVID-19 (includes both symptomatic and asymptomatic), CAP, and normal chest CT scan images. The images were assimilated from multiple resources for training the model precisely. The data collected from different resources are shown in Table 5. Scanning scheme used for scanning the image is diverse thus the model is able to learn all possible images. Image preprocessing has been applied to make the dataset a standardized one. A total of approximately 500 CT scan images were obtained for each class to maintain the data balance. The images were split for training, validation, and testing purposes which are shown in Table 6. The project was conducted on windows

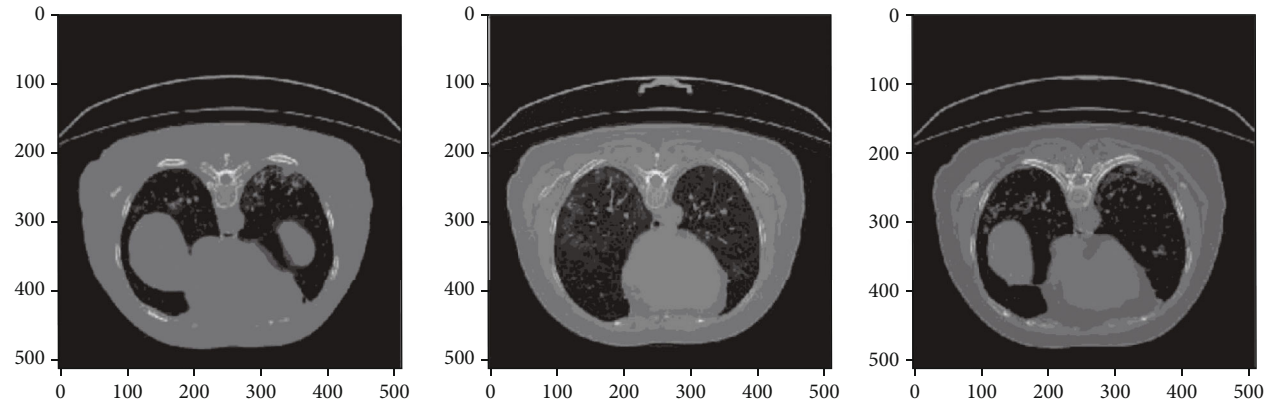

Figure 6: Colormap for COVID-19-affected chest CT scan images correctly classified by AlexNet+SVM and AlexNet+Random Forest.

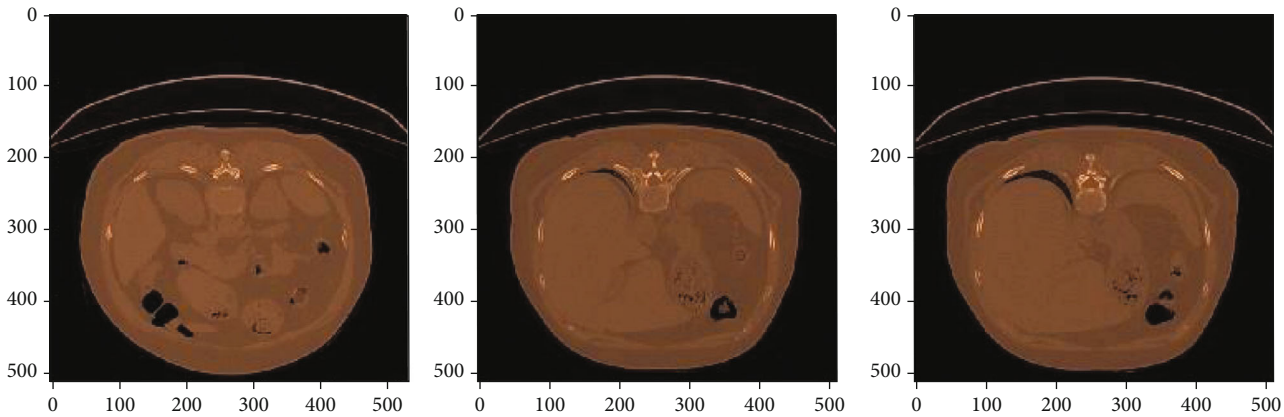

Figure 7: Colormap for CAP-affected chest CT scan images correctly classified by AlexNet+SVM and AlexNet+Random Forest.

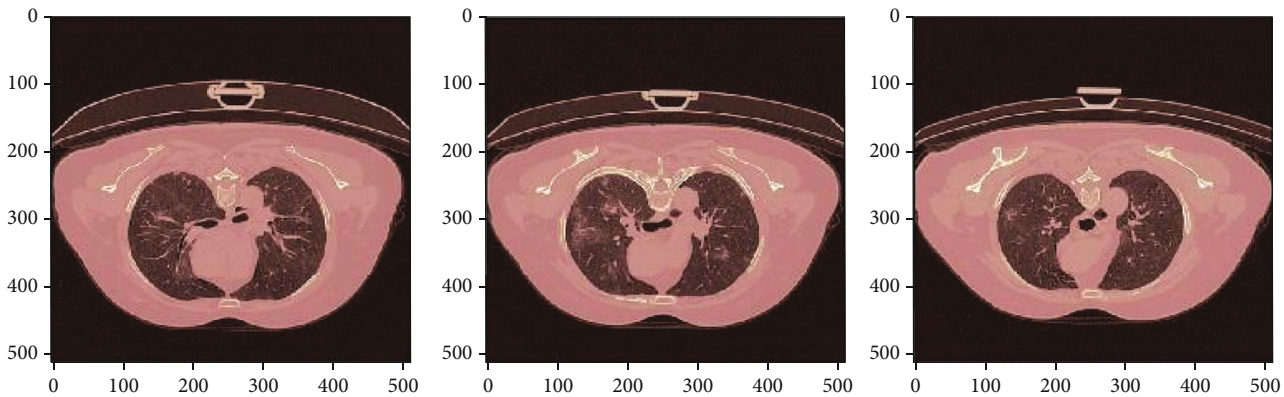

Figure 8: Colormap for normal chest CT scan images correctly classified by AlexNet+SVM and AlexNet+Random Forest.

platform using the Python software (Python Jupyter Notebook). Different packages like pandas for data loading and data accessing, numpy for array (matrix) creation, scikit-learn for machine learning classifiers, Keras's Tensorflow for deep learning classifiers, and matplotlib for plotting graphs are used in the implementation of the proposed work. These tools have been helpful in completely satisfying the requirements producing promising results.

3.2. Experimental Results. The COVID-19 images are correctly classified by the present model with greater precision and recall. Initially, about 111 images were tested for machine learning models like Support Vector Machine (SVM), Decision Tree, Naive Bayes, K-Nearest Neighbour (KNN), and Random Forest. Secondly, the images were trained and tested for deep learning models such as CNN, AlexNet, VGG-16, InceptionV3, and Resnet50. On further

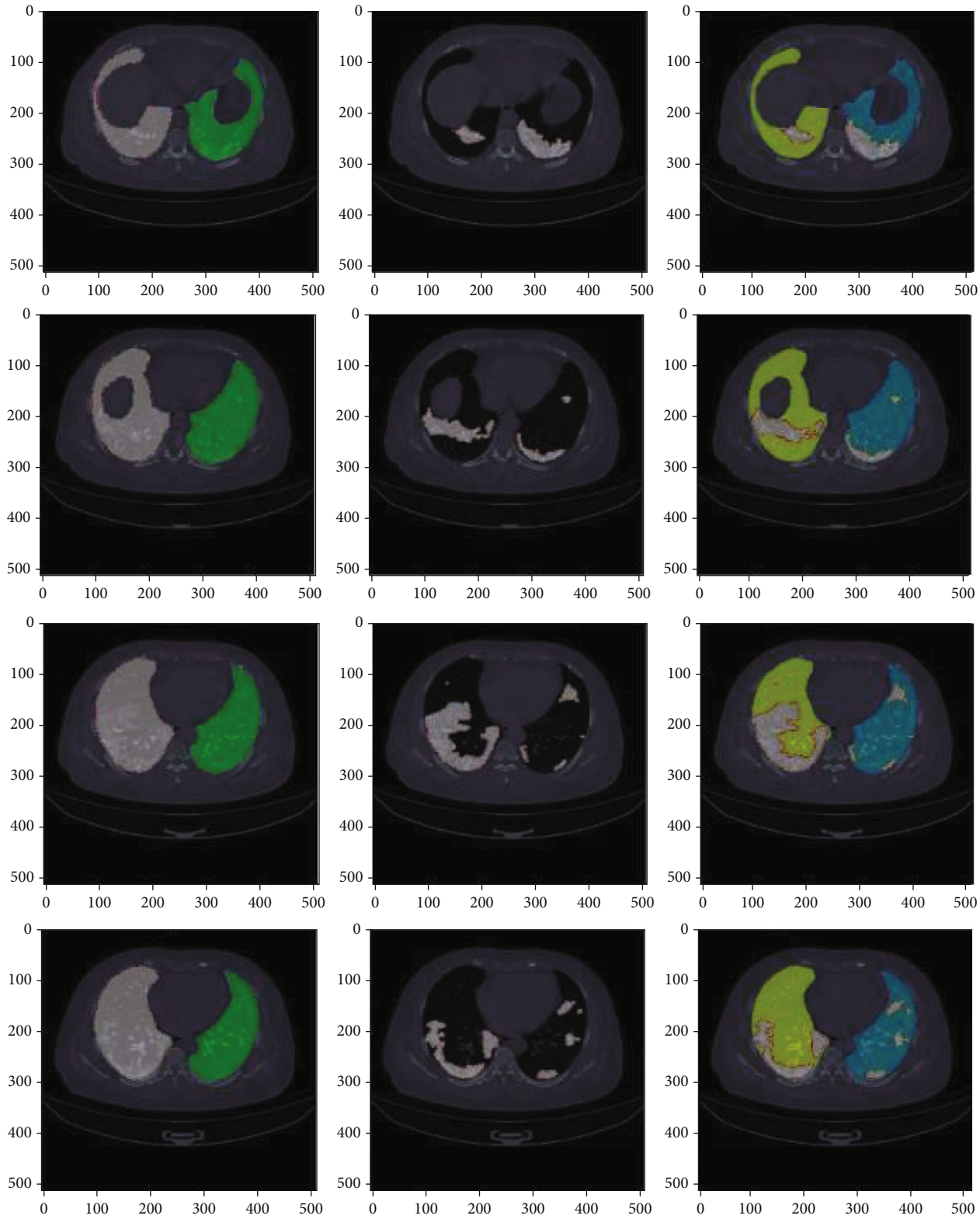

Figure 9: Images that were tested as negative by RT-PCR were actually positive cases and were correctly predicted as positive by the proposed work.

analysis, the fully connected layers for CNN models were removed, and the prediction was performed with machine learning models as hybrid learning models. This showed that the hybrid learning models such as AlexNet+SVM and AlexNet+Random Forest models yielded better results when compared with other models.

Table 7: Confusion matrix and classification report for different machine learning classifiers.

Models	Confusion matrix					Classification report				
	Category	COVID-19	CAP	Normal	Total	Category	Precision	Recall	F1Score	Specificity
SVM	COVID-19	104	7	0	111	COVID-19	0.93	0.92	0.92	0.96
	CAP	7	103	2	111	CAP	0.92	0.88	0.89	0.96
	Normal	1	6	104	111	Normal	0.93	0.98	0.95	0.96
	Total	112	116	106	333	Average	0.92	0.93	0.92	0.96
Random Forest	COVID-19	106	5	0	111	COVID-19	0.95	0.97	0.95	0.97
	CAP	3	106	2	111	CAP	0.95	0.95	0.95	0.97
	Normal	0	6	105	111	Normal	0.95	0.98	0.95	0.97
	Total	**109**	**111**	**107**	**333**	**Average**	**0.95**	**0.96**	**0.95**	**0.97**
Decision Tree	COVID-19	104	5	2	111	COVID-19	0.93	0.93	0.93	0.96
	CAP	3	103	5	111	CAP	0.92	0.91	0.91	0.96
	Normal	4	4	103	111	Normal	0.92	0.93	0.92	0.96
	Total	111	112	110	333	Average	0.92	0.92	0.92	0.96
Naive Bayes	COVID-19	82	20	9	111	COVID-19	0.73	0.86	0.79	0.87
	CAP	8	83	20	111	CAP	0.74	0.62	0.67	0.86
	Normal	5	29	77	111	Normal	0.69	0.72	0.70	0.87
	Total	95	132	106	333	Average	0.72	0.73	0.72	0.87
KNN	COVID-19	104	7	0	111	COVID-19	0.93	0.91	0.91	0.97
	CAP	6	103	2	111	CAP	0.92	0.88	0.89	0.97
	Normal	4	6	101	111	Normal	0.90	0.98	0.93	0.96
	Total	114	117	103	333	Average	0.92	0.92	0.92	0.97

Table 8: Confusion matrix and classification report for various deep learning classifiers.

Models	Confusion matrix					Classification report				
	Category	COVID-19	CAP	Normal	Total	Category	Precision	Recall	F1Score	Specificity
CNN	COVID-19	100	5	6	111	COVID-19	0.90	0.90	0.90	0.95
	CAP	5	101	4	111	CAP	0.91	0.89	0.89	0.95
	Normal	5	7	99	111	Normal	0.89	0.90	0.89	0.95
	Total	111	113	109	333	Average	0.90	0.90	0.90	0.95
AlexNet	COVID-19	105	3	3	111	COVID-19	0.94	0.94	0.94	0.97
	CAP	2	106	3	111	CAP	0.95	0.95	0.95	0.97
	Normal	4	2	104	111	Normal	0.93	0.93	0.93	0.97
	Total	**111**	**111**	**111**	**333**	**Average**	**0.94**	**0.94**	**0.94**	**0.97**
VGG-16	COVID-19	104	4	3	111	COVID-19	0.93	0.93	0.93	0.96
	CAP	3	104	4	111	CAP	0.93	0.93	0.93	0.95
	Normal	4	3	104	111	Normal	0.93	0.93	0.93	0.96
	Total	111	111	111	333	Average	0.93	0.93	0.93	0.96
Resnet50	COVID-19	102	6	3	111	COVID-19	0.92	0.93	0.92	0.96
	CAP	5	101	5	111	CAP	0.91	0.90	0.90	0.95
	Normal	3	6	102	111	Normal	0.92	0.93	0.92	0.96
	Total	110	113	110	333	Average	0.92	0.92	0.92	0.96
Inception v3	COVID-19	100	4	7	111	COVID-19	0.90	0.89	0.89	0.94
	CAP	6	100	5	111	CAP	0.90	0.91	0.90	0.95
	Normal	6	6	99	111	Normal	0.89	0.89	0.89	0.95
	Total	112	110	111	333	Average	0.90	0.90	0.90	0.95

Table 9: Confusion matrix and classification report for the proposed work, CNN for feature extraction, and various machine learning models for classification.

Models	Confusion matrix					Classification report				
	Category	COVID-19	CAP	Normal	Total	Category	Precision	Recall	F1Score	Specificity
CNN+SVM	COVID-19	104	4	3	111	COVID-19	0.93	0.93	0.93	0.97
	CAP	3	104	4	111	CAP	0.93	0.93	0.93	0.97
	Normal	4	3	104	111	Normal	0.93	0.93	0.93	0.97
	Total	111	113	109	333	Average	0.93	0.93	0.93	0.97
CNN+Random Forest	COVID-19	104	3	4	111	COVID-19	0.94	0.93	0.93	0.96
	CAP	3	103	5	111	CAP	0.93	0.93	0.93	0.96
	Normal	5	5	101	111	Normal	0.91	0.92	0.91	0.97
	Total	112`	111	110	333	Average	0.93	0.93	0.93	0.96
CNN+Decision Tree	COVID-19	101	4	6	111	COVID-19	0.91	0.92	0.92	0.95
	CAP	3	101	7	111	CAP	0.91	0.92	0.92	0.96
	Normal	5	5	101	111	Normal	0.91	0.89	0.90	0.96
	Total	109	110	114	333	Average	0.91	0.91	0.91	0.96
CNN+Naive Bayes	COVID-19	104	3	4	111	COVID-19	0.94	0.93	0.93	0.91
	CAP	3	103	5	111	CAP	0.93	0.93	0.93	0.92
	Normal	5	5	101	111	Normal	0.91	0.92	0.91	0.91
	Total	112	111	110	333	Average	0.93	0.93	0.93	0.91
CNN+KNN	COVID-19	102	5	4	111	COVID-19	0.92	0.91	0.91	0.95
	CAP	4	102	5	111	CAP	0.91	0.91	0.91	0.95
	Normal	5	4	102	111	Normal	0.91	0.91	0.91	0.96
	Total	111	111	110	333	Average	0.91	0.91	0.91	0.95

Table 10: Confusion matrix and Classification report for the proposed work, AlexNet for feature extraction, and various machine learning models for classification.

Models	Confusion matrix					Classification report				
	Category	COVID-19	CAP	Normal	Total	Category	Precision	Recall	F1Score	Specificity
AlexNet+SVM	COVID-19	107	4	0	111	COVID-19	0.96	0.96	0.96	0.98
	CAP	1	108	2	111	CAP	0.95	0.97	0.96	0.97
	Normal	1	3	107	111	Normal	0.98	0.96	0.97	0.98
	Total	**109**	**113**	**109**	**333**	**Average**	**0.96**	**0.96**	**0.96**	**0.98**
AlexNet+Random Forest	COVID-19	102	5	4	111	COVID-19	0.92	0.92	0.91	0.96
	CAP	4	102	5	111	CAP	0.91	0.91	0.91	0.98
	Normal	5	4	102	111	Normal	0.91	0.91	0.91	0.98
	Total	111	111	110	333	Average	0.91	0.91	0.91	0.98
AlexNet+Decision Tree	COVID-19	104	4	3	111	COVID-19	0.94	0.94	0.94	0.97
	CAP	3	103	4	111	CAP	0.93	0.93	0.93	0.97
	Normal	4	3	104	111	Normal	0.93	0.93	0.93	0.96
	Total	111	111	111	333	Average	0.94	0.94	0.94	0.97
AlexNet+Naive Bayes	COVID-19	93	8	10	111	COVID-19	0.84	0.82	0.83	0.91
	CAP	10	93	8	111	CAP	0.84	0.83	0.83	0.90
	Normal	10	11	90	111	Normal	0.81	0.83	0.82	0.91
	Total	113	112	108	333	Average	0.83	0.83	0.83	0.91
AlexNet + KNN	COVID-19	104	3	4	111	COVID-19	0.94	0.94	0.94	0.94
	CAP	4	103	40	111	CAP	0.93	0.94	0.93	0.93
	Normal	3	4	104	111	Normal	0.94	0.93	0.93	0.94
	Total	111	110	112	333	Average	0.94	0.94	0.94	0.94

Table 11: Confusion matrix and classification report for proposed work, VGG-16 for feature extraction, and different machine learning models for classification.

Models	Confusion matrix					Classification report				
	Category	COVID-19	CAP	Normal	Total	Category	Precision	Recall	F1Score	Specificity
VGG-16+SVM	COVID-19	105	2	4	111	COVID-19	0.95	0.95	0.95	0.97
	CAP	3	105	3	111	CAP	0.94	0.95	0.94	0.97
	Normal	2	4	105	111	Normal	0.94	0.95	0.94	0.97
	Total	110	111	112	333	Average	0.94	0.94	0.94	0.97
VGG-16+Random Forest	COVID-19	106	2	3	111	COVID-19	0.95	0.95	0.96	0.97
	CAP	3	106	2	111	CAP	0.95	0.95	0.95	0.97
	Normal	3	3	105	111	Normal	0.94	0.95	0.94	0.97
	Total	112	111	110	333	Average	0.95	0.95	0.95	0.97
VGG-16+Decision Tree	COVID-19	104	4	3	111	COVID-19	0.94	0.94	0.94	0.96
	CAP	3	103	4	111	CAP	0.93	0.94	0.93	0.96
	Normal	3	4	104	111	Normal	0.94	0.93	0.93	0.96
	Total	111	110	112	333	Average	0.94	0.94	0.93	0.96
VGG-16+Naive Bayes	COVID-19	94	7	10	111	COVID-19	0.85	0.86	0.86	0.93
	CAP	7	94	10	111	CAP	0.85	0.85	0.85	0.92
	Normal	8	9	94	111	Normal	0.85	0.82	0.84	0.93
	Total	109	110	114	333	Average	0.85	0.84	0.85	0.92
VGG-16+KNN	COVID-19	103	4	4	111	COVID-19	0.93	0.94	0.93	0.96
	CAP	3	103	4111	333	CAP	0.94	0.93	0.93	0.96
	Normal	4	4	103	111	Normal	0.93	0.94	0.93	0.96
	Total	110	112	110	333	Average	0.93	0.94	0.93	0.96

Table 12: Confusion matrix and classification report for proposed work, Resnet50 for feature extraction, and machine learning models for classification.

Models	Confusion matrix					Classification report				
	Category	COVID-19	CAP	Normal	Total	Category	Precision	Recall	F1Score	Specificity
Resnet50+SVM	COVID-19	104	4	3	111	COVID-19	0.94	0.95	0.94	0.94
	CAP	3	104	4	111	CAP	0.94	0.93	0.93	0.93
	Normal	3	4	104	111	Normal	0.94	0.94	0.94	0.94
	Total	110	112	111	333	Average	0.94	0.94	0.94	0.94
Resnet50+Random Forest	COVID-19	105	3	3	111	COVID-19	0.95	0.95	0.95	0.97
	CAP	3	104	4	111	CAP	0.94	0.95	0.95	0.97
	Normal	3	3	105	111	Normal	0.94	0.94	0.95	0.97
	Total	**111**	**110**	**111**	**333**	**Average**	**0.95**	**0.95**	**0.95**	**0.97**
Resnet50+Decision Tree	COVID-19	102	4	5	111	COVID-19	0.92	0.93	0.93	0.96
	CAP	4	103	4	111	CAP	0.93	0.92	0.93	0.96
	Normal	4	5	102	111	Normal	0.92	0.92	0.92	0.96
	Total	110	11	111	333	Average	0.92	0.92	0.92	0.96
Resnet50+Naive Bayes	COVID-19	97	7	7	111	COVID-19	0.87	0.87	0.87	0.94
	CAP	7	96	8	111	CAP	0.88	0.86	0.87	0.94
	Normal	8	6	97	111	Normal	0.86	0.86	0.86	0.93
	Total	112	109	112	333	Average	0.87	0.86	0.86	0.94
Resnet50+KNN	COVID-19	102	5	4	111	COVID-19	0.92	0.92	0.92	0.95
	CAP	5	101	5	111	CAP	0.91	0.92	0.91	0.96
	Normal	4	4	103	111	Normal	0.93	0.92	0.93	0.96
	Total	111	110	112	333	Average	0.92	0.92	0.92	0.96

Table 13: Confusion matrix and classification report for proposed work, Inception V3 for feature extraction, and various machine learning models for classification.

Models	Confusion matrix					Classification report				
	Category	COVID-19	CAP	Normal	Total	Category	Precision	Recall	F1Score	Specificity
IncpetionV3+SVM	COVID-19	103	4	4	111	COVID-19	0.93	0.93	0.93	0.95
	CAP	4	102	5	111	CAP	0.92	0.93	0.92	0.96
	Normal	4	4	103	111	Normal	0.93	0.92	0.94	0.96
	Total	111	110	11	333	Average	0.93	0.93	0.93	0.96
Inception V3 + Random Forest	COVID-19	102	5	4	111	COVID-19	0.92	0.92	0.92	0.96
	CAP	4	103	4	111	CAP	0.91	0.91	0.91	0.96
	Normal	5	5	101	111	Normal	0.91	0.92	0.91	0.95
	Total	111	113	109	333	Average	0.91	0.92	0.92	0.96
InceptionV3+Decision Tree	COVID-19	101	5	5	111	COVID-19	0.91	0.91	0.91	0.95
	CAP	5	101	5	111	CAP	0.91	0.90	0.91	0.95
	Normal	5	6	100	111	Normal	0.90	0.90	0.90	0.95
	Total	111	112	110	333	Average	0.91	0.90	0.91	0.95
InceptionV3+Naive Bayes	COVID-19	96	9	6	111	COVID-19	0.86	0.86	0.86	0.93
	CAP	6	96	9	111	CAP	0.86	0.85	0.86	0.93
	Normal	7	9	95	111	Normal	0.89	0.88	0.88	0.93
	Total	108	112	107	333	Average	0.87	0.87	0.87	0.93
InceptionV3+KNN	COVID-19	101	5	5	111	COVID-19	0.91	0.92	0.91	0.95
	CAP	4	102	5	111	CAP	0.92	0.91	0.92	0.95
	Normal	5	5	101	111	Normal	0.96	0.91	0.91	0.95
	Total	110	112	111	333	Average	0.91	0.92	0.92	0.95

Figure 6 shows the colormap images for COVID-19-affected CT scan images which were correctly classified by AlexNet+SVM and AlexNet+Random Forest. Figure 7 shows the correctly classified CAP images, and Figure 8 shows the correctly classified normal CT scan images. These images in Figures 6–8 show the infected region in CT scan images which are then classified as CAP or COVID-19. The normal CT scan image does not have any infected region pointed in the image. The COVID-19 image shows an infected region in the left lower lobe region. This identification of the infected region is performed using Jet Colormap and Turbo heat map provided in python.

To compare this work with RT-PCR, 12 sample images of 3 patients are taken to test the model. All these images in Figure 9 are classified correctly by AlexNet+SVM and AlexNet+Random Forest, which are found to be negative by RT-PCR. The infected regions are also shown in the images using the colormap function provided by python.

Various metrics used to analyse different models are discussed below. F1-score, precision, and recall are defined in Eq (7), Eq (8), and Eq (9). Accuracy of a model shows how correctly the images are classified. The precision of the model determines the reproducibility of values or how many values are predicted correctly. Recall of a model shows how many correct values are discovered among all classes. F1-score takes precision and recall into account in order to calculate a balanced average value.

$$F1 - \text{score} = 2.\frac{(\text{precision} * \text{recall})}{(\text{precision} + \text{recall})}, \tag{7}$$

where precision and recall are defined in Eq (8) and Eq (9). These values are in fact calculated from a Confusion matrix that is built using test data images.

$$\text{precision} = \frac{T_p}{T_p + F_p} \tag{8}$$

where T_p is the number of images observed as positive and predicted as positive and F_p is the number of images observed as negative and predicted as positive.

$$\text{recall} = \frac{T_p}{T_p + F_n}, \tag{9}$$

where T_p is the number of images observed as positive and predicted as positive and F_n is the number of images observed as positive and predicted as negative. Recall is also called sensitivity.

The specificity is defined in Eq (10).

$$\text{Specificity} = \frac{T_n}{T_n + F_p}, \tag{10}$$

Table 14: Performance analysis with and without image preprocessing.

Model	With preprocessing					Without preprocessing				
	Accuracy	F1-score	MAE	RMSE	Specificity	Accuracy	F1-score	MAE	RMSE+	Specificity
SVM	93.39%	0.92	0.229	0.054	0.96	91.11%	0.91	0.298	0.089	0.94
Random Forest	95.19%	0.95	0.218	0.049	0.97	94.23%	0.94	0.227	0.054	0.96
Decision Tree	93.12%	0.92	0.262	0.063	0.96	92.02%	0.92	0.265	0.077	0.94
Naive Bayes	72.69%	0.72	0.795	0.396	0.87	69.63%	0.69	0.803	0.412	0.78
KNN	92.49%	0.92	0.226	0.051	0.97	90.15%	0.90	0.321	0.093	0.92
CNN	90.01%	0.90	0.314	0.087	0.95	89.45%	0.89	0.356	0.097	0.92
AlexNet	94.59%	0.94	0.206	0.061	0.97	93.78%	0.93	0.226	0.049	0.94
VGG-16	93.69%	0.93	0.227	0.051	0.96	91.82%	0.92	0.225	0.051	0.93
Resnet50	91.59%	0.91	0.272	0.077	0.96	91.18%	0.91	0.299	0.065	0.93
InceptionV3	89.78%	0.89	0.313	0.082	0.95	87.43%	0.86	0.391	0.099	0.94
CNN+SVM	91.12%	0.91	0.281	0.082	0.97	88.73%	0.89	0.366	0.096	0.93
CNN+Random Forest	92.49%	0.93	0.227	0.052	0.97	89.99%	0.90	0.325	0.088	0.93
CNN+Decision Tree	90.99%	0.91	0.271	0.078	0.96	88.31%	0.88	0.347	0.093	0.93
CNN+Naive Bayes	82.85%	0.83	0.456	0.123	0.91	79.56%	0.80	0.478	0.178	0.87
CNN+KNN	91.89%	0.92	0.253	0.061	0.95	89.56%	0.89	0.312	0.079	0.90
AlexNet+SVM	**96.69%**	**0.97**	**0.217**	**0.043**	**0.98**	**95.12%**	**0.95**	**0.217**	**0.047**	**0.93**
AlexNet+Random Forest	96.09%	0.96	0.225	0.049	0.98	95.11%	0.95	0.213	0.047	0.95
AlexNet+Decision Tree	93.09%	0.93	0.225	0.050	0.97	92.45%	0.92	0.223	0.053	0.92
AlexNet+Naive Byes	83.13%	0.83	0.421	0.099	0.91	80.55%	0.81	0.492	0.153	0.86
AlexNet+KNN	93.39%	0.93	0.220	0.055	0.94	90.91%	0.91	0.279	0.050	0.91
VGG-16+SVM	94.59%	0.95	0.205	0.061	0.97	93.69%	0.93	0.221	0.045	0.93
VGG-16+Random Forest	95.19%	0.95	0.200	0.054	0.97	93.34%	0.93	0.22	0.049	0.94
VGG-16+Decision Tree	93.39%	0.93	0.214	0.043	0.96	91.23%	0.91	0.277	0.080	0.93
VGG-16+Naive Bayes	84.68%	0.85	0.419	0.083	0.92	82.87%	0.83	0.455	0.122	0.88
VGG-16+KNN	93.09%	0.93	0.261	0.062	0.96	92.45%	0.92	0.227	0.053	0.92
Resnet50+SVM	93.69%	0.94	0.227	0.050	0.97	91.78%	0.93	0.220	0.048	0.94
Resnet50+Random Forest	94.29%	0.94	0.201	0.059	0.97	86.45%	0.86	0.399	0.087	0.93
Resnet50+Decision Tree	92.19%	0.91	0.278	0.079	0.96	89.10%	0.89	0.369	0.101	0.93
Resnet50+Naive Bayes	87.08%	0.87	0.389	0.100	0.94	85.18%	0.85	0.402	0.077	0.90
Resnet50+KNN	91.89%	0.92	0.249	0.058	0.96	88.99%	0.89	0.337	0.088	0.91
InceptionV3+SVM	92.79%	0.93	0.220	0.047	0.99	89.99%	0.90	0.319	0.091	0.92
InceptionV3+Random Forest	91.89%	0.92	0.236	0.059	0.96	87.91%	0.88	0.320	0.079	0.93
InceptionV3+Decision Tree	90.69%	0.91	0.266	0.070	0.95	88.45%	0.88	0.340	0.091	0.91
InceptionV3+Naive Bayes	86.18%	0.86	0.411	0.078	0.93	84.72%	0.85	0.416	0.081	0.91
InceptionV3+KNN	91.29%	0.91	0.288	0.075	0.95	90.11%	0.90	0.311	0.090	0.93

where T_n is the number of images observed as negative and predicted as negative and F_p is the number of images observed as negative and predicted as positive.

The accuracy for all the models can be calculated by Eq (11).

$$\text{Accuracy} = \frac{T_p + T_n}{T_p + T_n + F_p + F_n}, \tag{11}$$

where T_n is the number of images observed as negative and predicted as negative. The Root Mean Square Error (RMSE) value for all the images can be evaluated using Eq (12).

$$\text{RMSE} = \sqrt{\frac{\sum_{j=1}^{n}\left(y_j - y_j'\right)^2}{n}}, \tag{12}$$

where y_j is the actual value, y'_j is the predicted value, and n is the total number of images.

The Mean Absolute Error (MAE) can be calculated using [26].

$$\text{MAE} = \frac{\sum_{j=1}^{n}\left|y_j - y_j'\right|}{n}, \tag{13}$$

where y_j is actual value, y'_j is predicted value, and n is the total number of images.

The Confusion matrix is often used to analyse the performance of the classification models using predicted class label for test images against known class label for test images. Classification report is used to evaluate the quality of prediction of class labels by classification models. The Confusion matrix and classification report for the models built using conventional machine learning classifiers are presented in Table 7. It is obvious that Random Forest has produced better results with the precision of 0.95, recall of 0.96, and specificity of 0.97 when compared with other machine learning classifiers. The Confusion matrix and classification report for models constructed using deep learning techniques are analysed and shown in Table 8. It is seen that AlexNet has produced better prediction outcomes with the precision of 0.94, recall of 0.94, and specificity of 0.97. The Confusion matrix and classification report for the proposed hybrid learning models are presented in Tables 9–13. The proposed works performed better than other classifiers. AlexNet+SVM has produced better results with the precision of 0.96, recall of 0.96, and specificity of 0.98 when tested for 333 test images. Resnet50+Random Forest has also produced better outcomes with precision, recall, and specificity of 0.95, 0.95, and 0.97, respectively. The feature extraction produces only necessary features to be trained and remove unnecessary features that are not vital for the classification task. This also helps the model to be faster in training and testing the classification models.

The outcomes of the models when trained for images before preprocessing and after preprocessing are also compared. There is a visible difference in results and it shows the significance of preprocessing the images. This analysis report is presented in Table 14. When comparing the outcome with studies that are featured in Table 3, the presented hybrid learning models have produced better results.

Thus, the prediction of COVID-19 using the classification model has been constructed in a robust way and it helps in quicker prediction of COVID-19. AlexNet model takes 13 minutes 25 seconds for training and 6 minutes 38 seconds for testing. VGG-16 model takes 20 minutes 43 seconds for training and 12 minutes 30 seconds for testing. InceptionV3 model takes 34 minutes 12 seconds for training and 20 minutes 12 seconds for testing. Resnet50 model takes 43 minutes for training and 21 minutes for testing. As the model gets deeper, it takes more time to train and test the images. The time taken to run the models is inversely proportional to a number of layers. RT-PCR which is used as a standard reference takes 1-2 days in India for confirming a patient to be infected by COVID-19 or not. When compared to RT-PCR, the present model aids in quicker prediction and can aid radiologist in carrying out further treatment and procedures. The accuracy of this model is also quite promising to perform the prediction when compared with RT-PCR. The CT scan images that were tested as negative by RT-PCR are also correctly predicted by these models. Often, the medical images are unclear with lesions and tissues being captured in CT scan images which can impede the prediction task. In order to overcome these difficulties, various image preprocessing techniques were applied. The image preprocessing techniques that are incorporated has an impact on accuracies and results. These techniques provide better resolution, high quality, and high-definition images for carrying out the prediction. In conclusion, the models presented in this study have produced better results in terms of outcomes (accuracy) and quicker prediction even in the early stages. In short, the proposed work can be used for this global public health emergency situation which requires immediate attention.

4. Conclusion

Early detection of COVID-19 is vital for treating and isolating the patients in order to avoid the spread of the virus. RT-PCR is contemplated as the standard technique, but it is reported that chest CT could be used as a rapid and reliable approach for scanning of COVID-19. The proposed hybrid learning models are able to detect COVID-19 with chest CT scan images with an accuracy of 96.69%, sensitivity of 96%, and specificity of 98% for AlexNet+SVM model. Even though there is overlap in patterns of abnormalities in CAP- and COVID-19-affected CT scans, these models are capable of performing well with greater accuracy, sensitivity, and specificity using multisource data assimilation. Finally, reliable models are proposed to distinguish COVID-19 and CAP from CT scan images.

Data Availability

MedRvix BioRvix NEJM JAMA Lancet https://www.kaggle.com/c/covidct/data Radiopedia https://radiopaedia.org/articles/imaging-data-sets-artificial-intelligence Zenodo https://zenodo.org/record/3757476#.YBVbtWRN0zQ GitHub https://github.com/ieee8023/covid-chestxray-dataset.

Ethical Approval

This study does not involve human participants, and hence, ethical approval is not required.

Conflicts of Interest

On behalf of all the authors, the corresponding author state that there is no conflict of interest.

Authors' Contributions

V.P performed the supervision, project administration, writing, reviewing, and editing. V.N performed the data curation and formal analysis and wrote the original draft. S.J.S.R performed the conceptualization, investigation, and methodology.

References

[1] N. Zhu, D. Zhang, W. Wang et al., "A novel coronavirus from patients with pneumonia in China, 2019," *New England Journal of Medicine*, vol. 382, no. 8, pp. 727–733, 2020.

[2] WHO, *Coronavirus Disease 2019 (COVID-19) Situation Report–39*, World Health Organization, 2020.

[3] H. Shi, N. Xiaoyu Han, Y. Jiang, O. Cao, J. Alwalid, and C. Zheng, "Radiological findings from 81 patients with COVID-19 pneumonia in Wuhan, China: a descriptive study," *The Lancet Infectious Diseases*, vol. 20, no. 4, pp. 425–434, 2020.

[4] F. Pan, T. Ye, P. Sun et al., "Time course of lung changes at chest ct during recovery from coronavirus disease 2019 (COVID-19)," *Radiology*, vol. 295, no. 3, pp. 715–721, 2020.

[5] X. Xie, Z. Zhong, W. Zhao, C. Zheng, F. Wang, and J. Liu, "Chest ct for typical coronavirus disease 2019 (COVID-19) pneumonia: relationship to negative rt-pcr testing," *Radiology*, vol. 296, no. 2, pp. E41–E45, 2020.

[6] P. Huang, T. Liu, L. Huang et al., "Use of chest CT in combination with negative RT-PCR assay for the 2019 novel coronavirus but high clinical suspicion," *Radiology*, vol. 295, no. 1, article 200330, pp. 22-23, 2020.

[7] Y. Fang, H. Zhang, J. Xie et al., "Sensitivity of chest CT for COVID-19: com-parison to RT-PCR," *Radiology*, vol. 296, no. 2, pp. E115–E117, 2020.

[8] Q. Sun, X. Xu, J. Xie, J. Li, and X. Huang, "Evolution of computed tomography manifestations in five patients who recovered from coronavirus disease 2019 (COVID-19) pneumonia," *Korean Journal of Radiology*, vol. 21, 2020.

[9] T. Ai, Z. Yang, H. Hou et al., "Correlation of chest ct and RT-PCR testing for coronavirus disease 2019 (COVID-19) in China: a report of 1014 cases," *Radiology*, vol. 296, no. 2, pp. E32–E40, 2020.

[10] Committee, NH: General office of national health committee, *Notice on the Issuance of a Program for the Diagnosis and Treatment of Novel Coronavirus (2019-ncov) Infected Pneumonia (Trial Revised Fifth Edition)*, Policy document of the State Administration of Traditional Chinese Medicine, 2020.

[11] X. Xiaowei, J. Xiangao, M. Chunlian et al., "Deep learning system to screen coronavirus disease 2019 pneumonia," 2020.

[12] J. Zhao, X. He, X. Yang, Y. Zhang, S. Zhang, and P. Xie, "Covid-ct-dataset: a ct scan dataset about covid-19," 2020, https://arxiv.org/abs/2003.13865.

[13] V. Shah, R. Keniya, A. Shridharani, M. Punjabi, J. Shah, and N. Mehendale, "Diagnosis of COVID-19 using CT scan images and deep learning techniques," *Emergency Radiology*, 2021.

[14] X. He, X. Yang, S. Zhang et al., *Sample-Efficient Deep Learning for COVID-19 Diagnosis Based on CT Scans*, vol. 1, Med Rxiv., 2020.

[15] M. J. Horry, S. Chakraborty, M. Paul et al., "COVID-19 detection through transfer learning using multimodal imaging data," *IEEE Access*, vol. 8, pp. 149808–149824, 2020.

[16] Y. Song, S. Zheng, L. Li et al., *Deep Learning Enables Accurate Diagnosis of Novel Coronavirus (COVID-19) with CT Images*, vol. 1, Med Rxiv., 2020.

[17] Z. Jianpeng, X. Yutong, L. Yi, S. Chunhua, and X. Yong, "Covid-19 screening on chest x-ray images using deep learning based anomaly detection," 2020, https://arxiv.org/abs/2003.12338.

[18] N. Ali, K. Ceren, and P. Ziynet, "Automatic detection of coronavirus disease (covid-19) using x-ray images and deep convolutional neural networks," 2020, https://arxiv.org/abs/2003.10849.

[19] E. E. D. Hemdan, M. A. Shouman, and M. E. Karar, "Covidx-net: a framework of deep learning classifiers to diagnose covid-19 in x-ray images," 2020, https://arxiv.org/abs/2003.11055.

[20] I. D. Apostolopoulos and T. A. Mpesiana, "Covid-19: automatic detection from x-ray images utilizing transfer learning with convolutional neural networks," *Physical and Engineering Sciences in Medicine*, vol. 43, no. 2, pp. 635–640, 2020.

[21] P. Sethy and S. Behera, *Detection of Coronavirus Disease (COVID-19) Based on Deep Features*, Preprints, 2020.

[22] A. Abbas, M. M. Abdelsamea, and M. M. Gaber, "Classification of COVID-19 in chest X-ray images using DeTrac deep convolutional neural network," 2020, https://arxiv.org/abs/2003.13815.

[23] P. Afshar, S. Heidarian, F. Naderkhani, A. Oikonomou, K. N. Plataniotis, and A. Mohammadi, "Covid-caps: a capsule network-based framework for identification of covid-19 cases from x-ray images," 2020, https://arxiv.org/abs/2004.02696.

[24] L. O. Hall, R. Paul, D. B. Goldgof, and G. M. Goldgof, "Finding covid-19 from chest x-rays using deep learning on a small dataset," 2020, https://arxiv.org/abs/2004.02060.

[25] M. Farooq and A. Hafeez, "Covid-resnet: a deep learningframework for screening of covid 19 from radiographs," 2020, https://arxiv.org/abs/2003.14395.

[26] H. S. Maghdid, K. Z. Ghafoor, A. S. Sadiq, K. Cur-ran, and K. Rabie, "A novel AI-enabled framework to diagnose coronavirus COVID-19 using smartphone embedded sensors: design study," 2020, https://arxiv.org/abs/2003.07434.

Hindawi
Disease Markers
Volume 2021, Article ID 6643586, 8 pages
https://doi.org/10.1155/2021/6643586

Research Article

A Novel Method for Accurate Quantification of Split Glomerular Filtration Rate Using Combination of Tc-99m-DTPA Renal Dynamic Imaging and Its Plasma Clearance

Xiaoxi Pang,[1] Fei Li,[1] Shan Huang,[1] Cheng'en Wang,[2] Tao Zhang,[1] Zihao Hu,[1] Hao Cheng,[1] Xinchen Tao,[1] and Wenrui Chang[1]

[1]*The Second Hospital of Anhui Medical University, Hefei, China*
[2]*Beijing Hospital, Beijing, China*

Correspondence should be addressed to Wenrui Chang; changwr@foxmail.com

Received 22 December 2020; Revised 2 February 2021; Accepted 27 February 2021; Published 15 March 2021

Academic Editor: Dong Pan

Purpose. To precisely quantify split glomerular filtration rate by Tc-99m-DTPA renal dynamic imaging and plasma clearance in order to increase its consistency among doctors. *Methods*. Tc-99m-DTPA renal dynamic imaging was performed according to the conventional radionuclide renal dynamic imaging by five double-blinded doctors independently and automatically calculated split GFR, namely, gGFR. Moreover, the conventional radionuclide renal dynamic imaging was assessed to only outline the kidney, blank background, and automatically calculated split GFR, gGFR′. The total GFR value of patients, tGFR, was obtained by the double-plasma method. According to the formula, Precise GFR (pGFR) = gGFR′/(gGFR′ + gGFR′) × tGFR. The precise GFR value of the divided kidney, pGFR, was calculated. The Kendall's *W* test was used to compare the consistency of gGFR and pGFR drawn by five physicians. *Results*. According to Kendall's *W* consistency test, Kendall's coefficient of concordance was 0.834, $p = 0.0001$ using conventional method. The same five doctors used blank background again and the same standard Gates method to draw the kidneys, which automatically calculated gGFR′. Using input formula, the pGFR was calculated and Kendall's *W* consistency test (Kendall's coefficient of concordance = 0.956, $p = 0.0001$). *Conclusion*. The combination of Tc-99m-DTPA renal dynamic imaging combined with the double-plasma method could achieve accurate split GFR, and because of the omission of influence factors, the consistency of pGFR obtained by different doctors using this method was significantly higher than that of conventional Tc-99m-DTPA renal dynamic imaging.

1. Introduction

Accurate renal GFR is critical for the clinical decision-making of hydronephrosis or renal cancer [1]. Inulin clearance rate is recognized as the gold standard for GFR measurement. However, this method is time-consuming, laborious, and expensive, which is difficult to be applied in clinical practice as well as in scientific research. At present, biochemical indicators or combined with Tc-99m-DTPA radionuclide renal dynamic imaging are often used to evaluate renal function, but there are obvious deficiencies in both laboratory and imaging examinations. For example, laboratory biochemical indicators have obvious lag and cannot obtain the divided renal function. GFR determination by dual-plasma method was highly consistent with inulin clearance rate, and the former procedure was simpler and more acceptable to patients. Therefore, this method has been recommended as the gold standard for GFR determination by the American Nuclear Medicine Association and named as true GFR (tGFR). tGFR has also been recommended by the International Society of Nephrology as a reference index for clinical and scientific research [2]. Ultrasonic, intravenous pyelography (IVP), and radionuclide renal dynamic imaging have many influencing factors, and their objectivity, repeatability, and accuracy are often questioned.

At present, there is no simple and accurate method to quantify the split glomerular filtration rate. The purpose of this study was to combine and complement radionuclide

renal dynamic imaging with double-plasma method to explore a new accurate quantitative method for the split glomerular filtration rate in patients with hydronephrosis. This study was approved by the institutional ethical committee of our hospital (NO. YX2021-006 (F1)).

2. Materials and Methods

2.1. General Information. 66 patients with hydronephrosis who were admitted before operation at the Second Hospital of Anhui Medical University were included in this study. There were no restrictions on age and gender among the subjects. Patients meeting the following conditions were included in this study: ① ultrasonography or CT diagnosis of hydronephrosis. This study retrospectively included 41 males and 25 females. The average age of subjects was 51.69 ± 15.19 years old.

2.2. Double-Plasma Sampling Method. The same technician took 5 mL of venous blood from the contralateral elbow of each patient at 2 h and 4 h after injecting Tc-99m-DTPA with renal dynamic imaging, respectively, and administered heparin anticoagulation. The serum was separated by centrifuging at 1500 g for 15 min. One mL of plasma was accurately extracted from each pipette, and the radioactivity counts of P1 and P2 were measured with radioimmunogamma counter for 60 s. The counts of radioactive P1 and P2 were substituted into GFR = [Dln (P1/P2)/(T2 − T1)] exP [(T1lnP2) − (T2lnP 1)]/(T2 − T1), and the total GFR value, namely, tGFR, is automatically calculated.

2.3. Gates Method for Radionuclide Kidney Dynamic Imaging. The Tc-99m-DTPA kit was purchased from Jiangsu Institute of Atomic Energy Medicine with the approval document H20013118, and radiochemical purity was >95%. GE Infinia Hawkeye 4 single photon emission computed tomography with low energy and high resolution collimator was adopted to select 140 keV energy peak, window width 20%, and matrix 64 × 64. The patient was fully hydrated (300-500 mL of regular drinking water) 20-30 min before the examination, and the height and weight were measured and routinely recorded. The patient was then placed in the supine position with the probe placed in the lower back, and the SPECT field of view included both the kidneys and the bladder. Immediately after intravenous injection of 5 mCi Tc-99m-DTPA, images were acquired in front and rear positions of the dual probe. A total of 30 frames were collected at 1 frame/2 s immediately after injection, and 20 frames were collected at 1 frame/60 s. Afterwards, an empty syringe was collected for 6 s to obtain the residual drug count.

Five attending physicians who were blinded to the patient details used independent ROI technology with the areas of interest double kidney outline and background (Figure 1), and input intravenous injection of Tc-99m-DTPA radioactive count and the patient's height and weight in the computer to automatically generate double kidney time-radioactive curve, and calculate the double kidney GFR, standardization, and body surface area; the unit is $mL{\cdot}min^{-1}{\cdot}(1.73\,m^2)^{-1}$.

2.4. Accurate Quantification of Renal GFR. The original data of the nuclide kidney dynamic imaging was independently transferred to the postprocessing workstation by each physician who was double-blinded. The professional software was used for processing. After the same conventional operation, points of renal $gGFR_{left}'$ and the split renal $gGFR_{right}'$ were automatically calculated. According to the following formula, accurate GFR of kidney segmentation was automatically calculated (Formula 1): accurate GFR of left kidney: $pGFR_{left} = gGFR_{left}'/(gGFR_{left}' + gGFR_{right}') \times tGFR$ and accurate GFR of right kidney: $pGFR_{right} = gGFR_{right}'/(gGFR_{left}' + gGFR_{right}') \times tGFR$.

2.5. Statistical Analysis. The SPSS 19.0 statistical software was used for statistical analysis of the data. The measurement data conforming to the normal distribution was expressed as $(x \pm s)$. The correlation of double-plasma sampling method GFR with uric acid, creatinine, urea nitrogen, and cystatin C was analyzed by Pearson's correlation and linear regression. The Gates method and the consistency of pGFR were applied to Kendall's W test by different physicians. A p value <0.05 was considered statistically significant.

3. Results

3.1. Characteristics of the Patients' Information. All patients involved were diagnosed as hydronephrosis by ultrasonography or CT scan. The tGFR in 66 patients was 89.62 ± 46.57 mL/min. The result of gGFR left evaluated by five physicians, respectively ($n = 66$): 41.56 ± 17.04, 43.76 ± 17.74, 45.68 ± 19.41, 40.94 ± 16.45, and 44.84 ± 21.75 mL/min, and the gGFR right: 44.67 ± 17.65, 46.04 ± 18.15, 42.79 ± 16.63, 49.87 ± 20.83, and 44.72 ± 20.97 mL/min. The result of pGFR left evaluated by five physicians, respectively: 46.45 ± 32.04, 44.53 ± 32.44, 45.93 ± 30.63, 46.90 ± 33.46, and 48.39 ± 35.74 mL/min, and the pGFR right: 43.20 ± 31.60, 45.08 ± 31.41, 43.68 ± 30.80, 42.72 ± 32.13, and 41.22 ± 32.15 mL/min.

3.2. GFR of Double-Plasma Method and Results of Biochemical Examination. The tGFR in 66 patients was 89.62 ± 46.57 mL/min; the creatinine was 85.59 ± 31.32 μmol/L; the cystatin C was 0.83 ± 0.45 mg/L; the uric acid was 324.95 ± 118.71 μmol/L, and the urea nitrogen was 6.32 ± 2.17 mmol/L.

GFR of double-plasma method showed moderate negative correlation with serum creatinine, cystatin C, urea nitrogen, and uric acid. The correlation coefficients (r) were -0.692, -0.527, -0.454, and -0.424, respectively; the coefficient of determination (R^2) were -0.479, 0.278, 0.206, and 0.172, and the p values were 0.0001, 0.0001, 0.0001, and 0.001, respectively (Figure 2).

3.3. The Consistency of GFR Measured by Conventional Gates Method. Five double-blinded doctors independently used the standard Gates method to outline the background and the kidney and calculated each kidney GFR. The result was 43.46 ± 19.08 mL/min. The results of the five doctors were checked for consistency by Kendall's W test. Kendall

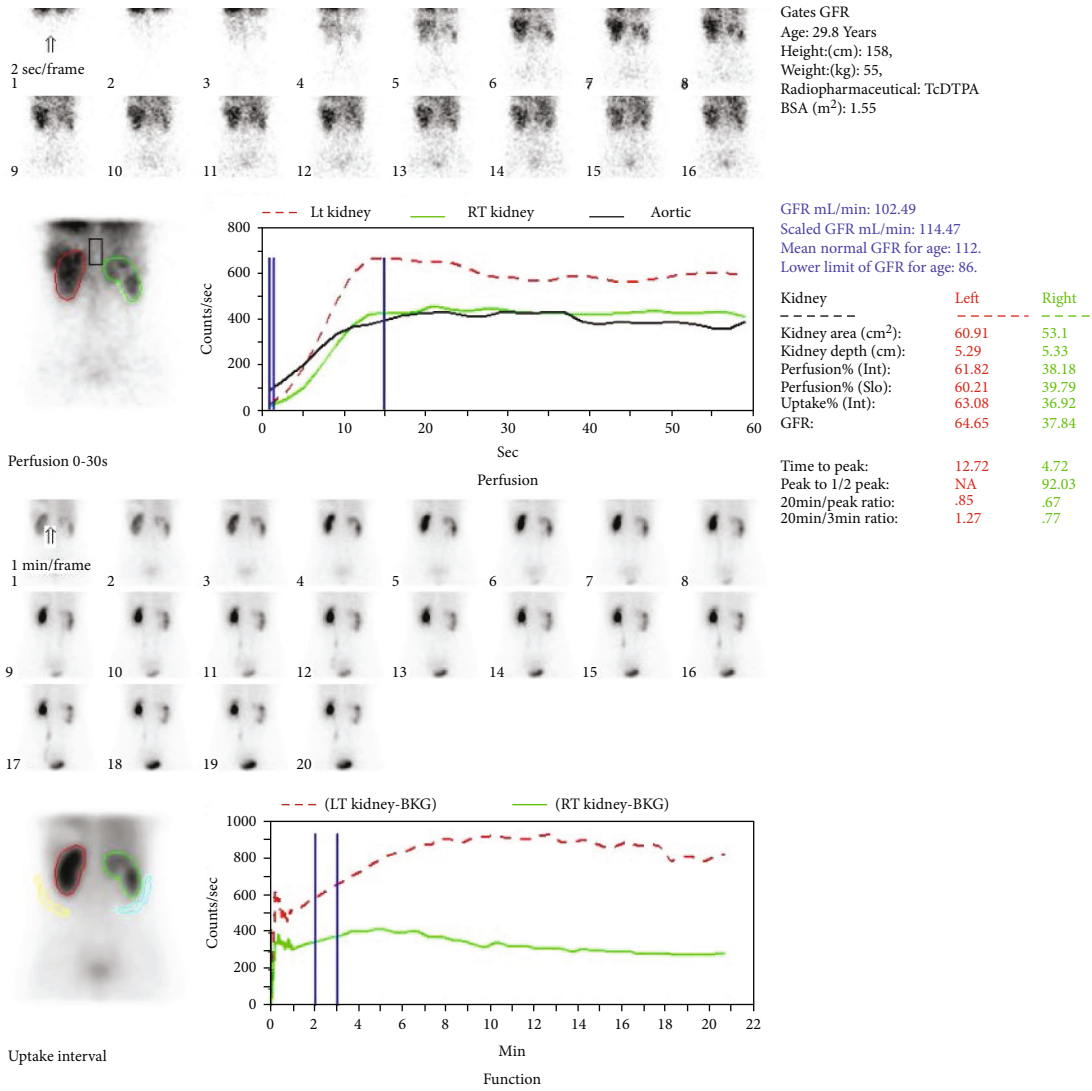

(a)

Figure 1: Continued.

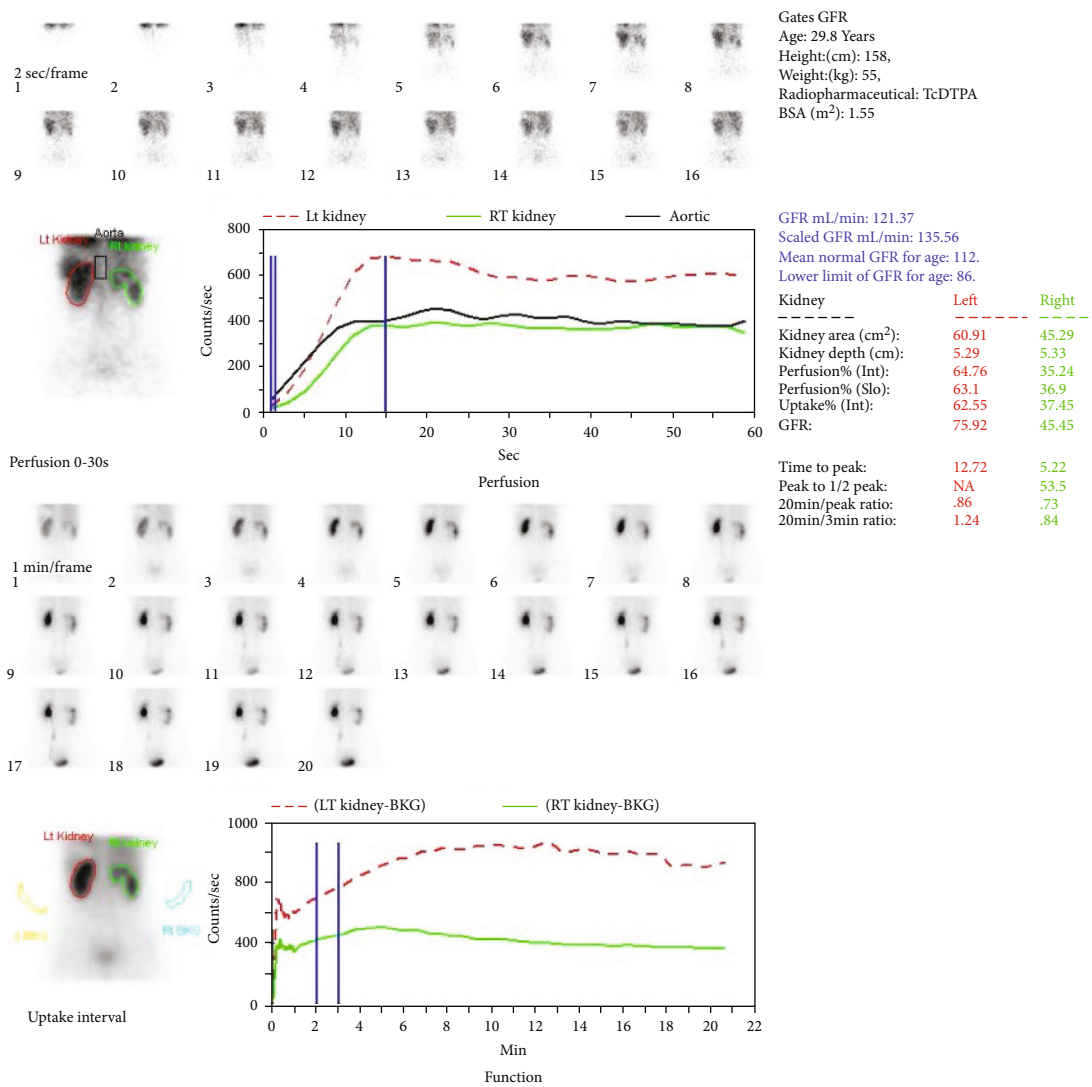

(b)

Figure 1: (a) The kidney and background were delineated according to the standard Gates method, and the GFR was automatically calculated. (b) Blank background, residual standard Gates method, delineation of kidney, and automatic calculation of gGFR′.

consistency coefficient of this group, Kendall's $W = 0.834$, $p = 0.0001$, which showed that the background results drawn by the five doctors were consistent.

3.4. Precisely Split GFR (pGFR) and Its Consistency. The above five double-blinded doctors independently automatically calculated each kidney $gGFR_{left}'$ and $gGFR_{right}'$, entered formula 1, and automatically calculated pGFR. The result was 53.78 ± 28.16 mL/min, with the exception that the background was not delineated, and other operations were the same as normal operations. The consistency of the pGFR results of the five doctors was tested by Kendall's W test. Kendall consistency coefficient of this group, Kendall's $W = 0.956$, $p = 0.0001$, which showed that the background results outlined by the five doctors had a high consistency.

4. Discussion

Inulin clearance is recognized as the gold standard for GFR, but this method is complicated and difficult to promote in clinical practice. The Tc-99m-DTPA multiplasma method has a correlation coefficient of 0.99 with inulin clearance, which is often used as a reference standard for determining renal GFR [3], but it has also failed to achieve widespread clinical acceptance due to the long examination time. The Tc-99m-DTPA double-plasma method has extremely high consistency with the multiple-plasma method, the correlation coefficient is 0.97-0.996, the average deviation is 2.8 mL/min [4], and compared with inulin clearance or the multiple-plasma method, it has better clinical acceptance. In clinical practice, biochemical indicators such as serum creatinine, cystatin C, uric acid, and urea nitrogen are more often used to reflect the state of renal function, but these

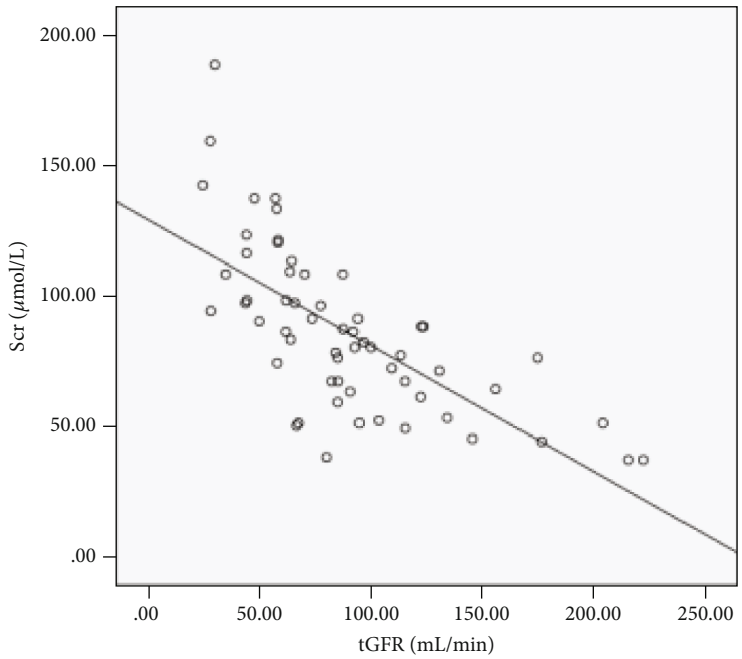

(a)

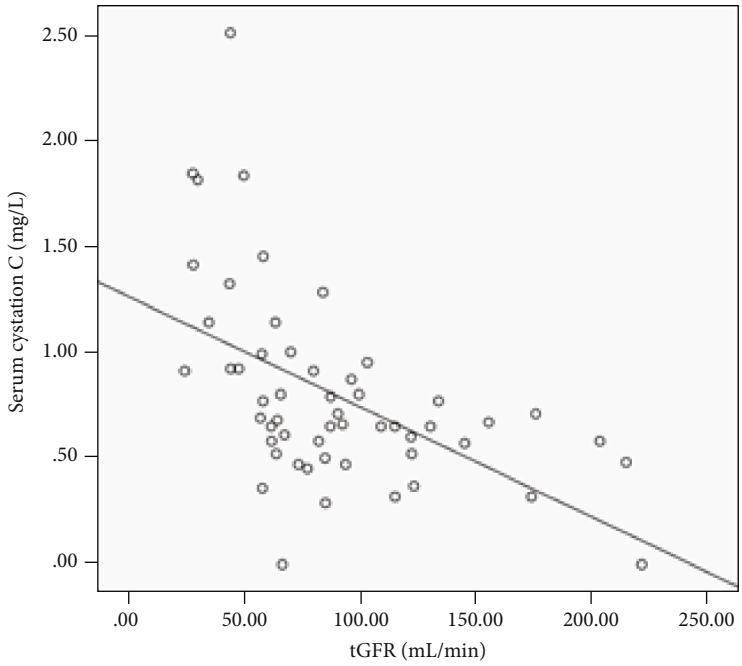

(b)

Figure 2: Continued.

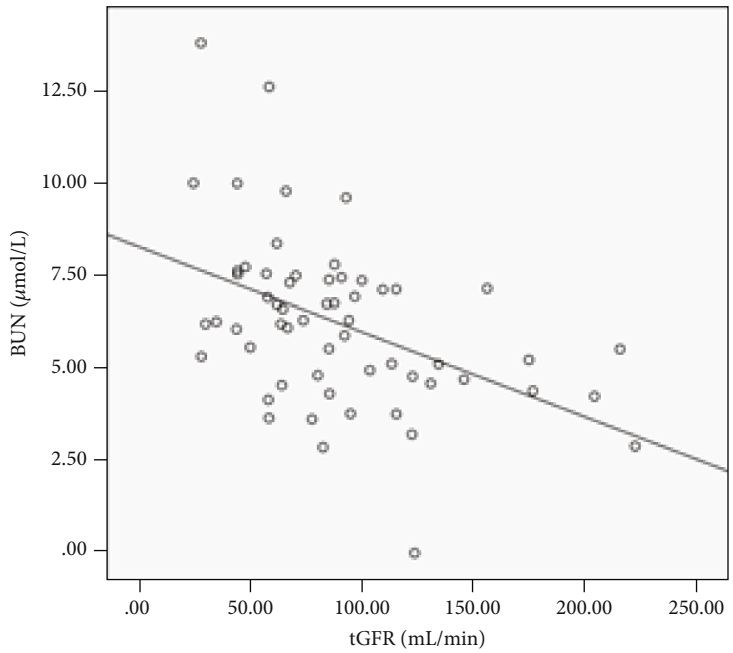

(c)

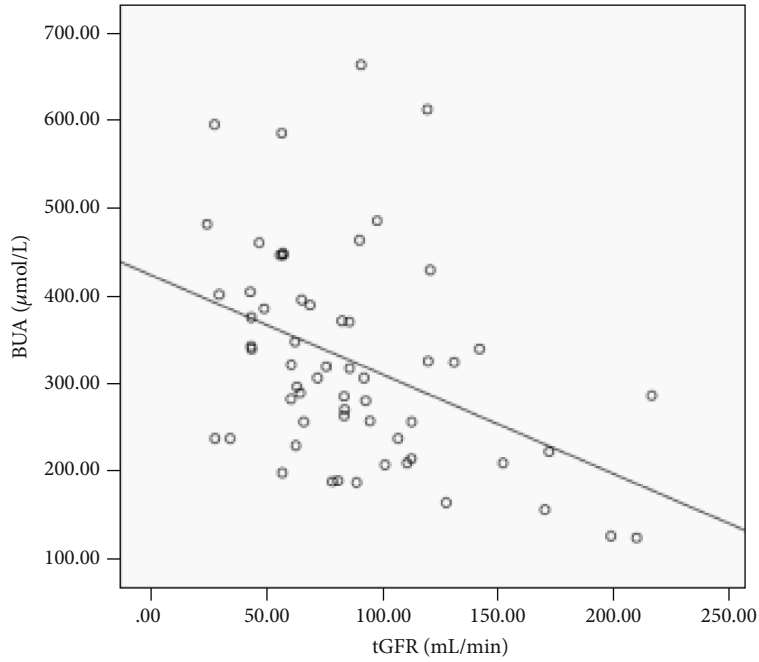

(d)

Figure 2: GFR of double-plasma method showed moderate negative correlation with serum creatinine, cystatin C, urea nitrogen, and uric acid.

indicators are affected by many factors, and numerous clinical studies have confirmed that these indicators work best when renal function is significantly impaired. In addition, none of the above methods can obtain points of renal GFR. Radionuclide renal dynamic imaging is currently the only clinical method that can reflect points of renal GFR and urinary tract information through multiple parameters [5]. It is more sensitive and reliable than other methods [6–8] and is widely used to evaluate renal function.

The method of quantification of renal glomerular filtration rate (GFR) by combining conventional radionuclide renal dynamic imaging and double-plasma method reported in this article can avoid the multiple influencing factors of renal dynamic imaging, as well as significantly improve the ROI of different doctors. The method shows consistency of the scored renal GFR and more importantly can obtain accurate points of renal GFR. This method is very useful for evaluating residual renal function in patients with hydronephrosis or renal cancer

and can provide an objective basis for urologists to perform nephrectomy and the extent of resection.

4.1. The Correlation between Double-Plasma Method and Biochemical Indexes. Creatinine clearance is closely correlated with inulin clearance [9] but is not as exact as inulin clearance in estimating GFR, since a small quantity of creatinine is secreted by the renal tubules [10]. The serum creatinine concentration is affected by factors such as age, gender, muscle composition, and diet. Some drugs and endogenous substances can also interfere with the results. The serum creatinine level will increase only when GFR is reduced to 50%.

The results of this study showed that tGFR was moderately negatively correlated with secreted creatinine, cystatin C, urea nitrogen, and uric acid ($r = -0.692$, -0.527, -0.454, -0.424, $p < 0.01$), and the coefficient of determination R^2 was -0.479, 0.278, 0.206, and 0.172, respectively. Hence, although these biochemical indicators can reflect the state of renal function to a certain extent, serum creatinine, cystatin C, urea nitrogen, and uric acid cannot accurately reflect the renal function, especially the points of renal function to estimate GFR. This is also consistent with previous research results.

This study on the correlation between tGFR and the abovementioned biochemical indicators found that the correlation with tGFR from high to low was serum creatinine, cystatin C, urea nitrogen, and uric acid.

4.2. The Consistency of Standard Gates Method. Tc-99m-DTPA scintigraphy is the most widely used method for estimation of GFR in clinical work [11]. However, numerous clinical studies have confirmed that radionuclide renal dynamic imaging is affected by many factors, such as the delineation of the kidney and the background area of interest (ROI), the attenuation coefficient of the radiation emitted by the radionuclide in the body, the net injection dose, the quality of the projectile injection, the kidney depth, and SPECT hardware equipment [12–15], resulting in unstable accuracy and repeatability, and in the case of severe hydronephrosis, the Gates method may significantly overestimate renal GFR.

In this study, five double-blinded doctors independently used the standard Gates method to delineate the background and the kidneys and calculate the points of renal GFR. The results of the five doctors were tested for consistency by Kendall's W test, and the group's Kendall's coefficient of concordance = 0.834, $p = 0.0001$, which showed high consistency between the five doctors and the automatically calculated results. There remained a 16.4% difference in the results between different doctors, that is, the renal GFR scored by the Gates method could not accurately divide kidney GFR. Numerous studies have tried to optimize the influencing factors of the ROI delineation method required by the Gates method to further improve the consistency of the ROI delineation of different doctors and obtain accurate renal GFR, but these issues have remained methodologically unresolved.

4.3. Accurate Quantitative Results and Consistency of Points of Renal Function. The double-plasma method is recognized as the gold standard for GFR and is commonly used in clinical and scientific research, but it cannot obtain the function of each renal GFR. Tc-99m-DTPA renal dynamic imaging is currently the only method to obtain renal GFR, but its results are affected by many factors, as described above. Although numerous optimization studies have been conducted on the influencing factors of renal dynamic imaging, there is no simple and accurate quantitative method for points of renal function.

In this study, the advantages of points of renal function could be obtained with the accurate total GFR quantification of double-plasma method and renal dynamic imaging. By organically combining the two, five double-blinded doctors independently obtained accurate points of renal GFR, and the consistency of their results was tested by Kendall's W. The Kendall's coefficient of concordance Kendall's $W = 0.956$, $p = 0.0001$, which indicated extremely high consistency in the background results outlined by the five doctors, and was also significantly higher than the consistency of the results obtained by the conventional standard Gates method.

The results of this study showed that the double-plasma method combined with Gates renal dynamic imaging can obtain accurate points of renal GFR, and this method has extremely high consistency between the results drawn and calculated by different doctors. This method should be validated in further multicenter studies in different units.

Data Availability

All data included in this study are available upon request by contact with the corresponding author.

Conflicts of Interest

The authors declare that they have no conflicts of interest.

References

[1] W. C. Huang, A. S. Levey, A. M. Serio et al., "Chronic kidney disease after nephrectomy in patients with renal cortical tumours: a retrospective cohort study," *The Lancet Oncology*, vol. 7, no. 9, pp. 735–740, 2006.

[2] M. D. Blaufox, M. Aurell, B. Bubeck et al., "Report of the radionuclides in nephrourology committee on renal clearance," *Journal of Nuclear Medicine*, vol. 37, no. 11, pp. 1883–1890, 1996.

[3] K. Itoh, "Comparison of methods for determination of glomerular filtration rate:Tc-99m-DTPA renography, predicted creatinine clearance method and plasma sample method," *Annals of Nuclear Medicine*, vol. 17, no. 7, pp. 561–565, 2003.

[4] D. G. Waller, C. M. Keast, J. S. Fleming, and D. M. Ackery, "Measurement of glomerular filtration rate with technetium-99m DTPA: comparison of plasma clearance techniques," *Journal of nuclear medicine*, vol. 28, no. 3, pp. 372–377, 1987.

[5] C. L. Zhang, Q. Li, L. Zuo et al., "Measurement of glomerular filtration rate with renal dynamic imaging:comparison with two-sample method," *JOURNAL OF PEKING UNIVERSITY(-HEALTH SCIENCES)*, vol. 6, pp. 612–615, 2004.

[6] O. Carlsen, "The gamma camera as an absolute measurement device: determination of glomerular filtration rate in 99mTc-

DTPA renography using a dual head gamma camera," *Nuclear Medicine Communications*, vol. 25, no. 10, pp. 1021–1029, 2004.

[7] J. L. Fang, Z. P. Chen, H. Guang et al., "Application of 99Tcm-DTPA to evaluate the renal function of living donors," *Chinese Journal of urology*, vol. 29, pp. 31–34, 2008.

[8] P. Xiaoxi, Z. Hao, C. XueHong, W. Zhengjiang, L. Jiangyan, and Z. Junlin, "SPECT and CT in evaluating preoperative renal function of patients with unilateral hydronephrosis," *Chinese Journal of Medical Imaging*, vol. 2, pp. 120–124, 2015.

[9] J. Brod and J. H. Sirota, "The renal clearance of endogenous "creatinine" in man," *The Journal of Clinical Investigation*, vol. 27, no. 5, pp. 645–654, 1948.

[10] I. Meschan, "Background physiology of the urinary tract for the radiologist," *Radiologic Clinics of North America*, vol. 3, pp. 13–28, 1965.

[11] N. Prasad, S. Barai, S. Gambhir et al., "Comparison of glomerular filtration rate estimated by plasma clearance method with modification of diet in renal disease prediction equation and Gates method," *Indian journal of nephrology*, vol. 22, no. 2, pp. 103–107, 2012.

[12] P. Xie, J.-M. Huang, X.-M. Liu, W. J. Wu, L. P. Pan, and H. Y. Lin, "99mTc-DTPA renal dynamic imaging method may be unsuitable to be used as the reference method in investigating the validity of CDK-EPI equation for determining glomerular filtration rate," *PLoS One*, vol. 8, no. 5, article e62328, 2013.

[13] M. Dopudja, B. Ajdinovic, L. Jaukovic, M. Petrovic, and Z. Jankovic, "Influence of the background activity region selection on the measurement of glomerular filtration rate using the Gates method," *Vojnosanitetski Pregled*, vol. 65, no. 10, pp. 729–732, 2008.

[14] M. Assadi, M. Eftekhari, M. Hozhabrosadati et al., "Comparison of methods for determination of glomerular filtration rate: low and high-dose Tc-99m-DTPA renography, predicted creatinine clearance method, and plasma sample method," *International Urology and Nephrology*, vol. 40, no. 4, pp. 1059–1065, 2008.

[15] Y. C. Ma, L. Zuo, C. L. Zhang, M. Wang, R. F. Wang, and H. Y. Wang, "Comparison of Tc-99mDTPA renal dynamic imaging with modified MDRD equation for glomerular filtration rate estimation in Chinese patients in different stages of chronic kidney disease," *Nephrology, Dialysis, Transplantation*, vol. 22, pp. 417–423, 2007.